Multifunctional photocatalytic substrates and textiles constructed via Layer-by-Layer self-assembly of Ag and TiO2 nanoparticles

Marvin Motay

▶ **To cite this version:**

Marvin Motay. Multifunctional photocatalytic substrates and textiles constructed via Layer-by-Layer self-assembly of Ag and TiO2 nanoparticles. Material chemistry. Université de Strasbourg, 2018. English. NNT : 2018STRAF030 . tel-01997470

HAL Id: tel-01997470

https://theses.hal.science/tel-01997470

Submitted on 29 Jan 2019

HAL is a multi-disciplinary open access archive for the deposit and dissemination of scientific research documents, whether they are published or not. The documents may come from teaching and research institutions in France or abroad, or from public or private research centers.

L'archive ouverte pluridisciplinaire **HAL**, est destinée au dépôt et à la diffusion de documents scientifiques de niveau recherche, publiés ou non, émanant des établissements d'enseignement et de recherche français ou étrangers, des laboratoires publics ou privés.

UNIVERSITÉ DE STRASBOURG

ÉCOLE DOCTORALE DES SCIENCES CHIMIQUES (ED 222)

Institut de Chimie et Procédés pour l'Energie, l'Environnement et la Santé
(ICPEES/CNRS UMR 7515)
et
Institut Charles Sadron
(ICS/CNRS UPR 22)

THÈSE présentée par :

Marvin MOTAY

soutenue le : **03 juillet 2018**

pour obtenir le grade de : **Docteur de l'université de Strasbourg**
Discipline/ Spécialité : Chimie / Chimie des matériaux et photocatalyse

Multifunctional photocatalytic substrates and textiles constructed *via* Layer-by-Layer self-assembly of Ag and TiO_2 nanoparticles

THÈSE dirigée par :

M. KELLER Nicolas	Directeur de recherches, ICPEES, CNRS/Université de Strasbourg
M. DECHER Gero	Professeur, ICS, CNRS/Université de Strasbourg

RAPPORTEURS :

Mme. Karine GLINEL	Professeur, Université catholique de Louvain
Mme. SUÁREZ GIL Silvia	Investigator, CIEMAT Madrid

AUTRES MEMBRES DU JURY :

M. KELLY Peter	Professeur, Manchester Metropolitan University
Mme. BALAN Lavinia	Chargée de recherches, IS2M, CNRS/Université de Strasbourg

MEMBRE INVITE :

Mme. PLOUX Lydie	Chargée de recherches, IS2M, CNRS/Université de Strasbourg

Acknowledgments

First of all, I would like to express my sincere gratitude to Doctor Nicolas Keller and Professor Gero Decher, for giving me the opportunity to do my PhD thesis under their supervisions. Their advices, support, kindness and patience were really helpful during my time as a PhD student.

I am thankful to the Institut CARNOT-MICA for the financial support for the PLASMOTEX project, which allowed me to work in the best conditions.

I am very grateful to Professor Karine Glinel, to Doctor Silvia Suarez Gil and Professor Peter Kelly for accepting to review my PhD work.

I would also like to thank Doctor Lavina Balan for her advice and help regarding the work on silver nanoparticles. Our discussions on the several aspects of the synthesis have led us to great results in this project. Likewise, I am thankful to Mohamed Zaier for teaching me the photoinduced synthesis of silver nanoparticles. In the same way, I am also thankful to Doctor Lydie Ploux for her advices regarding the antibacterial tests on model surfaces. I also thank Charline Soraru for performing the bacteria assays and all the analysis. I am also grateful to Doctor Marie-Hélène Desmont and Bernard Hezard for all their works concerning the bacteria assays on textile surfaces.

I am thankful to Doctor Bertrand Vileno (*POMAM*) and Doctor David Martel (*ICS*) for the EPR characterisations performed in this work. The long discussions with them have been very beneficial during this PhD work.

I would also like to thank Professor Christophe Clobeau-Justin (*LPC, Paris Saclay*) for the TRMC characterisations.

I am also thanking all the persons who helped me with the characterisation analyses: Thierry Dintzer (SEM, *ICPEES*), Doctor Marc Schmutz and Alain Carvahlo (cross-polisher and SEM, *ICS*), Loïc Vidal (TEM, *IS2M*), Vasiliki Papaefthymiou (XPS, *ICPEES*), Doctor Mélanie Legros (TGA, *ICS*) and Doctor Anne Boos (ICP-AES, *IPHC*).

In the same way I am thankful to Steven Bardey who worked very hard on the LbL blade-assisted deposition of silver nanoparticles, as part of his master thesis.

It goes without saying that I also thank all my colleagues and friends at the *ICPEES* and *ICS* who contributed to make every day at work an enjoyable life experience. Thank you Doctor Valérie Caps,

Doctor Matthias Pauly and Fabrice Vigneron. A special thank to Doctor Valérie Keller and Doctor Olivier Félix for their help and support during these 3.5 years.

Let us not forget all the administration staff, to which it was always a pleasure to talk to when I had to deal with all the paperwork. Thank you Katia Bruzzone, Odile Lemble, Jean-Marc Chauvelot, Magalie Meyer, Francine Jacky, Agnes Orb, Nathalie Weber and Véronique Verkruysse.

Thanks to the CAES Cronenbourg All-Star team for the weakly football sessions and the *Tournois Daniel Martina*, where we reached the finals every year (and won the tournament in 2015!). Thanks to all of the BJC membres and Laure Biniek, who helped me a lot with the organisation of events and the HCERES.

Thank you Anida Vydelingum Tayer, you can now say that one of your first students actually did learn to write and speak English.

Of course I am thankful to all my friends for their support during my PhD (in no particular order): Jeni Schwentzel, Ben Foit, Florian "JAP" Gelb, Paul Rouster, Christophe Higy, Julien Ferling, Alain Rach, Thomas Cottineau, Claire Holtzinger, Urelle Biapo, Marisa Rico Santacruz, Irene Gonzalez-Valls, Julien Massue, Edouard Breniaux, Yige Yan, Joanna Wojciechowska, Thomas Favet and Patricia Garcia Munoz.

Let me not forget Michel Tschopp for all the long talks (and bowling session) in the lab, the coffee sessions and the long football discussions. Thanks to Loïc Michel, who was always here when I had some technical problems with my bike. Thanks to Pauline Barrois who was here since the beginning and the end of this long PhD journey. Clément Marchal, you were supportive since our master's years, there have been a lot of good laughters during lectures, in the lab, parties and the Monday beer sessions!!! Thank you guys for always being here for me.

I also want to thank my friends and family for their support: Adrienne, Eloi, Christelle, Antonio, Luc, Léa, Xavier, Véronique, Michel, Yves, Evelyne, Papy and Mamy, Paty and Tata, Diane and Jayen. Thanks to my parents, without you I would never have made it this far. Of course, thank you Melodie for your unconditional help and support, as well as waking me up earlier so I could finish to write the manuscript.

A double thanks to all the people I forgot: you definitely belong here. Except you.

À Adrienne, Diane, Jayen, Maman et Papa

Table of contents

Acknowledgement **3**

Table of contents **5**

List of abbreviations **11**

Résumé en français (Summary in French) **13**

Introduction **33**

Chapter 1: Bibliography **37**

I Indoor air pollution **37**

I.1 Main indoor air pollutants 37

I.1.1 Volatile Organic Compounds 37

I.1.2 Contamination by bacteria 39

I.2 Indoor air pollutant elimination strategies 41

I.2.1 Non-destructive approaches 42

I.2.2 Destructive approaches 42

I.3 Functionalised surfaces for VOC removal and degradation 44

II Heterogeneous photocatalysis **44**

II.1 Principle of heterogeneous photocatalysis 44

II.2 Physical parameters that govern the photocatalysis kinetics 47

II.3 Semiconductor materials used in photocatalysis 49

III Titanium dioxide photocatalyst **50**

III.1 Generalities and structures of titanium dioxide 50

III.2 Titanium dioxide properties in photocatalysis and antibacterial applications 51

III.2.1 Photocatalytic properties 51

III.2.2 Biocidal properties 54

III.3 Enhancing photocatalytic properties of titanium dioxide 56

IV Titania photocatalytic and biocidal properties enhancement with silver nanoparticles 57
IV.1 Silver nanoparticles 57
IV.1.1 Synthesis of silver nanoparticles 57
IV.1.2 Optical properties of silver nanoparticles 59
IV.1.3 Biocidal properties of silver nanoparticles 60
IV.2 Association of silver nanoparticles with titanium dioxide 62
IV.2.1 Silver deposition synthesis on titanium dioxide 62
IV.2.2 Enhancement of photocatalytic properties 63
IV.2.3 Enhancement of biocidal properties 65
V Multilayered thin film constructions *via* Layer-by-Layer self-assembly 66
V.1 Film construction methods 67
V.2 Layer-by-Layer self-assembly 68
V.2.1 Discovery, development and construction of Layer-by-Layer thin films 68
V.2.2 Influence of different parameters in the film construction 70
V.3 Versatility of Layer-by-Layer thin film construction 71
V.3.1 Material choices and range of applications 72
V.3.2 Choice of surfaces 75
V.4 TiO_2, silver film construction on textiles. Focus on LbL construction 76

Chapter 2: Materials and methods 81
I Material and substrate preparation 81
I.1 Materials 81
I.2 Substrate preparation 82
I.2.1 Preparation of model surfaces 82
I.2.2 Preparation of textile fibres 82
II Preparation of solutions and suspensions 83
II.1 Preparation of polyelectrolyte solutions 83
II.2 Preparation of titanium dioxide suspension 83
II.3 Preparation of silver-based photosensitive solutions 83
II.3.1 Preparation of silver photosensitive solution 83
II.3.2 Preparation of silver-titania photosensitive suspension 84
III Deposition methods 84
III.1 Multilayered thin film construction by Layer-by-Layer deposition 84
III.1.1 Dipping LbL deposition on model surfaces 84

III.1.2 LbL film construction in Quartz Crystal Microbalance cell 85
III.1.3 LbL film construction in capillaries 86
III.1.4 Blade-assisted LbL deposition of commercial silver nanoparticles 86
III.2 Photoinduced synthesis and deposition of silver nanoparticles 87
III.2.1 Synthesis/deposition of AgNP on LbL thin films using silver photosensitive solution ... 87
III.2.2 One-pot synthesis of AgNP in LbL thin films 88
III.3 Layer-by-Layer deposition on textile 88
IV Thin film characterisations 89
IV.1 Ellipsometry 89
IV.2 Quartz Cristal Micorbalance with Dissipation 91
IV.3 UV-Visible spectrophotometry 93
IV.4 Microscopy 94
IV.4.1 Scanning Electron Microscopy 94
IV.4.2 Transmission Electron Microscopy 95
IV.5 X-Ray Photoelectron Spectroscopy 96
IV.6 Time Resolved Microwavedconductivity 99
IV.7 Electronic Paramagnetic Resonance 101
IV.8 Chemical analysis 104
V Other characterisations methods 105
V.1 X-Ray Diffraction 105
V.2 Dynamic Light Scattering 106
VI Photocatalytic activity and performance of LbL thin films 107
VI.1 Gas-phase photocatalysis 107
VI.1.1 Experimental setup 107
VI.1.2 Test protocols and calculations 109
VI.2 Antibacterial activity 111
VI.2.1 Model surfaces 112
VI.2.2 Textile surfaces 112

Chapter 3: Titania and polyelectrolytes thin films – construction on model surfaces 115
I Film construction on model surfaces 115
I.1 Preparation and characterisation of P25 titania suspension 116
I.2 Titania and polyelectrolytes thin film construction and characterisation 118
I.2.1 Monitoring of film construction 119

I.2.2 Amount of titania deposited 124
II Gas-phase photocatalytic performances of LbL titania and polyelectrolytes films 127
II.1 Photocatalytic degradation results of formic acid by LbL films 127
II.1.1 Conversion of formic acid 128
II.1.2 Carbon dioxide formation 130
II.1.3 Influence of polyelectrolytes in photocatalytic tests 132
II.1.4 Quantum yield calculations 133
II.2 Discussion on unusual photocatalytic behavior of LbL titania film 136
II.2.1 Time Resolved Microwave Conductivity 136
II.2.2 Electronic Paramagnetic Resonance 139
II.2.3 Comparison with different types of LbL titania films 141
II.2.4 Discussion 144
III Antibacterial activity of LbL titania thin films on model surfaces 148
III.1 Film preparation 149
III.2 Control sample results 150
III.3 Titania thin films results 152
III.4 Comparison with gas-phase photocatalysis results 154
Conclusion 155

Chapter 4: Titania and silver nanoparticles hybrid thin films – construction on model surfaces 157
I Titania films containing commercial Ag nanoparticles 158
I.1 Blade-assisted LbL deposition of Ag nanoparticles 158
I.2 Characterisations and activity of titania and AgNP blade-assisted hybrid film 159
I.2.1 Characterisations 159
I.2.2 Activity of hybrid films 161
II Titania films containing photoinduced Ag nanoparticles 163
II.1 Stability of PEI/PSS/TiO_2 films submitted to AgNP photoinduced synthesis protocol 163
II.2 Classical Ag nanoparticles photoinduced synthesis on single layer pair films 165
II.2.1 Characterisations of photoinduced silver nanoparticles 166
II.2.2 Construction and characterisations of PEI/PSS/TiO_2/x%Ag films 168
II.2.3 Photocatalytic activity of PEI/PSS/TiO_2/x%Ag films 176
II.3 One-pot photoinduced synthesis of AgNP in PEI/PSS/(x%Ag-TiO_2) films 179
II.3.1 Characterisations of AgNP synthesised with the x%Ag-TiO_2 photosensitive suspension ... 180

II.3.2 Construction and characterisations of PEI/PSS/(x%Ag-TiO_2) films 182
II.3.3 Photocatalytic performances of of PEI/PSS/(x%Ag-TiO_2) films 192
III Biocidal activity of Ag and titania hybrid thin films 201
III.1 Choice of Ag-TiO_2 hybrid thin films 201
III.2 Biocidal properties of Ag-TiO_2 LbL thin film results and discussion 203
Conclusion 206

Chapter 5: Titania and silver-titania thin films – construction on textile surfaces 209
I Film construction on model surfaces 209
I.1 Titania and polyelectrolytes LbL film on textile 209
I.1.1 Monitoring of film construction 210
I.1.2 SEM characterisation 212
I.2 Silver-titania hybrid film constructed on textile 213
II Photocatalytic properties of functionalised textiles towards the degradation of HCOOH 215
II.1 Formic acid degradation by titania and polyelectrolytes LbL film coated on textile 215
II.2 Formic acid degradation by silver-titania hybrid film coated on textile 218
III Biocidal properties of functionalised textiles 220
III.1 Biocidal properties of PEI/$(PSS/TiO_2)_n$ films constructed on textile surfaces 220
III.2 Biocidal properties of Ag-TiO_2 hybrid films constructed on textile surfaces 222
IV Stability of films constructed on textile 225
III.1 Abrasion tests 225
III.2 Washing treatments 229
III.2.1 Washing treatments with 1 and 10 cycles 229
III.2.2 Dry cleaning 232
Conclusion 235

Conclusion and perspectives 237

References 243

Appendix 255

List of abbreviation

AgNP	Silver nanoparticles
AuNP	Gold nanoparticles
DLS	Dynamic Light Scattering
CVD	Chemical Vapour Deposition
EPR	Electronic Paramagnetic Resonance
LbL	Layer-by-Layer
LP	Layer pair
NP	Nanoparticle
PAA	Poly(acrylic acid)
PAH	Poly(allylamine hydrochloride)
PDDA	Poly(diallyldimethylammonium chloride)
PEI	Poly(ethylene imine)
PMA	Poly(methacrylate acid)
POSS	Poly(hedral oligomeric silesquioxanes)
PPA	Poly(phosphoric acid)
PSS	Poly(sodium styrenesulfonate)
PVD	Physical Vapour Deposition
PVS	Poly(vinyl siloxane)
QCM-D	Quartz Crystal Microbalance with Dissipation
SEM	Scanning Electron Microscopy
TEM	Transmition Electron Microscopy
TiNT	Titania nanotubes
TRMC	Time Resolved Microwave Conductivity
UV	UltraViolet
UV-A	UltraViolet-A
UV-C	UltraViolet-C
UV-Vis	UltraViolet-Visible
VOC	Volatile Organic Compounds
WF	Silicon wafer
XPS	X-Ray Photoelectron Spectroscopy
XRD	X-Ray Diffraction

Substrats et textiles multifonctionnels construits par assemblage couche-par-couche de nanoparticules d'Ag et TiO_2

Il est de nos jours admis que l'air intérieur est plus pollué que l'air extérieur. Selon les rapports de l'Organisation Mondiale de la Santé (*World Health Organization*, WHO), sur les 7 millions de morts prématurées en 2012 liées à la pollution de l'air dans le monde, 3,7 millions d'entre elles sont associés à la pollution de l'air intérieur [1], [2]. L'un des arguments les plus fréquemment avancés pouvant expliquer cette baisse de la qualité de l'air intérieur est lié à la dégradation des objets et des matériaux utilisés au quotidien au sein des foyers. Ces matériaux, comme le bois ou les peintures, sont en effet des sources d'émission de composés organiques volatiles (COVs), par exemple l'acétaldéhyde, l'éthylène ou encore le formaldéhyde [3], [4]. De plus la contamination de surface par des agents biologiques tels que les bactéries *Escherichia Coli*, contribue à augmenter la pollution intérieur. Bien que n'étant pas à la base des vecteurs de transmissions bactériennes, certains environnements dans les bâtiments peuvent devenir favorables à la prolifération des bactéries, notamment au niveau des climatiseurs, des déshumidificateurs, des chauffe-eaux ou encore des tuyaux de plomberie. La contamination par les bactéries devient alors possible de personne à personne par contact physique ou par la contamination des surfaces. Il est à noter que certaines bactéries peuvent être source de COVs. De nombreuses approches ont été étudiées afin de développer des dispositifs capables d'améliorer la qualité de l'air intérieur, basées sur des technologies non-destructrices (adsorption, filtration…) ou destructrices (ozonation, photolyse UV…). Ces technologies peuvent être de grands consommateurs d'énergie et parfois ne sont que des solutions de stockage ou de transfert de la pollution [3], [5]. En outre, la plupart de ces technologies ne permettent pas une action conjointe contre les agents chimiques et biologiques.

La photocatalyse hétérogène est un procédé basé sur l'utilisation d'un matériau semi-conducteur, permettant la mise en œuvre de réactions redox de surface à température ambiante, et notamment la dégradation de nombreuses molécules organiques (Fig. 1) [6], [7]. Ce procédé présente de nombreux avantages comme le fait d'être une technique dite « douce », peu coûteuse et verte, ciblant à la fois des polluants chimiques et biologiques, et pouvant opérer à température ambiante.

L'illumination d'un matériau semi-conducteur par un rayonnement d'une énergie supérieure ou égale à celle de sa bande interdite permet la génération au sein du matériau de paires électron/trou. Ces charges photogénérées peuvent alors se recombiner ou migrer à la surface du semi-conducteur, où elles peuvent alors être impliquées dans des réactions d'oxydo-réductions, qui permettent le cas échéant de minéraliser *in fine* la plupart des molécules organiques adsorbées. Le dioxyde de titane (TiO_2) est le semi-conducteur le plus utilisé en photocatalyse, notamment par l'intermédiaire d'une de ses références commerciales le TiO_2 P25 Aeroxide, en raison de la position relative de ses bandes de conduction et de valence, de son efficacité quantique, de sa stabilité photochimique et de son faible coût [8]. Cependant la génération des porteurs de charges n'est effective que sous irradiation UV-A et le taux de recombinaison des porteurs photogénérés demeurent plus élevé que le taux de migration vers la surface du semi-conducteur [9]. Ainsi, les recherches se sont focalisées sur l'amélioration des propriétés photocatalytiques du TiO_2 en utilisant différentes stratégies basées sur la mise en œuvre de morphologies et/ou de tailles de nanoparticules spécifiques, sur la modification de la structure chimique du TiO_2 (dopage anionique/cationique) ou encore en associant le TiO_2 avec d'autres matériaux [10], [11].

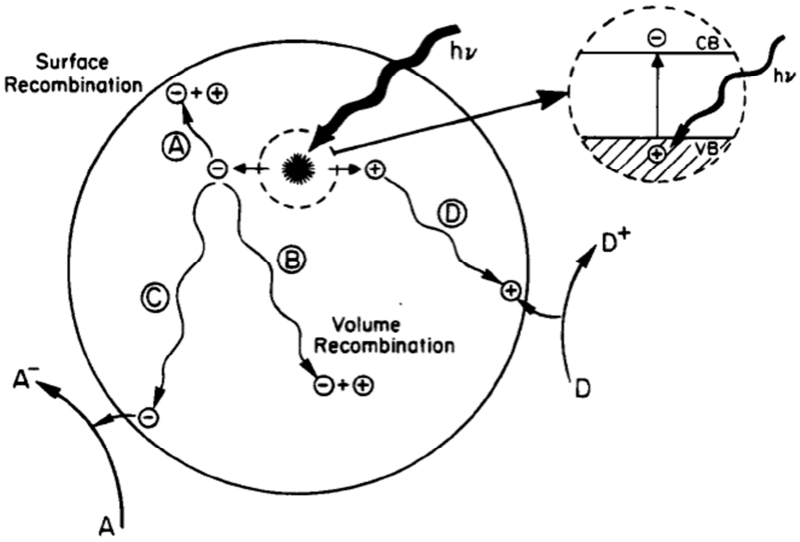

Fig. 1: Principe simplifié d'une réaction photocatalytique avec un matériau semi-conducteur sous irradiation hν [12].

L'association de TiO_2 avec des nanoparticules métalliques a déjà montré des effets bénéfiques et peut permettre l'exaltation des propriétés photocatalytiques du semi-conducteur lorsque mise en oeuvre de manière appropriée [13]–[15]. Il est rapporté dans la littérature que cette exaltation par des nanoparticules métalliques s'explique par:

- Un effet de trappe à électrons pour les électrons photogénérés par le TiO_2 sous irradiation UV-A, qui peut permettre de diminuer le taux de recombinaison des charges.

- Un effet plasmonique qui est fonction notamment de la nature et de la morphologie des nanoparticules métalliques. Ainsi cet effet permettrait d'améliorer les propriétés photocatalytiques du TiO_2 sous irradiation UV-A, voire sous lumière visible.

L'exaltation par ces deux types d'effet est cependant dépendante de la présence ou de la qualité du contact électrochimique entre le TiO_2 et les nanoparticules métalliques (barrières de Schottky, distance entre les deux matériaux,…), de la taille, de la morphologie et de la distribution des nanoparticules métalliques, ainsi que du ratio semi-conducteur/nanoparticules métalliques [10].

Ce travail s'est focalisé sur l'association de TiO_2 avec des nanoparticules d'argent (AgNP) comme nanoparticules métalliques en raison de leurs propriétés plasmoniques (facteur de qualité Q élevé), ainsi que leurs propriétés biocides [14], [16]. L'association de ces deux composés pourrait donc permettre l'exaltation des propriétés photocatalytiques du TiO_2 sous irradiation UV-A, ainsi que des propriétés bactéricides sous UV-A (TiO_2 et AgNP). De plus, l'association de TiO_2 avec AgNP a déjà montré des résultats prometteurs en photocatalyse.

L'objectif de cette thèse consistait à développer un procédé de fonctionnalisation des surfaces et des textiles par des films à base de nanoparticules de TiO_2 et d'argent, pour obtenir des surfaces et des textiles photocatalytiques multifonctionnels présentant des propriétés épurantes et auto-décontaminantes/bactéricides sous irradiation UV-A. L'approche retenue pour fonctionnaliser ces surfaces a été la technique du couche-par-couche (*Layer-by-Layer*, LbL) permettant la construction de films minces à base de matériaux de charges opposées, sur une surface préalablement chargée (Fig. 2) [17], [18]. L'immersion successive des substrats dans les solutions/suspensions contenant les matériaux à déposer, a permis la fabrication de films minces à base de nanoparticules (TiO_2 et Ag) et de polyélectrolytes, n'endommageant pas les surfaces et les fibres de textiles. Un deuxième aspect des travaux visait à mettre à profit l'association contrôlée des nanoparticules d'Ag et de TiO_2 pour exalter les propriétés photocatalytiques de ces films.

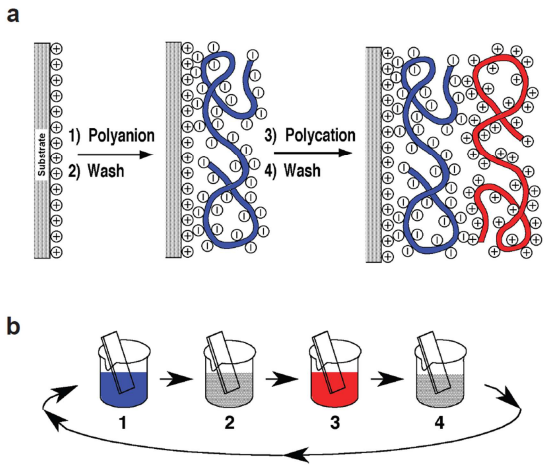

Fig. 2: (a) Schématisation de la construction d'un film multicouches de polyélectrolytes par la technique du LbL sur une surface plane. (b) Construction des films LbL par la méthode de trempage. Les étapes intermédiaires de rinçage dans de l'eau, permettent la surcompensation des charges et d'enlever l'excès de matériaux non adsorbé. La versatilité de cette technique lui permet d'utiliser différents types de matériaux, tels que des nanoparticules, et d'être appliquée sur des surfaces de géométries variées [17], [18].

Trois types de films - qui font l'objet de trois chapitres - ont ainsi été construits sur différents types de substrats, avec :

1. l'élaboration de films multicouches à base de nanoparticules de TiO_2 et de polyélectrolytes sur des surfaces dites « modèles »,

2. l'élaboration de films hybrides Ag-TiO_2 sur surfaces modèles, avec l'association des nanoparticules de TiO_2 avec des AgNPs par LbL, et la synthèse des AgNPs sur ou au sein des films,

3. le transfert des techniques de construction de ces films sur des surfaces textiles.

Dans le cas des différents systèmes, les films construits ont été caractérisés, testés pour la dégradation de l'acide formique en phase gaz sous irradiation UV-A (Fig. 3 et 4), puis des tests anti-bactériens ont été effectués sur les films afin d'évaluer leurs propriétés biocides.

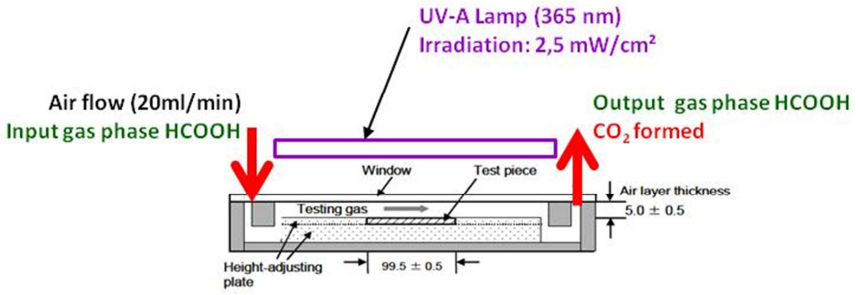

Fig. 3: Représentation schématique du réacteur photocatalytique dérivé du standard ISO 22197.

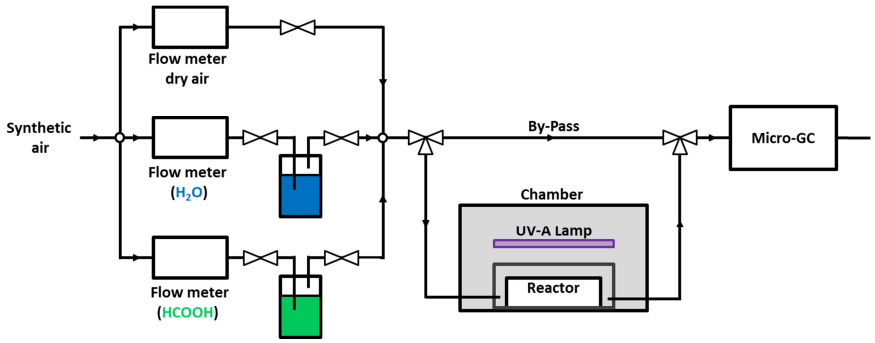

Fig. 4: Schéma du montage du test photocatalytique pour la dégradation de l'acide formique en phase gazeuse.

Cette thèse a été réalisée dans le cadre du projet PLASMOTEX, financé par l'Institut Carnot MICA d'Alsace, au sein d'un consortium de partenaires composé de l'Institut de Chimie et Procédés pour l'Energie, l'Environnement et la Santé (ICPEES, Strasbourg), de l'Institut Charles Sadron (ICS, Strasbourg), de l'Institut des Sciences des Matériaux de Mulhouse (IS2M) et du CRITT Aérial (Illkirch).

1. Films multicouches photocatalytiques à base de TiO_2 et de polyélectrolytes construits sur surfaces modèles

Etant donné le nombre très limité de méthodes de caractérisations physico-chimiques de surfaces irrégulières comme les textiles, une étude complète de la construction des films multicouches sur des surfaces modèles a été mise en œuvre pour optimiser les conditions de dépôt des différents composants et caractériser les films avant de fonctionnaliser des textiles et d'évaluer leurs propriétés. Ainsi des films multicouches à base de poly(éthylène imine) (PEI), de poly(styrène sulfonate) (PSS) et de TiO_2 P25 Aeroxide, ont été construits par le biais de la technique LbL par

trempage. Ces films PEI/(PSS/TiO_2)$_n$ ont été construits sur des surfaces modèles telles que des substrats en silicium et des lamelles de verre et de quartz, adaptés pour chaque technique de caractérisation.

Le suivi de la croissance des films PEI/(PSS/TiO_2)$_n$ a été effectué par ellipsométrie, spectroscopie UV-visible en transmission et microbalance à quartz, et a mis en évidence la construction régulière des films multicouches, dont la densité surfacique de TiO_2 a été estimée par analyses chimiques ICP-AES à 7 µg/cm² par paire de couches. Ces films restent transparents à la lumière UV et visible lorsque le nombre de paires de couches augmentent (au moins jusqu'à 10 paires de couches).

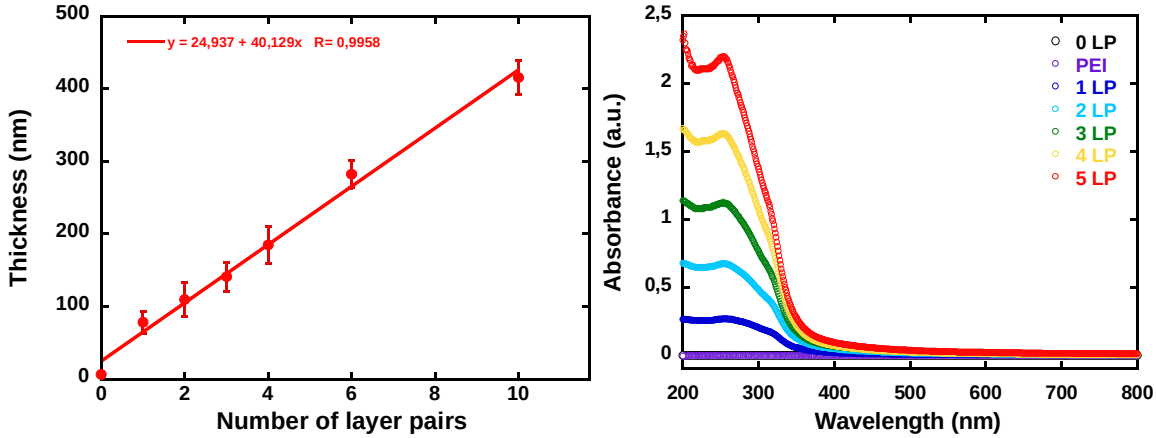

Fig. 5: Suivi de la construction des films PEI/(PSS/TiO_2)$_n$ (à gauche) par ellipsométrie pour des films construits sur wafer de silicium, (à droite) par spectrophotométrie UV-Visible pour des films construits sur des lamelles de quartz.

Les films multicouches PEI/(PSS/TiO_2)$_n$ se caractérisent par une excellente homogénéité, et ce même dans le cas du film composé d'une unique paire de couches. Ceux-ci montrent une bonne porosité, permettant l'accessibilité aux sites actifs pour le polluant gazeux à dégrader. Par ailleurs la caractérisation des films en coupe transverse par microscopie à balayage a permis d'estimer l'épaisseur des films à 40 nm par paire de couches. Cette valeur d'épaisseur reste cohérente avec les résultats obtenus par ellipsométrie.

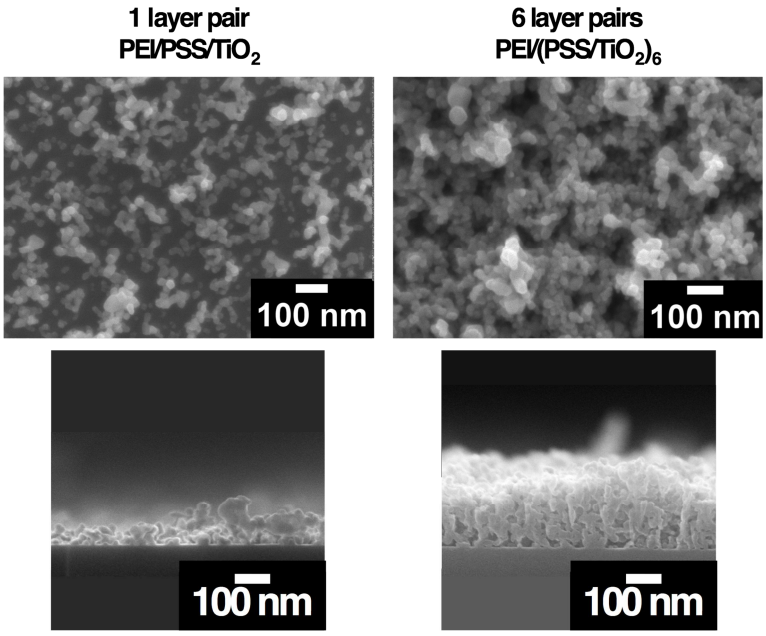

Fig. 6: Caractérisation par microscopie électronique à balayage des films multicouches contenant une et 6 paires de couches. Les images du bas représentent une coupe transverse des échantillons.

Les tests photocatalytiques réalisés sous UV-A (365 nm) ont mis en évidence un comportement très intéressant en fonction du nombre de paires de couches, différent du comportement habituel des revêtements à base de TiO_2 (*i.e*. augmentation quasi-linéaire puis stabilisation) (Fig. 7). En effet, un maximum de conversion de HCOOH, accompagné par un maximum de minéralisation en CO_2, est obtenu pour une unique paire de couches. L'efficacité des films ne contenant qu'une seule couche de TiO_2 est d'autant plus visible grâce au calcul des rendement quantiques globaux and efficaces des films PEI/$(PSS/TiO_2)_n$ sous irradiation UV-A (Fig. 8). De plus on peut noter que les concentrations de CO_2 formées sont quasi-stœchiométriques aux concentrations de HCOOH dégradées, ce qui indique que la dégradation photocatalytique des polyélectrolytes (PEI, PSS) est faible. Cependant une surproduction de l'ordre de 10-15 ppm_v a été observée (pour une concentration de HCOOH de 45 ppm_v) pour les films contenant une paire de couches PSS/TiO_2, indiquant une possible dégradation des polyélectrolytes. Globalement ce résultat est très intéressant d'un point de vue applicatif, car il limiterait les volumes de suspensions, de solutions et de photocatalyseur nécessaire pour élaborer les films tout en simplifiant le transfert de technologie, ce qui devrait jouer en faveur d'une meilleure accroche sur les fibres textiles.

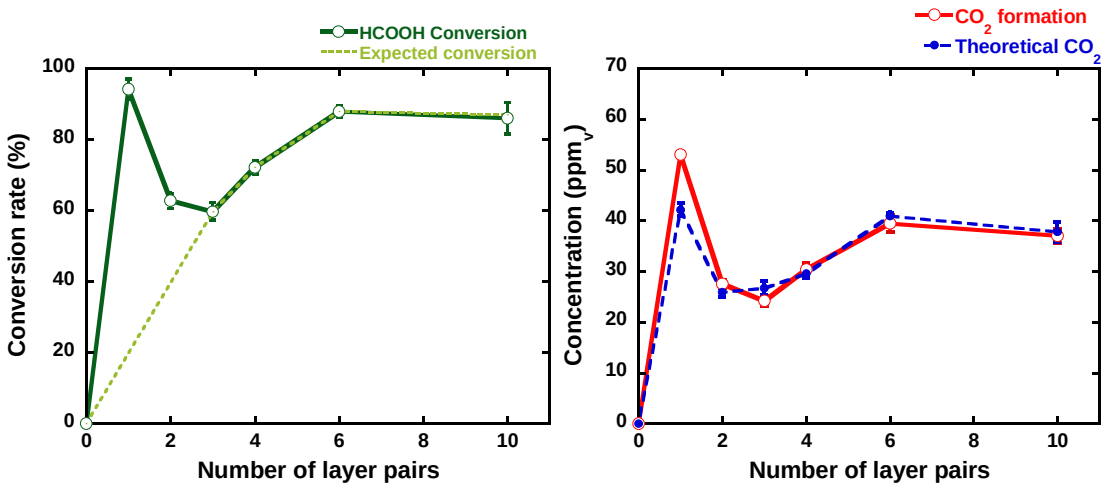

Fig. 7: Dégradation de l'acide formique et minéralisation en CO_2 sous UV-A par des films PEI/$(PSS/TiO_2)_n$. Conditions expérimentales : [HCOOH] = 45 ppm_{vol}, débit total = 20 mL/min, UV-A (2.5 mW/cm²), substrat modèle de 36 cm² (8 cm x 4.5 cm). A gauche : conversion d'acide formique en fonction du nombre de paires de couches. La courbe en pointillé montre un comportement classique de la dégradation d'un polluant en fonction de la concentration en TiO_2 ; la courbe pleine représente le comportement observé lors des tests photocatalytiques. A droite : formation de CO_2 montrant le même comportement que la conversion de l'acide formique ; la courbe en pointillé représente la concentration en CO_2 correspondant à sa formation stoechiométrique par rapport à la conversion de l'acide formique.

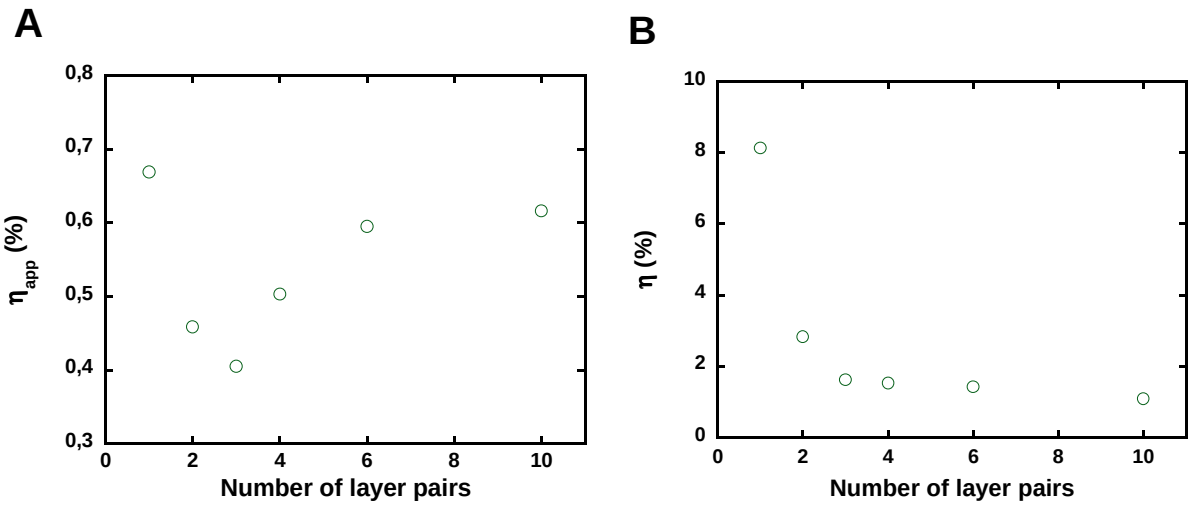

Fig. 8: Rendement quantique apparent (A) et efficace (B) des films PEI/$(PSS/TiO_2)_n$ en fonction du nombre de paires de couches. Le rendement quantique apparent se réfère à la quantité de photons reçue par le film, tandis que le rendement quantique efficace fait référence à la quantité de photons absorbée par le film.

Des tests photocatalytiques sans HCOOH ont mis en évidence une formation de CO_2 pour tous les films sous irradiation UV-A, avec une concentration de l'ordre de 10-15 ppm_v. Ce résultat suggère une dégradation du PEI étant donné que la concentration en CO_2 formée est indépendante du nombre de paires de couches. Cependant cette dégradation reste négligeable pour des films contenant plus d'une paire de couches PSS/TiO_2, lorsque les tests sont réalisés avec un flux d'air contenant de l'HCOOH. Des études complémentaires par *Time Resolved Microwave Conductivity* (TRMC) et Résonance Paramagnétique Electronique (RPE) ont été réalisées sur les films PEI/(PSS/TiO_2)$_n$ afin de comprendre le comportement non-conventionnel des films ne comportant qu'une seule paire de couche, ainsi que la présence du plateau de conversion obtenu à partir de 6 paires de couches.

Les caractérisations par TRMC et RPE ont montré un comportement conventionnel des films en fonction du nombre de paires de couches. Ainsi l'hypothèse d'un plus grand nombre de porteurs de charge photogénérés pour les films ne contenant qu'une seule couche de TiO_2 et celle d'un écrantage de la lumière lorsque le nombre de paires de couches augmente ont pu être exclues. Une hypothèse basée sur le rôle des polyélectrolytes en tant que barrières diffusionnelles à l'HCOOH, a pu être proposée en construisant des films de différentes architectures contenant plusieurs paires de couches de polyélectrolytes entre les couches de TiO_2. Une autre hypothèse concernant un changement de la structure des films en ajoutant des couches de TiO_2, a pu être émise pour expliquer la baisse en conversion d'HCOOH après le dépôt de plus d'une paire de couche PSS/TiO_2.

Les propriétés biocides des films multicouches PEI/(PSS/TiO_2)$_n$ ont été évaluées sous irradiation UV-A sur substrats modèles en utilisant des souches bactériennes médicinales *Escherichia coli* SCC1 ensemencées sur les films multicouches, la colonisation bactérienne des films étant caractérisée par microscopie confocale (Fig. 9). Les tests effectués ont mis en évidence l'existence d'une efficacité antibactérienne des films multicouches pour une illumination UV-A de 60 min dès une paire de couches, et qui atteint un plateau dès 3 paires de couches, pour lesquelles une diminution très significative du nombre de bactéries vivantes est observée. Ce comportement résulte directement de la taille micrométrique des bactéries.

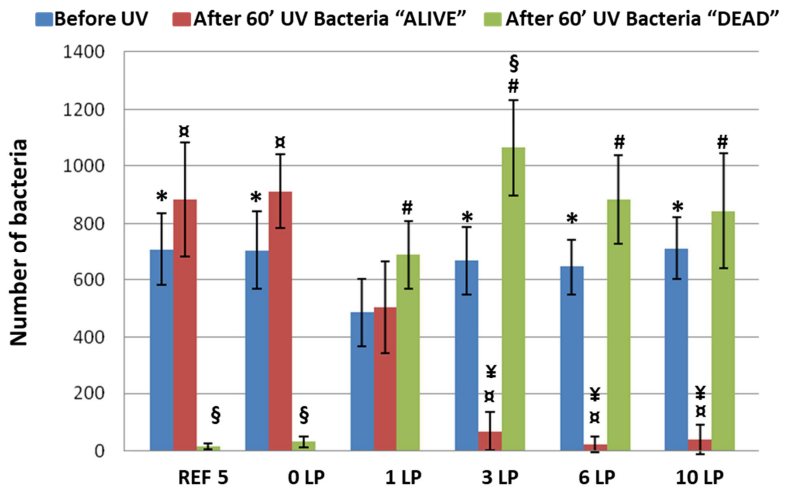

Fig. 9: Tests antibactériens des films multicouches PEI/$(PSS/TiO_2)_n$. Bactéries testées : *Escherichia Coli*, UV-A (2.5 mW/cm²), temps d'irradiation = 60 min, wafer de silicium de 2 cm². Le nombre de bactéries (*Escherichia coli* SCC1) dites « ALIVE » et « DEAD » est déterminé par microscopie confocale. « REF 5 » représente un film multicouches comportant 9 paires de couches de poly(styrène sulfonate), PSS, et de poly(diallyldimethylammonium), PDDA, $(PEI/(PSS/PDDA)_9)$. (*****) significativement différent de « 1LP before UV » ($p < 0.05$) ; (**¤**) significativement différent de « 1 LP after UV (ALIVE) » ($p < 0.05$) ; (**¥**) significativement différent de « 0 LP, 1 LP et REF 5 after UV (ALIVE) » ($p < 0.05$) ; (**#**) significativement différent de « 0 LP after UV (DEAD) » ($p < 0.05$) ; (**§**) significativement différent de « 1 LP after UV (DEAD) » ($p < 0.05$).

2. Construction de films hybrides contenant une seule couche de TiO_2 et de nanoparticules d'Ag sur des surfaces modèles

En raison de l'excellente activité photocatalytique observée pour une seule paire de couches, les travaux sur les films hybrides Ag-TiO_2 se sont focalisés sur les films ne contenant qu'une seule couche de TiO_2, i.e. PEI/PSS/TiO_2.

A titre de comparaison, des suspensions commerciales de nanoparticules d'Ag (AgNPs) de différentes tailles ont été utilisées dans un premier temps pour la construction des films multicouches. L'étape de dépôt d'AgNPs a été réalisée *via* une imprégnation de type « Doctor Blade » afin de pouvoir étaler la suspension d'AgNPs de manière contrôlée, tout en conservant les paramètres utilisés lors de la construction des films multicouches par trempage sur des surfaces modèles. Les analyses chimiques ont permis de mettre en évidence la présence d'AgNPs au sein des films. Les tests de réactivité de ces films ont montré une augmentation significative de la conversion d'HCOOH (de 12% à 27% de conversion pour un film contenant des AgNPs). Ces résultats nous ont confortés dans notre stratégie de réaliser des films LbL hybrides Ag-TiO_2.

L'approche retenue dans un deuxième temps pour la synthèse d'AgNPs est une synthèse par voie photochimique, i.e. photoinduite [19]. Cette méthode consiste à irradier sous UV-A (365 nm), une solution photosensible contenant un précurseur d'argent ($AgNO_3$) et un chromophore (Irgacure 2959) dissous dans un solvant (de l'eau en général). Dans cette approche, le chromophore activé agit comme un générateur de deux radicaux libres, l'un permettant la réduction des ions Ag^+ en leur forme métallique Ag^0, qui pourront ensuite former des AgNPs et l'autre permettant un contrôle de la taille et de la forme des AgNPs synthétisées.

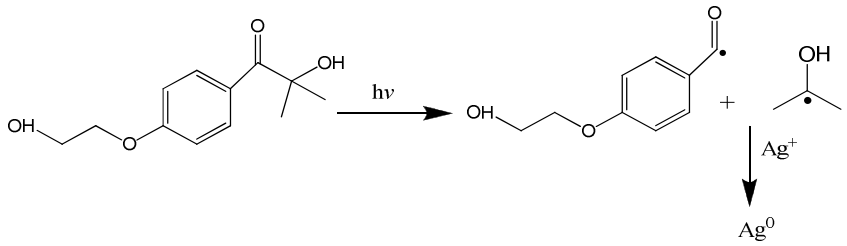

Fig. 10: Photo-clivage du chromophore Irgacure 2959 et réduction des cations Ag^+ lors de la synthèse photoinduite des nanoparticules d'argent.

Cette méthode de synthèse a été mise en œuvre sur surfaces modèles selon deux approches. L'une, dite « classique », a consisté à synthétiser les AgNPs sur les films multicouches construits au préalable. L'autre a consisté en la synthèse *in situ* des AgNPs dans la suspension de TiO_2 utilisée pour la construction du film ; il s'agit d'une synthèse *one-pot* combinant la construction d'une couche TiO_2-précurseur d'argent par LbL et la synthèse d'AgNPs directement au sein du film.

Ces deux approches ont été mises en œuvre avec succès et la synthèse des AgNPs a été confirmée par analyses chimiques, spectroscopie UV-Vis, microscopie électronique à transmission et par spectroscopie photoélectronique X (XPS). Dans les deux cas, les AgNPs ont été synthétisées en contact intime avec les nanoparticules de TiO_2 et possèdent une distribution de taille étroite et centrée sur 3-4 nm. Les caractérisations par XPS ont cependant suggéré que les AgNPs synthétisées selon l'approche *one-pot* seraient localisées non pas en surface, mais dans la porosité des films ou à l'interface PSS-TiO_2. De plus, les films construits par la méthode *one-pot* restent transparents après l'irradiation UV pour la synthèse des AgNP, rendant les films obtenus par le biais de cette méthode intéressants d'un point de vue applicatif.

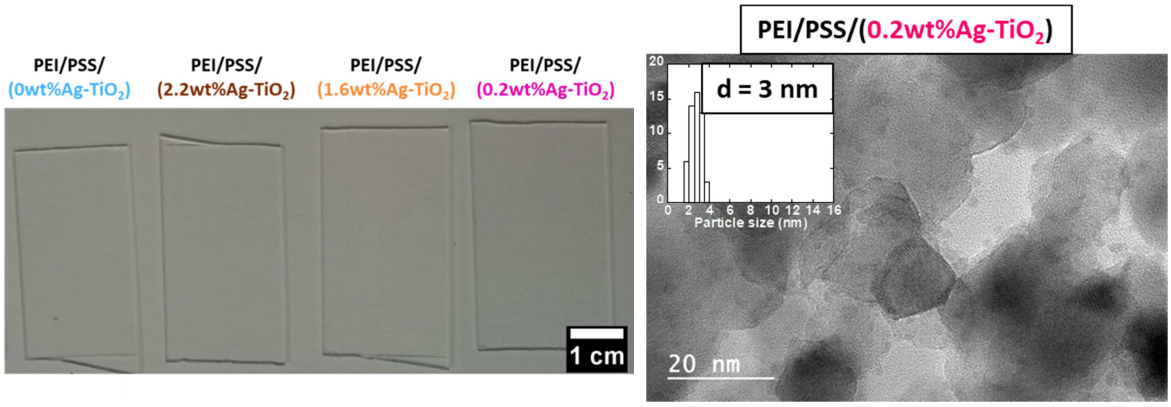

Fig. 11: (Gauche) Image des films PEI/PSS/(Ag-TiO_2) construits sur lamelle de verre. (Droite) Caractérisation par microscopie électronique en transmission de l'échantillon PEI/PSS/(0.2wt%Ag-TiO_2)

Les analyses chimiques des films réalisés selon l'approche *one-pot* ont montré que la concentration en précurseur d'Ag dans la suspension de TiO_2, influe à la fois sur la teneur en TiO_2 des films hybrides et sur le rapport massique Ag/TiO_2 (Fig. 12). Plus la quantité de TiO_2 déposée sur les films augmente, moins le rapport massique Ag/TiO_2 sera élevé.

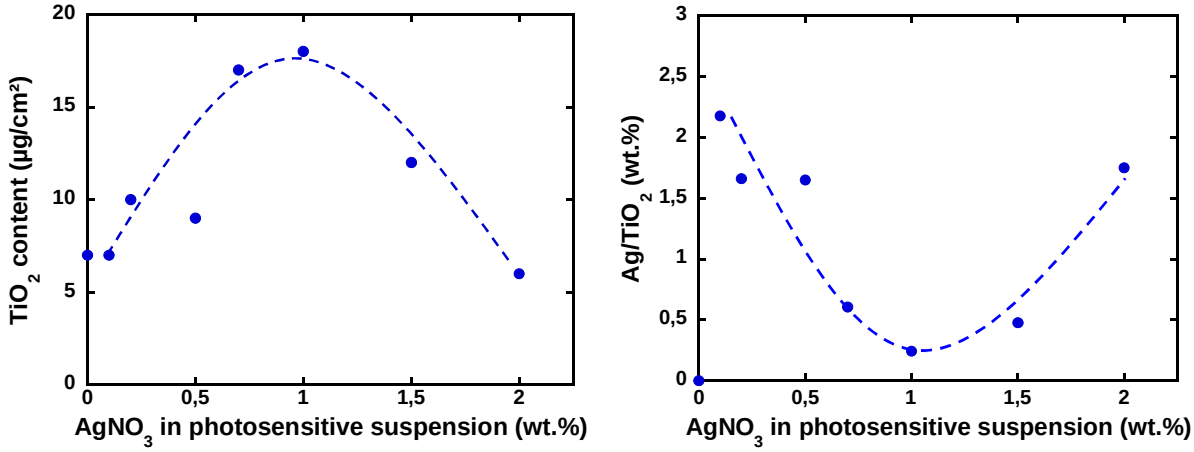

Fig. 12: Teneur en TiO_2 (gauche) et rapport massique Ag/TiO_2 (droite) des films hybrides PEI/PSS/(Ag-TiO_2) en fonction de la concentration en $AgNO_3$ dans la suspension photosensible.

Les résultats de tests de photocatalyse des films contenant des AgNPs synthétisées par la méthode « classique » ont donné des conversions plus élevées que des films dépourvus de AgNPs. Néanmoins le comportement photocatalytique le plus remarquable a été observé pour des films hybrides PEI/PSS/(Ag-TiO_2) obtenus par la synthèse *one-pot*, avec une exaltation très significative de l'activité

photocatalytique, et une conversion photocatalytique de l'acide formique d'autant plus élevée que le rapport massique Ag/TiO_2 des films PEI/PSS/(Ag-TiO_2) est faible (Fig. 13*g*). De plus, à teneur identique en TiO_2, les films hybrides possédant la quantité d'AgNP la plus faible permettent d'obtenir les meilleures conversions d'acide formique (Fig. 13*d*).

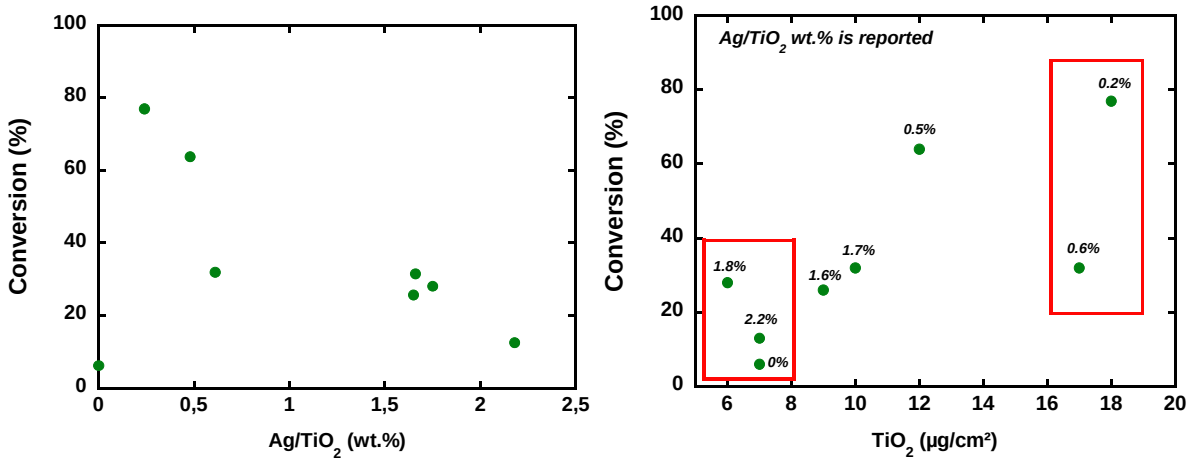

Fig. 13: Résultats des tests photocatalytiques de dégradation de HCOOH en phase gazeuse (gauche) en fonction du rapport massique Ag/TiO_2, et (droite) en fonction de la teneur en TiO_2 dans les films PEI/PSS/(Ag-TiO_2). Conditions expérimentales : [HCOOH] = 255 ppm_v, débit total = 20 mL/min, UV-A (2.5 mW/cm²), substrat modèle de 36 cm².

Les caractérisations par TRMC ont mis en évidence la génération d'une quantité plus importante de porteurs de charges sous irradiation en présence des AgNPs (Fig. 14). Il a été supposé qu'un effet plasmonique selon un mécanisme d'injection d'électrons chauds des AgNPs dans la bande de conduction du TiO_2 ou d'intensification du champ électromagnétique serait à l'origine de cette augmentation de l'efficacité photocatalytique des films hybrides Ag-TiO_2 sous irradiation UV-A. Bien que la TRMC n'ait pas mis en évidence un effet de trappe à électron, cette hypothèse n'est pas à exclure.

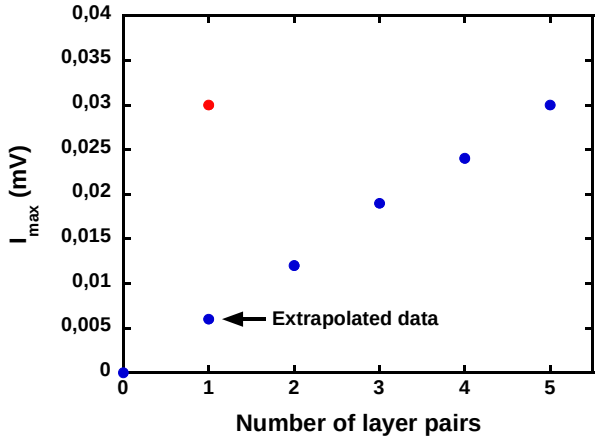

Fig. 14: Valeur de l'intensité maximale I_{max} caractéristique dérivée des mesures de TRMC sur les films PEI/$(PSS/TiO_2)_n$ (•) et PEI/PSS/(Ag-TiO_2) (•). Irradiation laser à 350 nm.

Au final, les trois méthodes utilisées pour construire les films contenant une couche de TiO_2 et des AgNPs, ont montré une meilleure activité photocatalytique que les films sans Ag. Cependant les films construits avec la méthode *one-pot* montrent une très forte exaltation des propriétés photocatalytiques du TiO_2. La Fig. 15 résume et compare quelques résultats obtenus en utilisant les 3 méthodes.

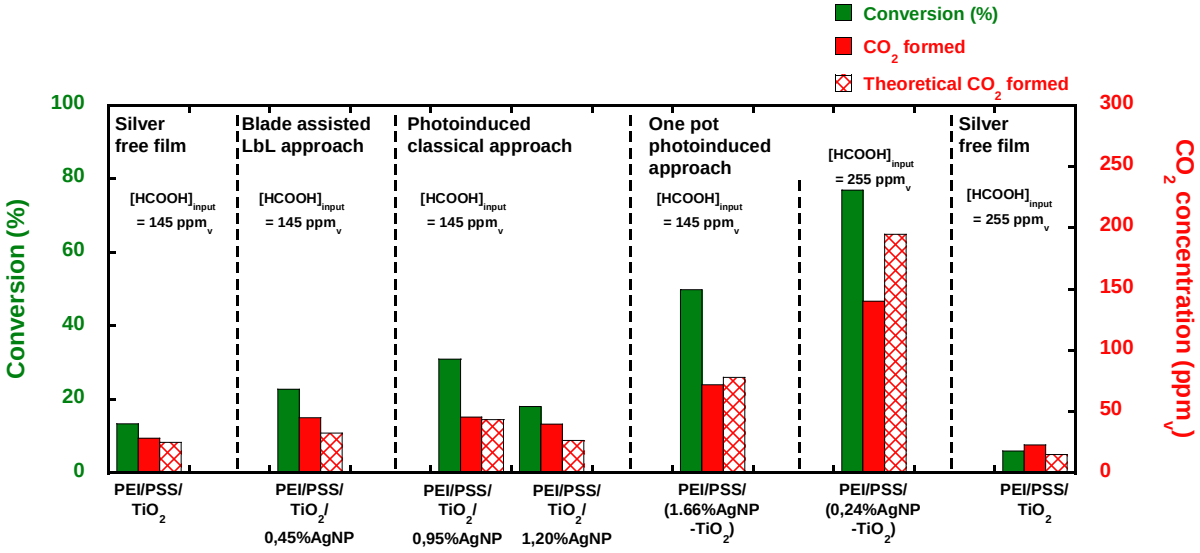

Fig. 15: Comparaison des performances photocatalytiques des films PEI/PSS/(Ag-TiO_2) préparés selon les 3 différentes méthodes. Conditions expérimentales : débit total = 20 mL/min, UV-A (2.5 mW/cm²), substrat modèle de 36 cm².

Des souches bactériennes médicinales *Escherichia coli* SCC1 ont été ensemencées sur les films multicouches hybrides PEI/PSS/(Ag-TiO_2) (synthèse *one-pot*) construits sur wafer de silicium. Seules deux concentrations en AgNPs ont testé testées dans cette étude (Fig. 16). Les résultats n'ont pas pu mettre en évidence une activité antibactérienne dans le noir probablement en raison de la faible teneur en AgNPs des films ou de leur présence dans la porosité des films ou à l'interface PSS/TiO_2 qui réduit leur accessibilité pour les bactéries. Sous irradiation UV-A en revanche, une augmentation importante des propriétés biocides des films a été obtenue pour les deux films hybrides PEI/(PSS/Ag-TiO_2), l'activité la plus importante étant observée pour le plus faible rapport massique Ag/TiO, en accord avec les résultats obtenus pour la dégradation de l'acide formique. Ceci confirme que le gain d'activité antibactérienne provient bien d'une amélioration des propriétés photocatalytiques intrinsèques des films hybrides.

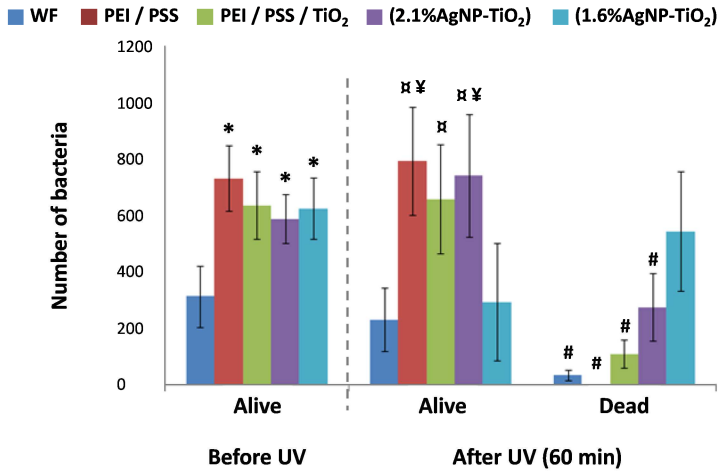

Fig. 16: Tests antibactériens des films multicouches PEI/PSS/(Ag-TiO_2). Bactéries testées : *Escherichia Coli*, UV-A (2.5 mW/cm²), temps d'irradiation = 60 min, wafer (WF) de silicium de 2 cm². (*) significativement différent de « WF before UV » ($p < 0.05$), (¤) significativement différent de « WF after UV » ($p < 0.05$), (¥) significativement différent de « 1.6%AgNP-TiO_2 after UV (ALIVE) » ($p < 0.05$), (#) significativement différent de « 1.6%AgNP-TiO_2 after UV (DEAD) » ($p < 0.05$).

3. Construction de différentes architectures de films sur des surfaces textiles

La technique LbL a pu être transférée avec succès des surfaces modèles à des supports textiles (polyester) pour la construction de films multicouches PEI/$(PSS/TiO_2)_n$ avec une densité surfacique estimée à 27 µg/cm² de TiO_2 par paires de couches déposées. La densité surfacique plus élevée s'explique par différence de géométrie entre les surfaces modèles et les textiles. Tout comme les

films construits sur surfaces modèles, les films obtenus sur surface textile sont poreux, ce qui permet aux molécules d'HCOOH de pouvoir diffuser au sein des films.

Les tests de réactivité ont montré que ces textiles fonctionnalisés par une seule couche de TiO_2 sont photocatalytiquement actifs sous UV-A pour la dégradation de HCOOH en phase gazeuse, avec un plateau de conversion obtenu pour des films contenant au moins 2 paires de couches (Fig. 17). Une surproduction en CO_2 a été observée pour tous les films, et a été associée à une dégradation photocatalytique des polyélectrolytes et possiblement des fibres de textile par le TiO_2. Les films construits sur textiles ont montré des propriétés auto-décontaminantes antibactériennes envers *Pseudomonas fluorescens*, *Staphylococcus aureus*, *Escherichia Coli* K12 et *Listeria monocytogenes* (tests effectués selon la norme BS ISO 27447, réalisés au CRITT-Aérial) (Fig. 18).

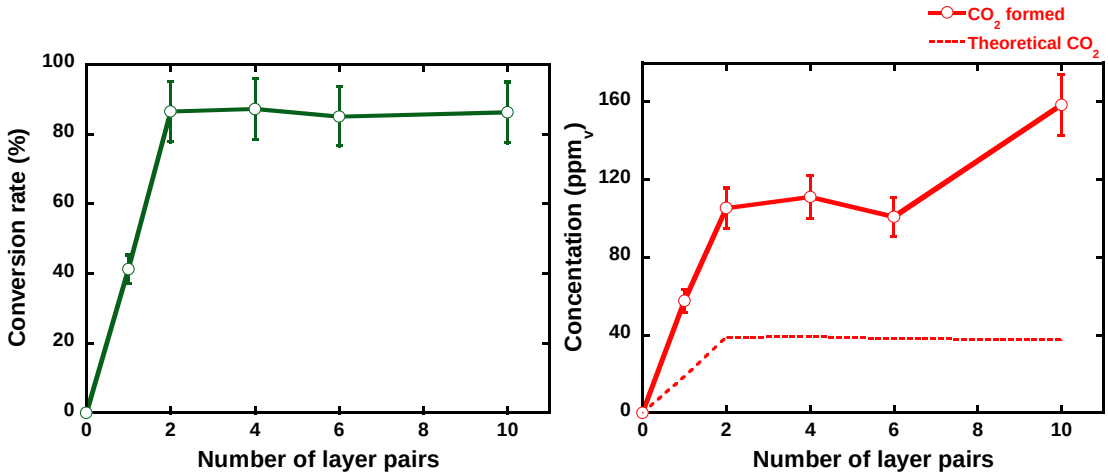

Fig. 17: Test photocatalytiques de dégradation de HCOOH en phase gazeuse pour les films $PEI/(PSS/TiO_2)_n$ construits sur textiles polyester. (A gauche) Conversion d'acide formique en fonction du nombre de paires de couches. (A droite) Formation de CO_2; la courbe en pointillé représente la concentration en CO_2 correspondant à sa formation stoechiométrique par rapport à la conversion de l'acide formique Conditions expérimentales : [HCOOH] = 45 ppm_{vol}, débit total = 20 mL/min, UV-A (2.5 mW/cm²), textiles en fibre de polyester de 36 cm².

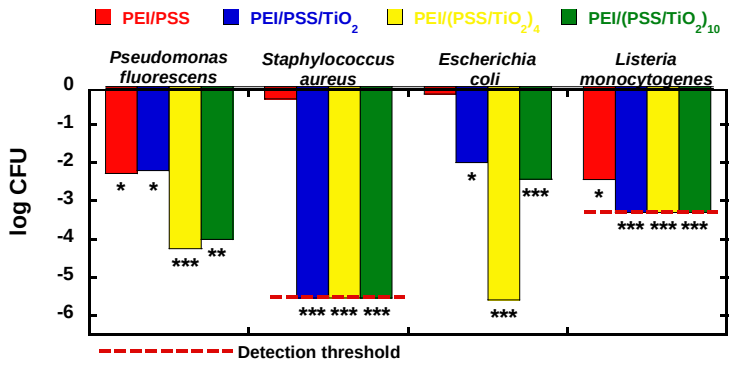

Fig. 18: Tests antibactériens des films multicouches PEI/$(PSS/TiO_2)_n$. Bactéries testées : *Pseudomonas fluorescens*, *Staphylococcus aureus*, *Escherichia Coli* K12 et *Listeria monocytogenes*, UV-A (2.5 mW/cm²), temps d'irradiation = 3 h, textiles en fibre de polyester de 2 cm². Tests effectués selon la norme BS ISO 27447. p : p-value ; (*) $p < 0.05$, (**) $p < 0.001$, (***) $p < 0.0001$

De même, l'approche consistant à associer la synthèse photoinduite des AgNPs et la construction des films par LbL a été validée sur textile. En effet, des films hybrides Ag-TiO_2 ne contenant qu'une seule couche de TiO_2 et dont les AgNPs ont été synthétisées selon la méthode *one-pot* ont été construits avec succès sur les surfaces textiles. Ces films ont montré un comportement analogue à celui des films hybrides sur surfaces modèles, et la construction de films hybrides permet d'améliorer le taux de dégradation d'HCOOH de manière très significative ainsi que l'activité biocide des films sous irradiation UV-A. Dans le cas d'HCOOH, les conversions obtenues sont d'autant plus élevées que le rapport massique Ag/TiO_2 est faible (Fig. 19).

Les tests antibactériens ont été réalisés en utilisant des souches bactériennes *Pseudomonas fluorescens* et *Escherichia coli* K12. A nouveau, les résultats n'ont pas pu mettre en évidence une activité antibactérienne dans le noir, mais il a été montré que l'activité biocide des films hybrides était nettement plus élevée que celle des films correspondants ne contenant que TiO_2, et d'autant plus que le rapport massique Ag/TiO_2 est faible (Fig. 20).

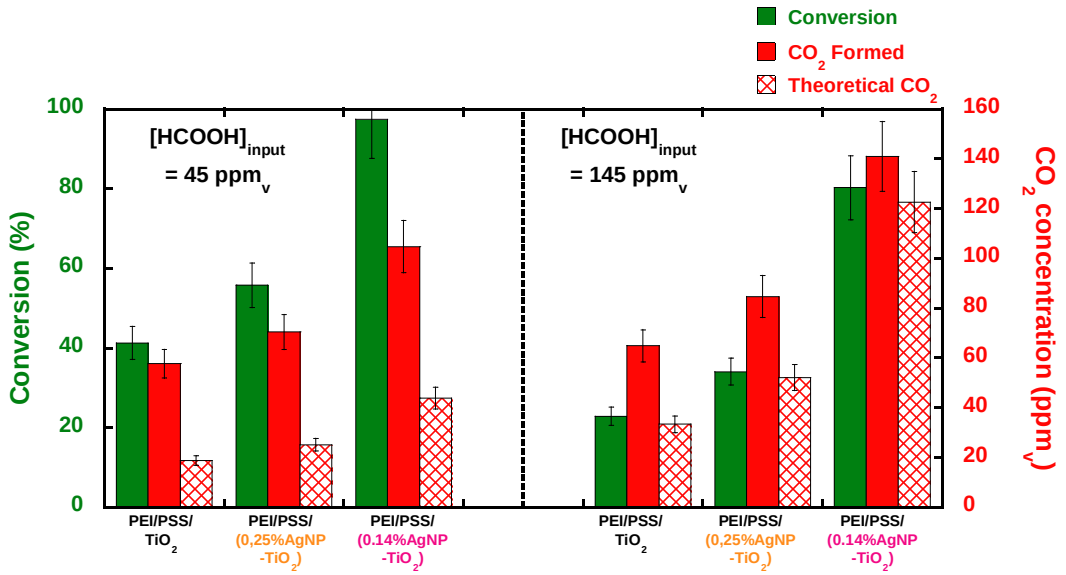

Fig. 19: Test photocatalytiques pour la dégradation de HCOOH en phase gazeuse pour les films PEI/PSS/(Ag-TiO_2) construits sur textiles. Conditions expérimentales : [HCOOH] = 45 ppm_v (à gauche), 145 ppm_v (à droite) , débit total = 20 mL/min, UV-A (2.5 mW/cm²), textiles en fibre de polyester de 36 cm².

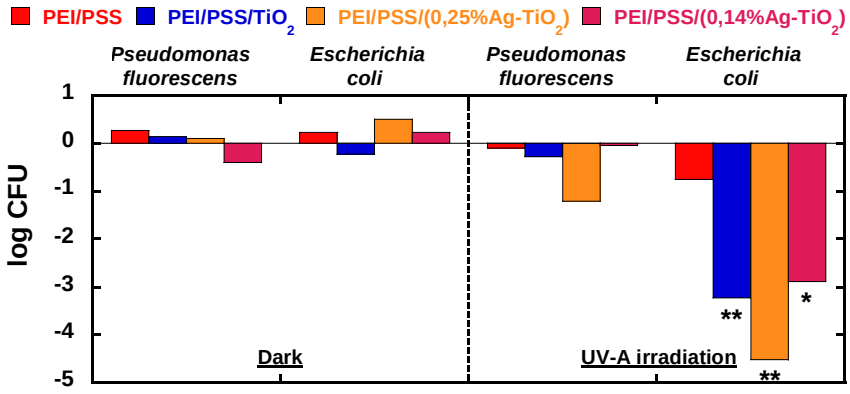

Fig. 20: Tests antibactériens des films multicouches PEI/PSS/(Ag-TiO_2). Bactéries testées : *Pseudomonas fluorescens* et *Escherichia Coli* K12, UV-A (2.5 mW/cm²), temps d'irradiation = 3 h, textiles en fibre de polyester de 2 cm². Tests effectués selon la norme BS ISO 27447. p: p-value ; (*) $p < 0.01$, (**) $p < 0.001$

Des tests normés d'abrasion (NF EN ISO 12945) et de lavage (NF EN ISO 105-C06 et NF EN ISO 105-D01) ont été effectués sur des films contenant 1 et 2 paires de couches (tests réalisés à l'Institut Français du Textile et de l'Habillement, IFTH, Mulhouse) afin d'évaluer la stabilité des films. On a pu noter que les films LbL présentent une excellente stabilité. En effet, il est remarquable que quels que

soient les tests de résistance mécanique et au lavage effectués, la teneur en TiO_2 (déterminée par analyse chimique ICP-AES) reste constante, bien qu'une légère modification de la structure des films ait pu être observée, les analyses MEB ayant montré qu'une partie du TiO_2 était également localisée dans les interstices entre les fibres des textiles. Les tests d'abrasion effectués sur les textiles n'affectent pas les performances photocatalytiques des textiles pour la dégradation de HCOOH en phase gazeuse, tandis qu'elles sont améliorées après un seul cycle de lavage effectués sur les films contenant 1 paire de couches, mais en revanche diminuées pour un lavage de 10 cycles. Les films contenant 2 paires de couches ont montré quant à eux une bonne stabilité photocatalytique vis-à-vis des cycles de lavage. En revanche, bien que la teneur en TiO_2 ne soit pas diminuée au sein des films, les tests de lavage à sec ont montré une baisse de l'activité photocatalytique des films, qui provient probablement de l'existence de résidus du perchloroethylène utilisé lors du lavage, qui peuvent bloquer les sites actifs du TiO_2.

Conclusion

Des films à base de nanoparticules de TiO_2 et des films hybrides à base de nanoparticules de TiO_2 et d'Ag ont été construits avec succès sur des surfaces modèles et des textiles par la technique du couche-par-couche, LbL. Ces films sont photocatalytiquement actifs sous irradiation UV-A pour la dégradation de HCOOH en phase gazeuse et présentent des propriétés biocides envers différentes souches bactériennes. Des surfaces et des textiles photocatalytiques multifonctionnels présentant des propriétés épurantes et auto-décontaminantes/biocides sous irradiation UV-A ont ainsi été préparés.

Les films PEI/$(PSS/TiO_2)_n$ construits sur surfaces modèles se caractérisent par une très bonne homogénéité, avec une faible teneur en TiO_2 (7 µg/cm²). Un comportement photocatalytique inhabituel a été observé pour ces films, avec une activité maximale pour les films ne contenant qu'une seule paire de couche PSS/TiO_2, et un plateau de conversion atteint à partir de 6 paires de couches. Ce résultat est très intéressant d'un point de vue applicatif. Par ailleurs les films ont présenté des propriétés antibactériennes dès une paire de couches PSS/TiO_2. Ce comportement photocatalytique avec un plateau d'activité biocides à partir de trois paires de couches, différent de celui observé lors des tests en phase gaz résulte directement de la taille microscopique des bactéries qui ne leur permet pas de diffuser au sein des films.

La deuxième partie de ces travaux s'est focalisée sur l'élaboration de films hybrides contenant des nanoparticules de TiO_2 et d'Ag. Trois types d'architecture de films contenant des AgNPs et une seule couche de TiO_2 ont été étudiés. Bien que ces architectures aient toutes trois montrées une amélioration des performances photocatalytiques pour la dégradation de HCOOH en phase gazeuse sous irradiation UV-A, les films construits avec la méthode *one-pot* ont montré la plus forte exaltation des propriétés photocatalytiques du TiO_2. Cette méthode a permis la synthèse *in-situ* des AgNPs dans le film, avec un contact intime entre les nanoparticules de TiO_2 et d'Ag. Il a été suggéré que les AgNPs se localisent dans la porosité des films et/ou à l'interface du PSS et du TiO_2. Les analyses par TRMC ont suggéré qu'un effet plasmonique serait responsable de cette amélioration. D'autres parts, ces films ont montré un apport positif des AgNPs pour les tests antibactériens.

Les techniques de construction, le LbL pour les films PEI/$(PSS/TiO_2)_n$, et l'approche *one-pot* pour les films PEI/PSS/(Ag-TiO_2), ont été transférées avec succès sur des surfaces textiles (polyester). Tout comme les films construits sur surfaces modèles, les textiles fonctionnalisés sont photocatalytiquement actifs avec une seule couche de TiO_2 pour la dégradation en phase gaz de HCOOH, et sont antibactériens sous UV-A vis-à-vis de différentes souches de bactéries. Par ailleurs les textiles contenant une ou 2 paires de couche PSS/TiO_2 ont montré une bonne résistance à l'abrasion et à différents types de lavages. Sur textile, l'élaboration de films hybride Ag-TiO_2 *via* la synthèse *one-pot* des AgNPs a permis d'exalter très fortement à la fois les propriétés photocatalytiques pour la dégradation de HCOOH, et les propriétés antibactériennes des films vis-à-vis de deux souches de bactéries sous illumination UV-A.

Introduction

In the context of air pollution, it is now recognised that indoor air is often more polluted than outdoor air [1], [20]. Moreover contamination by biological agents can also contribute to the deterioration of indoor air quality [21]. Several strategies have been investigated to improve indoor air quality by removing pollutants and are focussed on air purification processes based on either non-destructive or destructive approaches [5]. One of the destructive approaches is heterogeneous photocatalysis. This process is found to be one the most green and cost-effective process for removal of both chemical and biological pollutants [6], [11], [22]. Heterogeneous photocatalysis requires the activation of a semi-conductor material, usually titanium dioxide, under an appropriate irradiation source. If suitably associated with different materials, like metallic nanoparticles, it is possible to enhance the photocatalytic properties of titanium dioxide [23], [24].

Another challenge of using this destructive approach is the incorporation of the process without interfering with people's everyday life. As a result, strategies of surface modifications and functionalization have been investigated. In this frame, Layer-by-Layer self-assembly thin film construction has shown to be a useful coating technique on different types of surfaces, that provides specific properties according to the materials used for the film construction [17], [18]. This construction has been already used successfully in order to provide photocatalytic activity, as well as antibacterial properties to surfaces [25].

The main aim of this work was to functionalise a textile with silver and titania nanoparticles *via* the Layer-by-Layer self-assembly construction technique. This textile will present simultaneously photocatalytic properties against chemical pollutants (under UV-A irradiation) and biocide properties (with or without UV-A irradiation). Thus, the main tasks of the project were:

- the elaboration of multilayer titania films with and without silver nanoparticles on model surfaces, with their characterisation
- the evaluation of the films' photocatalytic performances under UV-A irradiation in the degradation of a gaseous pollutant
- the evaluation of the films' biocide properties under UV-A irradiation

- the transfer of the films construction technique from model surfaces to textile surfaces, with evaluation of the photocatalytic activity towards gas-phase pollutants, and the biocide properties.

This thesis is part of the PLASMOTEX project funded by the *Institut Carnot MICA* (Mulhouse, France), an institute specialised in functional materials. This work was realised at the *Institut de Chime des Procédés pour l'Energie, l'Environnement et la Santé* (ICPEES, UMR 7515, Strasbourg, France) under the supervision of Dr. Nicolas Keller, and the *Institut Charles Sadron* (ICS, UPR 22, Strasbourg, France) under the supervision of Pr. Gero Decher. This project also involved collaborations with the *Institut des Sciences des Matériaux de Mulhouse* (IS2M, UMR 7361, Mulhouse, France) with Dr. Lavinia Balan and Dr. Lydie Ploux, and with *CRITT Aerial* (Illkirch, France) with Dr. Marie-Hélène Desmonts.

This PhD thesis will consist in three main parts in regards to the type of material used for constructing the multilayered films. As a result this thesis will be divided in 5 chapters:

The first chapter is a literature review on the main concerns about indoor air pollution and bacterial contamination, followed by a review of the different techniques to solve this problem, with a focus on photocatalysis. A background on the use of titanium dioxide in photocatalytic applications toward the degradation of pollutants and bacteria will be addressed, followed by a discussion on the enhancement of its photocatalytic properties by metallic nanoparticles. A part on silver nanoparticles with their synthesis, their properties (optical and biocide) will be described, followed by discussion on their association with titania in order to enhance both photocatalytic activity and biocide properties of titania. The last part will be dedicated to film construction using titania and silver nanoparticles, and especially to the Layer-by-Layer (LbL) self-assembly thin film construction on several type of surfaces, with a focus on textiles.

The second chapter is a description of the materials and methods used in this work. The chapter will start with a description of the different types of materials used, as well as their synthesis and their use in LbL self-assembly thin film constructions. The second part will be a description of the characterisation techniques used on the constructed multilayered thin films, and will be followed by the description of photocatalytic tests performed on these films, as well as the evaluation of their biocide properties under UV-A irradiation, in the last part.

The construction of titania and polyelectrolytes LbL films on model surfaces will be addressed in the third chapter. This chapter will be divided in three sections, which will be focussed on the characterisations of the titania and polyelectrolytes films with a focus on the monitoring of the film construction, followed by the evaluation of their photocatalytic performances towards the degradation of gas phase formic acid taken as a model reactant, and the evaluation of their biocide properties. Antibacterial tests will be implemented using *Escherichia Coli* as a model bacteria.

The fourth chapter will be focused on the construction and characterisation of LbL films containing silver and titania nanoparticles and polyelectrolytes on model surfaces. In this chapter, three methods of silver nanoparticle deposition or synthesis will be presented and characterised, using commercially available silver nanoparticles, as well as a photoinduced synthesis approach. In this frame, a new one-pot process combining the photoinduced synthesis of silver nanoparticles and the LbL film elaboration will be highlighted. Photocatalytic activity of the hybrid films will be evaluated for the degradation of gas phase formic acid under UV-A. The antibacterial tests under UV-A will be presented for the type of film construction which presented the best gas-phase photocatalytic results, using *E. Coli* as the target bacteria.

In the fifth chapter, the transfer of the LbL self-assembly film construction from model surfaces to textile surfaces will be presented and divided in three parts. The first part will be dedicated to the construction of the LbL films containing titania and polyelectrolyte. The films will be characterised and tested for the degradation of gas phase formic acid under UV-A. A section regarding the stability of the film after several types of washing treatments and mechanical test will be addressed. The second part of this chapter will be dedicated to the construction of silver and titania nanoparticles and polyelectrolytes on textile surfaces, using the combined one-pot photoinduced synthesis/LbL construction approach highlighted during the study on model surfaces. The films will be characterised and tested for the degradation of gas-phase formic acid under UV-A . The last part of this chapter will be focused on the evaluation of the biocide properties of the titania LbL films, with and without silver nanoparticles. Different types of bacteria will be used in the antibacterial tests.

The final chapter of this thesis will be a general conclusion, with the main results obtained in these investigations. Some perspectives and the possible future works will be presented.

Chapter I: Bibliography

I Indoor air pollution

Air pollution is the largest environment risk to health worldwide [2]. Since the first report of the World Health Organisation (WHO) on air pollution in 1958, lists of pollutants were established year by year with the aim of alerting public opinion, policy makers and subsequently of diminishing their production in our daily life. In 2006 the first discussion regarding the development of a guideline on indoor air quality was initiated, and later published in 2010. Although outdoor air has been also a concern for a longer period of time, it is now recognised that indoor air is often more polluted than outdoor air [20].

Several strategies have been investigated to improve indoor air quality by removing pollutants. They have included pollution air source control and increasing ventilation. Although these strategies present many advantages, controlling the pollution air source is challenging and ventilation may bring outdoor pollutants within people's living space, while remaining a technology based on the physical transfer of pollutants. Therefore most investigations are focussed on air purification processes by using either a non-destructive approach (e.g. filtration, adsorption) or a destructive approach (e.g. thermal oxidation) [5]. Moreover these processes have to be economically applicable while retaining a certain standard in people's way of living.

I.1 Main indoor air pollutants

I.1.1 Volatile Organic Compounds

In western societies, studies have shown that people spend 80% of their time in indoor environments, i.e. houses, offices, cars and shops [26]. As a result, people started to complain about odour annoyances, headache, coughs, nausea, fatigue as well as eye, nose, throat and skin irritations. These symptoms are associated to the sick building syndrome (SBS) which is used to describe a situation in which the occupants of a building experience acute health or comfort related effects due to time spent indoors [27]. This issue has been linked to the low quality of indoor air, which has

become an issue of great concern. The importance of Volatile Organic Compounds (VOCs) as pollutants in indoor air, has been pointed out in many documents such as e.g. the WHO Air Quality Guidelines for Europe in 2010 [2]. WHO reported that air pollution caused about seven millions premature deaths in 2012, 3.7 millions being related to indoor air pollution [28]. VOCs are defined by their boiling point that ranges between 50°C and 250°C at standard atmospheric pressure. In indoor air, they are issued from a large variety of sources, including the utilisation of consumer household products, the emission from adhesives, building materials, furnishing, clothing, paints and associated supplies, and combustion processes [21]. More than 350 VOCs have already been measured at concentrations higher than 1 ppb in indoor air [29]. The main VOCs and their possible sources are listed in Table 1.

VOCs	Possible Sources
Formaldehyde	Pesticides, flooring materials, insulating materials, wood-based materials, machine, coatings and paints
Toluene	Pesticides, flooring materials, insulating materials, wood-based materials, paints, adhesives, gasoline, combustion sources
Acetaldehyde	Wood-based materials, flooring materials, HVAC system
Paradichlorobenzene	Ceiling materials, wood-based materials, pesticides
Ethylbenzene	Furniture, paints, adhesives, gasoline, combustion sources
Methylene chloride	Flooring materials, furniture, HVAC system, coatings and paints
Chloroethylene	Flooring materials, coatings and paints, dry-cleaned clothes
Carbon tetrachloride	Coatings and paints, industrial strength cleaners
Chloroform	Pesticide, glue
Naphthalene	Insulating materials, mixed materials, wall painting
Other VOCs (e.g., esters and ketones)	Plastics, resins, plasticizers, solvents usage, flavors, perfumes, paints, disinfectants, adhesives

Table 1: Main encountered VOCs with their possible sources [26].

VOCs are also characterised by their threshold limit value (TLV) which corresponds to the concentration at which a worker can be exposed every day without adverse effects. TLV (expressed in mg/m^3 or ppm) are generally one to four orders of magnitude lower than the threshold for irritation effects [30].

In our study, though formic acic is not one of the main encountered VOCs, formic acid (HCOOH) will be used as a gas-phase model pollutant, as formic acid is the main reaction intermediate (by-product) that is formed during the photocatalytic oxidation of formaldehyde, one of the most problematic VOCs from indoor air, and one of the main reaction intermediates observed in the photocatalytic degradation of many high molecular weight VOCs such as acetone or 2-butanone. Also formic acid can be directly mineralised into water and carbon dioxide without the formation of any gaseous reaction intermediates (Eq. 1).

$$HCOOH + \frac{1}{2}O_2 \rightarrow CO_2 + H_2O \quad \text{(Eq. 1)}$$

In addition, formic acid can give rise to irritation [31]. The cytochrome oxidase complex at the terminal end of the respiratory chain in the mitochondria can be inhibited, resulting in histotoxic hypoxia. Hence tissues and organs with high oxygen consumption (optic nerve, brain, heart and kidney) may be vulnerable to formic acid exposures.

I.1.2 Contamination by bacteria

Despite the fact that investigations on indoor air quality improvement are focussed on the elimination of chemical agents, contamination by biological agents must not be overlooked [21]. Indeed biological agents may be responsible for respiratory disease, asthma, allergies. Although buildings do not harbour populations of infectious agents, some building environments favour the development of mould, fungi, bacteria and in rare cases viruses. For instance, *Legionella* bacteria are known to proliferate in warm and humid environments. Buildings may provide an ideal proliferation environment through air humidifiers, air conditioning cooling towers, warm water supplies, and plumbing systems [1]. WHO has also specified that the dampness (humidity), for which bacteria growth is suitable, also contributes to the chemical and biological degradation of materials, so consequently also contributing to the decrease in indoor air quality [1], [2].

In humid environments bacteria can adhere to surfaces, resulting in biofilm formation. These biofilms can grow and develop on different types of surface (bio or inert) and will do some most readily on surfaces that are rougher, more hydrophobic, and coated by surface conditioning films [32], [33]. The processes governing biofilm formation are shown in Figure 1. Once developed, detachment of biofilm parts may occur, which will eventually lead to the formation of other biofilms on a different surface, thus repeating the cycle of biofilm formation processes.

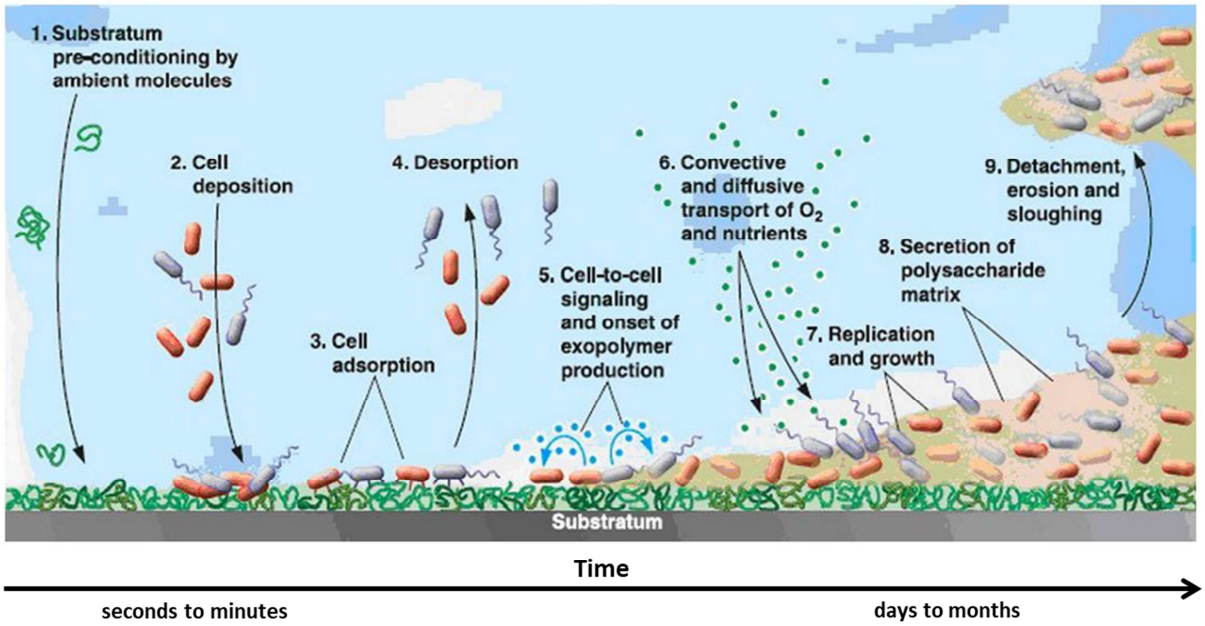

Figure 1: Processes governing biofilm formation [33], [34].

Surfaces contaminated by bacteria can also be considered as an important transmission vector for pathogens. Contamination by bacteria of persons is indeed possible through direct transmission, but also bacterial infections can be transmitted from person to person *via* physical contact, and with contaminated surfaces. This contamination may occur at any type of surfaces such as e.g. in houses, public places or hospitals (Figure 2) [21], [35]–[37]. In fact it is found that bacteria can have a persistence time from days to months on dry inanimate surfaces [37]. While humid environment improve persistence for most types of bacteria, *Staphylococcus aureus* bacteria were found to have a higher persistence time in a dry environment. Low temperatures have been also found to play a role in bacteria persistence and the influence of the type of surfaces is still under debate [37]–[39].

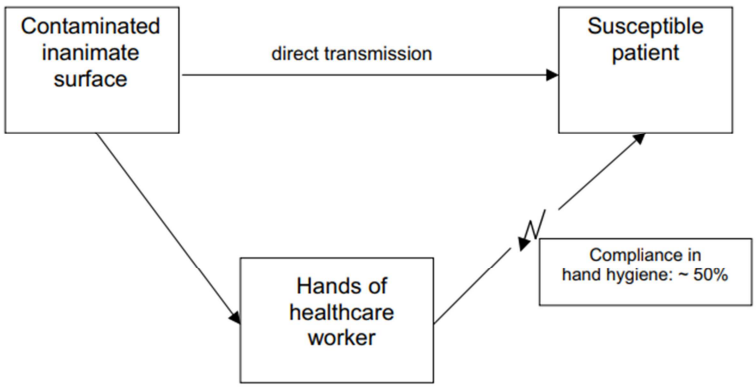

Figure 2 : Common modes of transmission in medical environment, from inanimate surfaces to susceptible patients [37].

On textiles, one can note that survival of Gram negative bacteria such as e.g. *E. Coli* or *Pseudomonas Aeruginosa* has been observed from 2 h to more than 60 days, and periods of months have been reported for *Staphylcocci* and *Enterococci* on polyester [40]. Last but not least, rapid multiplication of numerous microorganisms on textiles can also be responsible for deterioration staining and the generation of very unpleasant odours.

It is noteworthy that the growth of mould, fungi and bacteria will subsequently emit spores, cells, fragments and VOC into indoor air [2].

In this project *Escherichia Coli*, *Pseudomonas Fluorescens*, *Staphylococcus Aureus* and *Listeria Monocytogens* bacteria will be used in order to evaluate the antibacterial properties of TiO_2-based films.

I.2 Indoor air pollutant elimination strategies

When it comes to air purification and treatment, 4 recommendations were identified by Nazaroff in order to improve indoor air quality [41].

- Indoor emission must be minimised
- A dry indoor environment should be maintained
- Ventilation should be adequate
- Outdoor pollution should not enter into the environment

Beside control of the emission source, air cleaning devices have to be used. Several methods using either non-destructive or destructive approaches were investigated and are available on the market. However when dealing with VOC elimination, three major aspects must be taken simultaneously into consideration [42]:

(i) Toxicity and safety: the process should not release any toxic by-products

(ii) Power consumption: for large scales or domestic devices, energy consumption must be kept low.

(iii) Ageing of the process: the process should be able to run over hundreds or thousands of hours.

This section will describes some processes, while taking into consideration the recommendations for VOC elimination.

I.2.1 Non-destructive approaches

Filtration is probably the simplest method used for removing suspended particles from indoor air [3], [5]. This method requires the use of a filter that is an essential component in all air conditioning systems. However mechanical and electronics filters are progressively saturated by particles and lose their prime properties. In addition the used filters need to be replaced for not being considered as a secondary source of contamination, since the accumulated particles can provide a suitable environment for the development of bacteria. Electronic filtrations have been developed in order to enhance filtration properties. This method is based on the generation of ions, which are then dispersed into the air. These ions will be able to attach to particles, making them chemically charged, which will be eventually trapped by filters. However the possibility for the particles to adhere on surfaces and walls, or interact with an oppositely charged particle, resulting in bigger size particle, may occur. Moreover hazardous particles can be generated by the filters, as well as pollutants and VOCs. Furthermore mechanical and electronic filters are not able to retain gases, so that the technique becomes ineffective for the elimination of VOCs.

On the other hand the adsorption approach (physico-chemistry filtration) has demonstrated effective VOC removal with the ability to retain pollutants at the surface of the adsorbent material. The adsorbants used have included a large range of materials, such as activated carbon, zeolites, silica, alumina, clays and polymers [43]–[46]. No destruction is achieved with this method, the target pollutants being transferred from the gas phase to the solid phase. Also a high humidity rate slowly influences the pollutant absorption efficiency. Thus the saturated adsorbant may then produce hazardous wastes, and regular replacement of the saturated adsorbent is therefore necessary [5]. It was also found that airborne bacteria can adsorb on the material, especially for activated carbon due to its high biocompatibility properties [47]. Bacteria adhesion was prevented by impregnating silver ions on zeolite materials and reduced silver on activated carbon, providing biocidal properties to the adsorbent materials [47], [48]. Nonetheless modifications or associations with other materials may increase significantly the cost of the adsorption method [5].

I.2.2 Destructive approaches

A plasma is a ionised gas produced by high voltage electrical discharges consisting of electrons, positive ions and neutral particles, either atoms or molecules [5], [42], [49]. When the plasma is not thermodynamically stable, this type of plasma is called cold plasma. This technique can be used as a

particle filter (aggregation of particles when the plasma is generated by pulsed corona), but can also produce UV-A irradiation, and thereby can oxidise molecules and remove viruses and bacteria. Free radicals can also be formed in the presence of humidity and oxygen, which will promote further degradation of gas-phase pollutants. Although it may require lower energy compared to other plasma techniques (i.e. thermal plasma), this method has appeared to not be efficient in the elimination of gas pollutants with low concentrations [50].

Ozonation is a method based on the use of indoor ozone generators as air purifiers. Oxygen molecules are exposed to a corona discharge or UV-irradiation to produce ozone, which will be able to eliminate odours and microbial agents due to the oxidising properties [5]. However, studies have shown that indoor ozone concentrations in the range 50–100 ppb_v (exposure limits) does not guarantee an efficient removal of indoor VOC pollutants [51]. Moreover it appeared that this technique cannot compete with moderate ventilation.

The UV photolysis method is based on the UV irradiation of contaminants such as viruses, bacteria, chemicals, mites and mould. This method can be achieved under room temperature and pressure conditions and requires the use of a 185-254 nm range UV-C lamp [5]. Its efficiency depends of the molar absorptivity of the target at the wavelength used, the intensity of the light source, the initial concentration of VOC/gas pollutant, the relative humidity and the concentration of the oxidant. Although oxidation of gases was obtained through UV photolysis, the generated by-products can be as harmful as the initial targeted VOCs. Ozone production may also occur while using this destructive approach [52]. Moreover the use of a lamp at these wavelengths requires high energy, power consumption, as well as safe confinement [3].

Photocatalysis is a destructive approach based on the use of UV and/or visible irradiation with less energy consumption, that has been studied for decades, and has proved its efficiency in the elimination of VOCs and of many pollutants [10], [11]. Photocatalysis promotes the degradation and mineralisation of contaminants in the air by using a semiconductor material and an irradiation source in the presence of oxygen. The semiconductor plays the role of heterogeneous catalyst, and is activated by radiation with adequate wavelengths. Photocatalysis is a valuable alternative to thermal catalysis, which requires higher temperatures of reaction, versus room temperature for photocatalysis. Compared to other techniques, photocatalysis benefits from low maintenance costs and low energy consumption, and from being efficient towards a large range chemical targets, with different chemical functions, as well as towards a large variety of microorganisms. The next part of this chapter will be fully dedicated to the description of heterogeneous photocatalysis.

I.3. Functionalised surfaces for VOC removal and degradation

Since the improvement of indoor air quality could be resolved with the use of technologies made of different type of materials (e.g. zeolites or clays in the adsorption method), the implication and use of these technologies should not interfere in people's daily life. As a consequence the incorporation or deposition of materials on walls or furniture appears to be a suitable method. For instance the functionalization of floors, wallpapers, ceiling, paints or textiles, allowing them to be used as "smart" surfaces, while keeping their primary function [53]. Photocatalysis is a destructive approach that has been investigated and used for the degradation of pollutants (in liquid and gaseous phase) by irradiating semi-conductor materials. Functionalising material surfaces with photocatalytic semi-conductor materials, has allowed these surfaces to be used for indoor air VOC degradation and bacteria killing [6], [54]. The development and investigations on smart textiles for a wide variety of applications has a growing interest by proving them photocatalysis properties [55]–[59]. By functionalising the textile fibres by photocatalyitic materials, these textile surfaces should be able to improve indoor air quality by degrading gaseous pollutants, and have biocidal properties which will prevent both bacteria direct transmission and biofilm formation. At the moment functionalization of textiles on an industrial scale by using an actual coating technique like dip coating, spraying or padding, demonstrates low activity and durability against VOCs. Thermal treatment that allows fixation of materials on surfaces is not applicable on textile fibres. Suitable coating techniques on different surfaces that do not damage textile fibres have been investigated [57].

II. Heterogeneous photocatalysis

II.1 Principles of heterogeneous photocatalysis

Classical heterogeneous catalysis can be decomposed in 5 independent steps [6], [7]:

(1) External and internal transfer of the reactants in the fluid phase to the surface and further within the porosity respectively
(2) Adsorption of at least one of the reactants
(3) Reaction in the adsorbed phase
(4) Desorption of the products

(5) Internal and external transfer of the products within the porosity and further from the interface region, respectively

Usually thermal activation is required in order to promote the catalytic reaction. Photocatalytic reaction occurs in the third step with a substitution of thermal activation by a photonic activation. This reaction can be carried out in several media that are gas phase, organic liquid solution and aqueous solution. This process requires a semiconductor material that will be able in its excited state to undergo chemical transformation to reactants, thus forming reaction intermediates (by-products) and regenerates itself after each cycle of interactions [60].

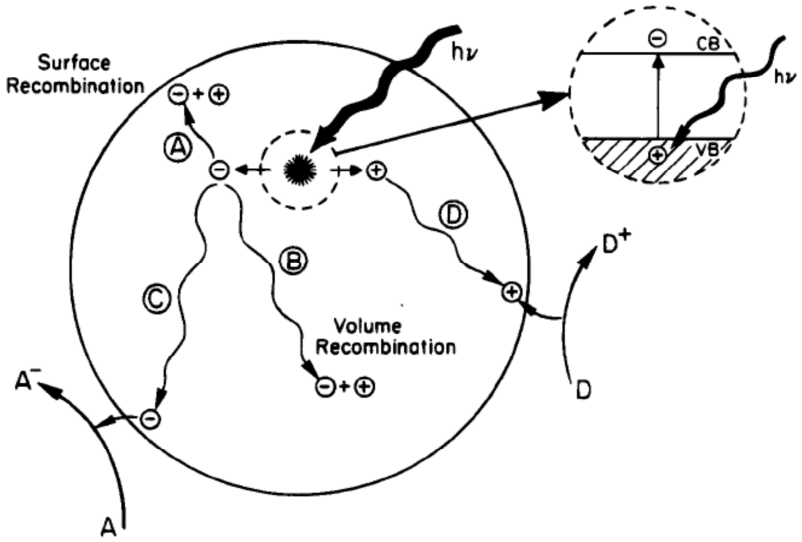

Figure 3 : Photocatalytic process over a semiconductor isotropic nanoparticle material when being illuminated (hν). Charged carriers are photogenerated in the bulk (mechanism showed on the top right of the schematic); Charge carriers may undergo different pathways: recombination of the photogenerated charge carriers at the surface (pathway A) or within the bulk (pathway B) of the nanoparticles, migration of electron (pathway C) and hole (pathway D) towards the surface; Electrons may reduce acceptor molecules A, and holes may oxidise donor molecules D [12].

The photocatalytic reaction mechanism is summarised in Figure 3 and goes as follow [12]. When a semiconductor material is illuminated with a photon with an energy equal or higher than its band gap E_G ($h\nu \geq E_G$), a free electron (e^-) from the valence band is promoted to the conduction band (CB), thereby a hole (h^+) is created in the valence band (VB) [6], [7]. Thus electron-hole pairs (e^-/h^+) are created within the bulk of the semiconductor material. The photogenerated carriers may then migrate towards the surface of the semiconductor material to undergo reactions with adsorbed molecules according to their redox potentials. Electrons will allow the reduction of acceptor molecules A, whereas donor molecules D will be oxidised by holes. The hole transfer corresponds to

the cession of an electron by the donor molecule to the solid. The reactions go according the following equations:

$$\text{semiconductor} + h\nu \rightarrow e^-_{CB} + h^+_{VB} \quad \text{(Eq. 2)}$$

$$A_{(ads)} + e^- \rightarrow A^-_{(ads)} \quad \text{(Eq. 3)}$$

$$D_{(ads)} + h^+ \rightarrow D^+_{(ads)} \quad \text{(Eq. 4)}$$

Electrons and holes that do not undergo at the surface or within the bulk of the semiconductor material, either relaxation (de-activation) or recombination, will interact with reactant molecules, reaction intermediates or adsorbed water [61]. The recombination process is responsible for the decrease in photocatalytic activity illustrated by a competition with reduction and oxidation reactions with molecules at the surface of the material [6], [61], [62]. Characterisation by spectroscopy such as transient absorption spectroscopy, transient diffuse reflectance spectroscopy and time-resolved microwave conductivity measurements has allowed the determination of the time scale range of the main processes taking place in the activated semiconductor material during irradiation (Figure 4 and Table 2) [9], [61], [63]–[66]. Enhancement of photocatalytic properties of semiconductors by preventing recombination process will be discussed in the section dealing with TiO_2 photocatalysts.

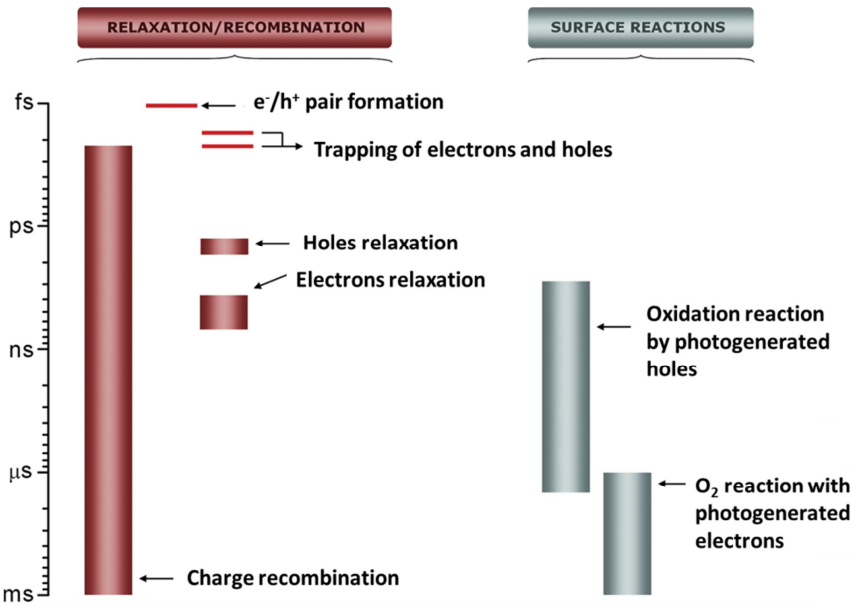

Figure 4 : Time scale range of the main processes taking place in the irradiated semiconductor material. Schematic based on the diagram of Kubacka *et al* [61].

Process	Characteristic times	
Charge carriers generation	Very fast	(fs)
Holes trapping	Fast	(10 ns)
(Shallow) electrons trapping	Dynamic equilibrium	(100 ps)
(Deep) electrons trapping	Irreversible	(10 ns)
Electrons recombination	Slow	(100 ns)
Holes recombination	Fast	(10 ns)
Interfacial reaction with holes	Slow	(100 ns)
Interfacial reaction with electrons	Very slow	(ms)

Table 2 : Characteristic times of possible charge carrier reactions within titania semiconductor material [9]

II.2 Physical parameters that govern the photocatalysis kinetics

Depending on the photocatalytic reaction toward a certain molecule/pollutant, adequate photoreactor and type of lamp have to be used to provide the highest photocatalytic reaction rate [6]. Figure 5 illustrates the influence of the important physical parameters which are governing the photocatalytic kinetics and photocatalytic activity, represented by the reaction rate, r. First the reaction rate is proportional to the mass of photocatalyst before reaching a plateau at which full absorption of photons by the solid occurs. By a certain mass value, the reaction rate levels off and becomes independent of the mass of catalyst. This parameter is related to the geometry and the working conditions of the photoreactor. For higher quantities of photocatalyst, a screening effect of the excess semiconductor occurs, masking parts of the photosensitive materials/surface.

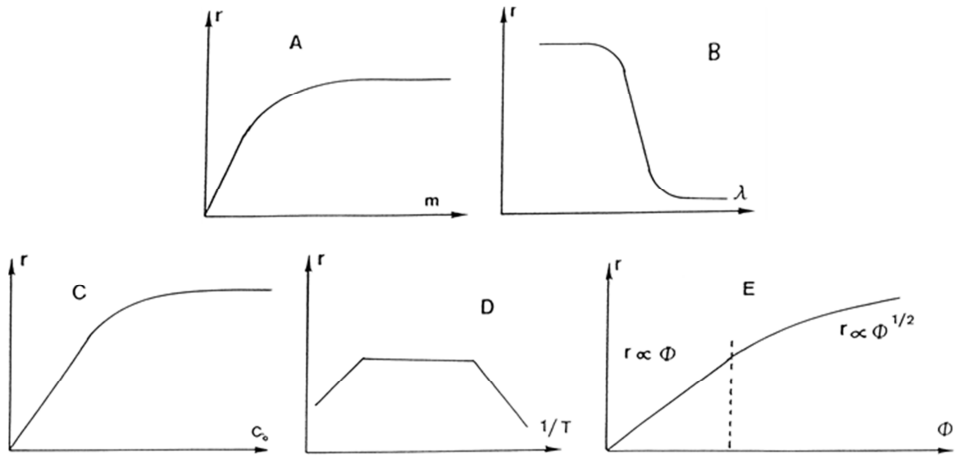

Figure 5 : Different parameters that influence the photocatalytic reaction rate *r*. (A) mass *m* of photocatalyst, (B) λ irradiation wavelength, (C) initial concentration C_0, (D) temperature T and (E) radiant flux ϕ [6].

When a photocatalyst is illuminated, the irradiation energy has to be equal or higher than the band gap energy. Therefore wavelength follows the absorption spectrum of the photocatalyst. For instance titanium dioxide (TiO_2) in its anatase form has a band gap of 3.2 eV, allowing a photoexitation with wavelength values lower than 388 nm (UV-A).

The initial concentration of reactant also influences the photocatalytic reaction rate. As heterogeneous catalysis kinetics follows a Langmuir-Hinshelwood mechanism, the reaction rate is dependent of the concentration of reactant that is adsorbed on the active sites of the catalyst surface [6], [7], [67]. At low concentration the reaction is in most of the cases a first order reaction, whereas at high concentration, it turns into a zero order reaction.

Although heating is not required to initiate photocatalytic reaction, when temperature reaches low values (< 0°C), higher activation energy is required to provide the same reaction rate as that of room temperature. Here desorption of the reactant product is not favoured and therefore the reaction rate is decreasing. The reaction rate is then limited by the desorption step. On the other hand, the reaction rate is also decreasing when the reaction is realised at “high” temperatures (> 80°C), but in this case the adsorption of the reactant is not favoured even though low activation energy is required. The adsorption step is then the rate-limiting step. Note that those temperatures are indicative.

Regarding the illumination intensity (i.e. radiant flux ϕ), a proportional rate increment is observed with increasing the radiant flux. However by increasing the intensity, the reaction rate is still increasing but is found to be proportional to $\phi^{1/2}$ before to be non-depending on the radiant flux [6].

Thus the photocatalytic reaction should be realised within the light regime with a proportional reaction rate to ϕ. The change in regime has been estimated at the laboratory scale (Phillips HPK 125 UV, 125 W) to occur at 25 mW/cm² radiant flux for an optimal use of the light [6].

II.3 Semiconductor materials used in photocatalysis

As previously mentioned, photocatalysis relies on the use of a semiconductor material as a photocatalyst. The ideal photocatalyst should (1) provide photoactive properties, (2) utilise visible and/or near UV light when irradiated, (3) be biologically and chemically inert, (4) have good photostability (corrosion resistant), (5) be inexpensive and (6) non-toxic [68]. Moreover in the case of oxidation photocatalysis, a suitable photocatalyst should have on one hand a conduction band redox potential that is higher than the one of $O_2/O_2^{-}\bullet$ couple, on the other hand a valence band redox potential that is lower than the one of $OH\bullet/H_2O$ couple. Indeed $O_2^{-}\bullet$ superoxydes radicals and OH• hydroxyl radicals will be able to react with organic/inorganic molecules (reactant and reaction intermediate) to be eventually degraded into the final reaction products (CO_2, H_2O, etc.).

Among many semiconductor materials, metal oxides like TiO_2, ZnO, $SrTiO_3$, SnO_2, WO_3 or Fe_2O_3, and metal chalcogenides like CdS, CdSe and ZnS, have been investigated and used in many photocatalytic reactions [62], [68]. Their band gap and redox potential value are presented in Figure 6. In contrary to many semiconductor candidates that may not be presented as ideal photocatalyst, the redox potential of both $O_2/O_2^{-}\bullet$ and $OH\bullet/H_2O$ couple (respectively -0.33 eV and +2.60 eV) are in agreement with the band gap position of TiO_2, with conduction and valence bands being at +2.7 eV and -0.5 eV respectively [69], [70]. TiO_2 has been widely chosen in photocatalysis applications due to its chemical (photo)stability, high quantum yield, low cost for commercial forms, as well as being non-toxic [10], [71], [72]. These applications have included e.g. self-cleaning surfaces, water and air purification, antifogging surfaces, photovoltaic, biocidal applications and energy production [73]–[77].

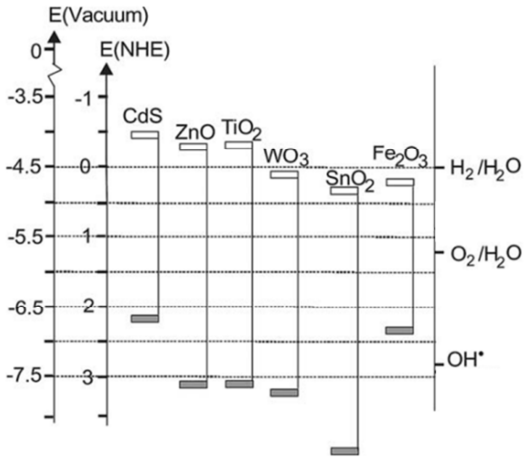

Figure 6 : Band gap and redox values of different semiconductor photocatalysts, using normal hydrogen electrode (NHE) as a reference. Adapted from Carp *et al.* graph [54].

III. Titanium dioxide photocatalyst

III.1 Generalities and structures of titanium dioxide

Titanium dioxide (titanium (IV) oxide or titania) has a chemical formulation of TiO_2 and can be found in 4 different crystalline polymorphic forms in nature that are anatase, rutile, brookite and monoclinic TiO_2 (B) [54]. The most common representation is the view of the crystal structures as networks of edge- and/or corner-linked distorted TiO_6 octahedron building blocks (Figure 7). In the case of anatase, the oxygen atoms form a body centred cubic stacking and TiO_6 octahedra are linked by sharing edges. In the rutile phase, the oxygen atoms build a hexagonal compact structure, in which TiO_6 octahedra are linked by their corners.

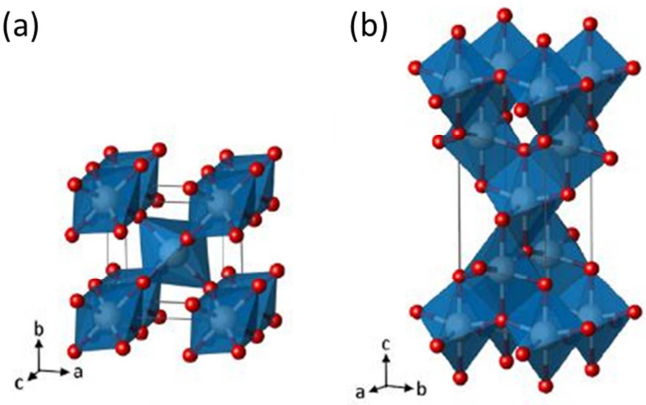

Figure 7: Crystal structure of TiO_2 in its rutile (a) and anatase (b) phase (Ti (white); O (red)) [78].

Anatase and rutile phases have an average Ti–O distance of 1,93 Å and 1.97 Å respectively. In regards to thermodynamics, the rutile phase is more stable than the anatase phase. However it has been shown that at low temperature, as well as in small particles, anatase is the preferred phase. Both structures display different band gap values, which are 3.2 eV for anatase, corresponding to a wavelength of 385 nm, and 2.8-3.0 eV for rutile corresponding to about 410 nm in wavelength. Therefore anatase TiO_2 can be only activated by near UV photons, while rutile TiO_2 has an absorption threshold at the beginning of the visible light region.

In terms of material surfaces, titania exhibits amphoteric properties due to the hydroxyl groups on the TiO_2 surface ("titanol" TiOH), which takes part in the following acid-base equilibrium:

$$TiOH_2^+ \underset{-H^+/+H^+}{\overset{pKa_1}{\longleftrightarrow}} TiOH \underset{-H^+/+H^+}{\overset{pKa_2}{\longleftrightarrow}} TiO^- \qquad \text{(Eq. 5)}$$

III.2 Titanium dioxide properties in photocatalysis and antibacterial applications

III.2.1 Photocatalytic properties

The anatase titania phase is characterised by a conduction band and a valence band separated by an energy gap of 3.2 eV. Hence when this semiconductor is excited by a photon with equal or higher energy than its band gap, an electron from its valence band can be promoted to the conduction band, with the creation of e^-/h^+ pair. The reaction usually goes as follow:

$$TiO_2 + h\nu \rightarrow e^-_{CB} + h^+_{VB}$$ (Eq. 6)

As the energy required is 3.2 eV, a wavelength smaller than 388 nm is needed, so that anatase titania is only active in the UV range. Once the material is irradiated the charge carriers will usually recombine. However in the presence of charge carrier scavengers or surface defect state, charge carriers may then be trapped and recombination may be prevented.

$$Ti^{4+} + e^-_{CB} = Ti^{3+}$$ (Eq. 7)

$$Ti^{4+} - OH + e^-_{CB} = Ti^{3+} - OH$$ (Eq. 8)

$$Ti^{4+} - OH + h^+_{VB} = Ti^{4+} - OH^+ \bullet$$ (Eq. 9)

The charge carriers can migrate to the surface of the nanoparticle for eventually undergoing reduction (for electrons) or oxidation (for holes) reactions with organic and inorganic molecules. In regards to the degradation of pollutants, the reactions involve mainly the redox couple $OH\bullet/H_2O$, and additionally the $O_2/O_2^-\bullet$ redox couple.

$$O_2 + e^-_{CB} \rightarrow O_2^- \bullet$$ (Eq. 10)

$$H_2O + h^+_{VB} \rightarrow OH \bullet + H^+$$ (Eq. 11)

The $O_2^-\bullet$ superoxide radical is also an intermediate towards the generation of other oxidising species such as $HO_2\bullet$, H_2O_2 and $OH\bullet$, according to the following reactions:

$$O_2^- \bullet + H^+ \rightarrow HO_2 \bullet$$ (Eq. 12)

$$HO_2 \bullet + H^+ + e^-_{CB} \rightarrow HO_2 \bullet$$ (Eq. 13)

$$HO_2 \bullet + HO_2 \bullet \rightarrow H_2O_2 + O_2$$ (Eq. 14)

$$H_2O_2 + e^-_{CB} \rightarrow OH \bullet + OH^-$$ (Eq. 15)

The pollutant can also be directly oxidised by the photogenerated holes as follow:

$$\text{pollutant} + h^{+}_{VB} \rightarrow \text{pollutant}^{+\bullet} \rightarrow \text{degradation products} \quad \text{(Eq. 16)}$$

The OH• radicals oxidise the pollutants mainly via two mechanisms:

(i) by removing a hydrogen atom from C-H, N-H or O-H bonds, as follows:

$$R - H + OH\bullet \rightarrow R\bullet + H_2O \quad \text{(Eq. 17)}$$

(ii) by electrophilic addition on π bonds or aromatic rings, as follows:

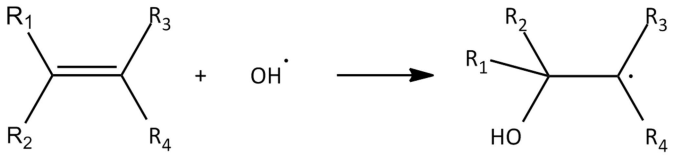

(Eq. 18)

In the case of formic acid, the possible reactions can be written as follow [79]:

$$h^{+}_{vb} + HCOOH \leftrightarrow HCOO\bullet + H^{+} \quad \text{(Eq. 19)}$$

$$OH\bullet + HCOOH \rightarrow HCOO\bullet + H_2O \quad \text{(Eq. 20)}$$

$$HCOO\bullet + O_2 \rightarrow CO_2 + H^{+} + O_2^{-}\bullet \quad \text{(Eq. 21)}$$

All photogenerated carriers do not migrate toward the surface of TiO_2. In fact the charge carrier photogeneration is a fast process (scale of femtosecond) whilst migration of charge carriers occurs in the scale of 100 ns-ms [9]. Recombination is a semi-fast process (10-100 ns) which results in a higher occurring chance than migration toward the semiconductor surface. This is mostly due to the presence of lattice defects, crystal imperfections and impurities [80]–[82]. Therefore the morphology of titania and the way to immobilise it on surfaces are crucial in order to avoid as much recombination as possible.

III.2.2 Biocidal properties

The ability of TiO_2 to degrade a wide range of organisms is a direct consequence of the photocatalytic activity of TiO_2 for oxidising adsorbed chemical molecules. Indeed microrganisms can be first seen as a complex arrangement of high molecular weight molecules. Therefore titania is also one the most convenient choices as a photocatalyst for use in biocidal applications. However the exact degradation mechanism of bacteria in photocatalysis has yet to be explained. In late 1980 it was assumed that the bacteria's coenzyme A allows the transfer of an electron to the photogenerated holes of titania powder upon UV-A irradiation, resulting in the oxidation of coenzyme A [83]. Eventually the bacteria's respiratory behaviour was affected, leading to the death of the bacteria. Later investigations by Sunada et al. revealed that once titania, in contact with a bacteria membrane, is irradiated by UV light, destruction of *E. Coli* bacteria's outer membrane occurs (Figure 8) [77]. This was explained by the reaction between reactive oxygen species (e.g. $OH\bullet$, $HO_2\bullet$, $O_2^-\bullet$ and H_2O_2), formed by photogenerated charge carriers, with the bacteria's outer membrane lipopolysaccharide. Once partially degraded, the permeability of the cell membrane is increased and reactive oxygen species will further react with the lipopolysaccharide membrane, but also with the second protection layer of the bacteria cell: the peptidoglycan layer. A longer time is required to degrade the peptidoglycan layer compared to the outer membrane. Kiwi and Nadtochenko investigated the degradation of all membrane component of the *E. Coli* membrane by TiO_2 P25 Degussa film [84], [85]. Results showed that lipopolysaccharide were indeed rapidly degraded and peptidoglycan was the hardest layer to degrade. They also noticed that the rate of degradation of the lipopolysaccharides of *E. Coli* was slower than the degradation rate of lipopolysaccharide samples. They concluded that the structure of the bacteria's outer membrane affects the degradation rate of the lipopolysaccharides. Further degradation of peptidoglycan layer will eventually lead to an increase in permeability of the bacteria cells. At this point, leakage of ions (like potassium) and small molecules can be observed, and cell damage becomes irreversible [86]. Reactive oxygen species will therefore be able to reach the bacteria's cytoplasmic membrane and undergo reactions with membrane lipids. Higher molecular weight component (e.g. proteins) will then leak and further degradation of the membrane will lead to cell lysis and therefore loss of cell viability. Degradation of the internal components of the cell then occurs, followed by complete mineralisation.

As mentioned above, reactive oxygen species are found to be the principal cause of the photocatalytic degradation of bacteria. However in contact with the titania surface, direct degradation of cellular components by the photogenerated electrons and holes, may also occur [85]. Hydroxyl radicals $OH\bullet$ were shown to be the major ROS involved in short range killing of many bacteria, whereas hydrogen peroxide H_2O_2 is believed to degrade bacteria membranes from a longer

range [86], [87]. Although O_2^-• is also believed to play a role in the degradation of bacteria membrane, it is most likely to convert to its acidic form HO_2•, which will then oxidise the bacteria membrane [88].

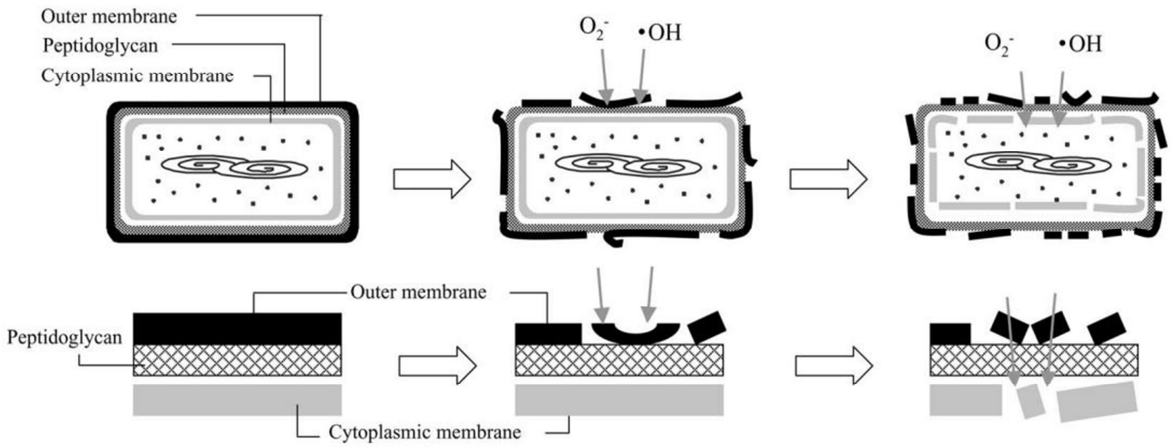

Figure 8: Degradation of the bacteria cell membrane by reactive oxygen species upon UV irradiation of TiO_2 film [77]. The bottom images show a schematic magnification of the bacteria membrane during degradation.

In addition to the photocatalytic properties of TiO_2 against bacteria, the use of small-size nanoparticles, whether metallic or metal oxides, are thought to also have an impact on bacteria killing [89], [90]. Although silver nanoparticles are known for their biocidal properties, Sondi et al. showed that cell death was not associated to the release of toxic Ag^+ ions from the nanoparticles, but rather by the accumulation of small-size nanoparticles inside the bacteria wall cells [91]. This eventually led to bacteria death due to an increase in cell membrane permeability. This nanoparticle size effect on bacteria killing was also observed by Simon-Deckers *et al.,* where <25 nm rutile and anatase TiO_2 phase nanoparticles both showed toxicity towards *E. Coli* bacteria in the dark [92]. Loss in bacteria viability when exposed to small size Al_2O_3 nanoparticles was also observed, while ZnO, CuO and Fe_2O_3 small size nanoparticles also displayed biocidal properties [89], [90]. It must be noted that spherical shape nanoparticles were found to be more cytotoxic than the one with elongated shape. One can also note that the effect of nanoparticle size is observed when the bacteria are in contact with nanoparticles from a suspension. Immobilisation of the nanoparticle may therefore prevent toxicity of small size nanoparticles. Nanoparticle charge surface may also induce cell killing when being positively charged [92]. In fact it was found that negatively-charged nanoparticles did not

present biocidal properties in the dark, due to the electrostatic repulsion of negative surface charges of the cell and those of nanoparticles.

III.3 Enhancing photocatalytic properties of titanium dioxyde

Titania in its anatase crystallized form is still considered to be actually the most efficient photocatalyst under UV-A irradiation. However the main issue with this type of TiO_2, is that charge recombination of the photogenerated carriers will occur more frequently than migration to the surface of the material to initiate photocatalytic reactions [9]. In order to prevent as much as possible the charge carriers recombination, modifications of titania have allowed to induce electronic and chemical effects, and to enhance the photocatalyic properties of this semi-conductor material. These modifications have included changes in TiO_2 composition, morphology, chemical structure, size, or an association with other elements and/or materials [10], [11].

The suitable association of TiO_2 nanoparticles with metallic nanoparticles have shown enhancement of the photocatalytic properties upon UV irradiation [23]. In fact metallic nanoparticles can act as electron traps that will prevent charge recombination within the semiconductor material. In order to have the electron trapping effect upon UV-irradiation of TiO_2, the metallic nanoparticles must have an intimate contact with the semiconductor material and the Fermi level of the metallic nanoparticles should be lower than the energy of the conduction band of TiO_2. Thus the photogenerated electrons will be able to migrate from the TiO_2 conduction band to the metal, lowering the e^-/h^+ charge carrier recombination rate [24]. Metal nanoparticles may also act as a catalyst in the reduction reaction due to the photogenerated electron storage. Figure 9 illustrates the electron trapping when a TiO_2 nanoparticle, associated with gold nanoparticle, is irradiated by UV light.

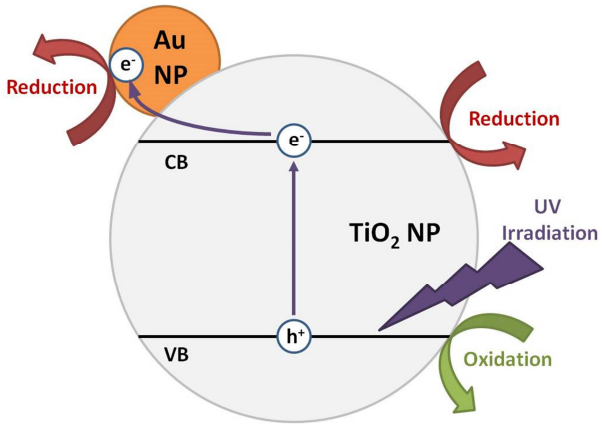

Figure 9: Association of TiO_2 with gold nanoparticles (AuNP) which act as an electron trap once TiO_2 is irradiated by UV light. The figure is based on schematic of Friehs *et al.* [93].

It must be mentioned that when electron trapping by metallic nanoparticles occurs, recombination sites will be located at the metal/TiO_2 interphase and enhancement of the photocatalytic properties of the TiO_2 can be inhibited. Therefore there is an optimum in metal content and size at the surface of TiO_2 nanoparticles, in order to keep the enhancement of TiO_2 photocatalytic properties upon UV-irradiation [24]. Nevertheless if the trapped electrons participate in reduction reactions (such as e.g. reduction of adsorbed oxygen), surface recombination of charge carriers will be prevented. This case is only true when the work function of the metallic nanoparticles is higher than that of TiO_2. Platinum, palladium, copper, silver and gold nanoparticles have shown to be good candidates for showing the ability to trap photogenerated electron when suitably associated with titania [24], [57], [74], [94].

IV – Titania photocatalytic and biocidal properties enhancement with silver nanoparticles

IV.1. Silver nanoparticles

IV.1.1 Synthesis of silver nanoparticles

Nanoparticle material morphologies have been promising since the past two decades to be excellent candidates in bionanotechnology applications [16]. Silver has been used for centuries for treatment

of burns, chronic wounds and also for water treatment, this material is a suitable candidate in its nano-sized form for investigations in biology related applications [58]. However it has been shown that the size, the stability and the nanoparticle shape are crucial in regards to the applications they are suitable for [95]. These parameters are strongly influenced by the nanoparticle synthesis which usually requires a metallic precursor, a reducing agent and a stabilising agent.

The most common silver nanoparticle (AgNP) synthesis is by chemical reduction [95]. Borohydride, citrate, ascorbate and elemental hydrogen are the usual reducing agents used in AgNP synthesis. First the reduction of silver ions to silver atoms (Ag^0) takes place, followed by the agglomeration into clusters which will lead to the formation of silver nanoparticles. The size of the nanoparticles depends on the type of reducing agent used in the synthesis. It has been shown that small nanoparticles can be obtained by using a strong reducing agent, like borohydride, whereas weaker reducing agents give larger particles. However the size polydispersity is high with a weak reducing agent, while size monodispersity can be achieved by using a strong reducing agent. Thus a two-step method was investigated in order to increase the larger size particle monodispersity by first using a strong reducing agent to synthesise small nanoparticles and then enlarging them by adding a weaker reducing agent [96]. The use of heat treatment on the particles allows shape control of AgNP [97], [98]. Thus spherical, pentagonal, triangle or nanoprism shape can be obtained. The use of a stabilising agent has allowed an improvement in size control of the metallic nanoparticles as well as preventing aggregation of the colloids [95].

Other nanoparticles syntheses are being investigated in order to reach maximum control of size and shape, however the major concern is that AgNP synthesis should be done by green processes due to modern development and industries. Since it is known that the irradiation of a silver salt (direct photolysis) or that the irradiation of a sensitizer in the presence of an AgNP precursor (photosensitisation), can reduce silver ions to their metallic forms, photochemical approaches to AgNP synthesis have been investigated in order reach these requirements [99]. The group of Lavinia Balan at the *Institut des Sciences des Matériaux de Mulhouse* (IS2M, Mulhouse) developed in an innovative AgNP photoinduced synthesis, used in this project [19], [100], [101]. This approach offers an easy, low cost and environmentally friendly coating process to generate AgNP monolayers on a surface (e.g. glass slide, polymers, copper grid), with a variety of optical properties over the whole visible range. One of the main advantages of this approach is its simplicity: no use of capping agents or multistep procedures being required prior to seeding of the AgNP. The AgNP photoinduiced synthesis is obtained upon UV-irradiation of a photosensitive formulation spread on a surface. This photosensitive formulation is composed of a silver precursor, $AgNO_3$, and a chromophore that are dissolved in a solvent (usually water). In this approach the chomophore acts as a free radical

generator, which will be obtained upon UV irradiation of the chromophore (Figure 10). The free radicals will be able to reduce silver ions, Ag^+, to their metallic state, Ag^0, which will then be able to associate into clusters and form AgNP. Since the chromophore is cleaved into two radicals, the first one will reduce silver ions, while the other will be responsible for the control of the size and shape of the AgNP synthesised.

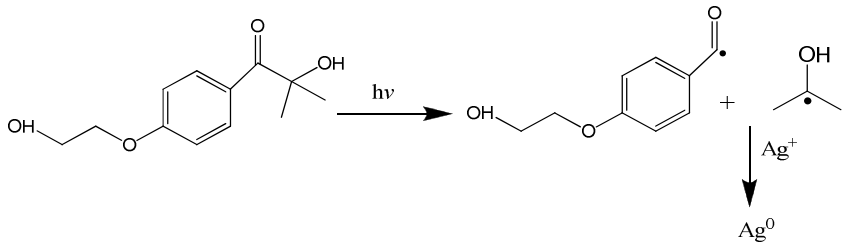

Figure 10 : Photo-cleavage mechanism of Iragure 2959 chromophore and reduction of silver cations [100].

The photo-assisted process is carried out at room temperature, under air and is completed within a few minutes. By playing with experimental parameters, the morphology of AgNP (size and shape) can be adjusted to tune the adequate plasmonic properties for a given application. These synthesis parameters have included the chemical composition (chromophore-silver precursor ratio, the type of chromophore, the nature of solvent), the irradiation time and the fluence of the actinic source.

IV.1.2 Optical properties of silver nanoparticles

The effect of the size and shape of the nanoparticles can be observed by investigating the optical properties of silver nanoparticles [97], [102]. As metallic nanoparticles, AgNPs exhibit surface plasmon resonance absorption due to the oscillation of the surface free electron when being subjected to electromagnetic radiation. This effect can be characterised by optical characterisations such as UV-Visible spectroscopy where the maximum absorption correlates to the plasmon resonance frequency. Mock *et al*. investigated on the spectral properties of AgNP depending on their size and shape [97]. The size variation was obtained by using different concentrations of silver precursor, while heat treatment is required to control the shape of the nanoparticles. The result showed that while increasing the size of AgNP, a red shift is obtained, and a blue to red shift is obtained by changing the nanoparticle geometry (Figure 11).

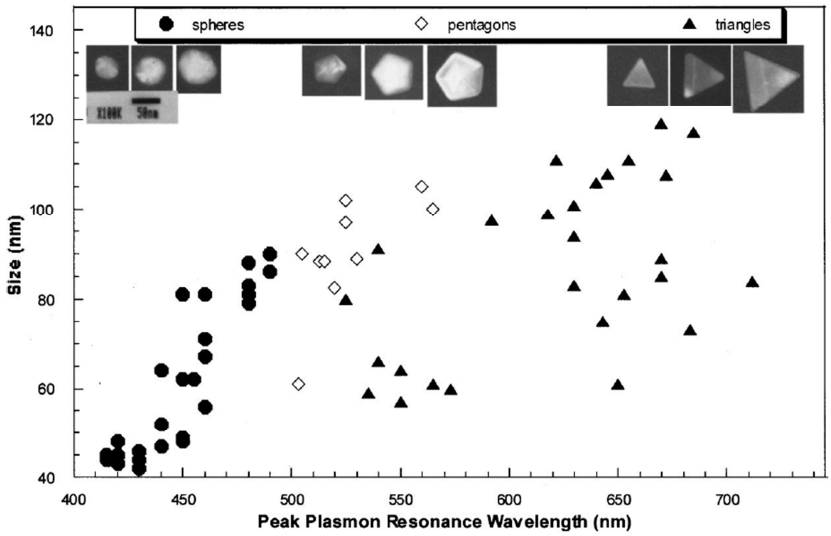

Figure 11: Size and shape of silver nanoparticle according to the peak of absorbance of AgNP plasmon resonance [97].

IV.1.3 Biocidal properties of silver nanoparticles

Silver is a compound that is known to provide good biocidal properties towards several micro-organisms. Thus silver-based materials have been used in a lot of antibacterial applications [16], [58]. Although metallic silver is inert, it may be highly reactive if it becomes ionised when exposed to dissolved oxygen in water medium. The reaction goes as follow [103]:

$$O_{2(aq)} + H_3O^+ + 4Ag_{(s)} \rightarrow 4Ag^+_{(aq)} + 6H_2O \qquad \text{(Eq. 22)}$$

Once ionised, silver can bind to cell tissue proteins which will then affect the structure of a cell membrane [104]. A loss of K^+ ions and a decrease of ATP level may occur when silver ions are bound to bacteria membrane phospholipids. Further biocidal properties may occur when silver ions interact with molecules inside the cells. In fact studies have shown that silver ions enter bacteria cells within 30 min of exposition and bind to cytoplasm components, proteins and nucleic acids [105]. Inhibition of the main respiratory chain proteins (e.g., cytochrome b) causes an increase of ROS inside the cell, which leads to oxidative stress, protein damage, DNA strand breakage, and, consequently, bacteria death [106]. It has been shown that silver has a strong affinity to sulphur and phosphorous compounds, which will allow them to bind to the bacteria's DNA and RNA, resulting in inhibition of bacteria replications [58], [107], [108].

Other studies have shown a direct effect from the AgNPs on bacteria. Though the toxicity mechanism of silver nanoparticles is still unclear, a lot of studies suggest that this mechanism is similar to the one of silver ions, that are interacting and binding to the bacteria's cell outer membrane, as well as interacting with membrane protein, components from the cytoplasm, DNA and RNA [104], [109]. Shrivastava et al. suggested that one of the possible antibacterial modes of silver nanoparticles action is the inhibition of signal transduction and growth by dephosphorylation of the peptide substrates on tyrosine residues [110]. As nanoparticles, the high surface-to-volume ratio should also allow an improvement of the antibacterial properties of silver against both Gram negative and Gram positive bacteria [11], [89], [111]. It was shown that silver presenting {111} facets provide better interaction with bacteria membrane, thus AgNPs with a high {111} facet should provide higher biocidal properties [107], [112]. Morones *et al*. investigated the AgNP size effect on the biocidal properties of the nanoparticles [113]. In this study they used commercial AgNPs of different sizes (1-100 nm) as suspensions which were added to bacteria media. They found that AgNPs smaller than 10 nm were presented good adhesion to the bacteria outer membrane and provided the best antibacterial properties. They associated that result to the {111} surface facets (determined by XRD analysis) of 1-10 nm AgNPs. They also noticed by TEM analysis that these small diameter sized AgNPs were able to penetrate the bacteria membrane and cytoplasm. These observations on the size effect of nanoparticles on cell membrane can be also found in the works of Azam *et al.* and Cai *et al.*, where the antibacterial properties of nanoparticles, whether metallic or not, used as suspension were studied [89], [111]. Investigations by Pal *et al.* highlighted the effect of AgNP shapes for Gram negative bacteria killing [114]. Here the nanoparticles were synthesised and different concentrations were added in the bacteria medium. Bacteria media containing spherical (39 nm) or triangular (40 nm) AgNP shapes were compared to bacteria media containing either Ag nanorods (133 nm in length and 16 nm in diameter) or $AgNO_3$. They found that silver nanoparticles presented a higher biocidal effect against *E. Coli* than Ag nanorods and $AgNO_3$. While triangular AgNPs gave an almost total bacteria growth inhibition, spherical AgNPs showed significant biocidal properties with the same concentration of triangular AgNPs. XRD analysis showed that triangular AgNPs were presenting more {111} facets than spherical AgNPs, which were mostly exposing {100} facets with a small percentage of {111} facets. Therefore the biocidal properties of AgNPs are not only size-dependant but also shape dependant.

Overall the exact bacteria degradation by AgNP is still under discussion. It must be mentioned that this mechanism can also be a combination of all mechanisms discussed in this section, due to silver in its nanoparticle form (AgNP) and in its ionised form (Ag^+). Figure 12 summarise the possible effect of AgNP and silver ions on bacteria.

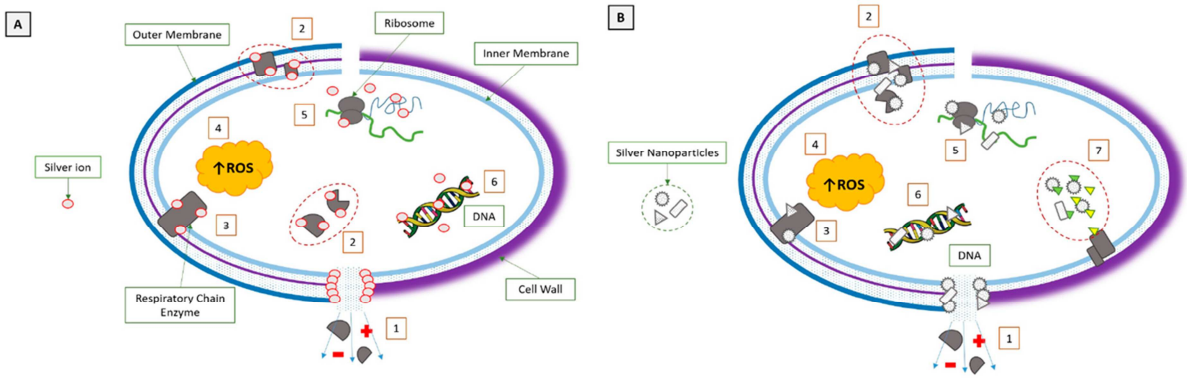

Figure 12 : A comparison of the silver ions (A) and silver nanoparticles' (B) mode of action to Gram-negative and Gram-positive bacteria (showed on the left and right on the diagram respectively. (1) Pore formation; metabolites and ions leakage (shown as "plus" and "minus"). (2) Denaturation of structural and cytoplasmic proteins; enzymes inactivation. (3) Inactivation of respiratory chain enzymes. (4) Increase of intracellular reactive oxygen species (ROS) concentration. (5) Interaction with ribosome. (6) Interaction with nucleic acids. (7) Inhibition of signal transduction [104].

IV.2. Association of silver nanoparticles with titanium dioxide

IV.2.1 Silver deposition synthesis on titanium dioxide

As discussed in section III.3, the photocatalytic properties of titania could be enhanced by suitably associating TiO_2 with metallic nanoparticles. However this enhancement is dependent on the size, the shape and the concentration of the metallic nanoparticles. Therefore the nanoparticle syntheses have to be well investigated in order to control all these parameters. In regards to AgNPs, the use of a reducing agent and a stabiliser has allowed control of the size and shape during the aqueous reduction synthesis [95]. By using this AgNP synthesis procedure and changing the aqueous medium by titania nanoparticles suspension, it is possible to synthesise AgNP on the TiO_2 nanoparticle [115]. The control of the size and shape of the silver nanoparticles is allowed by changing the pH of the suspension, the amount of reducing agent added and the agitation time. The investigations of Zhan *et al*. were dealing with the elaboration of a one-pot synthesis of Ag@TiO_2 nanocomposites for antibacterial application using a sol-gel method [116]. Although AgNP with a controlled size and shape were synthesised on TiO_2 with suitable contact, the synthesis required chemicals like acetonitrile and dimethylformamide which do not allow this synthesis to be considered as "green" [95]. Successful synthesis of AgNP on titania nanotubes was achieved by Miao *et al*. by adding a silver precursor during hydrothermal synthesis of titania nanotubes [117].

Although these studies described above are based on the addition of TiO_2 in the AgNP synthesis protocols, the first association of silver with a semiconductor material was reported by Baur and Perret, where the use of zinc oxide is photocatalytic properties allowed the reduction of a silver salt as a silver precursor to metallic silver [118], [119]. This early work highlighted the fact that not only metallic silver could be deposited *via* a physical or chemical pathway, but also synthesised by reducing a metallic precursor by semiconductor materials *via* photoreduction pathways. Several works demonstrated the photoreduction of silver salts on different titania morphologies under UV-A irradiations [120]–[124]. In these investigations the irradiation time is the main parameter in order to have size and shape control of AgNP synthesis. Contact with silver and titania can be improved by adjusting the pH above the isoelectric point of titania, allowing the negatively-charged titania surface (TiO^-) to interact with Ag^+ [121], [122]. Moreover methanol and ethanol used as diluting agents in the silver precursor solution act as hole scavengers during the irradiation process, so that the silver ion photoreduction was promoted [120], [122], [123]. However it was found that the use of a capping agent on TiO_2 nanotubes allowed better control of the polydispersity in size of the photoinduiced silver nanoparticles [124].

IV.2.2 Enhancement of photocatalytic properties

Most of the studies on the association of semiconductor materials with noble metal nanoparticles are recently focussed on plasmon resonance induced field effects and on the electron injection from metallic nanoparticles to the semiconductor. The enhancement of photocatalytic properties of titania by metallic nanoparticles that prevents the charge carrier recombination under UV-irradiation, is not as much covered in the literature [10], [24], [125]. In fact gold and silver nanoparticles exhibit electron trapping properties when used as small nanoparticles (3-5 nm in diameter) and cause a shift in the Fermi level [125], [126]. It has to be mentioned that in the case of providing better charge carrier separation on P25 Degussa TiO_2 associated with gold nanoparticles, this effect can be observed when 5 nm nanoparticles are located at the anatase and rutile junction of P25 TiO_2 [127]. As being a noble metal as well, the association of silver nanoparticles with titania, may lead to an enhancement of the photocatalytical activity of titania under UV-irradiation.

One of the effects that is provided by silver when associated with TiO_2 is an increase in the specific surface area, which promotes more reactive sites to be available to take part in the photoreaction [62], [122], [128]. This is effect can be demonstrated by synthesising AgNP during titania synthesis by the sol-gel method [128]. Different loads of silver were applied during the synthesis and a change of anatase phase to rutile phase was observed for a high load of Ag (8-10 mol%) in regards to titania. With lower loads of silver precursor (2-6 mol%), smaller size TiO_2 nanoparticles were obtained while

having an anatase structure. Thus, surface-to-volume ratio was increased and making the catalyst being expected to possess better photocatalytic properties than bare TiO_2 anatase nanoparticles.

The other effect of this metal-semiconductor association could be that silver nanoparticles can act as electron traps when titania is irradiated by UV-A light [125], [129]–[131]. In this mechanism, the photogenerated electron will be trapped by metallic silver nanoparticles toward the surface of a titania nanoparticle upon UV-A irradiation. Charge carrier recombination can therefore be prevented. Electrons will be able to react with O_2 molecules, while positive holes will react with OH and H_2O adsorbed molecules (Figure 13). Sobana *et al*. demonstrated this effect by reducing different concentrations of silver salts on TiO_2 anatase nanoparticles *via* photochemical approaches [129]. BET analysis showed a decrease of the specific surface area while increasing the concentration of silver salt. Although high AgNP size polydispersity was obtained for every Ag-TiO_2 nanocomposite, photocatalytic degradation of direct blue and direct red dies was improved when Ag was deposited on the semiconductor. Enhancement of the photocatalytic properties of TiO_2 was associated with AgNP acting as electron trapps upon UV-A irradiation.

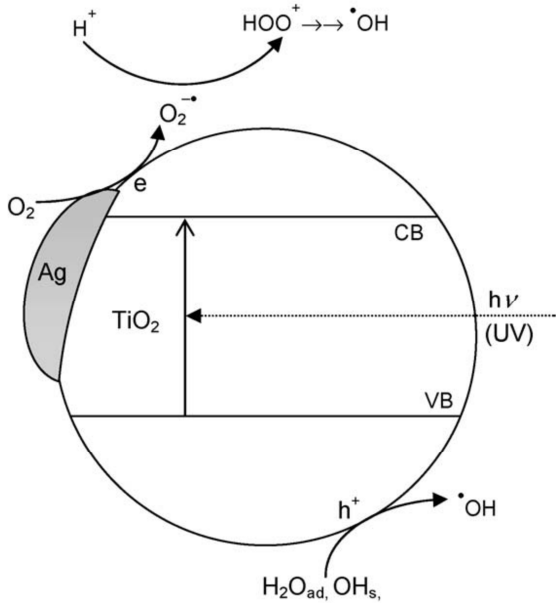

Figure 13: Photocatalytic pathway of TiO_2-silver nanocomposite under UV-irradiation [130].

Kowalska *et al* investigated on the influence of different TiO_2 crystal structures associated with photoinduced silver nanoparticles by monitoring the photodegradation of acetic acid and 2-propanol in liquid phase, under UV and visible light irradiation [122]. In their works the authors could see the two effects that provide AgNP described in this section. Photoinduced synthesis of AgNPs on small

titania anatase crystallites led to fine metallic deposits. On one hand the higher photocatalytc activity of Ag@TiO_2 material for the degradation of acetic acid under UV-A light was attributed to electron storage in AgNP, and was backed-up by time-resolved microwave conductivity (TRMC) analysis. On the other hand the association of AgNP on TiO_2 nanoaprticles has allowed the material to exhibit photocatalyic properties under visible light due to the surface plasmon resonance of the metal nanoparticles. The same group also investigated the biocidal activity of this composite against *E. Coli* bacteria. This investigation will be discussed in the section below.

IV.2.3 Enhancement of biocidal properties

By associating AgNP to titania, not only the biocidal properties of titania could be enhanced by providing a better charge separation as well as an electron trapping to the metallic nanoparticles with UV-irradiation, the composite material could also benefit from biocidal properties in the dark due to the presence of AgNP [57], [84], [85], [95], [122], [129]. Although several investigations have demonstrated that antibacterial properties of titania were enhanced by suitable association of silver nanoparticles to titania nanoparticles, and that AgNP allowed biocidal activity in the dark, the bacteria degradation mechanism has yet to be fully understand [57], [95], [116], [122], [124], [132].

The investigation of Kowalska *et al* showed that the association of Ag (2wt%) onto different types of TiO_2 by photodeposition, allowed high polydispersity in the size and shape of the AgNP [122]. This Ag@TiO_2 composite could provide better photocatalytical properties to the semiconductor under UV-irradiation for the degradation of acetic acid and methanol, but also the biocidal properties were enhanced under UV-irradiation and in the dark depending on the size of the AgNP. The antibacterial properties were investigated using two methods: (1) small paper disks (1 cm in diameter) were saturated with Ag@TiO_2 photocatalyst (1 g/L) and placed in Petri dishes in which bacteria (Gram negative *E. Coli*) were spread afterwards. In this method the inhibition zone around the paper disk were measured, however results did not give any inhibition zone on the paper disk. The authors concluded that despite the unsuccessful result in antibacterial properties, the coating method showed that the Ag@TiO_2 composite was stable. (2) The second method was by adding the Ag@TiO_2 composites into the bacteria suspension. The suspension bacteria-composite was irradiated by UV light and 0.5 ml of the suspension was taken after different irradiation time, placed in an Agar plate and incubated overnight. The viability of bacteria was then measured and the authors found that the composite that have small size AgNP (i.e. Ag@TiO_2 composite with finer crystallite), were the sample that allows a biocidal activity in the dark. All others composites with bigger sizes presented antibacterial properties under UV-irradiation. Although biocidal activity in the dark was obtained with small photogenerated AgNP, these particle sizes could only be obtained by associating the Ag

precursor with small titania crystalline of 8 to 15 nm in diameter. The viability of the bacteria could have been affected not only by the biocidal properties of AgNP, but also by the structure modification of the bacteria membrane where small particles could penetrate the Gram negative outer membrane, leading to higher permeability and eventually cell death [89], [111], [113]. As the composite coating did not show any biocidal activity in the dark using their first method (i.e. deposition of the composite on a paper disk with bacterial spreading afterwards), UV-irradiation of the sample would have provide more information on the enhancement of the biocidal properties of titania in the Ag@TiO_2 composite film. These results could have given an indication on which type of crystalline and size of titania associated with a certain size diameter of AgNP should be used as a film in order to provide an adequate biocidal activity under UV-irradiation. The deposition method on paper disks has not been discussed and characterised, thus one should assume that Ag@TiO_2 composite could have aggregated on the paper disk, which results in a decrease on the surface-to-volume ratio. Therefore inferior biocidal activity with this method could be observed compared to the other method were Ag@TiO_2 is put in a bacteria suspension [11]. Moreover this could also give an explanation on the biocidal activity absence in the dark with this method since less AgNP are reacting with bacteria.

V. Multilayered thin film constructions via Layer-by-layer self-assembly

In this project, titania and silver nanoparticles will be immobilised/deposited on textile surfaces in order to provide them with photocatalytic properties. However nanoparticles tend to agglomerate into large aggregates, therefore limiting the exposure of the catalyst surface to its environment and light source. Moreover nanoparticles immobilised on a surface should be homogeneously distributed and give a porous structure.

Layer-by-Layer self-assembly is an easy, versatile and low-cost coating technique that allows the construction of homogeneous thin films on every type of surfaces, making it suitable for film construction on textile. Nanoparticles have been successfully used in this type of construction and showed porous structures at a nanoscale level.

The work of this project is to design a TiO_2 and silver nanoparticle thin film constructed on textile *via* Layer-by-Layer (LbL) self-assembly. Therefore this part is focused on multilayered films containing these nanoparticles deposited mainly on model surfaces and other types of more complex surfaces.

Layer-by-Layer self-assembly thin films constructed on textiles will be described in the last section of this sub-part. The discussion will be focussed on thin films for photocatalysis and antibacterial applications.

V.1. Film construction methods

There is a wide variety of available functionalization techniques that can be classified in two categories: top-down and bottom-up approaches [133]. The top-down approach is based on the reduction of a large dimension material to the nanometre scale. The final architecture is well structured and controlled, providing the desired properties. Usually top-down approaches are based on lithography techniques, in which a material is usually protected by a mask and the exposed part is etched away. This technique has been frequently used for integrated circuits fabrication, but is not suitable for textiles. Moreover in this project, a silver-titania hybrid film must be obtained and AgNP must be in contact with the titania nanoparticles, making the top-down approach not so convenient for obtaining this material.

The bottom-up approach on the other hand, allows the controlled assembly of smaller size materials such as atoms, molecules and aggregates. The possibility to associate different types of materials with this approach allows the final material to be multifunctional, making this approach more suitable for associating silver and titania nanoparticles. The main challenges encountered in the bottom-up approach are related to the surface preparation and conditioning for the controlled deposition of the atoms, control of impurities and site uniformity, quality of the reactants, etc. A wide variety of nanofabrication methods have been widely used and investigated, that included e.g. vapour phase deposition (chemical and physical, i.e. CVD and PVD), sol-gel fabrication and molecular self-assembly [116], [134], [135].

CVD essentially involves the process of dissociation of molecules of the gaseous reactants, which subsequently react chemically to form various structures when activated by heat, light, or plasma discharge [133]. In PVD methods, materials are evaporated by e.g. electron beam, ion beam, plasma, or laser. The evaporation material is vaporised with the supplied energy and solidifies on the surface of the substrate. Both CVD and PVD processes are usually carried out in an ultra-high to high vacuum environment, allowing the vapour to reach the substrate without interacting in the reaction chamber with any other gaseous atoms. Although these two approaches have been used for functionalising textile fibres, these two approaches are expensive due to the high energy required, as well as the use of different cathodes in order to deposit different materials on a surface [136], [137].

In comparison to CVD and PVD processes, the sol-gel process is more cost-effective and has been implemented for the fabrication of nanostructured functional metal oxide materials. In fact this approach has been widely used for synthesising titania in its nanopowder form [138]. The sol-gel process relies on a combination of primarily metal precursors in solution, deposition of the precursors on suitable substrates and subsequent heat treatment to cause oxidation and/or sintering of the final products. By adding a second metal precursor in the solution, it is also possible to obtain composite materials with the sol-gel process. Zhang et al. made a sol-gel solution containing silver nitride and titanium(IV) isopropoxide in order to obtain a silver-titania composite nanopowders, with different silver contents [116]. These composites showed good antibacterial properties under ambient light. Sol-gel treatment on textiles has shown to be feasible by adapting the material synthesis parameters (e.g. temperature, pH...) to the textile fibres [139]. However sol-gel titania requires most of the time a calcination step for increasing the material crystallinity, which will lead to the destruction of the fibres.

Surfaces and particles can also be functionnalised by self-assembly methods [133]. This approach is a process by which molecules assemble themselves without the presence of outside interactions. A typical example is the formation of the lipid bilayer of cell membranes. Different strategies have been used in order to control self-assembly system, one of them being the Langmuir-Blodgett method, that allows the construction of monolayers on flat surfaces [140]. This technique is based on the transfer of amphiphilic molecules from the air-water interface onto a solid substrate. However the Langmuir-Blodgett method has received less attention due to the difficulties of avoiding defects during the deposition, which could be induced by the substrate topography and size as well as difficulties in the scaling-up process [17], [133]. As a result this technique may not be suitable to functionalise textile surfaces.

V.2. Layer-by-Layer self-assembly

V.2.1 Discovery, development and construction of Layer-by-Layer thin films

In the 90s, the group of Decher developed the Layer-by-Layer (LbL) deposition technique, an easy and versatile film construction technique with nanoscale precision and controlled thickness using a single deposition process [17], [18]. This bottom-up construction is based on the consecutive adsorption of at least two compounds from a solution or colloid suspension by electrostatic

interactions, covalent bonds, Van der Waals interactions, hydrogen bonds or hydrophobic interactions. Originally this technique was achieved by depositing polyelectrolytes on a charged surface. The film construction begins with the adsorption of negatively-charged polyelectrolytes (polyanion) on a positively-charged surface (substrate). Once the charge overcompensation is reached, a negatively-charged surface is obtained and the surface is then washed to remove the excess polyelectrolytes. Weakly adsorbed materials are also removed thus limiting the complexation with complementary materials. Next polycations are adsorbed, via electrostatic interaction, on the surface of the substrate containing polyanion layer, followed by another rinsing step, leading to the construction of the first pair of polyanion/polycation layers. These 4 steps can be repeated until the desired thickness of the film is reached. Figure 14 illustrates the deposition steps on a charged flat surface.

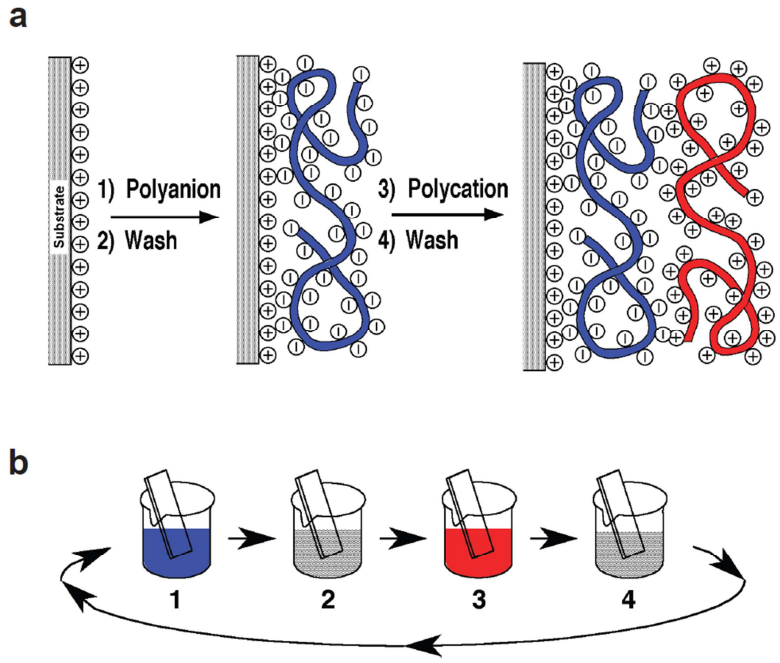

Figure 14: (a) Construction of polyelectrolyte LbL films on a charged flat surface. Once the polyanion (in blue) and the polycation (in red) are successively deposited, a pair of layers has been constructed. (b) LbL thin film construction *via* the dipping deposition technique. The substrate is alternately immersed in the polyanion solution (1) and in the polycation solution (3), with a rinsing step between each immersion (2 & 4) [17], [18].

Ladam *et al* investigated the film construction by zeta potential measurements where the inversion of charges was highlighted after each deposition step of poly(sodium styrenesulfonate) (PSS) and poly(allylamine hydrochloride) (PAH) layer on a bare silica surface (Figure 15) [141]. This inversion of charge was explained by the nature of polyelectrolytes, which are composed of long carbonated

chains [18]. Some areas of the chains will interact with the surface of the sample, whilst the other part will stay free. It must be noted that surface neutrality is maintained due to the counter-ions contained within the polyelectrolyte solutions. Once a polyanion is interacting with the surface of a coated polycation (and reciprocally), counter-ions will be ejected and form ionic bonds. Thus a first pair of layer (LP) made of polyanion and polycation is constructed and the deposition steps of the polyelectrolytes can therefore be repeated.

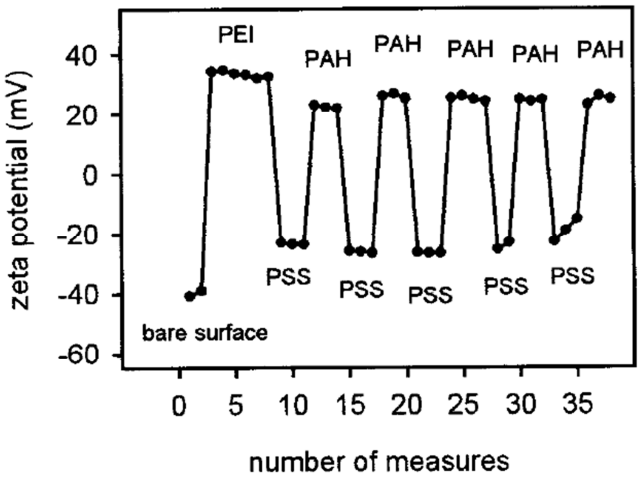

Figure 15: Zeta potential measurement of a PEI/(PSS/PAH)$_5$ film showing the inversion of charge during film construction [141].

Originally investigations of LbL film constructions were made by constructing the film by dipping the substrate directly in the polyectrolyte and rinsing solutions for a time, but other construction methods were investigated for building multilayered films, such as spraying multilayered films [142], [143]. All construction techniques display advantages and drawbacks, for examples dipping constructions required a longer time for the adsorption of the materials at the surface of the substrate, compared to dipping and spin coating, however this leads to better homogeneity of the film at the surface, as well as thicker films, and solutions/suspensions are not wasted. More recently new deposition methods were investigated through electromagnetic [144] and fluidic approaches [145].

V.2.2 Influence of different parameters in the LbL film construction

The first films constructed via LbL technique were polyelectrolyte multilayered films. The physics behind the formation of the polyelectrolyte multilayers are similar to the physics behind the polyectrolyte complex formation [18], [146]. Therefore the temperature, the type of salt and its concentration used in the polyelectrolyte solution, the density of charges as well as the pH of the

solution, are key parameters in the construction of the multilayered thin films. For instance, charge densities of weak polyelectrolytes are highly pH-dependent, which may result in different growth regime mechanisms, thicknesses and film assembly architectures. When using weak polyelectrolytes poly(allyl amine hydrochloride) (PAH) and poly(acrylic acid) (PAA) in LbL film construction ($(PAH/PAA)_n$ film), it was found that a slight change in pH, allows interdiffusion of the polyelectrolytes within the film, providing further an exponential growth to the film, compared to a linear growth at neutral pH [147], [148]. Regarding the influence of the temperature, results led to the conclusion that thicker films are constructed at high temperature due to the swelling of the film and interdiffusion of polyelectrolytes.

Another parameter that may influence the film construction is the contact time between the sample surface and the material to be deposited. The deposition time may vary depending on the type of materials to be deposited in order to achieve regular growth of the film with a good surface homogeneity [145]. While a fast adsorption of the charged material is observed when being in contact to an oppositely charged surface, a longer stabilisation time can be required in order to allow optimum rearrangement of the deposited materials [146]. For instance, polyelectrolytes may have a conformational change from a linear to a random coil structure while increasing the stabilisation time, that can affect the structure of the film [149].

V.3. Versatility of LbL thin film construction

The LbL self-assembly technique allows the construction of films with oppositely-charged materials on a charged surface. As the construction is governed by different types of interactions, a wide variety of charged materials, as well as different types of charged surfaces may be used for film constructions. Enhanced or new properties are thus provided to the host substrate/surface, which explain why interest in this type of thin film construction has grown during the past two decades. Films containing different types of charged materials lead to a wide variety of applications such as e.g. catalysis, optics, energy, membrane and biology. Figure 16 illustrates schematically the versatility of LbL self-assembly technique.

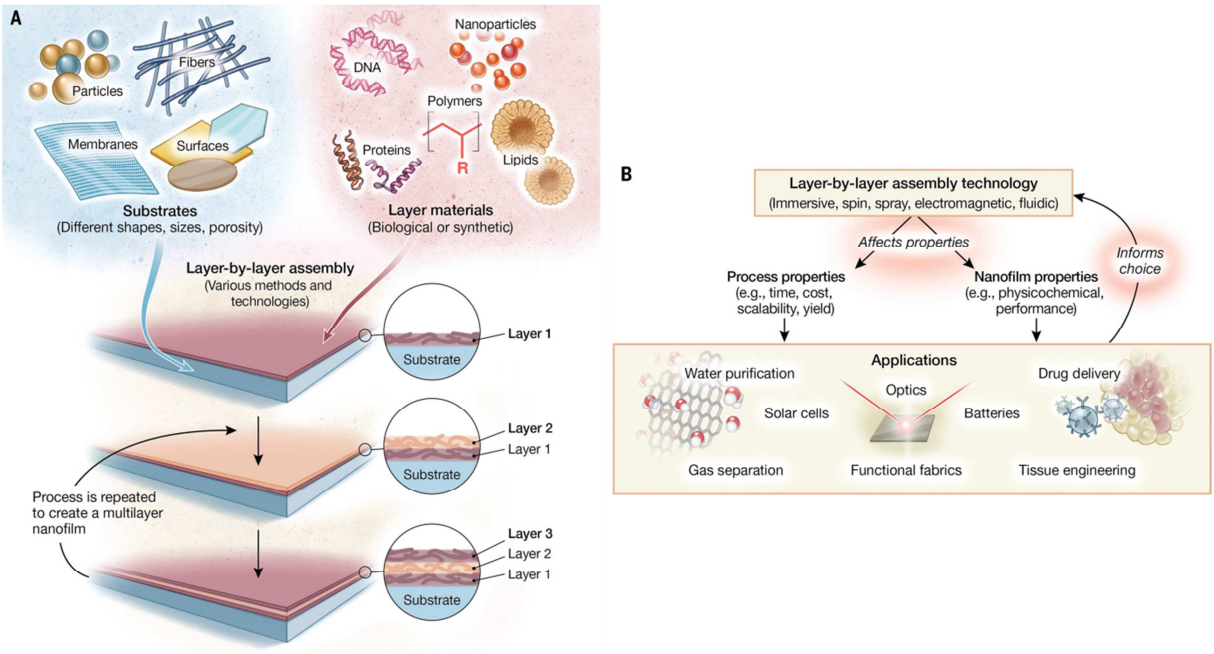

Figure 16: (A) Schematic overview of LbL self-assembly. (B) Influence of LbL self-assembly on films, process properties and applications area [145].

V.3.1 Material choices and range of applications

Originally the LbL films were constructed by depositing polyelectrolytes layers [17]. Later works showed that the LbL self-assembly method allows different types of materials to be associated, in terms of physico-chemical nature and morphology. These studies have included LbL construction with organic materials (e.g. polymer [17], [18], [146], cellulose [150], [151], protein [152], [153], virus [154], DNA [155]) and inorganic materials (e.g. nanoparticles [149], [156]–[159], nanowires [160], nanotubes [161], zeolites [162], clays [163]). The choice of materials for constructing the multilayered thin films has allowed a wide variety of applications, including biology, optics, energy, membrane and catalysis [18], [145].

V.3.1.1 Use of semiconductors materials

Semiconductor material nanoparticles, such as WO_3, Nb_2O_5 or ZnO have been used in LbL film construction, but most of the research is focused on TiO_2 for photocatalysis applications [25]. Due to its amphoteric properties, and when used as a suspension at a given pH, whether acidic or alkaline, the surface of titania can be charged and therefore can be used in LbL film construction. The first investigation on a polymer/TiO_2 LbL system has been published by Sasaki *et al* where negatively-charged titania was used with PDDA as a polycation [164]. The construction of several PSS/TiO_2 pairs of layers provided superhydrophilicity properties to the film after 2 pairs of layers [165]. These

superhydrophilicity properties have also been observed by Lee *et al* in LbL films containing only negatively-charged SiO_2 and positively-charged anatase TiO_2 nanoparticles STS-100 (Ishihara Sangyo Kaisha (ISK), Ltd.), hence providing antifogging properties, but also antireflexion and self-cleaning properties [73].

Prya *et al*. compared a PSS/TiO_2 LbL film, to TiO_2 films constructed by drop-casting and spin coating, using the degradation of rhodamine B dye [166]. Results showed that although drop casting and spin coating TiO_2 films are faster to construct, the degradation of the dye was more efficient with PSS/TiO_2 LbL film, as well as being more stable and reusable. Rongé *et al* evaluated the photocatalytic performances of 5 layer pair PSS/TiO_2 LbL thin films [149]. The films were prepared using different deposition times, either for PSS or TiO_2, which affected the density of the 5 pairs of layer films. When increasing the density, the photocatalytic performances of the film dropped for the degradation of methylene blue dye, whilst improving for the degradation of gas-phase ammonia (NH_3). They suggested that the LbL film structure has to be tuned in order to provide the suitable photocatalytic performance for the degradation of a target molecule.

V.3.1.2 Use of metallic nanoparticles

In Layer-by-Layer thin film construction, polymer films containing metal nanoparticles have been investigated in order to provide catalytic properties to the films. Several types of metallic nanoparticles like Au, Pt or Pd have been used in LbL film construction [17], [156]–[158]. The films were constructed by (a) replacing the polycation or polyanion layer with nanoparticle layers, (b) by incorporating the nanoparticle precursor within the film construction and reducing it afterwards to the metallic state. Although polyelectrolytes have been used as an intermediate layer in nanoparticles, the investigations of Lee *et al.* and Wang *et al.* led to the fabrication of LbL films containing exclusively nanoparticles via an electrochemical LbL deposition approach [73], [167].

AgNP have been mainly used in LbL in order to provide antibacterial properties to LbL coated materials [168], [169], [159], [170]. Podsiadlo *et al*. constructed multilayer thin films composed of polyelectrolytes, clays and silver nanoparticles that presented high mechanical strength and biocidal properties [159]. The aim was to design a new type of composite via LbL self-assembly as potential bone implants. The films presented good mechanical properties as well as being biocidal towards *E. Coli* and biocompatible. Dubas *et al.* demonstrated the construction of 20 pairs of layer films containing positively-charged poly(diallyldimethylammonium chloride) and negatively-charged poly(methacrylate acid) (PMA) capped silver nanoparticles on two different textile surfaces [170]. Here the nanoparticles were synthesised by a photoinduced approach (UV irradiation of $AgNO_3$ and PMA (1:1) solution) prior to being used as a solution for the film construction. Films of up to 20 pairs

of layers were successfully constructed, exhibiting a red colour due to the immobilisation of AgNPs onto the surface, as well as bactericide properties against *Staphylococcus aureus*.

V.3.1.3 Association of TiO_2 and silver nanoparticles in LbL self-assembly

Although research on the association of TiO_2 and metal nanoparticles, as well as investigations of LbL titania or AgNP thin films, has been reported, the association of these two materials in LbL self-assembly film is still relatively new and has yet to be further investigated [25].

The first investigation that involved TiO_2, Ag and LbL self-assembly has been reported by Koktysh et al. [171], [172]. They synthesised a Ag@TiO_2 core-shell system, and further used this positively-charged core-shell system in suspension in acid media as a building unit to construct a PDDA/(PAA/Ag@TiO_2)$_n$ film on glass slides. However later studies with this system did not focus on the possible contribution of silver in the film. In fact Ag@TiO_2 core-shells were put in a concentrated solution of ammonium hydroxide in order to have titania nanoshells prior the film construction. This PDDA/(PAA/TiO_2)$_n$ biocompatible film, with nanoshell TiO_2, displayed a strong ion selectivity which contributed in neurochemical detection and nerve tissue monitoring. Eventually AgNP did not contribute in the final application.

Xiao *et al.* investigated the coating of titania nanotube arrays (TiNTs) by different metal nanoparticles *via* LbL self-assembly [173]. Here AgNPs were synthesised prior to deposition for the film construction. The AgNPs were capped by citrate, providing a negative charge at the surface of the nanoparticles, and were used in the LbL film construction with poly(acrylic acid) (PAA) and poly(allylamine hydrochloride) (PAH), resulting in TiNTs/PAA/PAH/(Ag/PAH)$_n$ films. The films showed an enhancement of the photocatalytic activity of TiNTs when compare to bare TiNTs using the photodegradation of methyl orange in liquid phase under UV light as a test reaction. Photoelectrochemical measurements were performed and confirmed the results obtained with the photocatalytic tests. The influence of the number of Ag layers was also investigated. It was proposed that AgNPs were acting as an electron trap once the TiNTs were irradiated and that the slowest e^-/h^+ pair recombination was obtained for a film containing a single layer deposition of AgNPs. Mahlambi *et al*. synthesised different metal-ion-doped-TiO_2 (m-TiO_2) catalysts and used them for constructing PAH/(PSS/(m-TiO_2))$_n$ LbL films. Ag-TiO_2 catalysts were synthesised by the sol-gel method. The film was then tested for the degradation of liquid phase Rhodamine B under visible light [174]. The photodegradation of Rhodamine B was improved while increasing the number of pairs of layers of PSS/Ag-TiO_2.

V.3.2 Choice of surfaces

One of the main advantages that provides LbL self-assembly film construction is that the films can be constructed on a wide variety of surfaces, in terms of geometry, chemical nature and even roughness. Such surfaces include the likes of polymers and metallic surfaces, or even stents and nanoparticles [171], [175]. By choosing the appropriate materials to deposit, a surface may present properties which will be related to the one of the materials chosen. For instance, when investigating the biocompatibility of TiO_2 nanoparticles, a PSS/TiO_2 LbL film was constructed on different surfaces. While PDMS and PMMA surfaces do not promote cell adhesion and proliferation, the construction of a PSS/TiO_2 LbL film on the samples surfaces have allowed fibroblast cell adhesion and proliferation [165]. When studying the effect of the surface geometry, regular growth of nanoparticle LbL films is still observed but can be influenced by the surface geometry. The group of Robert E. Cohen constructed $(SiO_2/TiO_2)_n$ LbL nanoparticles films on nanochannel arrays (700 nm wide, 10µm in depth) [176]. Results showed that the nanoparticle films were thinner in confined geometry due to surface charge-induced electrostatic depletion of the deposited species. They suggested that LbL deposition of nanoparticles were more sensitive to the surface geometry than the polymer/nanoparticle assembly. Furthermore bridging of the nanochannels was observed when increasing the number of pairs of layer.

TiO_2 LbL films have also been used for photocatalytic applications on different types of surface. Table 3 lists a few examples of TiO_2 LbL thin films constructed for photocatalytic applications on different types of surfaces. AgNPs have been mainly deposited on model surfaces to characterise the LbL film [159], [168], [169]. However AgNPs are widely used in textile industries, hence research on LbL Ag-containing films built on textiles could be a promising approach, and the polyelectrolyte coating could act as a polymer matrix for the nanoparticles [57], [170]. A few examples of AgNP LbL films constructed on textiles are reported in the following section.

Surface	Deposited materials	LbL film	Application	References
Electrode	PDDA Capped-TiO_2 nanoparticles	PDDA/(capped-TiO_2)$_n$	Photovoltaic cell	[75]
Electrospun polymer nanofibermesh	POSS Polyhedral Oligomeric silesquioxanes TiO_2 nanoparticles	(POSS/TiO_2)$_n$	Water remediation, Photodegradation of Bisphenol A under solar irradiation	[177]
Glass Polystyrene Silicon wafers	PSS PVS PAA PPA Polyphosphoric acid TiO_2 nanoparticles	(TiO_2/PSS)n (TiO_2/PVS)$_n$ (TiO_2/PAA)$_n$ (TiO_2/PPA)$_n$	Degradation of Methyl Orange under UV-A irradiation	[178]
Bacterial cellulose	PAH PAA Au nanoparticles TiO_2 nanoparticles	((PAH+TiO_2)/PAA)$_n$/ (PAH+TiO_2)/AuNP	Solar fuels production; H_2 production under solar irradiation	[179]
Textile	PEI WO_3+TiNT titania nanotubes	PEI/(WO_3+TiNT)$_n$	Degradation of chemical warfare agent simulant under solar light	[180]

Table 3: Examples of LbL thin films constructed on different types of surfaces for photocatalytic applications.

V.4. TiO_2, silver film construction on textiles. Focus on LbL construction

Many applications are currently investigated in the field of smart textiles technology, such as organocatalyst, biosensors and anti-microbial textiles [55], [56], [181]. In regards to textiles containing nanoparticles, the main objectives are to stabilise the nanoparticles without any reduction of their properties. One approach is based on the chemical stabilisation of nanoparticles on the fibers. While Ti atoms can bind to carboxylic groups through different modes (monodentate or bidentate), TiO_2 surfaces can interact with textile hydroxyl groups or lattice oxygen atoms through

hydrogen bonding . Most of the studies made for functionalising TiO_2 onto textiles were focused on a dip-coating approach, in which textiles are immersed in a TiO_2 suspension before being rinsed, dried and sometimes undergoing thermal treatments. Textiles functionalised by TiO_2 are still under investigation due to the properties that the semi-conductor provides to textile: UV-protection [182], self-cleaning [183], air purification [76] etc. The attachment of TiO_2 through the use of a chemical spacer on cotton textile, has also been reported [184]. When poly-carboxylic acids are used as a spacer, one of their carboxylic group will bind to a hydroxyl group of cellulose (ester bond), while the other spacer's carboxyl group will bind to TiO_2 via electrostatic interaction.

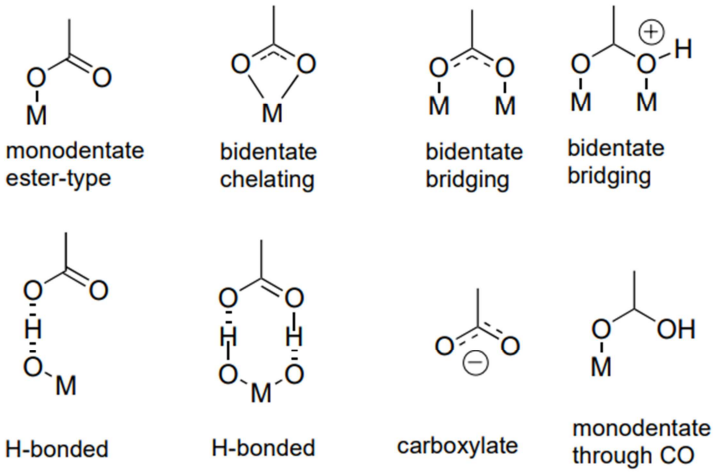

Figure 17 : Possible binding modes of a COOH group with a metal oxide (TiO_2) [185]

The other approach is by directly synthesising the nanoparticles on the fibres [186]. For instance Daoud et al. used a sol-gel method on cotton fibres, to synthesise anatase titanium dioxide onto them [182], [187]. The results showed a dense film with 20 nm particle size in diameter and showed good UV protection properties. Depending on the type of materials to be deposited/synthesised on textile surfaces, both approaches may involve modification of the textile fibres by e.g. plasma treatment or UV-irradiation, prior to the deposition/synthesis of nanoparticles [188], [189].

Layer-by-Layer self-assembly takes its versatility advantage for being used as a coating method on textiles. Moreover polyelectrolytes can be easily coated on silk and wool fibers since they present natural electrostatic features. As for neutral fibers, chemical modifications like etching or molecule grafting are required in order to construct an LbL film onto them. For instance, cotton can be coated if the fabric is immersed in a high pH solution due to the presence of negative charges on the glucose monomer in these conditions [190]. Likewise nylon fibres can be negatively charged when being immersed in an alkaline solution, due to the deprotonation of nylon's carboxylic groups. Plasma

activation of synthetic textiles, like polyester, allows the fibres to be negatively charged and be used for LbL assembly-film construction onto them. LbL self-assembly has not received a lot of interest on textiles materials until now, mainly due to the lack of characterisation methods for this irregular type of surface.

As mentioned in section V.3.1.1, TiO_2 may be used in LbL self-assembly as positively-charged or negatively-charged materials in the film construction. Polyester textiles with $(PEI/TiO_2)_n$ and $PEI/(PSS/TiO_2)_n$ LbL coatings have been investigated by Carré *et al*. for antibacterial applications under solar irradiation [40]. The high self-decontaminating activity of $(PEI/TiO_2)_n$ functionalised textile was assigned to a synergistic effect within the layer system, due to the association of both biocidal photocatalytic activity of TiO_2 layers, and biocidal activity of PEI layers. By contrast, $PEI/(PSS/TiO_2)_n$ films were of interest for evidencing the solar light photocatalytic antibacterial activity of the functionalised textiles, by masking the biocidal activity of PEI.

Studies conducted by Truong-Phuoc *et al*. were focused on the construction of a TiO_2/PAH and SnS_2@TiO_2/PAH films on polyester fibres for the degradation of a chemical warfare agent simulant deposited as droplets on the textiles [191]. They found that the homogeneity of the photocatalytic film could be tuned by the type of LbL deposition technique used in the film construction, for obtaining better photocatalytic activity. In their work dipping, spray-assisted and rolling-assisted techniques were applied on textile fibres. Rolling-assisted methods provided a more homogeneous film on the textiles fibres, resulting in a better photocatalytic activity for the degradation of chemical warfare agent simulant under solar irradiation.

In the case of AgNPs, surfaces charges are not available and cannot be directly used in LbL film construction and therefore modifications of the particles may be required to be used in this film construction method. These modifications may involve nanoparticles functionalization by another compound, incorporation of the nanoparticles within the same layer of a material to be adsorbed in the film, or directly to synthesise the AgNPs within the film after introducing of the silver precursor in the LbL film [170].

The group of Lu et al. investigated the *in situ* photoinduced synthesis of AgNP on silk fibers by soaking the fibres in $AgNO_3$ aqueous solution. At first the investigations were made on degummed silk fibres, with the use of an amino acid as a linker to bind the silver ions [192]. Ag clusters were then generated on the silk fibers, providing antibacterial properties to the modified textile against *E. Coli* and *S. Aureus*. However the density of Ag clusters was low due to a lack of strong binding between silver and the fibers, as well as silver being easily oxidised (Figure 18) [193]. Therefore they elaborated LbL-modified silk fibres where the polyelectrolyte film could act as a polymer matrix for

the synthesis of AgNPs. A $(PAA/PDDA)_8$ LbL film was first constructed onto the silk fibres prior being soaked in the $AgNO_3$ solution, and allowing to bind subsequently to the PAA carboxyl group at the surface of the film. This strategy allowed a time-extension of the antibacterial effect up to 24 h against *E. Coli* and 12 h for *S. Aureus*.

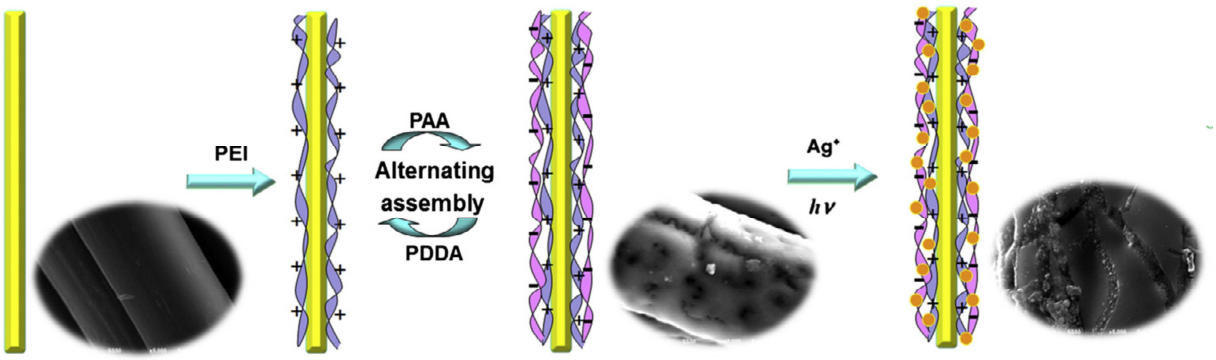

Figure 18: AgNP photoinduced synthesis on $PEI/(PAA/PDDA)_8$ LbL film constructed on silk fibers [193].

Chapter 2: Materials and methods

I – Materials and substrates preparation

I.1 Materials

Aeroxide® titanium dioxide P25 was provided by Degussa-Evonik (Germany) as a fine powder.

Polyelectrolytes used in the Layer-by-Layer thin film construction:
Poly(ethyleneimine) (PEI), $M_w \approx 750\,000$ g/mol, 50 wt. % in water from Sigma Aldrich.
Poly(sodium 4-styrenesulfonate) (PSS), Mw ≈ 70 000 g/mol, from Sigma Aldrich.
Poly(diallyldimethyliammonium chloride) (PDDA), Mw ≈ 100 000 – 200 000 g/mol, 20 wt.% in water from Sigma Aldrich.

Nitric acid (HNO_3) 68% was bought from Prolabo. Sodium chloride (NaCl) >99.9% was provided by Roth. Formic acid (HCOOH) with reagent grade >95%, silver nitrate ($AgNO_3$) with purity >99% and (1-[4-(2-hydroxyethoxy)-phenyl]-2-hydroxy-2-methyl-1-propane-1-one (Irgacure 2959) were purchased from BASF.

20 nm and 5 nm Silver Nanosphere (spherical nanoparticles) NanoXact, 0.02 mg/ml functionalised by citrate (in Milli-Q water) were purchased from NanoComposix Europe (Czech Republic) (respectively AGCN20-50M and AGCN5-50M).

Milli-Q water (ultrapure water) with a resistivity of 18.2 MΩ.cm was obtained from a Milli-Q gradient (Millipore, Molsheim, France) at 25°C. Hellmanex III (Hellma Analytics) was purchased from Sigma Aldrich. Ethanol (99.5% absolute anhydrous) was bought from Carlo Erba.

Silicon wafers with an orientation of <100> were purchased from WaferNet INC (San José, CA, USA). Glass slides (microscope slides) were purchased from Roth (Germany). Quartz slides (Suprasil) with 1 mm in thickness, were purchased from Thuet B. France (Blodelsheim, France). Gold coated quartz crystals (AT-cut quartz crystals with a fundamental frequency of 5 MHz), used for QCM-D characterisations, were purchased from Q-sense – Biolin Scientific (Sweden).

Woven polyester textile fabrics with a density of 75 g/m² and an average fibre diameter of 20 µm were purchased from Ouvry SAS (Lyon, France).

I.2 Substrate preparation

I.2.1 Preparation of model surfaces

Silicon wafers (4.5 x 8 cm), glass (2.5 x 4.5 cm) and quartz slides (1.2 x 3.2 cm) were prepared as follow. The substrates were immersed in a 2 % v/v Hellmanex solution in distilled water and sonicated (ultrasound bath) for 15 min. The substrates were then rinsed with copious amounts of distilled water and then immersed in an ethanol-Milli Q water solution (50:50 v/v) and sonicated for 15 min. The substrates were then dried using compressed air and activated for 3 min using an oxygen plasma (Plasma Cleaner, Harick Plasma, New York, USA), with a power of 10,2 W applied to the radiofrequency coil. This process was repeated twice for quartz slides in order to activate both sides of the slides for UV-Visible spectroscopy characterisations. All substrates were used straight after plasma activation.

Gold coated quartz crystals for a quartz crystal microbalance with dissipation (QCM-D) characterisations were prepared by activating them with a UV-ozone activator (UV-Ozone ProCleaner™, BioForce NanoSciences, Ames, USA) for 20 min. Gold coated quartz crystals were used straight after activation.

I.2.2 Preparation of textiles fibres

Woven polyester (PES) textiles fabrics were cut with 6.5 x 4.5 cm geometry prior to cleaning. Textiles were then immersed in a 2% Hellmanex solution in milli-Q water for 24 h. The fabrics were then rinsed with copious amounts of Milli-Q water and immersed for 15 min in a 50:50 ethanol and Milli-Q solution. Textiles samples were subsequently rinsed once again with Milli-Q water and were dried in an oven for 3 h at 60°C. Textiles were finally placed in a desiccator for 24 h prior to gravimetric analysis, and activated by oxygen plasma cleaner for 1 min with a power of 10,2 W applied to the radiofrequency coil.

II – Preparation of solutions and suspensions

II.1 Preparation of polyelectrolyte solutions

Poly(ethyleneimine) (PEI) was prepared at a concentration of 1 g/L in Milli-Q water.
Poly(sodium 4-styrenesulfonate) (PSS) was prepared at a concentration of 1 g/L in Milli-Q water at pH 2.5 (adjusted by nitric acid HNO_3).
Poly(diallyldimethyliammonium chloride) (PDDA) was prepared at a concentration of 1 g/L with a sodium chloride salt concentration of 0.5 M in Milli-Q water.

II.2 Preparation of titanium dioxide suspension

2 g of Aeroxide® titanium dioxide P25 were added to 80 mL Milli-Q water with pH 2.5 (adjusted by HNO_3) and stirred for 1 h. The suspension was then sonicated using a tip-sonicator (Bioblock Scientific vibracell 75042 or Fisherbrand® Q700 Sonicator) with a power of 300 W for 25 min in order to prevent as much aggregation as possible. The suspension was cooled down to room temperature and centrifugated at 3700 rpm for 15 min to collect only the smallest titania aggregates. The remaining suspension was about 7 g/L and had a milky white colour. The suspensions were then placed in a container and the pH was checked prior to the film constructions.

II.3 Preparation of silver-based photosensitive solutions

Silver nanoparticles (AgNP) were synthesised using two different protocols:

- Photoinduced synthesis of AgNP on model surfaces and on Layer-by-Layer (LbL) thin film using a silver photosensitive solution.
- One-pot synthesis combining the photoinduced synthesis of AgNP and the LbL deposition of a hybrid layer of silver and titanium dioxide nanoparticles, using a silver-titania suspension.

The photosensitive formulation is composed of a silver precursor, a chromophore and a solvent.

II.3.1 Preparation of silver photosensitive solution

Originally 0.5 wt% of silver nitrate ($AgNO_3$) and 0.5 wt% of chromophore Irgacure 2959 were diluted in 3 ml of distilled water in a flask covered with aluminium for protection against light. The photosensitive solution was stirred for 1 h [19]. Studies of the influence of AgNP concentration

deposited on LbL films were performed by changing the concentration of $AgNO_3$ in the photosensitive formulation.

II.3.2 Preparation of silver-titania photosensitive suspension

The silver-titania photosensitive suspension was prepared using the same protocol as that used for the silver photosensitive solution, with the replacement of distilled water by the titania suspension.

0.5 wt% of chromophore Irgacure 2959 was diluted in 15 g of TiO_2 suspension in a flask covered with aluminium for protection against light. The photosensitive suspension was stirred for 1 h. 0.5 wt% of $AgNO_3$ was then added to the suspension, which was stirred for another 15 min before being used. Studies on the influence of the AgNP concentration synthesised in LbL films were performed by changing the concentration of $AgNO_3$ in the photosensitive TiO_2 suspension.

III – Deposition methods

III.1. Multilayered thin film construction by Layer-by-Layer deposition

III.1.1 Dipping LbL deposition on model surfaces

Layer-by-Layer (LbL) thin film constructions were performed using the dipping LbL technique by successively depositing oppositely-charged compounds on different types of surfaces. The LbL dipping construction was performed by an automated dipping robot, consisting of three motorised arms (x,y,z directions), a drying station, an interface from ISEL (Houdan, France) and a Labview program (Figure 19).

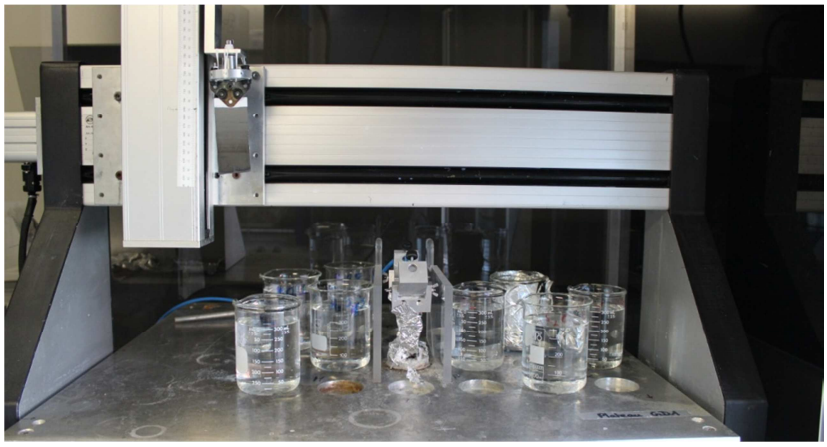

Figure 19: Dipping robot apparatus used for LbL film construction. The silicon wafer is hold by the motorised arm. The drying station is located in the middle of two groups of 4 beakers.

Once activated by an oxygen plasma, the substrate (4.5 x 8 cm) is immerged in a positively-charged PEI solution (1 g/L in Milli-Q water) for 20 min and rinsed by three successive immersions in Milli-Q water for 3 min (3x3 min). Due to overcompensation of charges, the substrate surface was positively charged. After being dried by compressed air, the substrate was dipped in a negatively-charged PSS solution (1 g/L in Milli-Q water at pH 2.5 adjusted by HNO_3) for 20 min. The substrate is then rinsed 3 times in acidic Milli-Q water (pH 2.5 adjusted by HNO_3) for 3 min and dried with compressed air. In the same way as previously stated, the substrate was immersed in a positively-charged TiO_2 suspension (12 g/L in Milli-Q water at pH 2.5 adjusted by HNO_3), rinsing in acidic Milli-Q water and dried with compressed air. The substrate surface was positively charged and the (PSS/TiO_2) pair of layers was constructed. The PSS and TiO_2 deposition steps were repeated until the desired number of pairs of layers was constructed. Films were labelled as $PEI/(PSS/TiO_2)_n$, n being the number of layer pair deposited.

III.1.2 LbL film construction in Quartz Crystal Microbalance cell

Gold coated quartz crystals were activated by UV-ozone and placed in a quartz crystal microbalance cell. The crystals were rinsed with injected Milli-Q water and film construction could start once stabilisation was reached. The polyelectrolyte solutions, the TiO_2 and the commercial silver nanoparticle suspensions were injected into the cell (600 µl at a 300 µl/min flow). Once injected, the solutions/suspensions were kept onto the substrates until stabilisation (full adsorption) was obtained. The substrates were rinsed by injecting 3 times Milli-Q water or acid Milli-Q water (according to the used solution or suspension) and the deposition steps were repeated for building the LbL film.

III.1.3 LbL film construction in capillaries

In order to avoid any contamination in titania suspension, polyelectrolytes and rinsing solutions, painted marks on capillaries were removed with an optical tissue soaked in ethanol. Glass capillaries were cleaned with an ethanol and water solution (50/50, v/v) in a sonicator bath for 15 min. They were rinsed with water and dried under compressed airflow. LbL film deposition inside capillaries was performed manually. The capillaries were first dipped in the PEI solution for 20 min followed by 3 rinsing steps (3x3 min) in Milli-Q water and dried with compressed airflow. Then, the capillaries were dipped in the PSS solution for 20 min followed by 3 rinsing step in acidic Milli-Q water (3x3 min, pH 2.5 adjusted by HNO_3) and drying steps. Similarly to the dipping step in PSS solution, the capillaries were dipped in TiO_2 suspension, followed by rinsing and drying steps. All the dipping in PSS solution and TiO_2 suspension were repeated to reach the desired number of PSS/TiO_2 layer pairs. Once films were constructed a final rinsing step in Milli-Q water (3x5 min) was performed on capillaries. The capillaries were eventually dried and the outside capillarie walls were cleaned with an optical tissue soaked in ethanol in order to remove undesired coating. The functionalised capillaries were then stored in a dry and dark place before electronic paramagnetic resonance characterisations.

III.1.4 Blade-assisted LbL deposition of commercial silver nanoparticles

Since the volume of the commercial silver nanoparticle suspensions was limited, a blade-assisted LbL deposition process was designed based on a *Doctor Blade* approach [194]. AgNP were then deposited on model surfaces with a controlled speed and pressure, following the LbL deposition parameters used in the dipping LbL process.

PEI/PSS/TiO_2 LbL film was constructed by the dipping technique on model surfaces prior to the blade-assisted deposition of AgNP. The substrate (2.25 x 8 cm) was placed on a support and a polytetrafluoroethylene (PTFE) blade was placed and fixed at 2 µm above the substrate, connected to a power source allowing horizontal translating motions (2.8 cm/s). 40 µl of AgNP suspension was placed on each edge of the substrate and in the middle. Two translation movements of the blade were required to spread the suspension. The suspension was stabilised on the substrate for 20 min and rinsed three times in milli-Q water following the same rinsing protocol than that used for the dipping LbL deposition.

III.2. Photoinduced synthesis and deposition of silver nanoparticles

Silver nanoparticles were synthesised on model surfaces and textiles at the *Institut des Sciences des Matériaux de Mulhouse* (IS2M, Mulhouse, France) via a photoinduced synthesis method. Two methods were used in this project: the deposition of the AgNP by synthesising them onto a pre-built LbL film, and a one-pot synthesis combining the photoinduced synthesis of AgNP and the LbL deposition of a hybrid layer of silver and titanium dioxide nanoparticles, using a silver-titania suspension.

All substrates were irradiated by a UV Lamp (Hamamatsu Lightningcure LC8 (Hg–Xe L8252)) fitted with a 365 nm elliptical reflector (Figure 20). A glass slide is placed on top of the samples during the AgNP synthesis, allowing UV-C irradiation to be masked. Due to the surface irradiation of the lamp, 36 cm² silicon wafer with LbL film constructed onto then, were cut using a diamond pen in 3 parts (≈ 12 cm²). Substrates were placed within 15.5 cm of the irradiation source and were irradiated for 10 min. Power received at samples' surface was 20 mW/cm².

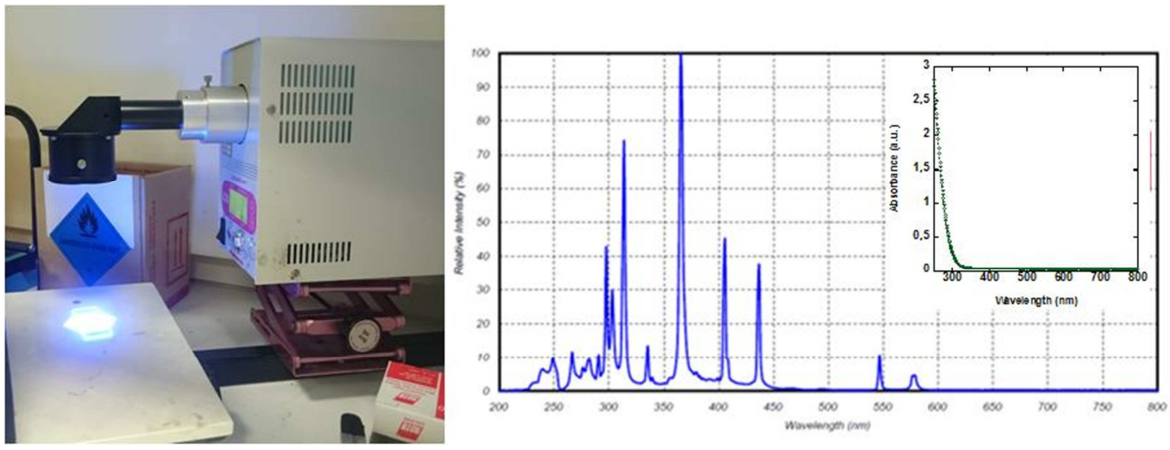

Figure 20 : (Left) the UV lamp used in the photoinduced AgNP synthesis. (Right) irradiance spectra of UV lamp, with transmission UV-visible spectrum of a glass slide in the inset.

III.2.1 Synthesis/deposition of AgNP on LbL thin films using silver photosensitive solution

Once the photosensitive solution was prepared ($AgNO_3$ and Irgacure chromophore in distilled water), 10 µl of the formulation is deposited onto a PEI/PSS/TiO_2 film built on model surfaces (2.5 x 4.5 cm; glass slides, silicon wafer…). A glass slide is placed onto the photosensitive solution and the substrate in order to spread the formulation onto the LbL film, and for preventing the film to be directly

irradiated by high energy UV irradiation. The substrate with the glass slide placed onto it is then irradiated by the UV light (10% of 200 mW/cm² maximum irradiance, in the 300-450 nm range) and the covered glass slide is removed after irradiation.

The influence of different concentrations of $AgNO_3$ (x% $AgNO_3$) in the photosensitive solution was investigated and PEI/PSS/TiO_2/x%AgNP films were synthesised.

III.2.2 One-pot synthesis of AgNP in LbL thin films

In this method, the photosensitive solution was prepared by using the TiO_2 suspension as the solvent ($AgNO_3$ and chromophore in the TiO_2 suspension), and was consequently used as the dipping suspension in the LbL film construction.

Once the formulation was prepared, the substrate (2.5 x 4.5 cm) with a PEI/PSS LbL film constructed onto it, was dipped in a flask containing the photosensitive solution for 20 min. The flask was covered with aluminium for protection against light. The substrate was then rinsed for 3x3 min in acidic Milli-Q water and covered by a glass slide afterwards. The substrate was irradiated by UV light for 10 min and the glass slide was removed.

The influence of different concentrations of $AgNO_3$ (x% $AgNO_3$) in the photosensitive solution was investigated and PEI/PSS/(TiO_2 + x% AgNP) films were synthesised.

III.3. Layer-by-Layer deposition on textiles

The multilayered thin film construction was performed on textiles following a manual dipping process. The textile fabrics (6.5 x 4.5 cm) were first activated by an oxygen plasma for 1 min. They were successively dipped in the solutions/suspensions and rinsed in Milli-Q following the same dipping LbL parameters described in Chap2 III.1.1. The drying process was performed by placing the fabrics in a centrifugal juice squeezer (Efbe Schott E2 Malina), in which the blades had been removed (Figure 21). The fabrics were centrifuged for 1 min between each layer deposition step. Once the desired number of pairs of layers was constructed, the textile fibres were then placed in a desiccator for 24 h prior gravimetric analysis. The samples were then placed in a dry and dark place prior other characterisations.

Figure 21: Centrifuge, where textile sample is placed on the edge of the tumble, used for draining most of water from textile fibres.

In the case of silver nanoparticle deposition, only the one-pot photoinduced synthesis of AgNP in LbL thin film was applied on textile fibres. Since the silver nanoparticle syntheses were performed at the IS2M laboratory, the PEI/PSS films were constructed first on textile fabrics and the fabrics were further cut in to 4.5 x 2.7 cm textile pieces in order to be fully irradiated by the UV-Lamp used for the silver nanoparticle synthesis. The (TiO_2 + AgNP) layers were deposited on the fabrics following the same method described in Chap 2 III.2.2.

IV – Thin film characterisations

IV.1 Ellipsometry

Ellipsometry was applied for monitoring the film construction on model surfaces and for allowing the film thickness to be estimated [195]. This non-destructive technique is based for the measurement of polarization of reflected light rays from the analysed surface, i.e. LbL films constructed on silicon wafers. The principles of this characterisation technique are briefly described below.

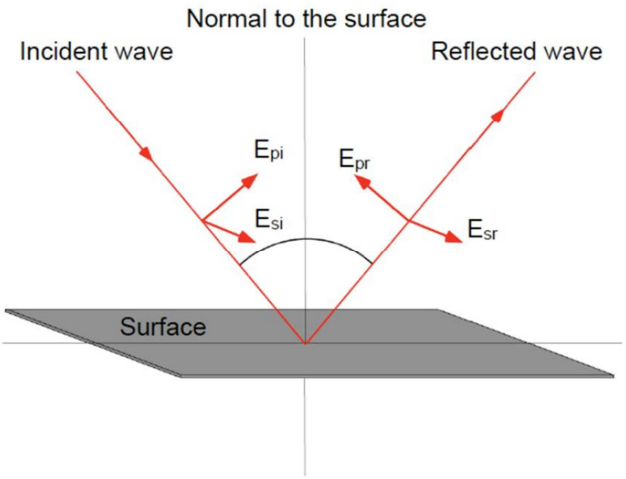

Figure 22: Schematic representation of an electromagnetic wave reflecting off a surface.

When an electromagnetic wave (in our case light) is reflecting off a planar surface, the electric field of each wave can be projected on the plane of incidence and on its normal. The reflection of the light on the surface can therefore be represented by two reflection coefficients r_s and r_p.

$$r_s = \frac{E_{si}}{E_{sr}} = |r_s|\exp(i\delta_s) \quad \text{(Eq. 23)}$$

$$r_p = \frac{E_{pi}}{E_{pr}} = |r_p|\exp(i\delta_p) \quad \text{(Eq. 24)}$$

$|r|$ is the modulus of the reflected electromagnetic field and δ the dephasing of the electromagnetic field. The subscript s and p correspond to the projection of the electromagnetic wave on the parallel to the surface plane (s) and perpendicular to the incident and reflective wave (p). The subscript i and r refer to the incident (i) and reflected (r) wavelength. The reflection of a wave is illustrated in Figure 22

Usually an ellipsometer is sensitive to the ratio of these two coefficients.

$$\frac{r_p}{r_s} = \tan(\Psi) \times \exp(i\Delta) \quad \text{(Eq. 25)}$$

tan (Ψ) represents the ratio of the modules ($|r_p|$and $|r_s|$) and Δ the dephasing induced by the reflection between δ_p and δ_s.

For a flat homogeneous thin film lying on a reflecting surface, the value of Ψ and Δ depend on:

- the refractive index and thickness of the film
- the refractive index of the substrate
- the angle of incidence and wavelength of the light used

In this work, the thickness of the LbL thin films made of polyelectrolytes, P25 titania and silver nanoparticles built on silicon wafers, was obtained by using a PLASMOS SD 2300 operating at a wavelength of 632.8 nm, with and angle of 70°. A constant refractive index (n) of the film was assumed due to the difficulty of determining the refractive index and the thickness (d) simultaneously at small layer numbers. This apparent film thickness, d, of the film, determined by imposing a constant value for the refractive index, n, equal to that of SiO_2 (n = 1.465) in the derivation of n and d from the ellipsometric angles psi (Ψ) and delta (Δ), was, while only required for film thicknesses below about 75 nm, for reasons of convenience used throughout the deposition of all layers. The film thickness corresponds to the average of 10 random position measurements of the film. The error bars were the standard deviations of these measurements and provide indications on the film thickness homogeneity.

IV.2 Quartz Crystal Microbalance with Dissipation

Quartz crystal microbalance with dissipation (QCM-D) is a sensitive technique that is able to measure the change in mass deposited on a piezoelectric material in the nanogram range [196]. Moreover this technique allows the use of a wide range of materials since specific properties such as reflectivity or optical transparency do not interfere with the analysis as long as the material can be deposited at the surface of the sensor crystal. In QCM-D characterisations, molecules or particles are bound to the upper electrode of the oscillating quartz crystal surface in liquid medium, leading to a decrease in frequency.

Figure 23 : Schematic representation of a gold-coated quartz crystal (left) and a cross section (right) of a deformed quartz crystal in grey with gold electrodes in yellow when an electric field is applied (picture adapted from Q-sense (Göteborg, Sweden) presentation of QCM).

The linear relation between the oscillating mass and resonance frequency is defined by Sauerbrey's equation:

$$\Delta m = -C\frac{\Delta f}{n} \qquad \text{(Eq. 26)}$$

In this equation, the variation of a resonance frequency (Δf) divided by the harmonic overtone (n) is proportional to the variation of the oscillating mass (Δm), where C is a coefficient of proportionality which depends on the geometric parameters of the crystal.

One can note that Sauerbrey's equation is valid only for adsorbed masses that are negligible compared to the weight of the quartz slide. Moreover it is assumed that the adsorbed materials are rigidly attached and evenly distributed over the surface.

In addition to resonance frequency measurements, a quartz crystal microbalance can monitor simultaneously the change of dissipation (ΔD). The dissipation is related to the viscoelastic properties (viscosity, friction induced by the slip of the deposited film on the quartz crystal, etc.) and to the structural changes in the adsorbed film on the quartz crystal surface.

In this work, quartz crystals were used for LbL thin film construction monitored by QCM. This characterisation provided an estimation of deposited materials using Sauerbrey's equation. Measurement could be acquired by transmitting an electric signal through the quartz crystal at its resonance frequency. The solutions or suspensions used for LbL film construction were injected in a QCM cell in which the quartz crystal has been placed. Once stabilisation was reached after rinsing steps, by injecting Milli-Q water (acidic or not), the next material injection was performed for LbL film construction. In this work, the QCM slide had a coefficient of proportionality of 17.7 ng/(cm²•Hz) and

calculations were made at the 3rd, 5th and 7th overtone. All QCM characterisations were performed on a QCM-D E4 (Q-Sense AB, Göteborg, Sweden).

IV.3 UV-Visible spectroscopy

UV-Visible (UV-Vis) spectroscopy provides information on the absorption properties of a sample. It is based on the intensity of a monochromatic radiation once it passes through (transmission mode) or reflects (reflection mode) from the sample, compared to the initial intensity. In liquid media, the absorbance measured by UV-Vis spectroscopy is related to the amount of molecules in the media being passed through by the light according to the Beer-Lambert Law:

$$A = -\log\left(\frac{I}{I_0}\right) = \varepsilon \cdot l \cdot c \qquad \text{(Eq. 27)}$$

Where A is the absorbance or extinction of the molecules, c is the concentration of molecules in the media, l is the optical pathway corresponding to the cell length, ε is the extinction coefficient and I_0 and I are the intensity of the incident light and transmitted light respectively.

UV-visible spectroscopy in transmission mode was used in order to monitor the film construction on quartz slides. Here the optical pathway, l, corresponds to the thickness of the quartz slide. Since LbL film thicknesses are within the nanometric range, the LbL film thickness is negligible in the optical pathway. From the absorption data, the amount of titania deposited per layer has been estimated using equation 6 [76].

$$\frac{m}{S} = \frac{A \cdot c_1 \cdot l_1}{A_1} \qquad \text{(Eq. 28)}$$

Here the m/S ratio corresponds to the mass of catalyst deposited per layer per surface area (g/m^2). A_1 is the suspension absorbance and A is the absorbance of one layer of the deposited material (all absorbance measurements were made at 300 nm). c_1 is the concentration of the titania suspension (g/m^3), l_1 the width of the quartz slide.

In the case of LbL films constructed on textile fibres, refection mode was applied for measuring the absorbance of LbL films. The UV-Vis spectrophotometer was equipped with an integrated sphere placed 8° angle in regards to the incident light normal. By consequence the reflective light is not

directed toward the opening where the incident light enters the sphere, but directed inside the sphere. This provides the measurement of all light being reflected and diffused within the sphere after being sent on the LbL film constructed on textile fibres.

In this work the samples were characterised with a UV-Visible Varian® 100 Scan spectrophotometer, equipped with a Labsphere DRA-CA-301 integrated sphere for the LbL films built on textile surfaces.

IV.4 Microscopy

IV.4.1 Scanning Electron Microscopy

Scanning Electron Microscopy (SEM) is a characterisation technique providing information on materials morphologies and sizes. This technique is based on the detection of secondary electrons excited from the sample surface under the impact of an electron beam (primary electrons) at the observed surface, providing images with details as small as 5 nm and a large depth of field.

This technique uses other primary electron interactions with the samples: backscattering electrons, absorption of the primary electrons, X-ray photons emission as well as near-visible photons. Each interaction may give information regarding the topography of the sample and/or its surface composition.

The electron beam, in which electrons are accelerated by an acceleration voltage between 0.5 to 30 kV, is emitted from an electron gun (e.g. tungsten filament) and is narrowed down to a fine beam by two or three condenser lenses to form a spot on the surface with a diameter below 10 nm. The final lens forming the electron spot on the sample is called the objective. The spatial resolution of the instrument is mainly determined by the objective and it cannot be lower than the diameter of the electron spot on the sample surface.

In this work, GEMINISEM (Zeiss) SEM from Institut de Chimie *et Procédés pour l'Energie, l'Environnement et la Santé* (ICPEES, Strasbourg, France) (Figure 24) was used to characterise the surface LbL films built on model surfaces and textile fabrics. Inlens and secondary electron (SE2) detectors were used with acceleration voltages of 3 kV for films built on model surfaces, whilst SE2 detector with 1-2 kV was used for films built on textiles. An ESB detector was used afterwards to show titania density variations along textile fabrics after abrasion and washing tests. Furthermore SEM Hitachi SU8010 from *Institut Charles Sadron* (ICS, Strasbourg, France) was used for characterising cross sections of titania and polyelectrolytes LbL films with an acceleration voltage of

10 kV. Films were cut by a cross section polisher IM4000Plus (Hitachi) using an argon beam and acceleration tension of 6 KeV.

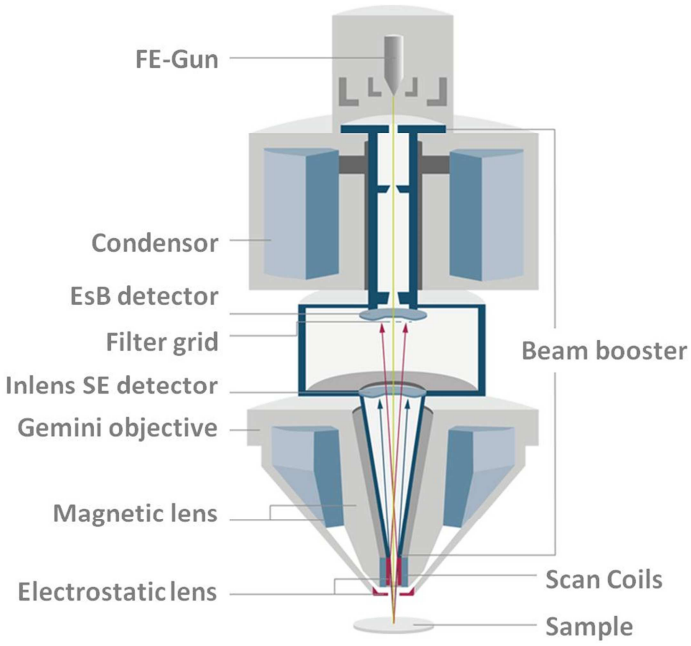

Figure 24 : Schematic cross-section of Gemini optical column with beam booster, Inlens detectors and Gemini objective (www.zeiss.com)

IV.4.2 Transmission Electron Microscopy

Transmission Electron Microscopy (TEM) allows us to obtain information on material morphology, size and structure. This technique is based on the recording of a bright field mode, meaning that the image is produced by the non-diffracted electron beam transmitted through a thin sample. The interaction between the electrons and the material leads to the recording of the image with nanometric resolution. Thicker regions of the sample or regions with a higher atomic number appear darker, whilst regions with no sample in the beam path appear brighter. A picture and a schematic of a TEM apparatus is shown in Figure 25.

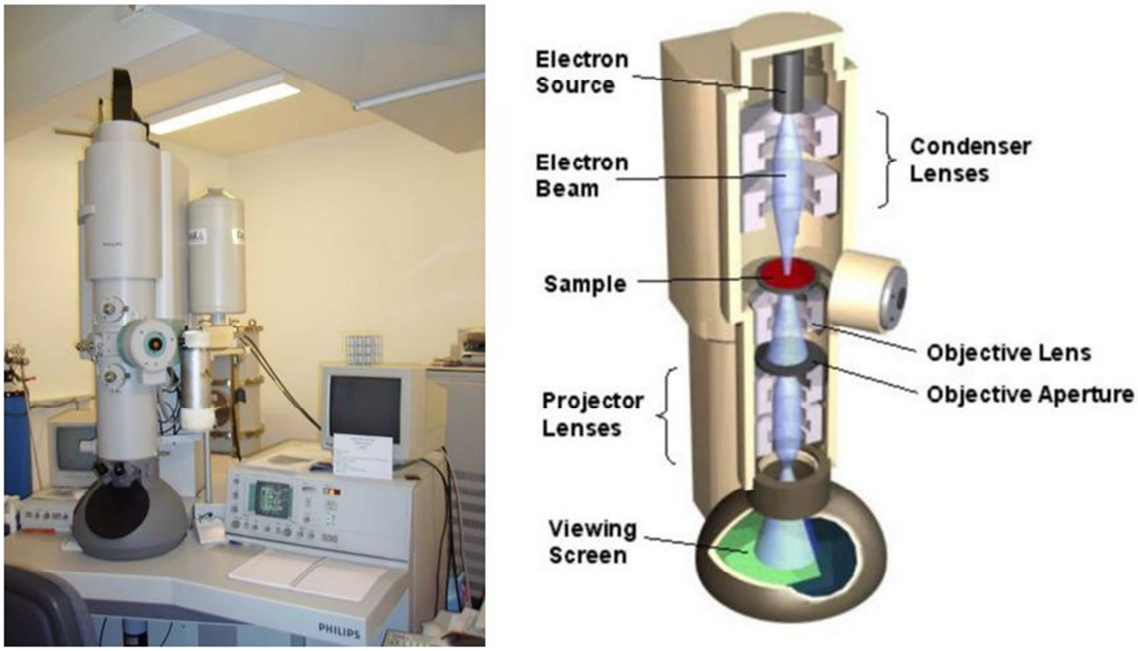

Figure 25: Picture of Philips CM200 TEM (left) and a schematic representation of TEM components (right).

TEM analyses of films were performed by constructing directly LbL films manually on the grid ((Formvar/C copper grid with 400 mesh size, Oxford instrument) by using LbL dipping parameters describe in CHAP 2 III.1.1. TEM grids were grabbed by tweezers during the whole LbL deposition process. Polyelectrolytes, titania suspension and photosentive solution were deposited dropwise (10 µl) on the TEM grids, followed by the 3 rinsing steps by dipping the grid in milli-Q water (acidic or not) while keeping the grid grabbed by the tweezers. Only films with a single layer pair (PSS/TiO_2 or PSS/(TiO_2+AgNP)) were constructed on TEM grids. TEM characterisation of photoinduced silver nanoparticles were synthesised directly on copper TEM grids by depositing the photosensitive solution containing TiO_2 nanoparticles and $AgNO_3$, onto the grids. TEM analysis were performed at the *Institut de Sciences des Matériaux de Mulhouse* (IS2M, Mulhouse, France) using a Philips CM200 equipped with thermo-ionic LaB6 filament operating at 200 kV. TEM pictures were analysed with ImageJ® software.

IV.5 X-Ray Photoelectron Spectroscopy

X-Ray Photoelectron Spectroscopy (XPS) is a non-destructive and semi-quantitative technique that measures the elemental composition of the sample surface by analysing the number of electrons and the kinetic energy emitted from the sample during its irradiation by X-rays under ultra-high vacuum

[197], [198]. In this work XPS analysis was used to study the elemental composition at the surface of LbL films constructed on model surfaces.

The X-ray photons excite the core electrons of the sample atoms with binding energy lower than the X-ray energy. Emitted photoelectrons from the sample atoms have a kinetic energy corresponding to the difference between the incident energy (from the X-ray) and the binding energy, subtracted from the work function, depending mainly on the spectrometer. While X-rays can easily pass through the material, the photoelectrons emitted are quickly diffracted and absorbed by the material. Only photoelectrons at the extreme outer surface (1-10 nm) are able to escape from the sample surface. XPS analysis is therefore only sensitive to the surface of the sample. Figure 26 illustrates the ejection of a 1s electron during XPS analysis.

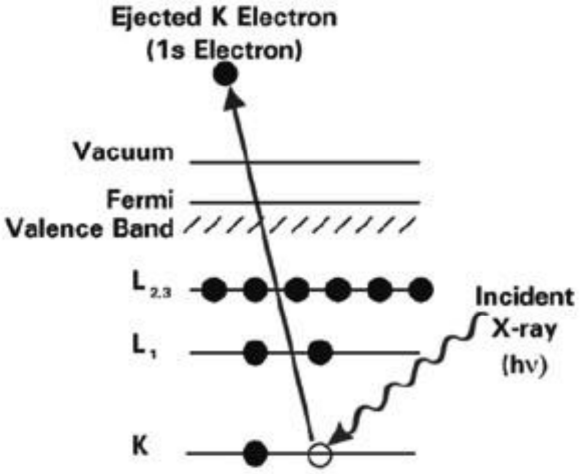

Figure 26 : Photoemission process involved during XPS surface analysis. Dark and white dots represent electrons and bars represent the energy levels within the analysed material.

XPS provides information on the chemical binding between the element and its neighbour atoms (i.e. its chemical environment). The chemical environment influences the electronic and oxidation state of the atoms and leads to chemical shift, assigned from electronegativity differences in the electrostatic model of atoms.

Data are acquired as an XPS spectrum which consists of a series of peaks corresponding to the binding energies of the emitted and ejected photoelectrons. For non-conductive materials such as semi-conductors, positive charges can accumulate at the solid surface, thus reducing the kinetic energy of emitted photoelectrons: the resulted binding energy will be overestimated. Therefore the

charge effect should be corrected by taking the sp^2 carbon 1s peak at 284.6 eV from contamination carbon as reference.

As a semi-quantitative analysis, the intensity of the peak is proportional to the relative surface concentration of the atoms from which the photoelectrons are emitted. Let us consider a sample with two elements A and B. The A/B surface atomic ratio is then described by the following equation:

$$\frac{C_A}{C_B} = \frac{I_A}{I_B} \times \frac{\sigma_B}{\sigma_A} \times \left(\frac{E_{cB}}{E_{cA}}\right)^{\frac{1}{2}} \times \frac{D_B}{D_A} \times \frac{\eta_B}{\eta_A} \quad \text{(Eq. 29)}$$

Here, I is the surface of the peak, σ is the photoionisation cross section as tabulated by Scofield which refers to the probability of an electron to be emitted from its electronic state [199]. E_c is the kinetic energy. D represents the transmission factor of the instrument depending on Ec. $\frac{D_B}{D_A}$ is equal to 1 when E_{cA} is almost equal to E_{cB}.η is the acquisition passage number.

In this work silver nanoparticles are synthesised in LbL films, therefore XPS characterisation allowed us to distinguish Ag(0) from other silver oxidation states [19], [100], [101]. However the binding energy of silver oxide compounds are found to be coincident with the one of their reduced form Ag(0) [200]. For instance the binding energy of metallic Ag, Ag_2O and $AgNO_3$ are found to be 368.3, 368.6 and 368.8 eV, respectively, in Ferraria et al. investigations (Figure 27).

The auger parameter is essentially the energy difference between a photoelectron and an Auger electron, hence is dependent of sample charging and work function. According to Gaarenstroom and Winograd, Auger parameter can be calculated from the following equation [200]–[202]:

$$\alpha + h\nu = E(Auger) + E_B\ (PE) \quad \text{(Eq. 30)}$$

Where α + hν is the Auger parameter, E(Auger) is the auger electron energy and E_B(PE) is the binding energy of the emitted photoelectron. In our case E_B(PE) corresponds to the binding energy of Ag $3d_{5/2}$, whilst E(Auger) is the kinetic energy of Auger Ag $M_4N_{45}N_{45}$ and Ag $M_5N_{45}N_{45}$.

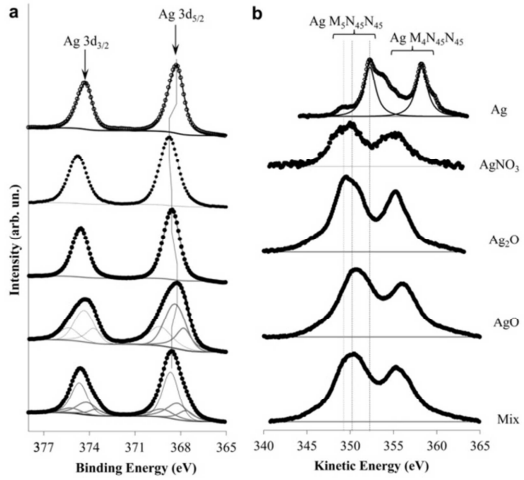

	Ag	$AgNO_3$	Ag_2O	AgO	Mix	Assignments
Binding energy (eV)						
Ag $3d_{5/2}$	368.3					Ag(0)
		368.8	368.6		368.7	Ag(I)
				367.8[0.45][a]	367.6	Ag(III)
				368.4[1.00]	368.2	Ag(I) in AgO
				369.4[0.53]	369.2	Ag(III) sat
				371.5[0.02]	371.4	Ag(III) sat
Auger parameters						
AP-$3d_{5/2}$, $M_4N_{45}N_{45}$	726.5	723.8	723.9	724.4	724.2	
AP-$3d_{5/2}$, $M_5N_{45}N_{45}$	720.5	718.3	717.8	718.4	718.1	
Chemical shifts (eV)						
Δ (3d photoelectron peaks)		0.5	0.3	0.2		
Δ (AP-$3d_{5/2}$, $M_4N_{45}N_{45}$)		2.7	2.6	2.1	2.3	
Δ (AP-$3d_{5/2}$, $M_5N_{45}N_{45}$)		2.2	2.7	2.1	2.4	

Figure 27 : Investigation on Auger parameters of different silver powders from Ferraria et al., "Mix" is a mechanical mixture of Ag_2O and AgO [200]. (Left) XPS spectrum with binding energy of Ag 3d (a) and kinetic energy of Ag MNN (b). (Right) modified table results from XPS spectrum and Auger parameters with their assignments.

XPS characterisations were performed on a Thermo VG Scientific equipped with X-Ray source consisting in aluminium Kα radiation (hν = 1486.6 eV). After charge effect subtraction, the spectra were decomposed assuming contributions with Doniach-Sunjic shape and a Shirley baseline subtraction, using CasaXPS software.

IV.6 Time resolved microwave conductivity

Time resolved microwaved conductivity (TRMC) characterisations allowed information on the charge carrier lifetime in the catalyst, in our case LbL films containing P25 TiO_2, polyelectrolytes and/or silver nanoparticles, to be obtained [203].

This technique is based on the measurement of the change of the microwave power reflected by a solid sample, ΔP(t), induced by its laser-pulsed illumination. The relative difference ΔP(t)/P is correlated to the difference of conductivity Δσ(t) according to the following equation.

$$\frac{\Delta P(t)}{P} = A\Delta\sigma(t) = Ae\sum_i \Delta n_i(t)\mu_i \qquad \text{(Eq. 31)}$$

Here A is a sensitivity factor, which is not time dependent but could be affected by a change in the microwave frequency and the dielectric constant. e is the electron charge, $\Delta n_i(t)$ is the number of

excess charge carriers, i, at time t, and μ_i is their mobility. $\Delta n_i(t)$ is associated to electrons in the conduction band because their mobility is much larger than that of the holes in the case of TiO_2.

The main data provided by TRMC are:

- the maximum value of the signal (I_{max}), which indicates the number of the excess charge carriers created by the pulse
- the decay process between to the excitation by the laser (at 10 ns), and the decay (I(t)) due to the decrease of the excess electrons (recombination or trapping processes).

The decay I(t) is related to the lifetime of charge carriers and a short and a long range are usually analysed. The short-range decay, fixed at 40 ns after the generation of the pulse, represented by the I_{40ns}/I_{max} ratio, reflects the recombination of charge carriers. Therefore a high value indicates a low recombination rate. The long-range decay, in this case fixed at 200 ns after the pulse, is related to slow processes involving trapped species, i.e., interfacial charge transfer reactions and decay of excess electrons controlled by the relaxation time of trapped holes. Decay of the TRMC signal can be described by the following equation.

$$I(t) = I_D \times t^{-k_D} \quad \text{(Eq. 32)}$$

Here I_D is the intensity of the signal due to charge carriers that recombine after 200 ns, and k_D is an adimensional parameter related to their lifetime. High k_D values represent fast decays of the TRMC signal. Similar I_{max} and I_D values indicate that charge carriers decay only by slow processes.

In this work TRMC measurements were performed at the *Laboratoire de Chimie Physique* (LCP, Orsay, France). Incident microwaves were generated by a Gunn diode of Ka band set at 30 GHz. The pulse light source is a Nd:YAG laser where the wavelength was set at 350 nm, with a light density of 1.3 mJ/cm². TRMC characterisations were performed on PEI/$(PSS/TiO_2)_n$ and PEI/PSS/(x%Ag-TiO_2) LbL films constructed on circled microscope glass slides.

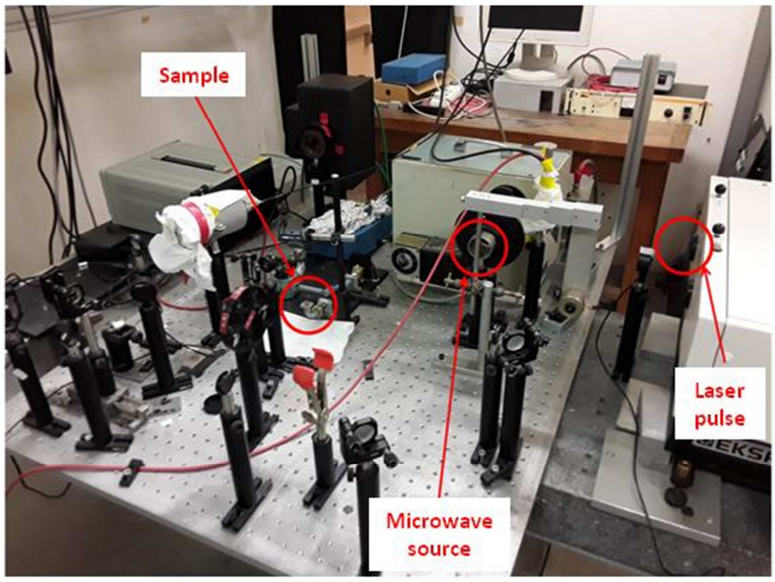

Figure 28 : Picture of TRMC set-up.

IV.7 Electronic Paramagnetic Resonance

EPR is a non-destructive radiospectroscopy technique that allows molecules containing unpaired electrons to be studied [204]. This technique is based on the Zeeman Effect and hyperfine interactions. In short, an unpaired electron can have two energy levels where the magnetic moment $\vec{\mu}$ of the electron is aligned with the magnetic field $\overrightarrow{B_0}$ or against it. Thus the spin of an electron (i.e. intrinsic angular momentum, $m_s = \pm \frac{1}{2}$) is $\vec{\mu}$ and $\overrightarrow{B_0}$ dependant. Therefore in a magnetic field B_0, the energy of these spins can be written as follow:

$$E_{\pm\frac{1}{2}} = \pm\frac{1}{2} g \beta_e B_0 \qquad \text{(Eq. 33)}$$

Where g_e is the g-factor (or Lande factor; for a free electron g ≈ 2.0023) and β is the Bohr magneton. In EPR, while following the selection rule for $\Delta m_s = \pm 1$, transition, these two energy levels are induced by absorbing an electromagnetic radiation of a ν frequency such as:

$$\Delta E = E_{+\frac{1}{2}} - E_{-\frac{1}{2}} = h\nu = g \beta_e B_0^{res} \qquad \text{(Eq. 34)}$$

Where h is Plank's constant and ν a micro-wave frequency called Larmor's frequency. While setting ν to a constant value and changing the magnetic field until reaching resonance phenomena (B_0^{res}) , the first derivative of absorption of EPR signal can be acquired (Figure 29).

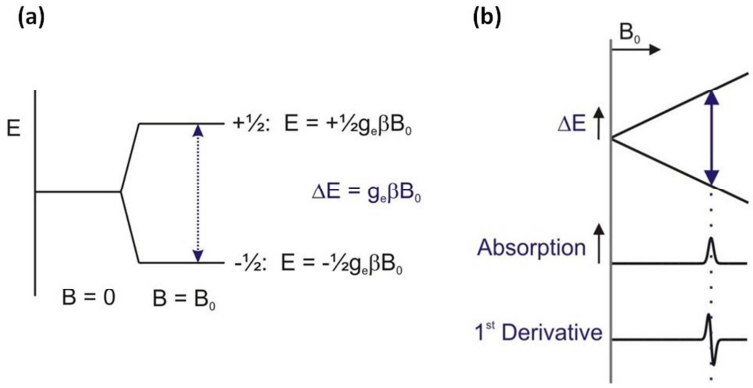

Figure 29: Energy level diagram of Zeeman interaction for an unpaired electron as function of the applied magnetic field $\overrightarrow{B_0}$. The vertical arrow represents the possible EPR transition according to the selection rule for $\Delta m_s=\pm1$ [205].

For a molecule that possesses an unpaired electron, EPR signal behaviour will derive from hyperfine coupling. Depending on the spin momentum (2I+1) possible alignments of the nuclear magnetic momentum towards $\overrightarrow{B_0}$, the resulting field adds or oppose to the field experienced by the electron. Figure 30 shows the EPR spectrum acquired for a system with an electron spin and a nuclear spin.

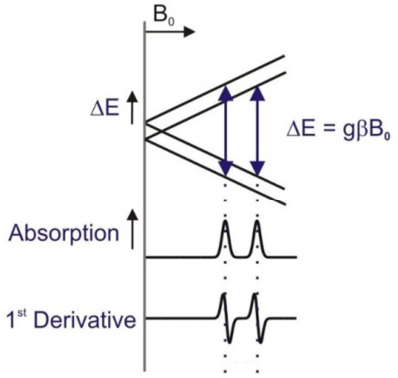

Figure 30 : EPR absorption and corresponding first derivative EPR signal from the hyperfine interaction between an electron and a surrounding nucleus. The vertical arrows represent the EPR possible transitions according to the selection rules $\Delta m_s = \pm1$ and $\Delta m_I = 0$ [205].

In order to detect photogenerated free radicals, a spin scavenging method was developed by using molecules that are able to trap spins [206], [207]. In our work, spin scavenging technique was chosen and decay of EPR TEMPOL (4-hydroxy-2,2,6,6-tetrametylpiperidine-1-oxyl, with nuclear spin I = 1) signal by free radicals photogenerated by titania LbL films, was probed (Figure 31). Indeed when paramagnetic TEMPOL molecules react with free radicals, the generated by-products are

diamagnetic and do not present any EPR signal. By irradiating (UV-A) a titania LbL film, in contact with a TEMPOL solution, photogenerated free radicals will be able to react with TEMPOL molecules and EPR TEMPOL signal can be probe in regards to the UV-A irradiation time. Once all TEMPOL EPR spectrums are acquired (i.e. disappearance of EPR signal), double integration is performed on every first EPR spectrum peak to get TEMPOL EPR signal intensity, which is proportional to the number of paramagnetic centre of TEMPOL.

In this work EPR characterisations were performed on LbL films built in capillaries, where an aqueous TEMPOL solution (50 µl, 200 mM) was introduced. A mixed solution containing TEMPOL and formic was introduced in functionalised capillaries afterwards, using different TEMPOL:HCOOH concentration ratios (1:1 and 1:5).

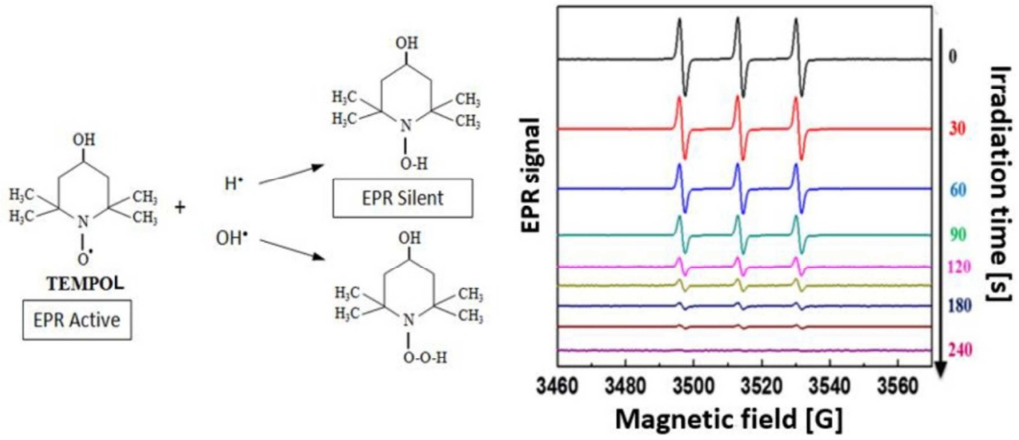

Figure 31: (Left) the chemical structure of TEMPOL and possible reaction pathways with radicals leading to diamagnetic by-products. (Right) decay of EPR TEMPOL signals upon UV-A irradiation time with TEMPOL paramagnetic properties being lost due to free radicals photogenerated by a LbL titania film [205].

All EPR characterisations were performed at room temperature. EPR spectrum was acquired prior UV-A illumination (t=0) in order to get the initial EPR intensity (I_0 = I(t=0)). The capillary was then placed in a quartz cavity surrounded by 4 UV-A lamps (365 nm, irradiance received for a lamp: 1.5 mW/cm² measured with a 1 A current) at a 1 cm distance from the sample, in a closed box (Figure 32). UV-A illumination lasted for 30 seconds and EPR spectrum was acquired. Illumination and EPR spectrum acquisition step were repeated until quasi disappearance of the TEMPOL EPR signal.

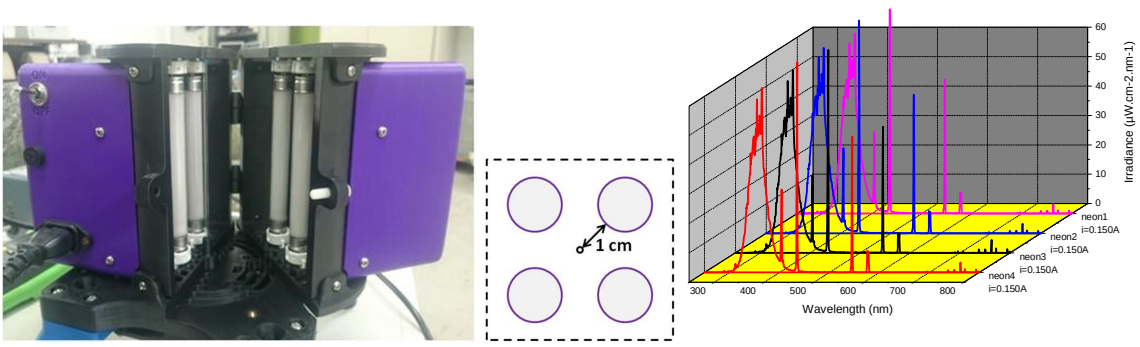

Figure 32: (Left) photo of irradiation box when being open. (Middle) schematic of a cross section viewed from the top of the closed irradiation box. The quartz cavity is located in the middle of the box with 4 UV-A lamps with a distance of 1 cm. (Right), the irradiance spectra of the 4 UV-A lamps used for illumination of functionalised capillaries.

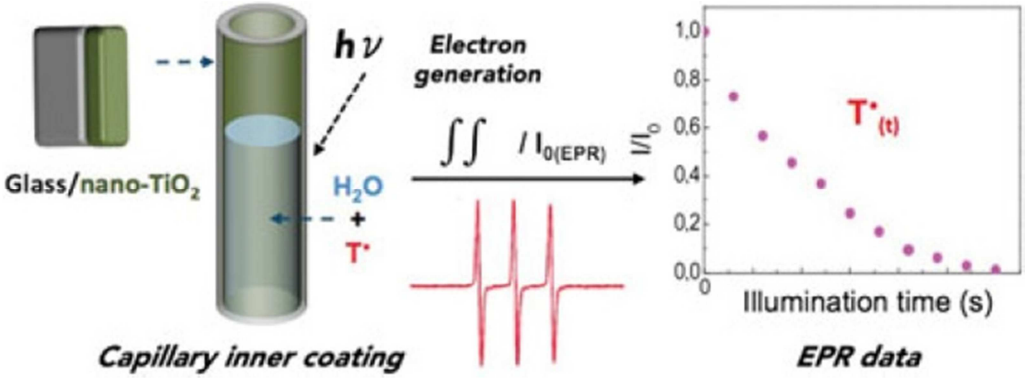

Figure 33 : Summary of EPR characterisations of LbL titania film constructed in capillary. Tempol (T•) solution is introduced in the functionalised capillary and EPR signal is acquired after each UV-A irradiation (hv). Double integrate is applied on the first EPR spectra peak to calculate intensity, and is normalised in regards to initial intensity. Normalised intensity values are reported afterwards in regards to illumination time [207].

EPR characterisations were performed at the *Institut de Chimie* (POMAM team, Strasbourg, France) on a Continuous-wave EPR X-band spectrometer (EMXplus from Bruker Biospin GmbH, Germany), equipped with a high-sensitivity resonator (4119HS-W1, Bruker).

IV.8 Chemical analysis

The amount of titanium in suspension and within the LbL film was obtained by ICP-AES (Inductively Coupled Plasma – Atmomic Emission Spectroscopy) analysis, while the Ag content was obtained by

ICP-MS (Inductively Coupled Plasma – Mass Spectroscopy) analysis. Each sample required acidic treatment prior to chemical analysis. Chemical analyses were performed by the inorganic analytic service at the *Institut Pluridisciplinaire Hubert Curien* (IPHC, Strasbourg, France).

V – Others characterisations methods

A couple of charaterisation methods were used in this work to characterise the P25 titania suspension. Although these characterisation techniques provided information prior the construction of films, they were not used on LbL films built on both model surfaces and textile fabrics.

V.1 X-Ray Diffraction

X-Ray Diffraction is a non-destructive technique that allows identification of crystal phase, phase composition and crystallite average size of crystalline materials. The XRD principle is based on constructive interference occurring when monochromatic X-rays are diffracted by a crystalline sample. The X-rays generated by a metallic anode are filtered to produce monochromatic radiation, collimated to concentrate, and directed toward the sample. The interaction of the incident rays with the sample then produces constructive interference when the diffracted rays satisfy Bragg's Law:

$$n\lambda = 2d_{hkl} \sin\theta \qquad \text{(Eq. 35)}$$

Where n is a positive integer, λ is the wavelength of incident wave, θ is the scattering angle, and d_{hkl} is the interplanar distance for lattice (hkl) planes.

This law relates to the wavelength of electromagnetic radiation of the diffraction angle and the lattice spacing in a crystalline sample. By scanning the sample through a range of 2θ angles, all possible diffraction directions of the lattice should be obtained due to the random orientation of the powdered material. XRD diffractogram is obtained by relating counts of diffracted X-rays with 2θ angle. Identification of phases is achieved by comparing XRD patterns to standard reference patterns.

XRD characterisations were performed on a Brucker D8 Advance diffractometer operating in a θ/2θ mode, equipped with a copper anticathode producing X-rays with wavelength of λ_{CuKal} = 1.5406 Å.

The database of patterns is from International Center for Diffraction Data's JCPDS files. In this work, only titania P25 suspensions were characterised by XRD in order to identify crystal phases in the suspension. 120 ml of the final suspension was evaporated for 48 h in order to obtain sufficient material to be characterised, whilst precipitated titania collected at the bottom of 2 centrifuged tubes was collected, rinsed with ethanol and evaporated prior XRD characterisation.

V.2 Dynamic Light Scattering (DLS)

Dynamic Light Scattering (DLS) is used to measure the size distribution of small particles in solution [208]. Nanoparticles subjected to light undergo elastic scattering and emit light in all direction. DLS consists of passing a laser through an analysed solution while a photodetector collects the light scattered. At the detector, the light scattered by the different particles undergo constructive or destructive interferences depending on the distance between the particles. Since the particles in solution are subject to Brownian motion, the interference changes and the intensity recorded by the captor may vary with time. The Brownian motion is a function of the size of the particles therefore it is possible to recover the size and distribution of the particles from the variation of scattered intensity. The data treatment is usually done using an autocorrelation function that measures the similarity of the curve to itself as function of the time lag considered. The slower the intensity variations are (large particles), the longer the curve stays similar to itself. The size calculated by DLS is based on the Stokes-Einstein equation, which supposes spherical particles.

$$\mathrm{d(H)} = \frac{\mathrm{k_B T}}{3\pi\eta \mathrm{D}} \qquad \text{(Eq. 36)}$$

where d(H) is the hydrodynamic diameter, k_B is the Boltzmann constant, T is the temperature, η is the viscosity of medium and D is the translational diffusion coefficient.

All measurements have been performed on a Zetasizer NanoZS device (Malvern Instrument, Ltd., UK) at a scattering angle of 173° and a wavelength of 632.8 nm (He/Ne laser) at 25°C. Each sample was measured 3 times and cuvettes (Malvern Instruments, Ltd., UK) were rinsed with Milli-Q water and acidic Milli-Q water (pH 2.5, HNO_3) prior to introduction of the titania suspension.

VI – Photocatalytic activity and performance of LbL thin films

VI.1. Gas-phase photocatalysis

VI.1.1 Experimental setup

The photocatalytic activity and behaviour of LbL films on model surfaces and on textiles have been assessed by their ability to degrade and mineralise gas-phase HCOOH under UV-A irradiation in a single-pass continuous gas flow reactor. The gas phase photocatalytic set-up was made of 3 parts:

- Generation of inlet polluted air flow
- Photocatalytic reactor
- Online analysis of inlet and outlet gases

The generation of the inlet polluted air flow is obtained by mixing 3 synthetic air flows: (i) dry air flow, (ii) humid air flow, (iii) gas-phase HCOOH containing air flow. Synthetic air was bubbled in a temperature controlled saturator containing liquid phase formic acid (HCOOH, Sigma Aldrich, >95%) at 15°C and atmospheric pressure. Thus the concentration of gas phase HCOOH was related to the vapour pressure of HCOOH at working temperature and pressure conditions. In the same way, synthetic air was bubbled in distilled water at 25°C and atmospheric pressure. Concentration in the gas phase was set by the vapour pressure in the working conditions. Water partial pressure was expressed in terms of relative humidity (RH): 100% of RH being defined as vapour pressure at 25°C and atmospheric pressure. These two air flows were then mixed with an additional synthetic air flow (dry air) to obtain the required pollutant-water-air ratio with a constant total air flow of 20 ml/min. Brooks 5850 massflow meters were used to control separately dry and humid air flows. Relative humidity was set at 50% (about 3% relative to the total atmospheric pressure). In-Flow Bronkhorst flow meter (Bronkhorst® High-Tech, the Netherlands) allowed the control of HCOOH containing air flow. The concentrations of gas phase HCOOH were set at 45 $ppm_{v,}$ 145 ppm_v or 255 ppm_v depending on the photocatalytic test.

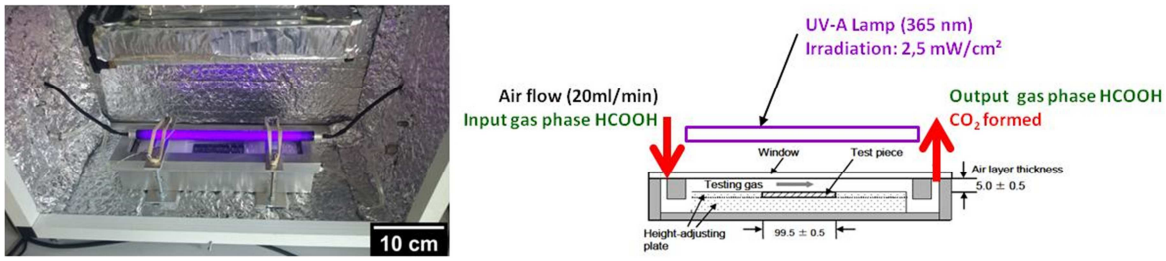

Figure 34: Photocatalytic reactor containing a LbL film built on silicon wafer. The reactor is placed in the thermostated chamber (left). Schematic representation of the photocatalytic reactor (right).

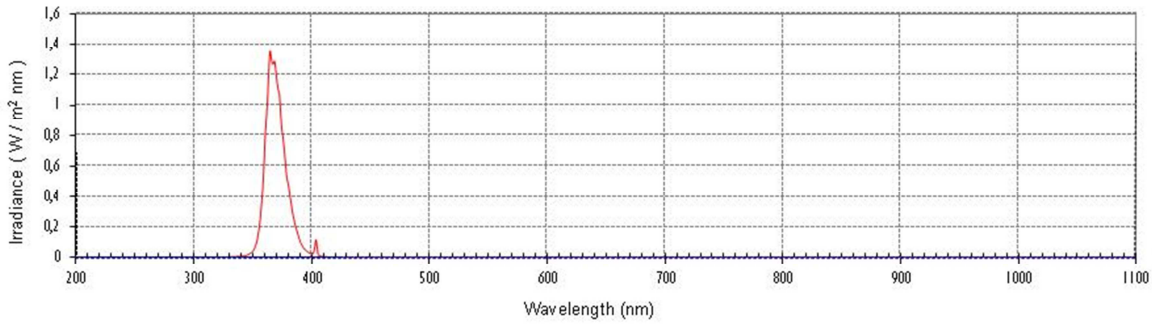

Figure 35 : Irradiance spectrum of the UV-A lamp used in this work.

The photocatalytic reactor was derived from that proposed in the ISO 22197 standard series. This reactor consisted of an aluminium chamber (260 mm in length x 50 mm in width x 40 mm in height) closed with a quartz window. A polytetrafluoroethylene (PTFE) support is located inside the aluminium chamber on which the pollutant flow passes. LbL films constructed on model surfaces (silicon wafers) and textiles were placed face-up in a cavity located at the centre of the PTFE support (Figure 34). While LbL films built on 36 cm² silicon wafer were directly in the cavity, films built on textiles required immobilisation on a silicon wafer support to test their photocatalytic activity. Therefore small pieces of double sided duct tapes (2 to 4 mm², Scotch®) were placed between corners of the textile fabrics and silicon wafer, allowing LbL films built on textiles to be irradiated in similar conditions than the films built on silicon wafers. A 8W UV-A lamp (Sylvania Blacklight Blue F8W/BLB T5) (Figure 35) with a spectral peak centred at 365 nm was placed above the reactor (1.5 cm), parallel to the photocatalytic film. An irradiance of 2.5 mW/cm² was measured at the top of the sample surface. The photocalytic reactor was placed in a thermostated chamber for maintaining a constant temperature of 25°C during the test according to ISO standards, since heat generated by the lamp during the irradiation could not be neglected. The whole photocatalytic set up is illustrated in Figure 36.

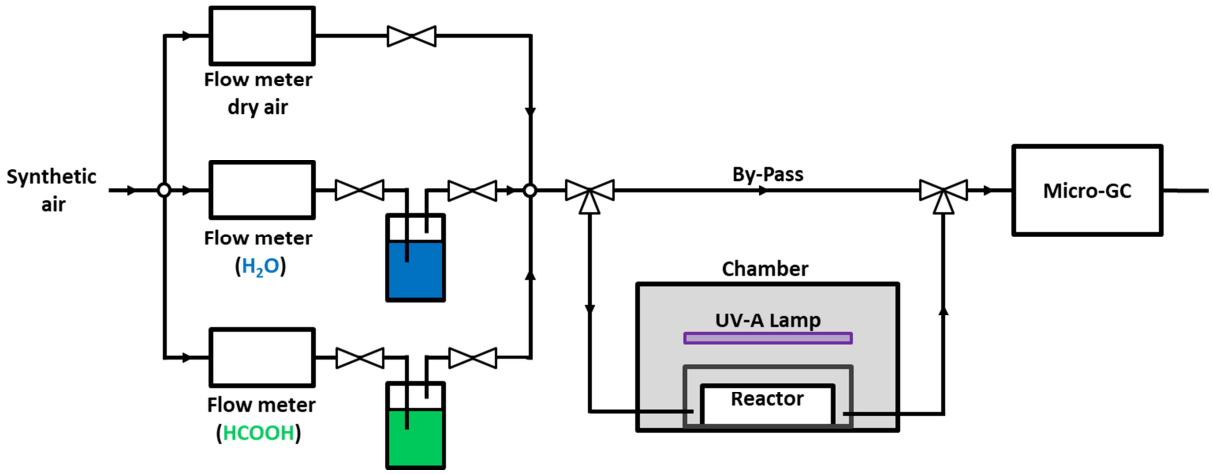

Figure 36: Gas-phase photocatalytic set-up.

A 4 column R3000A gas micro-chromatography (SRA instruments) equipped with thermal conductivity detectors (TCD), allowed the detection and the quantification of gas phase HCOOH and water contained in the inlet and outlet air flow, as well as of carbon dioxide produced on-stream with the LbL films. In this work helium was used as the carrier gas for chromatography columns and the parameters of each column are showed in Table 4.

Column name	Stationary phase	Column temperature (°C)	Column pressure (psi)	Molecule detected and Retention time (s)
Pora Plot Q	Divinylbenzene ethylene glycol	50	25	Carbon dioxide (41.57)
Stabiliwax	Polyethylene glycol	105	25	Water (59.70)
OV 1	Dimethylpolysiloxane	70	25	Formic acid (69.02) Water (54.01)

Table 4 : Column's settings for gas micro-chromatography.

VI.1.2 Test protocols and calculations

Micro gas chromatography allows monitoring of the concentration evolution for formic acid and carbon dioxide during the photocatalysis test. Tests started with stabilisation of humid air flow (40-50%) containing the gas phase model pollutant HCOOH in photocatalytic setup's by-pass. Once

stabilised, air flow is sent in the photocatalytic reactor containing LbL film to be tested. For assessing their photocatalytic activity, LbL films built with polyelectrolytes, titania and with or without silver nanoparticles required different stabilisation/adsorption times and irradiation times according to the materials used for the film construction, and to the type of substrate used. Typical stabilisation/adsorption and UV-A irradiation time parameters are described in Table 5.

Figure 37 shows the evolution with time of the concentrations of gas phase compounds during a typical photocatalyic test, before, during and after UV-A irradiation, for a polyelectrolyte and titania LbL film built on a silicon wafer. Start of UV-A irradiation by switching the lamp on is defined as the time t=0 for the photocatalysis test. When stabilised in the dark, whether before or after irradiation, HCOOH concentration should reach in both cases the defined value set by parameters at the beginning of the test. This HCOOH concentration is defined as the initial concentration, $[HCOOH]_{initial}$, which is calculated by taking the average of last 30 minutes HCOOH concentration values once stabilised (usually the last 30 min of the test), acquired by micro-gas chromatography. When LbL films are irradiated by UV-A light, the final HCOOH concentrations, $[HCOOH]_{final}$, is calculated by averaging the last 30 minutes concentration values acquired before switching off the lamp. Likewise averaging CO_2 concentration taken at the same time for calculating $[HCOOH]_{initial}$ and $[HCOOH]_{final}$, allows us to calculate both initial and final CO_2 concentration: $[CO_2]_{initial}$ and $[CO_2]_{final}$.

Samples	**Stabilisation/Adsorption (h)**	**UV-A Irradiation (h)**
Polyelectrolytes and TiO_2 LbL films built on silicon wafer	12-15	3
Polyelectrolytes and TiO_2 LbL films built on textile	12-15	6
Polyelectrolytes, TiO_2 and silver nanoparticles LbL films built on silicon wafer	15-24	24
Polyelectrolytes, TiO_2 and silver nanoparticles LbL films built on textile	15-24	24

Table 5: Stabilisation/adsorption and irradiation times used in photocatalytic tests.

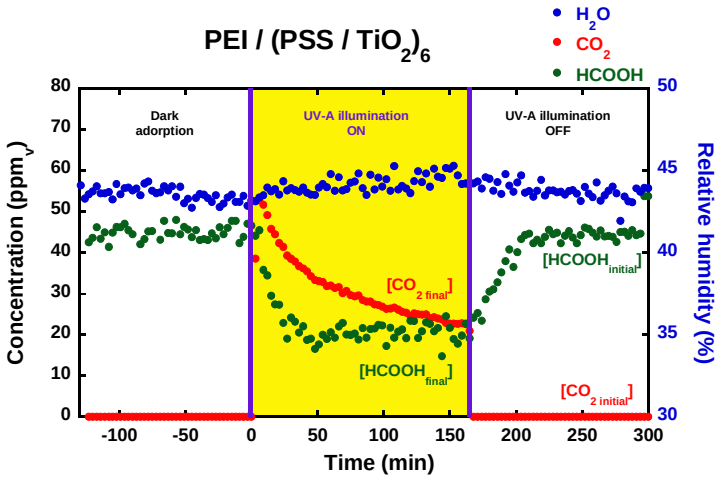

Figure 37: Photocatalytic activity of a PEI/(PSS/TiO_2)$_6$ LbL film

The photocatalytic performance of LbL films constructed on model surfaces and textiles fabrics are evaluated by calculating the HCOOH conversion rate and CO_2 selectivity. CO_2 theoretical concentration, corresponding to 100% selectivity to CO_2 is compared to the CO_2 concentration produced during the photocatalytic test. These terms are defined by the following equations:

$$\text{HCOOH Conversion (\%)} = \frac{[\text{HCOOH}_{\text{initial}}]-[\text{HCOOH}_{\text{final}}]}{[\text{HCOOH}_{\text{initial}}]} \times 100 \qquad \text{(Eq. 37)}$$

$$\text{Theoretical } CO_2\ (\text{ppm}_v) = [\text{HCOOH}_{\text{initial}}] - [\text{HCOOH}_{\text{final}}] \qquad \text{(Eq. 38)}$$

VI.2 Antibacterial activity

Two experimental procedures to test the biocidal activity of LbL films under UV-A irradiation and in the dark, were used in this work according to the type of surface on which LbL films were built. Films constructed on model surfaces were tested at the *Institut des Sciences des Matériaux de Mulhouse* (IS2M, Mulhouse, France) and performed by Charline Soraru within the group of Lydie Ploux, whilst films constructed on textiles were tested at the *Aérial-CRT* (Illkirch, France), performed and analysed by Bernard Hezard and Marie-Hélène Desmonts.

VI.1.1 Model surfaces

LbL films were constructed on 4 cm² (2x2 cm) silicon wafer substrates using the procedure described in Chapter 2.III.1.1. The last layer of each film was deposited manually using the LbL dipping deposition method at IS2M in order to prevent as much contamination at the surface of the film. TiO_2-Ag layer was deposited using the one-pot synthesis of AgNP in LbL films. Since the film surfaces cannot be sterilised by UV irradiation, the samples were rinsed in 3 consecutive baths for 3x10 min with sterilised milli-Q water. This allowed the removal of any non-adhered contaminants as well as further contamination.

Escherichia coli SCC1 bacteria suspension (fluorescent by Green Fluorescent Protein GFP chromosomal inclusion) (Abs_{600nm} = 0.1 OD, optical density) was seeded on film surfaces for 3 h at 30°C. The surfaces were then rinsed with sodium chloride (9 g/L) and were characterised using fluorescence confocal microscopy before and after UV-A irradiation (Sylvania Blacklight Blue F8W/BLB T5, spectral peak centred at 365 nm; lamp placed 2 cm above each sample, providing a 2.5 mW/cm² irradiance at the samples' surface) of the sample for 60 min. Metabolically active bacteria ("ALIVE") were counted before and after UV-A irradiation. Propidium iodide was used after UV-A irradiation to identify and count damaged bacteria ("DEAD").

Microscopy analyses were performed on 7 independent areas of each sample and every acquired picture was analysed using ImageJ® software.

The procedure was repeated 3 times on 2 samples of each LbL films.

VI.1.2. Textile surface

LbL films were constructed on 29.25 cm² (6.5x4.5 cm) textile fibres using the procedure described in section III.3, while TiO_2-Ag layer was deposited using the one-pot photoinduced synthesis of AgNP on PEI/PSS film constructed on textile surfaces (4.5 x 2.7 cm) described in section III.2.2. The textile fabrics were then cut in 4 cm² pieces and placed in small petri dishes. Each system consisted of 18 textiles samples (4 cm²) for bacterial assay.

Four types of bacteria were used to test the biocidal properties of LbL films constructed on textile fibres:

- *Escherichia coli* K12 CIP 54117 n°1311
- *Staphylococcus aureus* (pathogen) CIP 7625 ATCC 25923 n° 300
- *Pseudomonas fluorescens* CIP 6910 n° 1183

- *Listeria monocytogene* 4b (pathogen) CIP 7838 ATCC 13932 n° 367

Bacteria suspensions (20µL) were seeded on the sample surfaces in physiological water. The samples were then irradiated by UV-A light (lamp placed 1.5 cm above the samples) for 3 h (Figure 38). The samples were then placed in a physiologic water and tween mixture for bacteria regrowth, filtered on a Millipore membrane filter (47 mm in size and 0.45 µm of pore sizes) and rinsed 3 times with 10 mL of physiologic water. The number of bacteria was assessed after incubation of membranes on trypticase soy agar for 48h at 37°C.

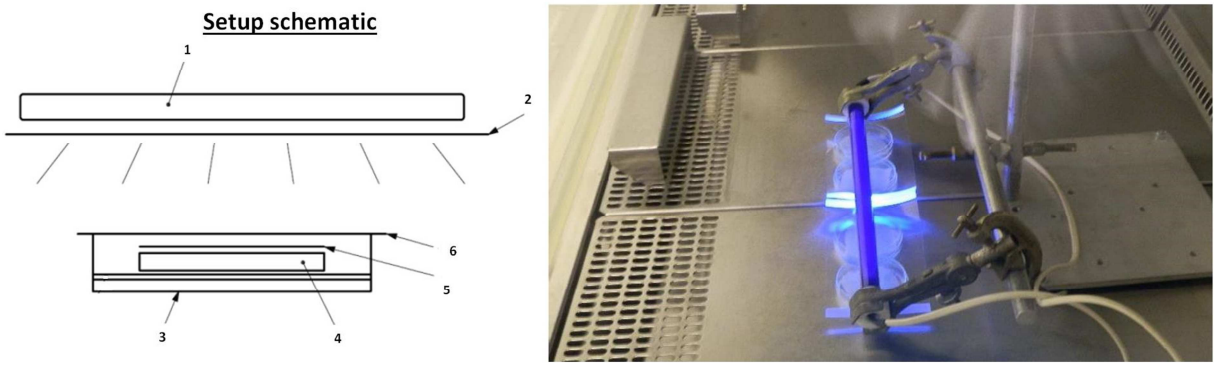

Figure 38 : Schematic (left) and picture (right) of the setup used in antibacterial assay on LbL films constructed on textile surfaces. 1 and 2 – UV-A lamp, 3 – Petri dish, 4 – textile placed on a support, 5 – glass slide, 7 – PCR sealing film.

Chapter 3: Titania and polyelectrolytes thin films – construction on model surfaces

Introduction

This chapter is focused on the elaboration, characterisation and photocatalytic performance evaluation of titania nanoparticle and polyelectrolyte LbL films built on model surfaces (i.e. silicon wafers, glass and quartz slides according to the characterisation technique). As far as photocatalytic activity is concerned, the tests consist first of the gas phase photocatalytic degradation of formic acid, and further in the evaluation of the antibacterial properties of the films. Films containing silver nanoparticles will be addressed in the next chapter.

The first part will be dedicated to the P25 titania suspension characterisations, followed by the LbL film construction and characterisations. Then the gas-phase photocatalytic activity of the films will be addressed in the second part, followed by a discussion. The biocidal properties of the PEI/$(PSS/TiO_2)_n$ LbL films will be discussed In the third and final part of this chapter.

I – Film construction on model surfaces

Layer-by-layer thin film assembly is based on the alternate deposition of oppositely-charged compounds onto a surface. This is realised by dipping the surface directly into the desired solution/suspension containing the desired materials. Since titania has amphoteric properties due to its surface groups ($TiOH_2^+$ or TiO^- respectively in acidic or alkaline media), negatively or positively-charged suspensions can be prepared by suitably adjusting the pH [22], [25]. Studies on LbL titania

thin films for photocatalytic, as well as antibacterial or even solar energy conversion applications are reported in the literature [25], [76], [149], [161], [166], [191], [207], [209]–[211]. These investigations highlighted the LbL film construction feasibility containing either positively- or negatively-charged titania. A positively-charged titania suspension was used in this project in order to allow the construction of LbL films with negatively-charged commercial silver nanoparticles, and the preparation of titania and silver precursor photosensitive solutions for the elaboration of titania-silver nanoparticle hybrid surfaces.

I.1 Preparation and characterisation of P25 titania suspension

Aeroxide® titanium dioxide P25 suspensions were prepared according to the protocol described in chap 2.II.2. This suspension preparation was adapted from a previous PhD student's experimental procedure from Decher's team, Marek Twardoch [205]. In this procedure, P25 TiO_2 was prepared in alkaline milli-Q water with the pH adjusted by tetrabutylammonium hydroxide (TBAOH), providing negative TiO_2 surface charges. Here, TBAOH was replaced by nitric acid (HNO_3) which provided positive TiO_2 surface charges. Once prepared, the suspensions had a milky white colour and were stable for a month. The initial concentration of suspensions was 25 g/L but the applied procedure made the final concentration drop to 12.25 ± 0.21 g/L (value obtained by chemical analysis, ICP-AES). X-Ray Diffraction analysis showed that both anatase and rutile phases were still present in the final titania suspension, as well as in the titania precipitate, resulting from the centrifugation step (Figure 39). In addition, XRD characterisations have allowed us to determine the anatase/rutile proportions in the suspension used for LbL, with the crystallite size (Table 6). The suspension was found to be composed of 92 wt.% anatase with mean crystallite size of 17 nm for anatase, and 22 nm for rutile. The anatase:rutile ratio was found to be similar to the one of P25 TiO_2 powder, with slightly smaller mean crystallite sizes (20 and 32 nm, respectively, for anatase and rutile in P25 TiO_2 powder). The centrifugation step removed some larger size TiO_2 crystallites from the TiO_2 suspension. Dynamic Light Scattering (DLS) analyses were performed three consecutive times on the same suspension. The suspension was further diluted in acidic milli-Q water (pH 2.5 adjusted by HNO_3) in order to obtain an attenuation of 10 (a.u). Results showed P25 aggregate diameter sizes centred at 91 nm ± 1 (Figure 40), which is as expected a slightly higher diameter size compared to the mean crystallite size derived from XRD.

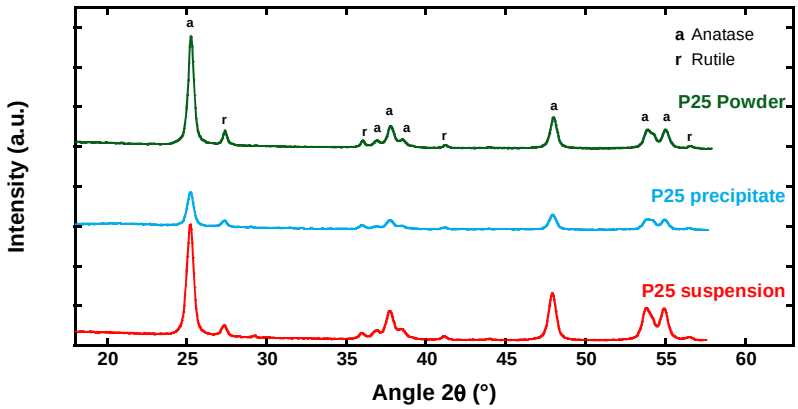

Figure 39 : XRD analysis of TiO_2 P25 as powder, precipitate and from the LbL suspension. a and r correspond to peak associated to anatase and rutile phase respectively.

TiO_2 samples	Weight fraction (wt.%)		Crystallite size (nm)	
	Anatase	Rutile	Anatase	Rutile
P25 Powder	91	9	20	32
P25 suspension	92	8	17	22

Table 6 : Weight fraction of anatase/rutile of TiO_2 P25 in the powder form and in the LbL suspension, with their crystallite sizes.

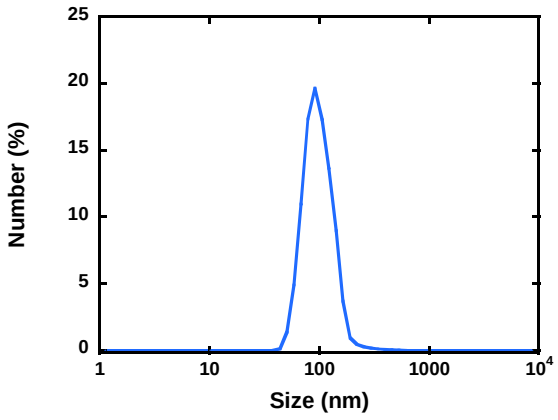

Figure 40 : Dynamic light scattering characterisation of the TiO_2 P25 suspension used for LbL films construction.

I.2 Titania and polyectrolytes film construction and characterisation

Positively-charged 1g/L poly(ethyleneimine) (PEI) was used as an anchor polyelectrolyte to promote adhesion of the film onto every surface in this project. Negatively-charged 1 g/L poly(sodium 4-stryresulfonate) (PSS) was deposited on the PEI layer and acted as a glue between consecutively deposited titania layers. In order to preserve the titania positive surface charges, PSS was dissolved in acidic milli-Q water at pH 2.5 adjusted by HNO_3.

The Layer-by-Layer assembled films were constructed by dipping successively the substrate in the polyelectrolyte solutions or in the titania suspension, with 3 rinsing steps by dipping (rinsing) the substrate in acidic milli-Q water. Dipping times in TiO_2 suspensions and in polyelectrolyte solutions, as well as the rinsing time in milli-Q water used in this project were similar to those in the PhD projects of Marek Twardoch and Dariya Dontsova [205], [212].

XRD characterisations were performed on a 10 layer pairs LbL film and a single layer pair LbL film constructed on silicon wafers (Figure 41). The single layer pair film showed to be composed of only anatase with 18 nm in diameter size, while the 10 layer pairs film was made of 95% anatase (22 nm) and 5% rutile (25 nm). However the rutile intensity peak of the 10 layer pairs film was found to be almost lost in the signal threshold, most likely due to a low titania content in the LbL film. The rutile phase may be also present in the single layer pair film, but the concentration may be too low to be detected by the apparatus. It must be mentioned that a peak could be found on the LbL film at a 33° angle. This peak is attributed to the silicon wafer and was confirmed by XRD characterisation a bare silicon wafer (XRD graph shown in Appendix 1). So, the results showed that no preferential deposition of anatase or rutile phase occured

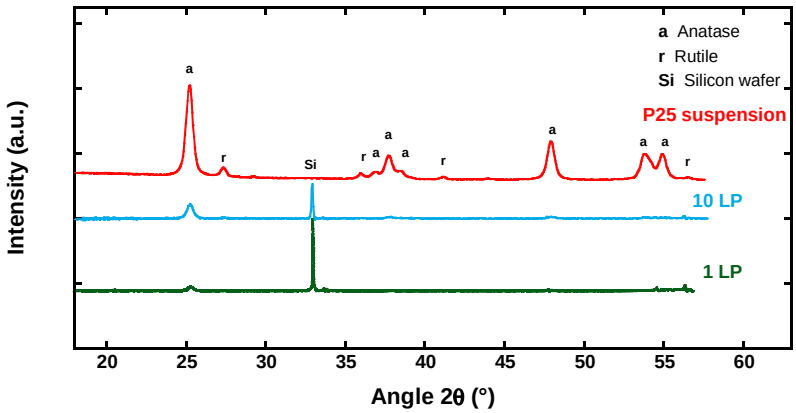

Figure 41 : XRD analysis of titania and polyelectrolytes LbL films.

Sample	Weight fraction (wt.%)		Crystallite size (nm)	
	Anatase	Rutile	Anatase	Rutile
LbL suspension	92	8	17	22
PEI/PSS/TiO_2	100	(*)	(*)	-
PEI/(PSS/TiO_2)$_{10}$	95	5	18	25

Table 7 : Weight fraction of anatase/rutile in TiO_2 LbL films, with their crystallite sizes. (*) peak intensity is too low for accurate measurement.

I.2.1 Monitoring of films construction

Figure 42 : Optical photographs of PEI/(PSS/TiO_2)$_n$ film deposited on silicon wafers. From left to right: bare silicon wafer, PEI/PSS film, PEI/PSS/TiO_2, PEI/(PSS/TiO_2)$_2$, PEI/(PSS/TiO_2)$_4$, PEI/(PSS/TiO_2)$_6$ and PEI/(PSS/TiO_2)$_{10}$.

The build-up of PEI/(PSS/TiO_2)$_n$ on silicon wafer (36 cm², 4.5 x 8 cm) was conducted by an automated dipping robot. The colours observed, arising from optical interferences, at the surface of the sample showed that titania was homogeneously coated on the substrate (Figure 42). LbL titania and polyelectrolyte films construction was monitored by ellipsometry (Figure 43). This characterisation technique provides an estimation of film thickness with an average increase in thickness of 40 nm per PSS/TiO_2 layer pairs deposited, which is slightly higher than the value of PEI/(PSS/TiO_2)$_n$ LbL films constructed in Dontsova's work (37 nm per layer pairs deposited). Each thickness value was obtained by measuring 10 different point areas randomly selected all along the surface of the silicon wafer, providing the error bars for each measurement as well. While the average aggregate size was found to be centred at 91 ± 1 nm, the thickness of the titania layer was found to be lower than DLS measurement, but higher than the crystallite size of anatase and rutile determined by XRD

characterisations. This may indicate that the sample's surfaces are not fully homogeneously covered by 20 nm TiO_2 particles, but rather by small-size TiO_2 aggregates with different sizes along the sample surface, providing an average thickness of 40 nm for the layers. This could be more pronounced for the single layer pair film, for which the average thickness of the layer was higher than that calculated for the next (upper) layers.

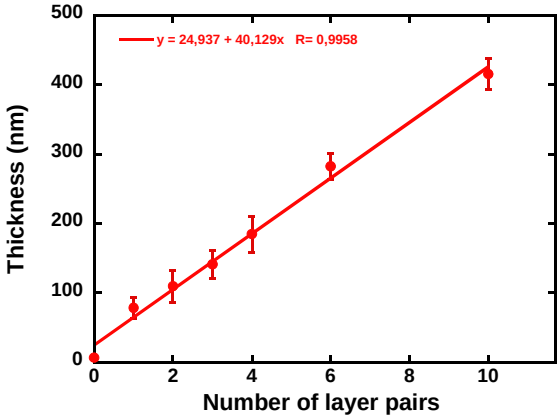

Figure 43: Ellipsometry characterisation of PEI/$(PSS/TiO_2)_n$ films. A linear increase in thickness is observed after deposition of each PSS/TiO_2 layer pair.

UV-visible spectrophotometry in transmission mode was applied for monitoring the film construction on quartz slides (Figure 44). Plasma treatment was applied on both sides of the quartz slide so that polyelectrolytes and titania layers are coated evenly on both sides. 6 layers of TiO_2 were able to be deposited on each side of the quartz slide (12 PSS/TiO_2 layer pairs in total) before reaching signal saturation in the UV-C region. The absorbance measured after each deposition step was therefore divided by two, for obtaining the absorbance increment corresponding to a single layer pair PSS/TiO_2 deposited and globally for measuring the absorbance of the PEI/$(PSS/TiO_2)_n$ films. An increase in absorbance in the UV region was observed while depositing TiO_2 layers on the substrate surface and absorbance values at 300 nm in wavelength were recorded, in regards to the number of layer pairs deposited. This chosen wavelength was suitable since PSS absorbs at 225 nm, which therefore does not affect absorbance results at 300 nm [76]. Results showed a linear increase of 0.28 in absorbance per layer pair, once again a slightly higher absorbance value than that found in Dontsova's work (0.2 per layer pair deposited). It is worth mentioning that the graph of the absorbance at 300 nm in regards to the number of layers shown in Figure 44 was constructed with 6 layer pairs film. This

graph could have been built using the actual acquired absorbance value of the film, and the linear increase in absorbance could have expressed for films up to 12 layer pairs.

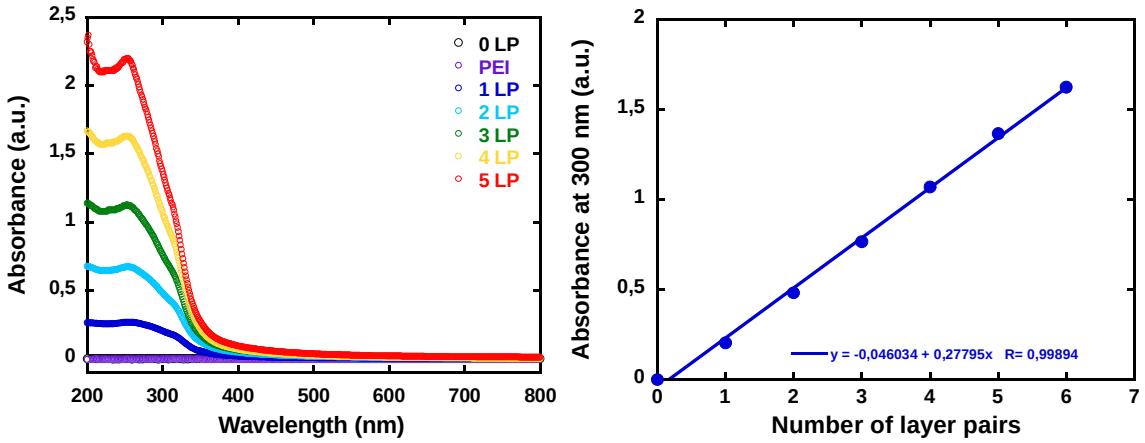

Figure 44: Transmission UV-Visible photospectrophotometry characterisation of PEI/(PSS/TiO_2)$_n$ film. (Left) film deposition on quartz slide with absorbance increment after each layer pairs deposited. (Right) reported absorbance at 300 nm in regards to the number of layer pairs deposited.

LbL film construction was also monitored by a quartz crystal microbalance with dissipation (QCM-D) by constructing the film on the quartz crystal slide using fluidic LbL deposition method [145]. A change in frequencies showed that polyelectrolytes and TiO_2 were successfully deposited on the quartz crystal (Figure 45).

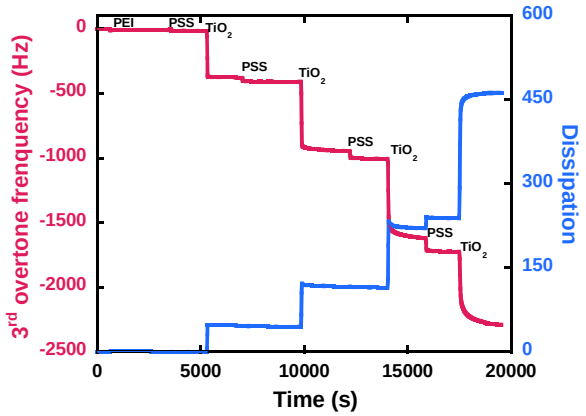

Figure 45: Monitoring PEI/(PSS/TiO_2)$_n$ film construction by QCM-D at the 3rd overtone. 4 PSS/TiO_2 layer pairs were deposited.

Scanning Electron Microscopy images of the PEI/(PSS/TiO_2)$_n$ film showed that titania nanoparticles were homogeneously distributed at a microscopic level. In comparison to a bare silicon wafer, it was

observed that the surface was not fully covered by TiO_2 nanoparticles for a single layer pair film. While increasing the number of layer pairs, surface coverage became total and the films became denser (Figure 46).

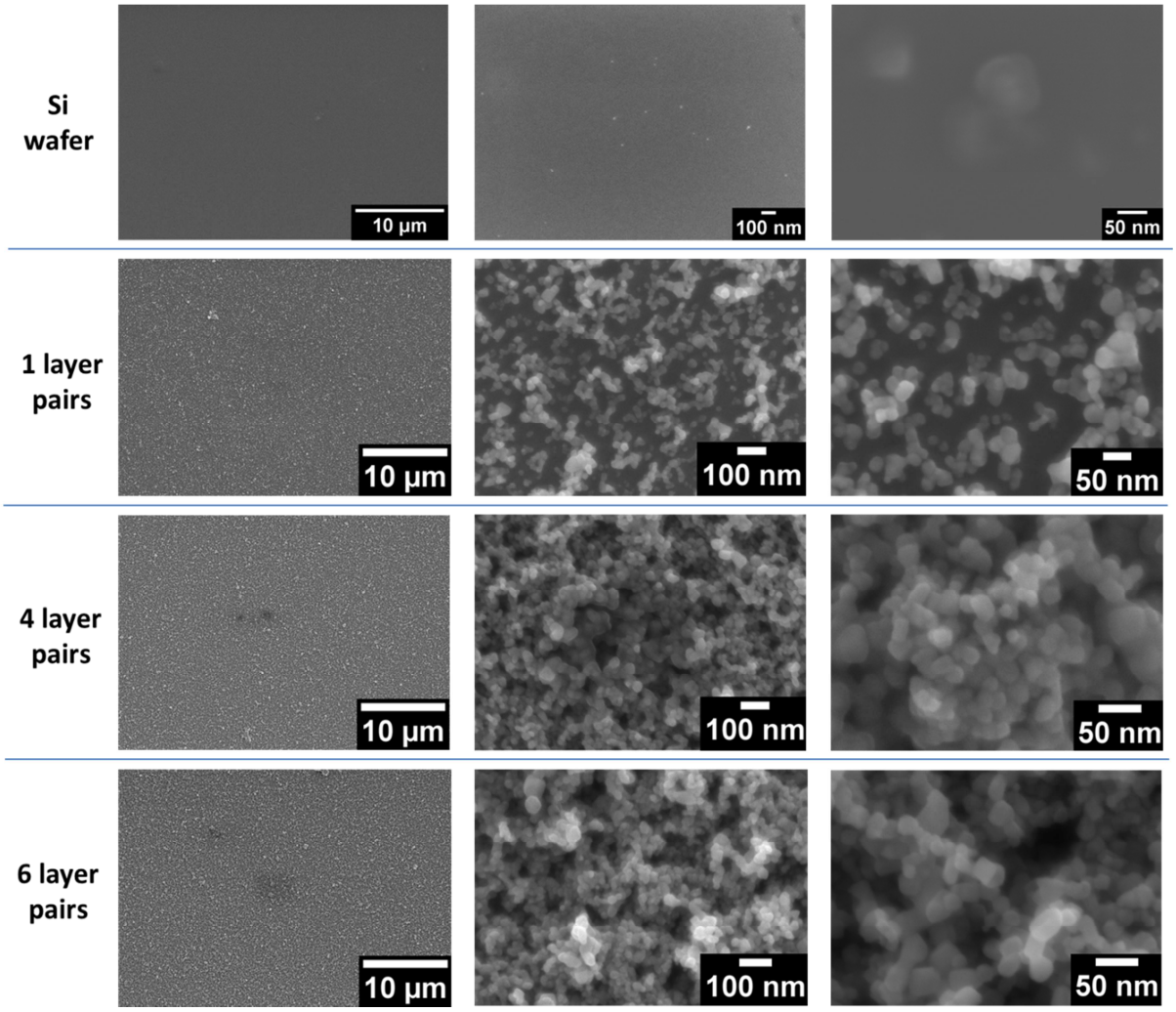

Figure 46 : SEM images of titania and polyelectrolytes LbL films, with different numbers of PSS/TiO_2 layer pairs.

SEM images of LbL films' cross sections with different PSS/TiO_2 layer pairs, did not showed a stratified structure with well defined polyelectrolyte and titania layers (Figure 47). However a porous structure could be observed from a single layer pair film which remained while increasing the number of layer pairs. This porous structure was also observed on PSS/TiO_2 LbL films on different surfaces, in the works of Dontsova and Rongé [76], [149], [212]. SEM characterisations of the films' cross section have allowed the thickness of the films to be determined and the results were compared to the ones obtained by ellipsometry (Table 8 and Figure 48). Result showed an increase of 43 nm in film thickness while increasing the number of the layer pairs, which was found to be similar to the

ellipsometry results (increase in 40 nm per layer pairs deposited). Transmission Electron Microscopy was performed on single layer titania film, and confirmed the narrow monomodal size distribution of TiO_2 crystallites (centred on about 20 ± 4 nm in comparison to 17-18 nm by XRD) (Figure 49).

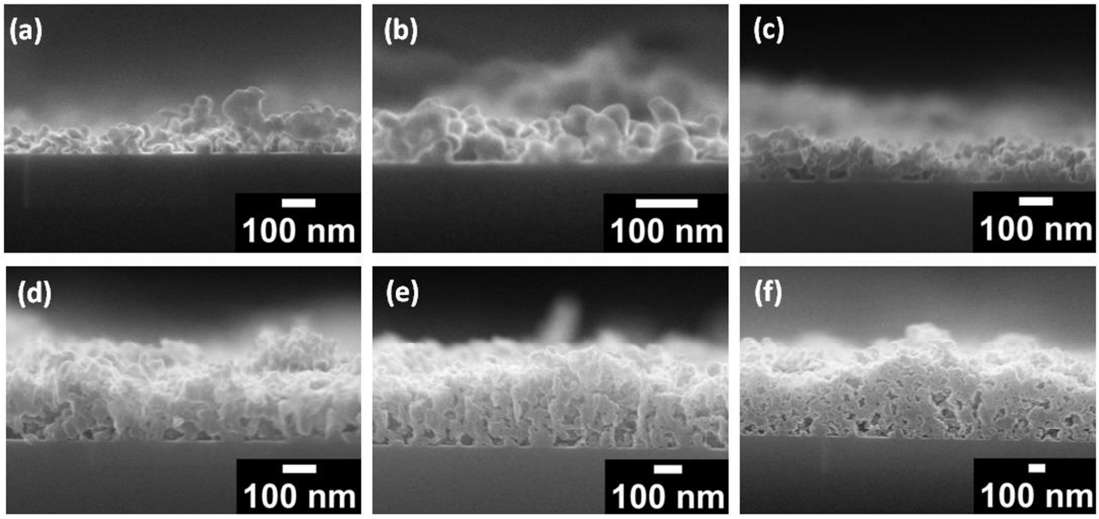

Figure 47: Cross section of PEI/$(PSS/TiO_2)_n$ LbL films deposited on silicon wafers. n=1 (a and b), n=2 (c), n=4 (d), n=6 (e) and n=10 (f). Brightness and contrast of SEM images were treated with Image J®.

Sample	**Ellipsometry (nm)**	**SEM cross section (nm)**
PEI/PSS/TiO_2	78 ± 15	65 ± 23
PEI/PSS/$(TiO_2)_2$	110 ± 23	97 ± 25
PEI/PSS/$(TiO_2)_3$	141 ± 20	-
PEI/PSS/$(TiO_2)_4$	185 ± 27	230 ± 33
PEI/PSS/$(TiO_2)_6$	282 ± 19	290 ± 36
PEI/PSS/$(TiO_2)_{10}$	416 ± 23	434 ± 50

Table 8 : Comparison of the film thickness obtained by ellipsometry and SEM characterisations.

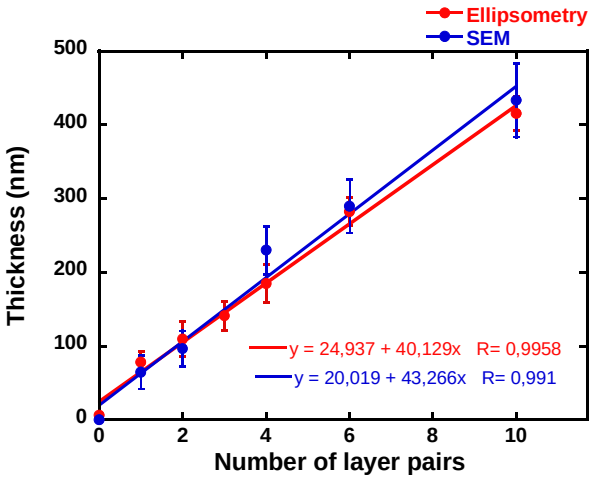

Figure 48 : Increase in thickness of PEI/(PSS/TiO_2)$_n$ LbL films obtained by ellipsometry and SEM characterisations.

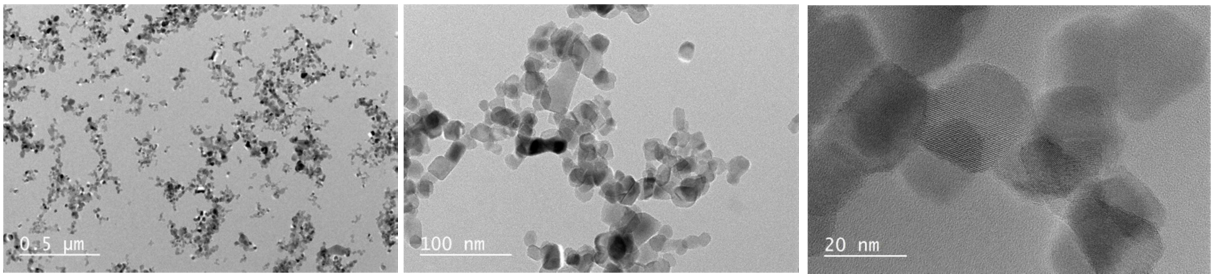

Figure 49: TEM images of a PEI/PSS/TiO_2 LbL film (single layer pair).

I.2.2 Amount of titania deposited

I.2.2.1 UV-Visible spectrophotometry

By neglecting the light scattering and assuming identical extinction values of TiO_2 in aqueous suspension and in LbL titania films deposited on quartz slide, the absorbance of the LbL titania film can be correlated to the amount of titania per layer deposited using the following equation:

$$\frac{m}{S} = \frac{c_1 \, l_1 \, A}{A_1} \qquad \text{(Eq. 28)}$$

Where $\frac{m}{S}$ is the amount of deposited material m per layer per surface area *S* of a substrate (g/m²), c_1 is the concentration of titania suspension (g/m^3), l_1 is the length of light pass (i.e. width of quartz

slide), A_1 is the absorbance of the LbL titania film on a quartz slide (value assessed at 300 nm, Figure 44). A is the absorbance of the suspension that can be calculated through the establishment of a calibration curve of the titania suspension absorbance against the TiO_2 suspension concentration (Figure 50). The estimated amount of titania deposited per layer was found to be 47 ± 5 mg/m² (4.7 ± 0.5 µg/cm²).

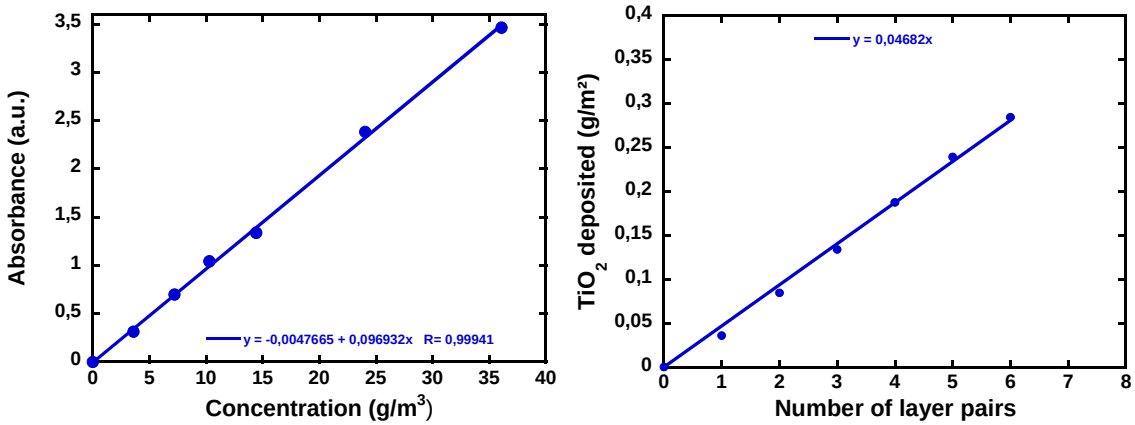

Figure 50: Amount of TiO_2 deposited per layer calculated from UV-Visible spectrophotometry data. Absorbance of TiO_2 suspension in regards to TiO_2 concentration (left); amount of TiO_2 deposited per layer pairs calculated from Dontsova's equation (right).

I.2.2.2 Quartz Crystal Microbalance with Dissipation

Mass of deposited TiO_2 on quartz crystal was estimated by using Sauerbrey equation:

$$\Delta m = -C \times \left(\frac{\Delta f_n}{n}\right) \quad \text{(Eq. 26)}$$

Δf_n was calculated by subtracting the average frequency of the compound deposited (after the rinsing step) by the average frequency of the previously deposited compound. Average frequencies were obtained using the frequency data acquired during the last 5 min of the prior deposition of next compound on quartz crystal. All data were assessed at the 3rd overtone (n = 3) and an average of 9.2 ± 0.9 µg/cm² of TiO_2 deposited was calculated. However this value includes also the amount of water adsorbed onto the film, which increased the mass of deposited material. Moreover the difference in changes of frequency while depositing materials has shown that the amount of PSS is increasing after every deposition step (values showed in Appendix 2). This can either indicate that more PSS is deposited after each deposition step, or that more water molecules are adsorbed on the film. This

can be explained by the superhydrophilicity of PSS/TiO_2 LbL films after 2 layer pairs have been deposited, observed by Kommireddy *et al*. [165]. High dissipation values highlight the adsorption of water on LbL films after each titania nanoparticle deposition. This suggests that PSS/TiO_2 does not act as a rigid film, but more like a viscous one. Comparison of the changes in frequency at the 3rd, 5th and 7th overtones confirms this hypothesis, since curves do not overlap (graph shown in Appendix 3). Therefore the amount of materials deposited in the films cannot be determined by QCM, or at least be overestimated. While the first layer deposited is reasonable to determine the amount of material deposited, the deposition of the next layers will not include the drying step using QCM. Moreover the exact modelling of dissipation and mass appeared too complex in this system.

I.2.2.3 ICP-AES analysis

ICP-AES chemical analyses were used on LbL TiO_2 films built on silicon wafers to provide the amount of Ti deposited on the films. Values were then calculated to obtain the TiO_2 amount deposited per layer. ICP-AES experimental procedure required 4 cm² samples (2x2 cm) to evaluate the amount of TiO_2 deposited on substrate surfaces. Studies on the amount of titania deposited were conducted on two types of 4 cm² sample to see if the amount of titania deposited could vary along the substrate surface. The first type of samples was LbL films constructed on three 36 cm² silicon wafers and then carefully cut with a diamond pen in several 4 cm² samples each; the second type of samples was LbL films directly built on three 4 cm² silicon wafer samples. Since the LbL dipping process allows charged materials to be coated on both sides of the sample, the wafer surfaces that were not plasma treated prior film construction, were cleaned with a velvet-soft tissue and ethanol to remove as much TiO_2 as possible. Hence the amounts of titania were obtained for a single side of the silicon wafer sample.

Single layer pair samples were used to study the possible variation of titania concentration on different areas of LbL film constructed on 36 cm² silicon wafers and between different films built on 4 cm² substrates (Figure in Appendix 4). Films constructed on 36 cm² were found to have an amount of 6.0 ± 1.1 µg/cm² of TiO_2 deposited, while 7.1 ± 0.5 µg/cm² of TiO_2 deposited was obtained on films constructed on 4 cm² samples. These results did not show any significant deposited TiO_2 concentration variation between the two.

The amount of TiO_2 deposited on several layers LbL films were obtained by cutting three samples of 4 cm² from a 36 cm² LbL film built on silicon wafers. Results showed a linear increase in the amount of titania deposited on silicon wafer with a density of 7.0 ± 0.7 µg/cm² per layer deposited (Figure 51).

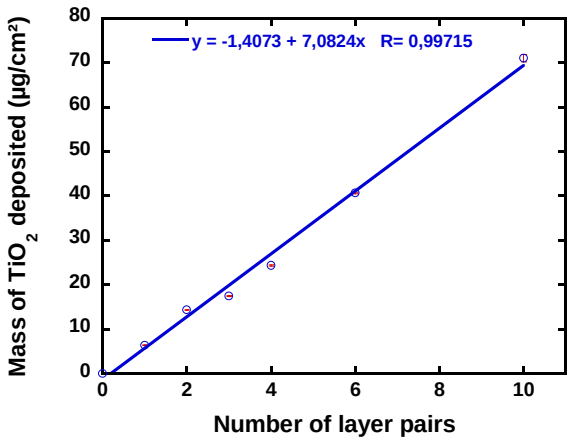

Figure 51: Mass of TiO_2 deposited investigated by chemical analysis ICP-AES. Error bars are too small to be clearly shown on the graph.

This result is slightly higher than that estimated by UV-Visible spectrophotometry, but lower than that observed through QCM-D characterisation. However assumptions and neglected parameters did not have to be made for ICP-AES characterisations. Therefore chemical analysis provides more accurate results and was used in the rest of the project to obtain the amount of materials (Ti and silver) deposited in LbL films. However, UV-Visible spectrophotometry remains a valuable characterisation method to get a quick estimation of the amount of TiO_2 deposited, compared to the time-consuming usually-externalised (sub-contracted) ICP-AES chemical analysis.

II – Gas-phase photocatalytic performances of LbL titania and polyelectrolytes films

Gas phase photocatalytic performances of LbL films were evaluated on the films built on 36 cm^2 silicon wafer samples, and the conversion of formic acid (HCOOH), as well as the CO_2 concentration formed, was assessed. The experimental procedure can be found in Chap 2.VI.1.

II.1. Photocatalytic degradation results of formic acid by LbL films

HCOOH stabilisation on LbL titania film lasted for 12 h with constant polluted gas concentration in photocatalytic reactor; it started during the evening/night, with UV-A irradiation usually starting on the next day. Low air flow of 20 ml/min was set in order to facilitate adsorption and diffusion of

HCOOH molecules in LbL films. The tests were performed at a total flow of 20 ml/min with a HCOOH concentration of 45 ppm_v (with 50% relative humidity), corresponding to a speed rate of 0.7 cm/s.

HCOOH conversion and CO_2 formation were evaluated in regards to LbL films with different number of layer pairs. UV-A illumination time was set for 3 h, which were sufficient to ensure stabilisation of HCOOH concentration.

II.1.1 Conversion of formic acid

Results showed that photocatalytic activity could be observed for a single layer pair film. However, the conversion evolution profile according to the number of layer pairs obtained was found to have unusual behaviour (Figure 52A). While increasing the number of layer pairs, the amount of titania increases as well. Therefore the reaction rate should be proportional to the amount of photocatalyst until the rate value reaches a plateau due to screening of incident light, masking parts of the titania surfaces in deeper layers. However 94% HCOOH conversion could be observed for a single layer pair film, with a decrease of conversion rate for films containing a second and third layer of titania, respectively 63% and 60%. After 4 layer pairs deposited, photocatalytic conversion started to increase (72%) and follows a usual trend in regards to the amount of catalyst. A conversion plateau is observed after 6 layer pairs deposited, with a conversion rate of about 86%, however lower than the conversion achieved on a single layer pair film. Assuming that the film is behaving as a normal photocatalytic film after 3 layer pairs, the expected conversion curve was then plotted by extrapolating the photocatalytic results obtained for 3 to 10 layer pairs films.

Results of photocatalytic tests are shown in Table 9 and the photocatalysis test curves for each layer pairs film are showed in Appendix 6. It must be mentioned that these results were assessed on $PEI/(PSS/TiO_2)_n$ LbL films constructed with the same titania suspension. The error bars were obtained by averaging the conversion results of three photocatalytic tests performed on three different films built from the same TiO_2 suspension. Each film was characterised by ellipsometry to evidence the reproducibility of the construction. Films constructed from a different suspension batch showed slightly different conversion rates from the one presented in Table 9, but the unusual behaviour of the films regarding their photocatalytic activity was still observed (results not presented).

Sample	Amount of TiO_2 deposited (µg/cm²)	Conversion (%)	HCOOH degraded (x10^{-11} mol HCOOH/µg TiO_2•min)	Expected HCOOH degraded (x10^{-11} mol HCOOH/µg TiO_2•min)
PEI/PSS	0	0	0	0
PEI/PSS/TiO_2	7 ± 0.7	94 ± 3	15.2 ± 0.3	2.9
PEI/PSS/$(TiO_2)_2$	14 ± 0.1	63 ± 2	4.2 ± 0.2	3.0
PEI/PSS/$(TiO_2)_3$	17 ± 0.1	60 ± 2	3.5 ± 0.1	3.0
PEI/PSS/$(TiO_2)_4$	24 ± 0.1	72 ± 2	2.8 ± 0.1	3.0
PEI/PSS/$(TiO_2)_6$	41 ± 0.2	88 ± 1	2.3 ± 0.1	2.0
PEI/PSS/$(TiO_2)_{10}$	71 ± 0.1	86 ± 5	1.5 ± 0.1	1.2

Table 9: HCOOH Conversion on titania and polyelectrolytes LbL films upon UV-A irradiation

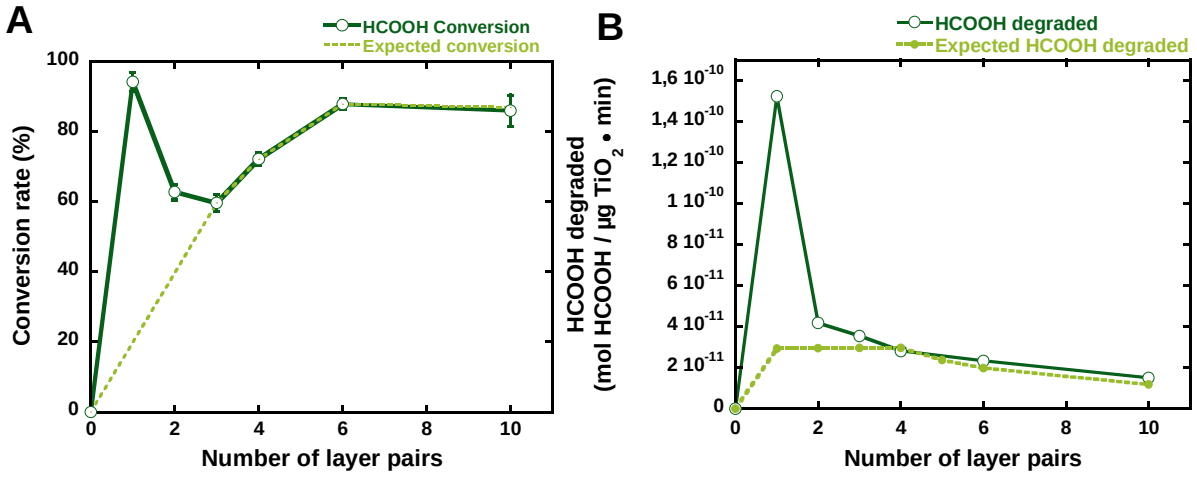

Figure 52: (A) Evolution of HCOOH conversion in regards to the number of layer pairs deposited in LbL films. (B) HCOOH degraded in mol per µg of TiO_2 per min in regards to the number of layer pairs. Experimental parameters: [HCOOH] = 45 ppm_v, air flow = 20 mL/min, speed = 0.7 cm/s, UV-A irradiance = 2.5 mW/cm², films built on 36 cm² silicon wafers.

By combining results obtained from gas-phase photocatalytic tests (mol of HCOOH) and chemical analysis (µg of titania in the film), the number of moles of HCOOH degraded per mol of titania per

minute was reported in Figure 52B as function of the number of layer pairs. According to the usual behaviour of the films, while increasing the amount of titania, degradation of HCOOH (in mol/µg TiO_2•min) remains constant until HCOOH conversion reaches the plateau region. The HCOOH degradation will then drop as the amount of titania is increased, highlighting the fact that most of the degradation of HCOOH in titania LbL films, is done by the upper layers of the films. This expected curve was plot in Figure 52B, assuming that 7 µg/cm² of titania is deposited every layer (Figure 51), and the number of HCOOH moles degraded were calculated using conversion values from the "expected conversion" curve of Figure 52A.

Likewise results were plotted by using actual values of HCOOH's mole degraded and TiO_2 content, calculated from actual conversion results and the amount of titania deposited in every film. These results showed a maximum HCOOH degradation rate per mass of titania for a single layer pair film, with a drastic drop for 2 layer pairs film. This curve is another way to evidence the unusual behaviour of the film for a single layer pair.

II.1.2 Carbon dioxide formation

Like the HCOOH conversion rate curve, the CO_2 formation curve followed the same trend by having a maximum CO_2 concentration formed for a single pair of layer film (Figure 53 and Table 10). The maximum concentration of CO_2 formed is observed for a single layer pair film and this concentration decreased once adding a second and a third PSS/TiO_2 layer pair (28 and 24 ppm_v, respectively). Then the concentration of CO_2 formed increases again and reaches a plateau at about 38 ppm_v after 6 layer pairs films. As observed in conversion rate results, the maximum value is reach for single layer pair film and not reached again while increasing the layer pair number.

Samples	CO_2 formation (ppm_v)	Theoretical CO_2 formation (ppm_v)
PEI/PSS	0	0
PEI/PSS/TiO_2	53 ± 1	42 ± 1
PEI/PSS/$(TiO_2)_2$	28 ± 1	26 ± 1
PEI/PSS/$(TiO_2)_3$	24 ± 1	27 ± 1
PEI/PSS/$(TiO_2)_4$	30 ± 1	30 ± 1
PEI/PSS/$(TiO_2)_6$	39 ± 2	41 ± 1
PEI/PSS/$(TiO_2)_{10}$	37 ± 1	38 ± 2

Table 10: CO_2 formation results on TiO_2 LbL films as a function of the number of layer pairs during photocatalysis test with formic acid.

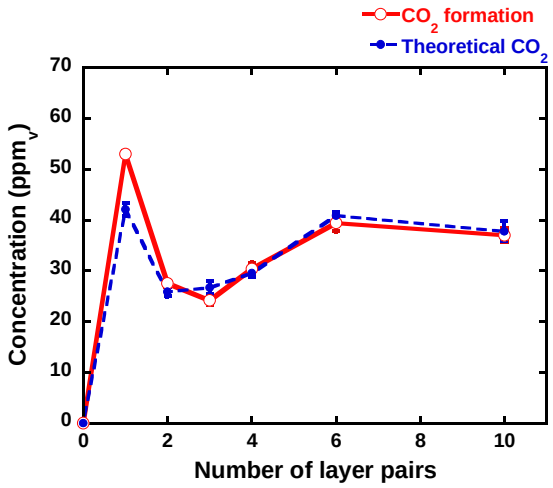

Figure 53: CO_2 formation on TiO_2 LbL films in regards to number of layer pairs during photocatalysis test with formic acid.

The theoretical amount of CO_2 was calculated by subtracting the output HCOOH concentration from the input HCOOH concentration and reported on CO_2 concentration formed (Figure 53, blue curve). Results showed an overproduction of 11 ppm_v for the PEI/PSS/TiO_2 LbL film. Therefore when irradiated during photocatalysis test, a single layer pair film PEI/PSS/TiO_2 may not only degrade gas phase formic acid, but may also degrade polyelectrolytes contained within the film. However the CO_2

concentration formed and the theoretical concentration values of CO_2 were found to be equal once a second layer pair is constructed, so that the LbL titania film is degrading mainly HCOOH and not polyelectrolytes.

II.1.3 Influence of polyelectrolytes in photocatalytic tests

Incorporation of polyelectrolytes in multilayered films may affect the photocatalytic activity of the catalyst: polyelectrolytes may block catalyst active sites, as well as being degraded by titania nanoparticles. Therefore photocatalytic tests without HCOOH were performed on LbL films as a controlled experiment to test the hypothesis of a photocatalytic self-degradation of PEI/$(PSS/TiO_2)_n$ LbL films upon UV-A irradiation. LbL films were irradiated by a UV-A lamp for a certain period of time to see if CO_2 (ppm_v) is formed during the tests, which can be related to the degradation of polyelectrolytes.

Results showed that CO_2 is formed in small amounts for every LbL film constructed on silicon wafer upon UV-A irradiation (Figure 54 and Table 11). Stabilisation of CO_2 was reached after an average time of 18 min for films up to 3 layer pairs and increased with adding PSS/TiO_2 layer pairs. Once stabilisation of CO_2 was obtained, the UV-A light remained lit for 60 min in order to evaluate further degradation of polyelectrolytes. Figure 54A shows a typical test curve obtained on a LbL titania film irradiated by UV-A light in the presence of a humid air flow. An average concentration of about 16 ppm_v of CO_2 was found for every LbL film. This average concentration remained stable with further irradiation time, showing that polyelectrolytes were still slightly degraded after an hour of irradiation. This average value was found to be close to the CO_2 overproduction in the PEI/PSS/TiO_2 single layer pair film in the photocatalytic test with gas phase HCOOH.

In addition to the initial degradation of the polyelectrolyte, the slightly higher CO_2 concentration observed at the beginning of the test before stabilisation could also be related to the desorption of the CO_2 molecules adsorbed within the LbL film, that is temperature activated (through a slight increase of temperature resulting from the switch-on of the UV-A lamp).

The formation of CO_2 is not proportional to the number of layers, so one hypothesis could be that the degradation of PEI is concerned rather than that of PSS, this could be related to the overproduction of CO_2 only for the single layer pair film.

Samples	CO_2 stabilised (ppm_v)	Time to reach stabilisation (min)
PEI / PSS	0	0
PEI / PSS / TiO_2	16	15
PEI / (PSS / TiO_2)$_2$	17	21
PEI / (PSS / TiO_2)$_3$	16	18
PEI / (PSS / TiO_2)$_4$	20	40
PEI / (PSS / TiO_2)$_6$	17	75
PEI / (PSS / TiO_2)$_{10}$	15	235

Table 11: CO_2 formation data when LbL titania films are UV-A irradiated. Air flow does not contain formic acid.

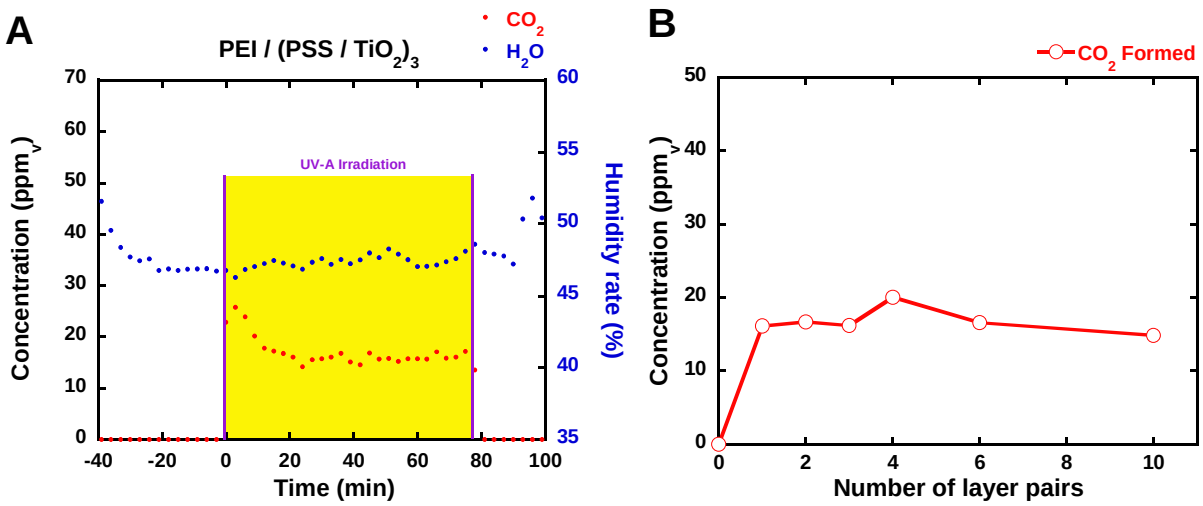

Figure 54: (A) Evolution of concentration curve for a 3 layer pairs LbL film; stabilisation is reached after 18 min. (B) Results of CO_2 concentration formed during UV-A irradiation in regards to the number of layer pairs deposited.

II.1.4 Quantum yield calculations

Conversion results for the photocatalytic degradation of formic acid have allowed quantum yields to be calculated. Quantum yield equations were derived from the equations reported, for instance, by Hugo de Lasa, Benito Serrano and Miguel Salaices [213]. They were first used on TiO_2 thin films by Pauline Barrois in her PhD at ICPEES/ICS laboratory [214]. Here, every quantum yield was calculated for a wavelength range from 300 to 800 nm.

Quantum yields are based on a "number ratio", either of photoconverted molecules over absorbed photons or over photons entering the reactor [213]. However different terminologies are found in the literature depending on the authors.

In term of terminology, we are using the apparent quantum yield η_{app}, which takes into account the reaction rate and the rate (flux) of photons emitted by the UV-A lamp (and more precisely the rate of photons received by the film). This yield is expressed by the following equation:

$$\eta_{app} = \frac{r}{\phi_{received}} \quad \text{(Eq. 39)}$$

where *r* is the reaction rate (in mol/min) and $\phi_{received}$ is the rate of received photons with:

$$\phi_{received} = \int_{\lambda_{min}}^{\lambda_{max}} \frac{P(\lambda)}{E(\lambda)}\, d(\lambda) \quad \text{(Eq. 40)}$$

P is the irradiation power at a given wavelength (in W) with $P(\lambda) = I(\lambda) \times 10^{-6} \times S$ with *I* being the irradiance received by the film surface (W.cm²) and *S* the surface area of the film (36 cm²). *E* is the photon energy (in J) with $E = \frac{hc}{\lambda}$.

The results of apparent quantum yield are shown in Figure 55A. Since apparent quantum yield is related to the reaction rate and to the photons received by the titania LbL film, and not to the absorption of the film, the results show a similar trend to the HCOOH conversion curve with maximum apparent quantum yield for a single layer pair film (0.67%), followed by a decrease in yield until 3 layer pairs film (0.41%). Apparent quantum yield then increases again up to a plateau level at about 0.6% for a 6 – 10 layer film.

Samples	Apparent quantum yield, η_{app} (%)	Quantum yield η (%)
PEI / PSS / TiO_2	0.67	8.13
PEI / (PSS / TiO_2)$_2$	0.46	2.83
PEI / (PSS / TiO_2)$_3$	0.41	1.62
PEI / (PSS / TiO_2)$_4$	0.50	1.53
PEI / (PSS / TiO_2)$_6$	0.60	1.43
PEI / (PSS / TiO_2)$_{10}$	0.62	1.10

Table 12: Quantum yields of obtained with PEI/(PSS/TiO_2)$_n$ LbL films built on silicon wafer.

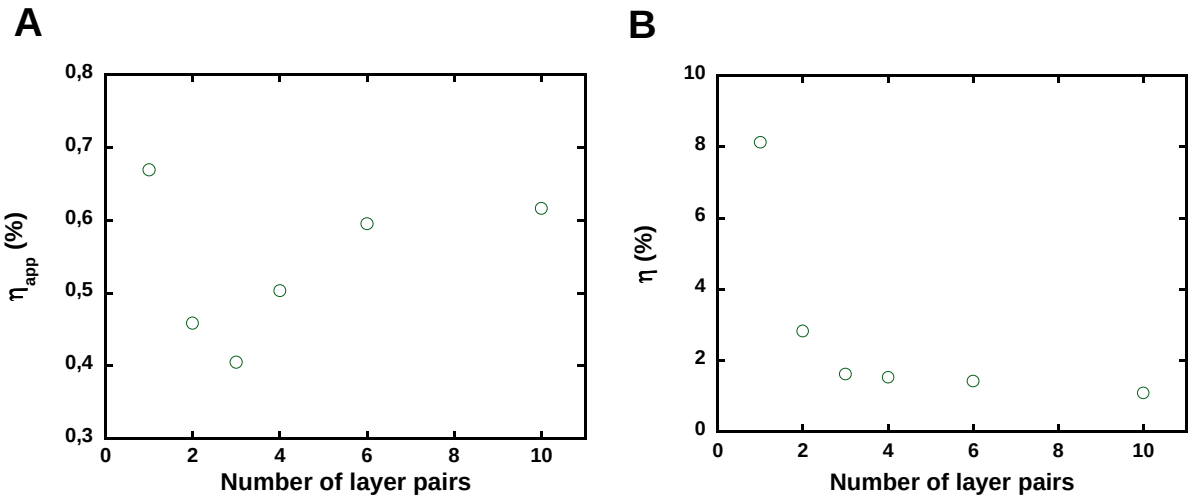

Figure 55: (A) Apparent quantum yield, η_{app}; (B) Quantum yield η.

On the other hand, efficient quantum yield (or quantum yield) η takes into account the number of photons that have been absorbed by the materials and were used for the generation of e^-/h^+ pairs in TiO_2. Efficient quantum yield can be expressed as the following equation:

$$\eta = \frac{r}{\Phi_{absorbed}} \qquad \text{(Eq. 41)}$$

where *r* is the reaction rate (in mol/min) and $\phi_{absorbed}$ is the rate of photons absorbed with:

$$\Phi_{\text{absorbed}} = \int_{\lambda_{min}}^{\lambda_{max}} \frac{P(\lambda) \times (1 - 10^{-A(\lambda)})}{E(\lambda)}\, d(\lambda) \qquad \text{(Eq. 42)}$$

P is the irradiation power at wavelength (in W) with $P(\lambda) = I(\lambda) \times 10^{-6} \times S$ with *I* being the lamp irradiance (W.cm²) and *S* the surface area of the film (36 cm²). A is the absorbance in transmission of LbL at every wavelength λ. *E* is the photon energy (in J) with $\mathrm{E} = \frac{\mathrm{hc}}{\lambda}$.

Here the trend follows a similar profile to the HCOOH degraded per mass of TiO_2 in regards to the number of layer pairs which shows that screening of the light is probably not the only cause of the decrease in efficient quantum yield (Figure 55B). Nevertheless an 8% efficient quantum yield for a single layer film has been calculated, which is 6-7 times higher than efficient quantum yields achieved over 6-10 layer pairs films.

We know that the number of photons entering the reactor is a parameter much simpler to measure. In the estimation of the quantum yield, the reflective surfaces can lead to approximation in the measurement, due to light back scattering or forward-scattering from the catalyst particles [215].

II.2 Discussion on unusual photocatalytic behaviour of LbL titania film

The photocatalytic results for the PEI/$(PSS/TiO_2)_n$ LbL films showed an unusual behaviour of HCOOH conversion in regards to the number of TiO_2 layers contained in the films, with the maximum conversion obtained for a single layer pair film (94 %). Different characterisations were performed on the films in order to understand this result.

II.2.1 Time Resolved Microwave Conductivity

Time Resolved Microwave Conductivity characterisations were performed at the *Laboratoire de Chimie Physique* (LCP, Orsay, France). This technique provides information on the number of excess charge carriers created by the TRMC pulse (I_{max}), as well as indications on life-time of charge carriers which may undergo recombination or trapping (I_{40ns}/I_{max}). Results here were focussed on the I_{max} values obtained for LbL films containing different layers of titania, while providing information on charge carriers life-time with I_{40}/I_{max} data.

Films containing several PSS/TiO_2 layer pairs were built on glass slides. A bare glass slide and a PEI/PSS film acted as control samples. TRMC characterisations did not give any signals for those two samples since photocatalysts were not deposited onto them. However no significant signal could be observed for a single layer pair film mainly due to the low amount of titania deposited on the film, resulting in the signals being lost in TRMC threshold. TRMC results for higher number of layer pairs are reported in Figure 56.

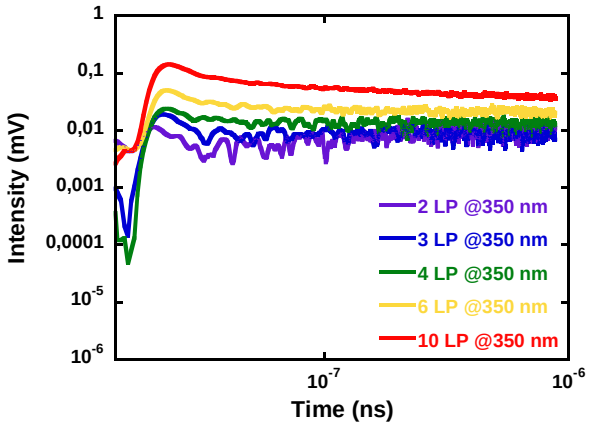

Figure 56: TRMC characterisations of PEI/$(PSS/TiO_2)_n$ films.

I_{max} and I_{40}/I_{max} were then plotted as a function of the number of layer pairs of PSS/TiO_2 deposited on the glass slides (Table 13 and Figure 57). I_{max} values showed that the number of generated charge carriers increases according to the number of layer pairs deposited. While the photocatalytic tests showed that the HCOOH conversion plateau is reached after 6 deposited layer pairs, TRMC results are showing that the number of photogenerated charge carriers is still increasing. In addition, the absence of a significant signal for the single layer pair film allowed us to rule out the hypothesis of the generation of an especially-high number of charge carriers in respect to the amount of TiO_2 contained in the single layer pair film.

The I_{40}/I_{max} ratio gave an indication on charge carrier life-times of the titania LbL films. Slight variation on the charge carriers' life-time in regards to the number of layer pairs deposited was observed. However no general trend could be evidenced.

Sample	I_{max} (mV)	I_{40}/I_{max} (mV)
$PEI/(PSS/TiO_2)_2$	0.012	0.471
$PEI/(PSS/TiO_2)_3$	0,019	0.574
$PEI/(PSS/TiO_2)_4$	0.024	0.537
$PEI/(PSS/TiO_2)_6$	0,051	0.417
$PEI/(PSS/TiO_2)_{10}$	0.144	0.445

Table 13 : I_{max} and I_{40}/I_{max} values of $PEI/(PSS/TiO_2)_n$ LbL films obtained by TRMC characterisations.

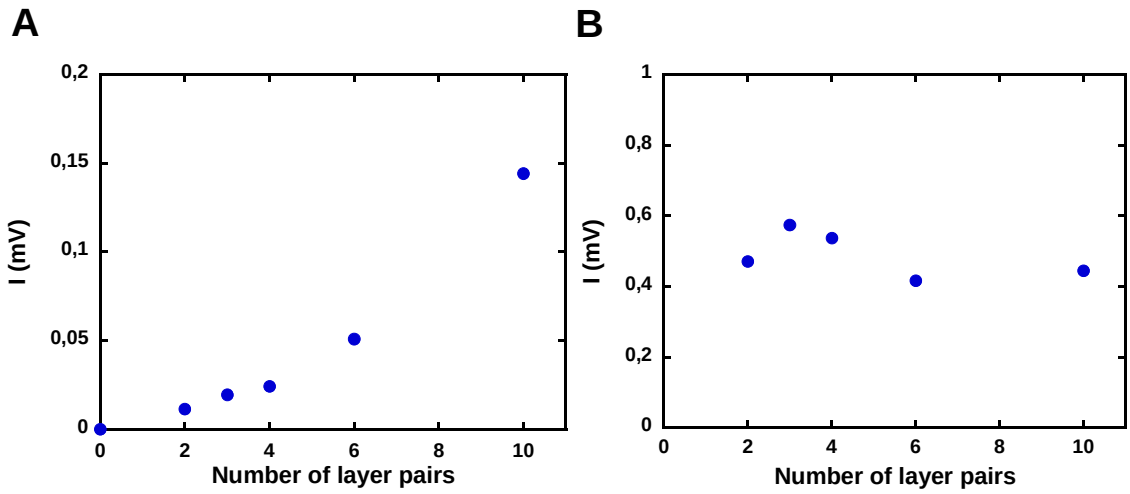

Figure 57: Information on charge carriers in regards to number of layer pairs deposited. A: I_{max}; B: I_{40}/I_{max}.

Overall these results showed a traditional trend where the number of photogenerated charge carriers is related to the number of layer pairs deposited in the film: the more titania in the film, the more charge carriers will be generated. No change in charge carrier life-times in regards to the number of TiO_2 layers was observed. More characterisations of titania LbL films by TRMC have yet to be investigated in more depth since these investigations are not found in the literature. TRMC characterisation is challenging due to the low amount of TiO_2 contained in LbL films with low numbers of layer pairs. Nevertheless results did not show any similarity with HCOOH degradation photocatalysis tests and has allowed us to rule out an hypothesis regarding the number of photogenerated charge carriers being responsible of the unusual behaviour of the photocatalytic activity of the single layer pair LbL film.

II.2.2 Electronic Paramagnetic Resonance

Electronic paramagnetic resonance (EPR) characterisations were performed at the *Institut de Chimie* (POMAM team, Strasbourg, France). This technique can provide information on radicals photogenerated by PEI/(PSS/TiO_2)$_n$ films by monitoring TEMPOL (4-hydroxy-2,2,6,6-tetrametylpiperidine-1-oxyl) decay signal functions in regards of the UV-A illumination time every 30 seconds [205], [207]. This process is called spin-scavenging. Indeed, being a stable radical, TEMPOL loses its paramagnetic properties by reacting with small weight free radicals such as OH• and H•, generated from water molecules contained in an aqueous TEMPOL solution [216]. Studying the TEMPOL decay kinetics can be related to the amount of radicals generated at the surface of TiO_2 in the film under UV-A.

This investigation was done by following a similar procedure from a previous PhD student from Decher's team, Marek Twardoch, by studying the TEMPOL decay signal placed in capillaries in which titania LbL films were constructed [205], [207]. Twardoch's investigations were made on PEI/(TiO_2/PDDA)$_n$ LbL films, constructed with negatively-charged titania, and used for monitoring TEMPOL spin scavenging. The results showed an increase in TEMPOL spin scavenging rate in regards to the number of TiO_2 layer contained in the LbL films.

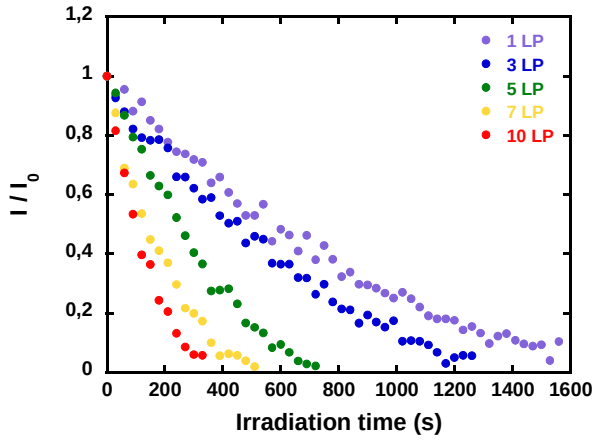

Figure 58: Tempol spin-scavenging by PEI/(PSS/TiO_2)$_n$ films, monitored by EPR.

Results showed that the kinetics of spin scavenging TEMPOL progresses according to the number of layer pairs deposited in capillaries (Figure 58). As such the TEMPOL EPR signal decay gets faster as the number of titania layers deposited in capillaries increases, showing that the amount of generated free radicals by the LbL films is related to the amount of TiO_2 contained in the film. This trend was

similar to Twardoch's with the investigation of TEMPOL EPR signal decay with negatively-charged titania LbL films. This experiment showed a classical behaviour of the PEI/$(PSS/TiO_2)_n$ film.

In addition to this study, HCOOH solution was introduced into the TEMPOL solution to see if the chosen model pollutant molecule may have an effect on the TEMPOL spin scavenging. This study was only performed on a 10 layer pair film.

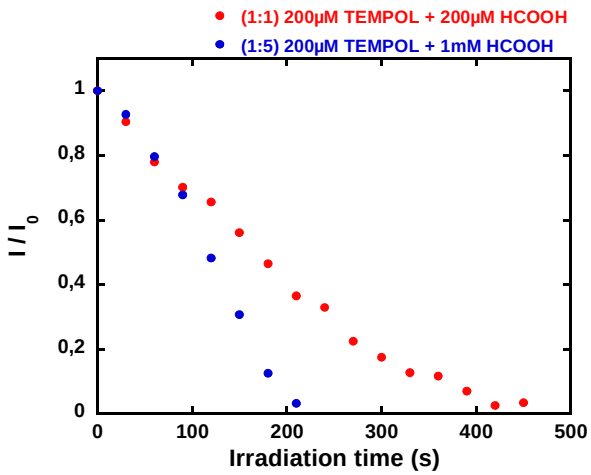

Figure 59 : Evolution of TEMPOL spin-scavenging by a PEI/$(PSS/TiO_2)_{10}$ film, using a mixed solution of TEMPOL:HCOOH.

Solutions with two TEMPOL:HCOOH ratios were investigated, while keeping the same TEMPOL concentration from previous experiment (Figure 59). Thus 1:1 and 1:5 ratio solutions were placed in capillaries containing 10 layer pair LbL films. Mixed solutions with the same concentration ratio showed a similar trend to that of 10 layer pair films for spin scavenging TEMPOL without HCOOH, with similar irradiation time to observe the full disappearance of the TEMPOL EPR signal. Therefore HCOOH does not have an influence on TEMPOL spin scavenging at a 1:1 ratio. However an interesting result, which was never observed in EPR characterisations on TiO_2 and polyelectrolytes LbL film, was obtained using a higher concentration of HCOOH. By increasing HCOOH concentration (1:5 ratio), delay of the EPR TEMPOL signal was expected since competition between TEMPOL spin scavenging and HCOOH degradation may occur. However the decay of the TEMPOL EPR signal was found to be similar to the one with a 1:1 ratio, until 90 s of UV-A irradiation, where a drastic decay of the TEMPOL EPR signal was observed. Moreover, the total disappearance of the TEMPOL EPR signal occurred even faster than for the TEMPOL EPR signal measurement with a TEMPOL solution only. We suggest two hypotheses to explain this result.

- According to the mechanism reported for the degradation of HCOOH, the HCOO• radical is generated from the degradation of HCOOH by LbL films, so that it may also react with TEMPOL, resulting in an accelerated TEMPOL spin scavenging process. Although the reaction of TEMPOL with HCOO• is a possibility, this reaction is not favoured due to the presence of TEMPOL's 4 methyl group (steric hindrance) [216], so that TEMPOL may react with HCOO• only after a critical (high) concentration is reached. So, the TEMPOL EPR signal decay acceleration (due to reaction with both OH• and HCOO• radicals) would be observed after a certain irradiation time.
- The other hypothesis is that HCOOH requires a longer diffusion time to reach the deeper layers in the film. When reacting with the deeper irradiated layer, more HCOO• radicals will be produced, leading to a higher probability to react with TEMPOL.

It is worth noting that these two hypotheses may occur at the same time, and it cannot be overlooked. Overall EPR characterisations of PEI/$(PSS/TiO_2)_n$ LbL films did not show an unusual behaviour of the film regarding the decay of the TEMPOL EPR signal according to the number of layer pairs. But, the addition of HCOOH in the TEMPOL solution highlighted a possible diffusion issue of HCOOH molecules in the films, in order to be degraded upon UV-A irradiation.

II.2.3 Comparison with different types of LbL titania films

While TRMC and EPR characterisations did not show unusual behaviour observed in photocatalytic tests, with maximum photocatalytic effect with single layer pair films (i.e. PEI/PSS/TiO_2), HCOOH has been found to need 90 s of UV-A irradiation to be degraded by titania using EPR TEMPOL spin-scavenging. This could suggest that HCOOH diffusion in LbL film could be hindered by polyelectrolytes used for the LbL film construction. Moreover polyelectrolytes may block TiO_2 photoactive sites, which results in a drop of conversion rate and CO_2 formation. Photocatalytic tests without formic acid showed that polyelectrolytes are slightly degraded by TiO_2 upon UV-A irradiation but did not highlight any hindrances. In order to test this hypothesis, several film architectures using polyelectrolytes layer pairs as spacers between titania layers, were tested by monitoring HCOOH degradation and CO_2 formation.

Polyelectrolytes layer pairs were constructed using negatively-charged PSS (1 g/l at pH 2,5 adjusted by HNO_3) and positively-charged poly(diallyldimethyliammonium chloride) (PDDA, 1 g/l with 0.5M of sodium chloride) by the dipping LbL process, using PEI/$(PSS/TiO_2)_n$ film dipping parameters. 8 polyelectrolytes layer pairs were used as titania layer spacers. $(PSS/PDDA)_8$ layers had an average

thickness of 20 nm (ellipsometry) and will be addressed as a "polyelectrolytes layer". Names and architecture specifications of LbL titania films are described in Table 14.

Sample name	**Architecture specifications**	**Name for a 4 TiO_2 layers film**
$PEI/(PSS/TiO_2)_n$	Reference film TiO_2 as "final layer"	$PEI/(PSS/TiO_2)_4$
$PEI/[PSS/TiO_2/(PSS/PDDA)_8]_n$	$(PSS/PDDA)_8$ deposited after every TiO_2 layers. $(PSS/PDDA)_8$ as "final layer"	$PEI/[PSS/TiO_2/(PSS/PDDA)_8]_4$
$PEI/PSS/TiO_2/[(PSS/PDDA)_8/PSS/TiO_2]_n$	$(PSS/PDDA)_8$ deposited between every TiO_2 layers. TiO_2 as "final layer"	$PEI/[PSS/TiO_2/(PSS/PDDA)_8]_3/PSS/TiO_2$
$PEI/[(PSS/PDDA)_8/PSS/TiO_2]_n$	$(PSS/PDDA)_8$ deposited before every TiO_2 layers. TiO_2 as "final layer"	$PEI/[(PSS/PDDA)_8/PSS/TiO_2]_4$

Table 14: Labels and description of titania and polyelectrolytes LbL films containing layers of $(PSS/PDDA)_8$.

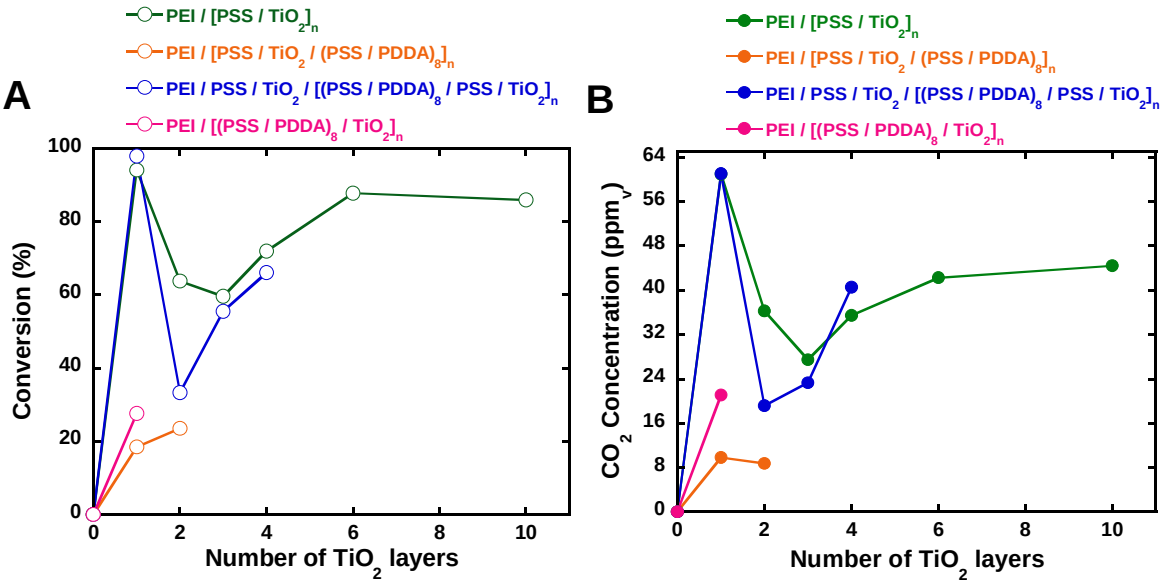

Figure 60 : Degradation of gas-phase HCOOH under UV-A light using LbL titania film with different types of architecture. (A) HCOOH conversion rate in regards of number of TiO_2 layers deposited; (B) CO_2 formation in regards of number of TiO_2 layers deposited Experimental parameters: [HCOOH] = 45 ppm_v, air flow = 20 mL/min, speed = 0.7 cm/s, UV-A irradiance = 2.5 mW/cm², films built on 36 cm² silicon wafers.

These films were tested for degradation of gas-phase HCOOH under UV-A irradiation, and compared to PEI/$(PSS/TiO_2)_n$ films (Figure 60). The photocatalytic activity of PEI/$[PSS/TiO_2/(PSS\ /PDDA)_8]_n$ films showed significant lower results in HCOOH conversion (19%) and CO_2 formation (8 ppm_v). These results suggested that $(PSS/PDDA)_8$ polyelectrolyte layers deposited onto titania layer are hindering HCOOH diffusion in LbL films, therefore decreasing the HCOOH conversion and CO_2 formation. As expected, the first titania layer deposited on PEI/$PSS/TiO_2/[(PSS/PDDA)_8/PSS/TiO_2]_n$ showed a photocatalytic activity result similar to the one of the PEI/PSS/TiO_2 reference films, since polyelectrolytes layers were not constructed on the film. Once $(PSS/PDDA)_8$ and PSS/TiO_2 layers were deposited, HCOOH conversion and CO_2 formation dropped respectively to 33% and 19 ppm_v. However these results were still higher than those of the PEI/$[PSS/TiO_2/(PSS/PDDA)_8]_n$ films. Interestingly when adding a 3rd and a 4th TiO_2 layer in PEI/$PSS/TiO_2/[(PSS/PDDA)_8/PSS/TiO_2]_n$, the results were once again similar to that of PEI/PSS/TiO_2 reference film. This could mean that HCOOH is diffusing at the same rate in both PEI/$PSS/TiO_2/[(PSS/PDDA)_8/PSS/TiO_2]_n$ and PEI/$(PSS/TiO_2)_n$ films, suggesting that depositing PSS/TiO_2 layer pairs on a PEI/PSS/TiO_2 film may already affect the HCOOH degradation kinetics. A PSS/TiO_2 layer pair was then deposited on a PEI/$(PSS/PDDA)_8$ and underwent photocatalysis testing. Since polyelectrolytes were not deposited on top of the TiO_2 layer, it was

expected to have similar photocatalytic results to a PEI/PSS/TiO_2 film. Results still showed a lower HCOOH conversion and CO_2 formation compared to reference films, but higher than PEI/PSS/TiO_2/$(PSS/PDDA)_8$ (with only one layer of TiO_2). This later TiO_2-polyelectrolyte architecture suggested that polyelectrolytes used for film construction may not only act as diffusion barriers for molecules, but also may influence the structure of the film.

II.2.4 Discussion

Generally speaking, the photocatalytic performance of the film can be considered to result from several aspects:

- the amount of TiO_2 in the film, here expressed in $\mu g/cm^2$,
- the absorption of light by TiO_2 within the film, and consequently the creation of the electron and hole photogenerated charges
- the availability of the photogenerated charges at the TiO_2 surface, that results from the charge transfer to the surface, i.e. from the recombination ratio in the TiO_2 crystallites,
- the diffusion of the gaseous reactants within the film, and their subsequent adsorption at the surface of the irradiated TiO_2 crystallites.

The various characterisation methods implemented during the monitoring of the film construction (ellipsometry, chemical analysis, UV-Visible spectrophotometry, QCM) provided evidence of regular construction of the films with increasing number of layer pairs, with a regular increase in the film thickness and in the TiO_2 amount in the film. So, the photocatalytic film is expected to follow a usual behavior when increasing the amount of TiO_2 in the film, with a linear increase until the conversion reach a plateau level, due to a light screening effect for particles from the bottom layers by the ones of the upper layers.

However, this light screening effect was not observed during the UV-Visible spectrophotometry measurements. Linearity in the absorbance increase per layer was observed at least until 12 layer pairs. This linearity could be assigned to the nanometric thickness of the films, and the titania and polyelectrolyte films were not thick enough to suffer from any light screening effect, as is usually observed in TiO_2 films. So, one can expect that the light absorption by the TiO_2 layers is in first approximation similar, whatever the layer considered.

One should also add, that although films were built on silicon wafers, the possible reflection of the incident light on the partially uncovered substrate could not explain the so high photocatalytic activity observed for the single layer film compared to that expected (extrapolated). The number of

HCOOH molecules that can be degraded could at the great maximum be doubled, while there is a factor of about 6 between both activities.

In addition, TRMC measurements confirmed that the number of photogenerated charges increases with increasing number of layer pairs, in agreement with the absence of any light screening until 10 layer pairs. Further, the absence of any significant signal for the single layer pair film evidenced that no unusual behavior was observed on the single layer pair film in terms of amount of charge carriers generated. No significant change in charge carriers' life time in regards to the number of layers could be observed.

By contrast, SEM characterisation (top-view and especially film cross-section view) revealed that the density of the films was dependent on the number of layers. Heterogeneity at the nanometric scale in the substrate coverage was evidenced on the single layer pair film, before full coverage of the substrate was observed. The films remained porous, however we are proposing that the film becomes denser with increasing number of layer pairs. So, we propose that the change of film structure could be the main reason of the unusual behaviour observed for the films with increasing number of layer pairs, on one hand on the single layer pair film achieving high photocatalytic performances, and another hand for understanding the conversion plateau observed for 6-10 layer pairs films, while no light screening was measured.

Hypothesis and understanding of the unusual behaviour of the film.

Works from Kim and Shitakori showed that the use of weak polyelectrolytes leads to thick films with high surface roughness, whereas strong polyelectrolytes such as PSS give rise to dense films [178]. Likewise, the use of different polyelectrolyte conformations, either fuzzy or extended when coated on surfaces for TiO_2-polymer films, leads to a difference in photocatalytic activity of the constructed films [211]. It was observed that TiO_2 LbL films constructed with polyelectrolytes with extended structures, showed lower photocatalytic activity than films constructed with polyelectrolytes with fuzzy structures. The polyelectrolyte extended structure may influence the diffusion of organic molecules in the titania LbL film, therefore limiting the photocatalytic activity of the film upon irradiation. Rongé *et al.* investigated the structural aspect of LbL PSS/TiO_2 films used for liquid and gas phase photocatalysis, as well as for the water splitting reaction [149]. By changing the deposition time of PSS and TiO_2 in 5 layer pair PSS/TiO_2 films, they were able to tune the structure of LbL films, affecting their photocatalytic activity toward liquid methylene blue degradation under UV-A. The films were tested by placing them in the methylene blue solution and the degradation of the molecule was monitored by UV-Visible spectrometry in transmission.

While keeping a PSS/TiO_2 deposition time ratio, they were able to construct denser film by increasing deposition time. A lower PSS/TiO_2 deposition time ratio gave film with less catalyst deposited, with film growth described as "island growth" leading to a hierarchical film structure containing pores and mesopores. By adding layers, the film structure has the opportunity to be self-organised and be more compact. Therefore new material (i.e. TiO_2 and/or PSS) is deposited in the interior of the films, reducing films' porosity [217]. Degradation of methylene blue was evaluated with 5 layer pairs film using different PSS/TiO_2 deposition ratios (Figure 61).

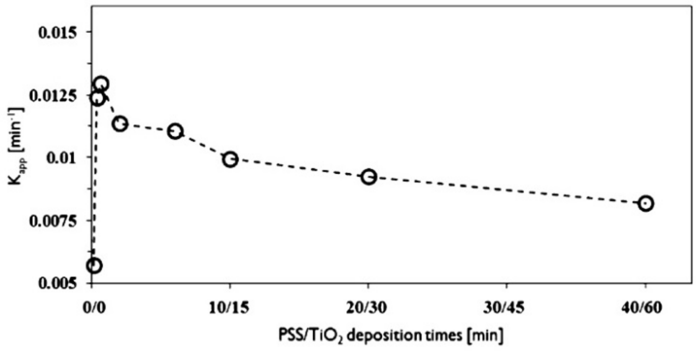

Figure 61: Methylene blue oxidation activity for LbL films with 5 layer pairs, prepared using different deposition times [149].

The optimum photocatalytic reaction was obtained for a 0.67/1 min deposition time for PSS/TiO_2 respectively. Increasing or decreasing the deposition time, in regards to 0.67/1 min deposition time ratio, both lead to a drop in LbL films photocatalytic activity suggesting that film density may affect photocatalytic performances. Changes in PSS and TiO_2 in LbL film content and structure was varied by changing the deposition time of one component, while keeping the deposition time constant for the other. They found that adding more titania leads to a drop of photocatalytic activity due to a higher film density (Figure 62). Further titania content in LbL films lead to even denser film and less permeable to methylene blue. Increase of photocatalytic activity was still observed but was associated to the activity of the outermost layers. This type of photocatalytic behaviour in Rongé's work is similar to HCOOH conversion and CO_2 formation results obtained in this PhD project. One can suggest that when a second PSS/TiO_2 layer is deposited, the film is self-organising and becomes more compact, making it less permeable to HCOOH molecules. While density increases by adding PSS/TiO_2 layer pairs, HCOOH degradation is still possible due to the activity of films outermost layers (as shown in Figure 52B), but the activity becomes limited by the diffusion of the reactants in the interval layer (diffusion regime), while the outermost layers could continue to operate in a kinetic regime. Depending on the terminology used, the permeable aspect can be related to the diffusion ability of

the reactant molecules in the film. Further specific photocatalytic experiments to be realised on films could evidence the establishment of the diffusionnal/kinetic regimes taking place within the TiO_2 and polyelectrolyte LbL films.

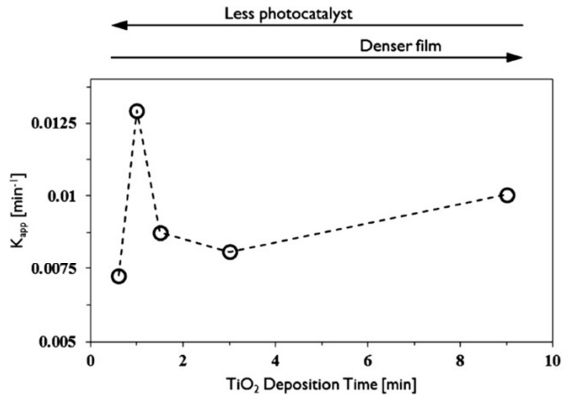

Figure 62: Methylene blue oxidation activity for LbL films with 5 layer pairs, prepared using different TiO_2 deposition times [149].

Rongé also investigated the deposition of PSS while keeping TiO_2 deposition constant (Figure 63). They stated that the role of PSS in this type of construction was a structure directing agent. When increasing deposition time, PSS may have the possibility to self-organise (i.e from fuzzy structure to an extended structure) and block the active sites of TiO_2. This hypothesis could be related to the drop in photocatalytic activity of PEI/[PSS/TiO_2/$(PSS/PDDA)_8$]$_n$ films where polyelectrolytes may self-organise to an extended structure, that lead to hindrance of TiO_2 active sites, as well as making films less permeable to HCOOH. When comparing Rongé's results with the photocatalytic tests performed on films containing several layers of poylelectrolyte, the $(PSS/PDDA)_8$ layer pairs in PEI/PSS/TiO_2/[$(PSS/PDDA)_8$/PSS/TiO_2]$_n$ and PEI/[$(PSS/PDDA)_8$/PSS/TiO_2]$_n$ film may not only influence film permeability but also the film structure. High polyelectrolyte content in these LbL films may not provide the same film density as the PEI/PSS/TiO_2 film, and polyelectrolytes may self-arrange to an extended structure and block TiO_2 active sites.

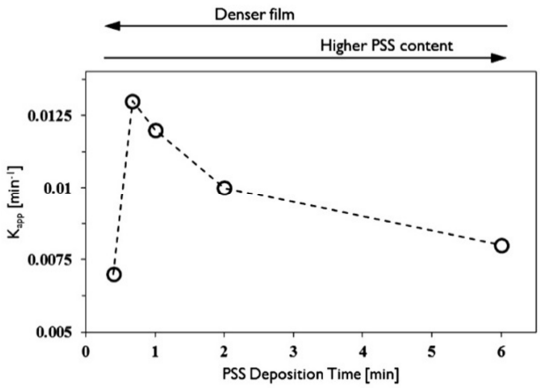

Figure 63 : Methylene blue oxidation activity for LbL films with 5 layer pairs, prepared using different PSS deposition times [149].

It has to be noted that Rongé investigated also the degradation of gas-phase ammonia (NH_3) by LbL films with different PSS/TiO_2 deposition time ratios. Denser films had the best activity and suggested that the molecule size will influence the film selectivity. So, films with lower density could provide better HCOOH conversion rates, for instance by changing the dipping time for PSS. Kniprath *et al*. observed an increase in adsorption of Rhodamine in PSS/TiO_2 films and attributed this to specific adsorption to PSS whereas Ma *et al*. found a proportional increase in photocatalytic activity with number of layer pairs for LbL films composed of TiO_2 and clays instead of polymer [218], [219]. By looking at Kim et al. investigations, one can assume that using weak polyelectrolytes for constructing titania LbL films may provide a structure not as dense as the one of the PEI/$(PSS/TiO_2)_n$ LbL film, and therefore providing better photocatalytic performances of titania LbL films towards the degradation of molecule [178]. The possibility of having an expected or unusual conversion rate in regards to the number of titania and weak polyelectrolyte layers has yet to be investigated. Nevertheless the photocatalytic degradation of gas phase HCOOH has shown that LbL films containing low amounts of titania (7 µg/cm²) are photocatalytically active under UV-A irradiation.

III – Antibacterial activity of LbL titania thin films on model surfaces

The antibacterial activity of titania and polyelectrolytes LbL films were evaluated under UV-A irradiation. Like the gas-phase photocatalytic tests, the biocidal properties of TiO_2 LbL films have to be investigated first on model surfaces before the films are constructed on textiles.

Bacteria assay were performed at the *Institut des Sciences des Matériaux de Mulhouse* (IS2M, Mulhouse, France) using an experimental procedure developed by Yige Yan during his PhD at ICPEES, in collaboration with Lydie Ploux (IS2M) [220]. Biocidal properties were evaluated on 4 cm^2 silicon wafer substrates with different types of LbL films constructed onto them:

- Reference samples with LbL films made of several polyelectrolyte layers,
- Titania LbL samples to evaluate the biocidal properties of films in regards to the number of PSS/TiO_2 layer pairs deposited

Escherichia Coli bacteria were used for evaluating the biocidal performance of TiO_2 LbL films under UV-A irradiation.

III.1. Film preparation

Bacteria assays require a strict procedure in which contamination from other bacteria, prior to the assay, may interfere with results. It is important to keep samples as clean as possible, as well as being sterile before proceeding to seed bacteria onto them. Therefore LbL film constructions needed some adjustments in the construction procedure in order to keep the samples as clean as possible.

Reference and titania LbL films were constructed using automated robot dipping apparatus with same dipping parameters as the films constructed for gas phase photocatalysis tests. Construction was stopped before deposition of the films' final layer. The last layer was then deposited in the IS2M lab a day before bacteria seeding. Films were then washed in 3 successive sterilised milli-Q water baths in a biosafety cabinet for 30 minutes in total. While films were not sterilised under UV-C due to possible degradation of the polyelectrolytes upon TiO_2 activation or direct degradation of polyelectrolytes, bacterial contamination was prevented with milli-Q baths. In order to evaluate titania LbL films stability for bacterial assay, films were immerged in NaCl solution (9 g/l) for 15 h. Ellipsometry results for LbL films are shown in Table 15.

Samples	Estimated thickness (nm) T = 0 h	Estimated thickness (nm) T = 15 h
$PEI/(PSS/TiO_2)_1$	37.6 ± 2.8	47.3 ± 3.9
$PEI/(PSS/TiO_2)_4$	140.8 ± 6.2	154.6 ± 6.3
$PEI/(PSS/TiO_2)_6$	222.9 ± 8.3	246.3 ± 4.7
$PEI/(PSS/TiO_2)_{10}$	371.6 ± 9.0	380.6 ± 7.8

Table 15: Evolution of LbL films' thicknesses after being immerged in 9 g/l NaCl solution.

Ellipsometry did not show any decrease in film thickness after being immerged for 15 h in 9 g/l NaCl solution. However an increase in thickness (10 – 20 nm) was observed and was related to swelling of the LbL films [18]. Therefore the film should remain stable when bacteria assays are performed on them.

The number of active bacteria ("ALIVE") before and after UV-A irradiation on reference and LbL samples was assessed, whilst damaged bacteria ("DEAD") were counted after UV-A irradiation.

III.2. Control sample results

Bacterial assays were performed on control samples in order to remove any possibility of biocidal properties from the sample surface and polyelectrolyte. Reference samples were labelled as follow:

- REF 1: PEI
- REF 2: PEI/PSS
- REF 3: PEI/PSS/PDDA
- REF 4: PEI/PSS/PDDA/PSS
- WF: silicon wafer

Reference samples REF 1, REF 2, REF 3 and REF 4 did not show any biocidal properties upon 60 min UV-A irradiation (Figure 64). In fact an increase in bacteria number can be observed, whilst low numbers of damaged bacteria were counted after irradiation. This effect is only possible if the UV-A lamp irradiation level is not powerful enough to allow bacteria killing. While using a 2 mW/cm² UV-A

lamp, this effect was also observed by Yige Yan where different irradiation times were used in his work [220]. Yan also found that 3 h of UV-A irradiation resulted in limited bactericidal effect using this lamp. One could note that poly(ethyleneimine) is also known for its antibacterial properties, therefore biocidal activity could have been observed for PEI –containing control samples. Carré et al. investigated the effect of PEI in titania LbL films constructed on polyester textiles, where both PEI and PEI/TiO_2 films displayed biocidal properties in the dark and under UV-A [40]. This biocidal effect was not observed in this project on PEI films built on silicon wafer. This could be explained by the different conditions used in our work for the LbL constructions, for instance we used a 1 g/L PEI concentration solution, while a 8 g/L PEI concentration was used in Carré *et al.* work. Moreover textile surface coverage allows more material to be coated on the fibres. The mass of the PEI deposited on fibres was not estimated, but should be lower than PEI deposited on silicon wafer in this project, which is estimated to be 119 ng/cm² by QCM-D (calculated on 3rd overtone).

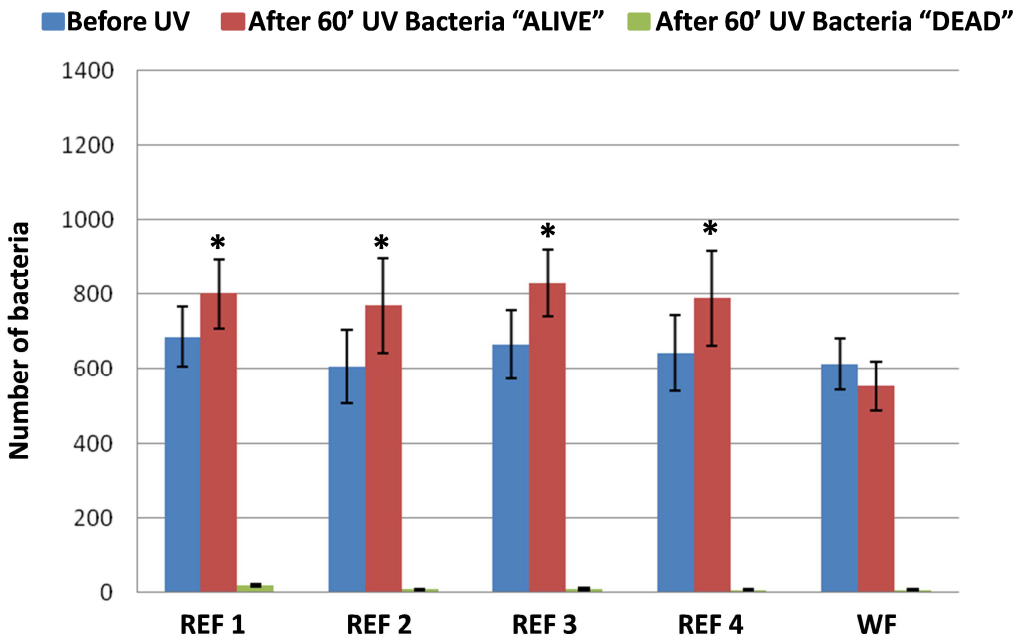

Figure 64: Bacteria assay on reference samples. Tested bacteria: *Echerichia Coli*, UV-A irradiance = 2.5 mW/cm², irradiation time = 60 min, films built on 2 cm² silicon wafers. (*) significantly different than WF (ALIVE) (*p*-value < 0.05)

The bacterial assay on the WF sample (bare silicon wafer) showed different biocidal behaviour in regards to the other reference samples. While the bacteria number is similar compared to other reference samples prior to UV-A irradiation, the bacteria number decreases after irradiation,

suggesting bacteria proliferation inhibition upon 60 min UV-A irradiation. This difference in behaviour could be attributed to the type of sample surface: UV-A exposition of bacteria on silicon wafer is more important than the one of polyelectrolytes LbL films. Therefore polyelectrolytes LbL film structures could provide more suitable bacteria adhesion than bare silicon wafer.

III.3. Titania thin film samples results

The nfluence of the number of PSS/TiO_2 layer pairs constructed on silicon wafers regarding LbL film biocidal properties was evaluated. In this investigation, another reference sample made of 10 polyelectrolytes layer pairs was constructed. Samples were labelled as follow:

- REF 5: PEI/PSS/$(PDDA/PSS)_9$
- 0 LP: PEI/PSS ; same film as REF 2
- 1 LP: PEI/PSS/TiO_2
- 3 LP: PEI/$(PSS/TiO_2)_3$
- 6 LP: PEI/$(PSS/TiO_2)_6$
- 10 LP: PEI/$(PSS/TiO_2)_{10}$

Since REF 5 and 0 LP samples are only made of polyelectrolytes film, the results should not show any biocidal properties, according to the previous investigations on the reference samples. Bacterial assays on these two samples were found to be echoing those of polyelectrolytes reference (Figure 65).

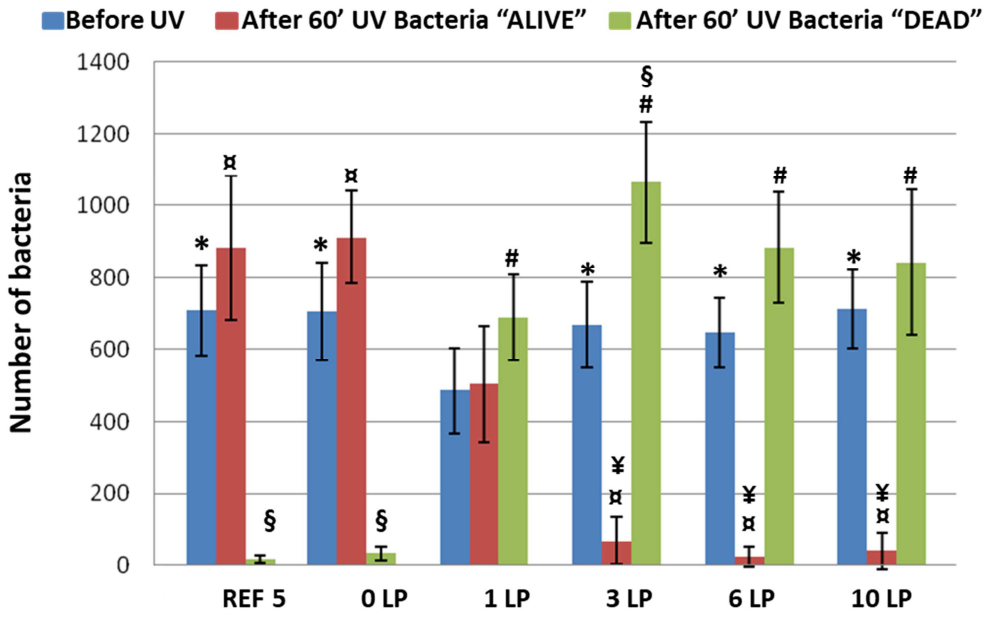

Figure 65: Bacteria assay on PEI/$(PSS/TiO_2)_n$ films, with REF 5 and 0LP used as control samples. Tested bacteria: *Echerichia Coli*, UV-A irradiance = 2.5 mW/cm², irradiation time = 60 min, films built on 2 cm² silicon wafers. (*) significantly different than 1 LP before UV (*p*-value < 0.05); (¤) significantly different than 1 LP after UV (ALIVE) (*p*-value < 0.05); (¥) significantly different than 0 LP, 1 LP and REF 5 after UV (ALIVE) (*p*-value < 0.05); (#) significantly different than 0 LP after UV (DEAD) (*p*-value < 0.05); (§) significantly different than 1 LP after UV (DEAD) (*p*-value < 0.05).

Titania LbL samples sample showed biocidal properties upon UV-A irradiation (60 min) from 1 LP to 10 LP. While the number of active bacteria ("ALIVE") decreased after irradiation, the number of damaged bacteria ("DEAD") increased significantly for 3, 6 and 10 LP samples. Almost all the bacteria observed on these samples were damaged after UV-A irradiation, showing maximum biocidal properties obtained for 3 layer pairs films. A single titania layer film showed an intermediate biocidal behaviour between the reference films and films with 3 and more PSS/TiO_2 layer pairs. In fact half of the bacteria observed on the 1 LP sample were found to be active whilst the other half was damaged. Since the reference samples used did not lead to bacteria death, biocidal properties of titania and polyelectrolytes films used in this work are only induced by titania nanoparticles once irradiated by UV-A light.

III.4. Comparison with gas-phase photocatalysis results

The biocidal properties of titania and polyelectrolyte films were evaluated on films that were tested for degradation of gas-phase formic acid under UV-A irradiation. These films were constructed using the same experimental procedure, with a slight variation for the bacterial assay, where the final layer (TiO_2) was deposited a day before bacteria seeding on film. This construction variation was made in order to make the film as clean as possible before the bacteria assay. The structure of the films is considered to be identical therefore making comparison of the two photocatalysis tests (i.e. gas-phase photocatalysis and evaluation of antibacterial properties) relevant.

The bacteria assay on TiO_2 LbL films upon UV-A irradiation for 60 minutes showed biocidal activity for single layer pair films with half of the bacteria remaining active, whilst the other half being damaged. Although bacteria assays were not performed on two layer pair films, almost all bacteria counted on 3 and more layer pairs samples were damaged. Therefore the maximum biocidal properties of PSS/TiO_2 films are observed for films containing at least 3 layer pairs, representing a minimum of 21 µg/cm² of titania deposited. In LbL biocidal property investigations, photocatalytic behaviour followed a classical activity of titania film where activity increases in regards to amount of photocatalyst deposited on substrate. However, this classical behaviour is not related to a light screening phenomenon, but is proposed to result from the micrometric size of *E. Coli*. Since *E. Coli* bacteria have micrometric size, diffusion into nanometric size film features does not occur, and the biocidal activity of the films directly results from the photocatalytic activity of the top-layer of the LbL films. The slight heterogeneity of the substrate coverage by TiO_2 for the single layer pair LbL film probably explained the slightly lower biocidal properties observed, with a lower TiO_2/bacteria contact. Since three layer pairs, the homogeneity of the film led to an enhanced contact between the TiO_2 surface and the bacteria external membrane, and a higher biocidal performance is achieved.

So one could suggest that the amount of titania, as well as film's structure, are parameters that governs antibacterial activity evaluation of titania and polyelectrolyte LbL films.

Chapter III: Titania and polyelectrolyte thin films construction on model surfaces – Conclusion

Layer-by-layer films containing titania nanoparticles and polyelectrolytes were successfully constructed on model surfaces. The film construction was monitored as a function of the number of layer pairs and the characterisations allowed us to give an estimation of film thickness (ellipsometry), morphology of film surface (SEM), and the amount of titania deposited (UV-Visible spectrophotometry, QCM-D and ICP-AES). They evidenced the building of an homogeneous and porous nanoparticles film, with an average thickness of 40 nm and a TiO_2 density of 7 µg/cm² per layer pair.

Photocatalytic degradation of gas phase formic acid, in a single-pass test mode, was used to evaluate the photocatalytic performances of titania and polyelectrolytes LbL films under UV-A irradiation. In this work, the influence of the number of PSS/TiO_2 layer pairs was investigated. Photocatalytic tests showed that films were able to degrade gas phase HCOOH with mineralisation into CO_2 with an unusual behaviour/trend in regards to the amount of TiO_2 deposited observed: a maximum photocatalytic activity was observed for a single layer pair film, which contains a very low amount of titania (7 µg/cm²), although films with a higher number of layer pairs did not suffer from any light screening effect due to the nanometric thickness of films. This unusual effect was explained by suggesting that films get denser by adding titania layers while remaining porous. This may result in a decrease in diffusion of HCOOH molecules and therefore a drop in photocatalytic activity. A second hypothesis is based on TiO_2 photocatalytic site hindrance by PSS. PSS deposition time may allow polyelectrolyte structure re-arrangement from fuzzy to extended conformation in/on LbL films. This may lead to TiO_2 photocatalyst sites being blocked by PSS, dropping photocatalytic activity. Moreover films may become less permeable to HCOOH by adding more polyelectrolyte layers as shown in films containing $(PSS/PDDA)_8$ layers, with consequence in terms of HCOOH diffusion within the films. A change of polyelectrolytes type or in PSS deposition time may lead to better photocatalytic activity of titania LbL films towards the degradation of gas-phase HCOOH.

Bacterial assays were performed on titania/polyelectrolytes LbL film under UV-A light. Biocidal activity towards *E. Coli* bacteria was evaluated in regards to the number of PSS/TiO_2 layer pair deposited. In these investigations, normal behaviour of photocatalytic activity in regards to the amount of titania deposited in films was observed, with biocidal effect for a film containing a single PSS/TiO_2 layer pair, and maximum biocidal effect observed from 3 layer pair films (i.e. 21 µg/cm² of titania). This was proposed to result from the micrometric size of the bacteria compared to the film structure.

Both photocatalytic degradation of gas-phase HCOOH and the antibacterial assays showed that PEI/(PSS/TiO_2)$_n$ LbL films were photocatalytically active for a single layer pair film. The single layer pair film was therefore selected for further elaboration of silver-titania hybrid films in Chapter 4.

Chapter 4: Titania and silver nanoparticles hybrid thin films – construction on model surfaces

Introduction

This chapter is focused on the elaboration, characterisations and photocatalytic performance evaluation of single layer pair PEI/PSS/TiO_2 LbL films containing silver nanoparticles, built on model surfaces (i.e. silicon wafers, glass and quartz slides according to the characterisation technique). These investigations were only made on LbL films with a single layer of TiO_2, due to the better photocatalytic performance of the film towards the degradation of gas phase HCOOH, compared to TiO_2 LbL films with several layer pairs. Three different approaches for depositing or synthesising AgNP in the single layer film will be described and their photocatalytic activity toward the degradation of gas phase formic acid, HCOOH, will be investigated. The evaluation of the biocidal properties of the films will be tested by using the films that provided the best photocatalytic activity for the degradation of HCOOH.

The first part will be dedicated to the deposition of commercial AgNP on a PEI/PSS/TiO_2 film, followed by the synthesis of AgNP using 2 methods based on a photoinduced approach. The third part will be dedicated to the evaluation of the biocidal properties of Ag-TiO_2 films.

I – Titania films containing commercial Ag nanoparticles

I.1 Blade-assisted LbL deposition of Ag nanoparticles

Commercial AgNP were used in this work to build Ag-Ti films by keeping LbL self-assembly parameters. Two challenges arose in these investigations. The first one was to get AgNP suspensions with charged surfaces in order to be coated on a pre-built PEI/PSS/TiO_2 LbL film. Our investigations were therefore focussed on AgNP suspensions stabilised with citrate (Figure 66).

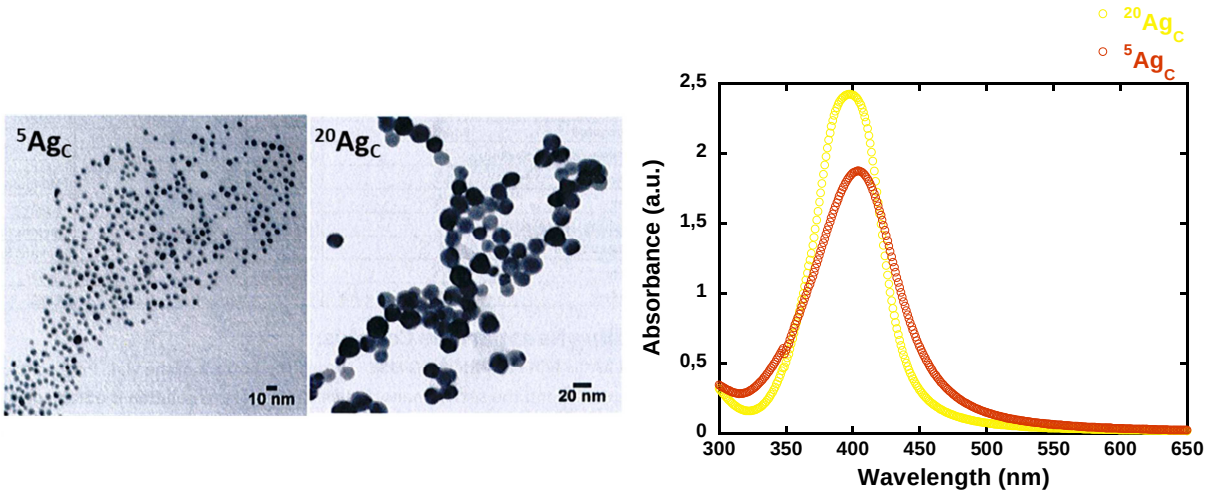

Figure 66: Characterisations of AgNP suspensions with TEM images taken from NanoXact (left), and UV-Visible spectroscopy in transmission (right).

Citrate provided negative charges at the surface of AgNP, allowing them to be deposited onto a positively-charged surface PEI/PSS/TiO_2 LbL film. Spherical AgNP suspensions (0.02 mg/ml) stabilised by citrate and with two different mean sizes (20 and 5 nm, named $^{20}Ag_C$ and $^{5}Ag_C$ respectively) were purchased from NanoXact (Czech Republic). The second challenge was related to the AgNP suspension volume availability. Usually the LbL films were built on 36 cm² silicon wafers and dipped automatically in 300 ml beakers containing the polyelectrolyte solutions or titania suspension. Volumes of 50 ml for both AgNP suspensions were therefore not convenient for dipping the usual size substrates. Moreover the substrate may contaminate AgNP suspensions when being dipped into them, eventually affecting the suspensions' stability. Therefore a blade-assisted LbL approach was developed in this work, which allowed us to get a homogeneous deposition of AgNP, with a controlled speed and pressure on the titania films, with sufficient suspension volume for covering the entire substrate surfaces.

This approach is based on the *Doctor Blade* technique that allows controlled coating of materials onto flat surfaces, using low amount of materials. This technique was already used successfully in materials science research, for making polymers or nanoparticles films [194], [221], [222]. In this project we first used a *Doctor Blade* device available from Brinkmann's team (SYCOMMOR, *Institut Charles Sadron*, Strasbourg) before using our own device and PTFE blades (Figure 67). The *Doctor Blade* device used at the beginning of the investigation required the 36 cm² silicon wafers to be cut in two parts (two times 2.25 x 8 cm, 18 cm²) due to the width of the PTFE blade (2 cm). By placing the blade 2 µm above the edge of the sample surface (18 cm²), it was found that placing 40 µL of AgNP suspension at the edges and the middle of the substrate surface (120 µL in total), with two translation motions, was sufficient to cover the entire surface of the wafer while preventing the suspension to entirely evaporate during the 20 min stabilisation. The complete blade-assisted LbL AgNP deposition method is described in Chapter 2.3.1.4.

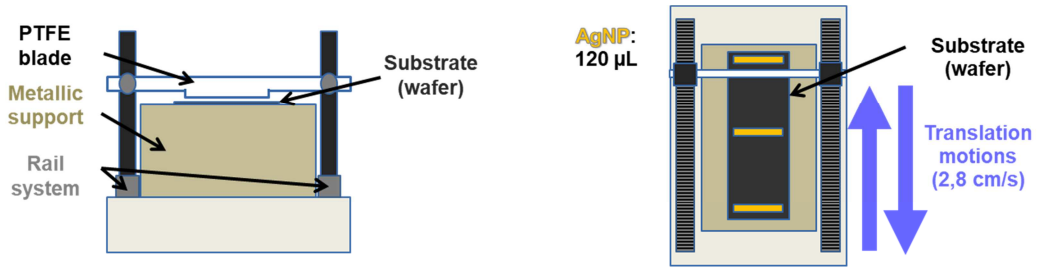

Figure 67: Schematic of the Doctor Blade device (not to scale). (Left) side view of the device, with a substrate placed on the metallic support and below the PTFE blade. (Right) top view of the device with 120 µl of AgNP suspension (yellow lines, 3x40µL) placed onto the substrate.

I.2 Characterisations and activity of titania and AgNP blade-assisted hybrid film

I.2.1 Characterisations

PEI/PSS/TiO_2/Ag_C films were characterised by ellipsometry, UV-Visible spectroscopy in transmission, Quartz-Cristal Microbalance and Scanning Electron Microscopy. Every characterisation technique did not provide proof of AgNP deposited onto PEI/PSS/TiO_2 films. However every characterisation showed that films were still stable after blade-assisted deposition of AgNP and no de-construction of the films was observed, with no change in thickness (Figure 68).

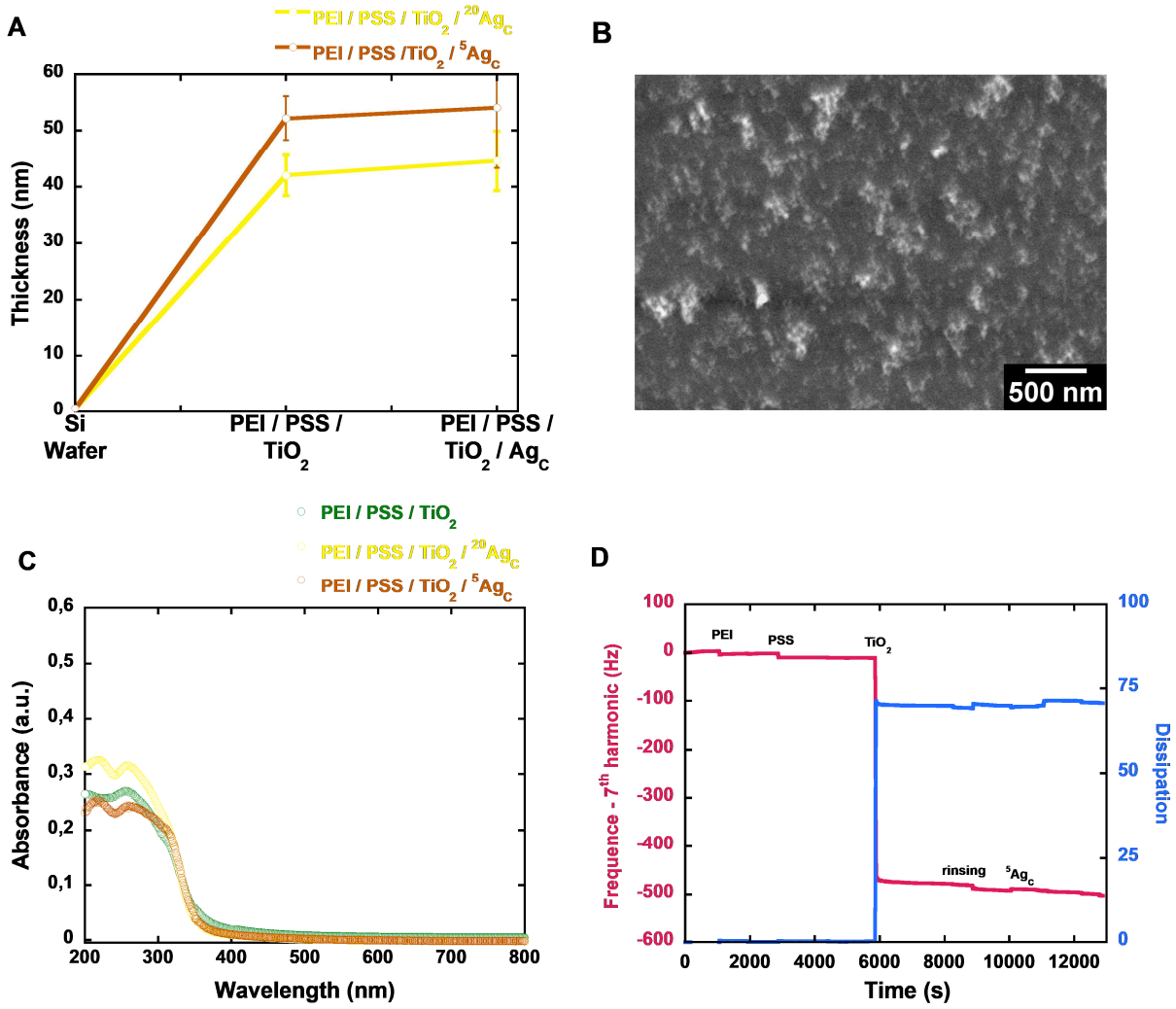

Figure 68 : Characterisation of PEI/PSS/TiO_2/Ag_C films. (A) ellipsometry performed on films constructed on silicon wafer, (B) SEM image of a PEI/PSS/TiO_2/$^{20}Ag_C$ film, (C) UV-Visible spectrophotometry of films constructed on quartz slides, and (D) QCM-D analysis of a PEI/PSS/TiO_2/$^{5}Ag_C$ film on QCM crystal slide.

A volume deposition of 120 µl of AgNP suspension on a PEI/PSS/TiO_2 film corresponds to a 2 wt.% amount of AgNP in regards to the TiO_2 content in the film (7 µg/cm²) for a silver deposition yield of 100%. However, a small volume of AgNP suspension may stay on the PTFE blade used for spreading the suspension on the film, and the rinsing step of the film in milli-Q water may remove AgNP which were not bound to the titania surface. Chemical analysis by ICP-AES showed that silver was present within the films and the amount of silver, in regards to the amount of titania deposited was reported to be 0.45 wt.% (0.34 at.%) and 0.15 wt.% (0.12 at.%) for films with $^{5}Ag_C$ and $^{20}Ag_C$ respectively. The higher silver content for $^{5}Ag_C$ could be explained by the fact that AgNP could better diffuse through the porosity of PEI/PSS/TiO_2 films due to the small size distribution compared to $^{20}Ag_C$. Also more

negative charges are found per unit mass of AgNP with smaller size particles, so that a stronger interaction could occur with TiO_2, leading to a higher number of AgNP interacting with TiO_2 in the film.

I.2.2 Activity of hybrid films

Since the AgNP blade-assisted LbL depositions were made on 18 cm² samples cut from a PEI/PSS/TiO_2 film built on 36 cm² wafer, the two 18 cm² parts on which the same type of Ag_C nanoparticles were coated onto them were reassembled and placed in the cavity of the reactor. Photocatalytic performances of the PEI/PSS/TiO_2/Ag_C films were evaluated using the degradation of gas phase formic acid in a single pass mode. Since highest conversion was obtained for single PSS/TiO_2 layer pair films with an input formic acid concentration of 45 ppm_v, the input concentration was increased in order to decrease the conversion obtained on the films, while keeping the same air flow set during the previous tests (i.e. 20 ml/min). Therefore the input concentration of formic acid was set at 145 ppm_v, and a drop from 94 to 13% in HCOOH conversion, and from 60 to 31 ppm_v in CO_2 formation was observed for the Ag-free PEI/PSS/TiO_2 reference film. The photocatalytic tests were performed 3 times on each film constructed on silicon wafers, allowing the calculation of the error bars. The results are showed in Table 16 and Figure 69.

Sample	**Ag content (wt.%/TiO_2)**	**HCOOH conversion (%)**	**CO_2 formed (ppm_v)**	**Theoretical CO_2 formed (ppm_v)**
PEI/PSS/TiO_2	0	13 ± 1	28 ± 1	17 ± 1
PEI/PSS/TiO_2/^5Ag_C	0.45	23 ± 1	45 ± 2	33 ± 2
PEI/PSS/TiO_2/$^{20}Ag_C$	0.15	27 ± 1	43 ± 2	38 ± 2

Table 16 : Photocatalytic results obtained on PEI/PSS/TiO_2/Ag_c films. Experimental parameters reported in caption of Figure 69.

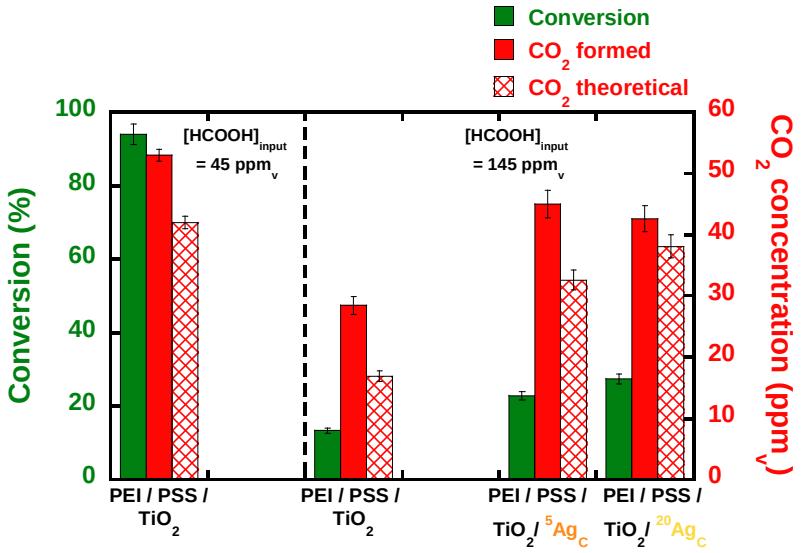

Figure 69: Photocatalytic activity of PEI/PSS/TiO_2 and PEI/PSS/TiO_2/Ag_C films expressed in terms of HCOOH conversion and CO_2 formation. Experimental parameters: [HCOOH] = 145 ppm_v, relative humidity = 50%, air flow = 20 mL/min, speed = 0.7 cm/s, UV-A irradiance = 2.5 mW/cm², films built on 36 cm² silicon wafers.

The photocatalytic conversion achieved on the two types of PEI/PSS/TiO_2/Ag_C films was found to be higher than that obtained with the silver-free reference film. Formic acid conversion rate was found to be 23% and 27% for PEI/PSS/TiO_2/$^{5}Ag_C$ (0.45 wt% AgNP) and PEI/PSS/TiO_2/$^{20}Ag_C$ (0.15 wt% AgNP) films respectively. In terms of CO_2 concentration, the concentrations formed were found to be relatively equal, however the difference between the theoretical amount of CO_2 formed and the actual CO_2 formed for PEI/PSS/TiO_2/$^{5}Ag_C$ was found to be higher than the one for the PEI/PSS/TiO_2/$^{20}Ag_C$ films. This result was associated with the higher AgNP content within the film therefore leading to higher citrate content. Also the 5 nm size AgNP sample contains a higher amount of citrate per unit weight of silver, when compared to the 20 nm size counterpart. Upon UV-A irradiation citrate could also be degraded thus leading to a higher concentration of CO_2 formed than the expected concentration. A control test with an air flow that did not contain formic acid could have highlighted this CO_2 formation due to the degradation of both citrate and polyelectrolytes.

II – Titania films containing photoinduced Ag nanoparticles

The synthesis of silver nanoparticles is based on a photoinduced approach that has been developed by the group of Lavinia Balan at the *Institut de Sciences des Matériaux de Mulhouse* (IS2M, Mulhouse, France) [19], [100], [101]. This synthesis is based on the use of a photosensitive solution composed of a silver precursor and a chromophore in a solvent, usually water, deposited on a surface (originally glass slides) and irradiated by UV-A. This reaction has allowed AgNP to be synthesised with controlled size and shape according to the type of solvent used and the irradiation time. Moreover this synthesis was successfully performes on different substrates such as glass slides, low density polyethylene film and polyvinyl chloride, making this type of synthesis convenient for coating AgNP on textile fibres. Originally the AgNP photosensitive solution was composed of water, referred to as a solvent, in which 0,5 wt.% of both chromophore and silver precursor $AgNO_3$ were dissolved.

In this work, the original synthesis was performed onto PEI/PSS/TiO_2 films and will be addressed as the “classical approach”. The classical approach was adapted afterwards in order to elaborate a one-pot photoinduced synthesis which combined the synthesis of AgNP and the LbL deposition of a hybrid layer of silver and titanium dioxide nanoparticles, using a silver-titania suspension as the photosensitive suspension (next section II.3). The detailed experimental procedures of the preparation of the photosensitive solutions and AgNP synthesis for both approaches are described in chapter 2.II.3 and chapter 2.III.3.

While 36 cm² samples (4.5 x 8 cm) were required for the photocatalytic tests, the UV lamp used for the AgNP photoinduced synthesis could only provide irradiation of a 16.24 cm² sample of a regular hexagonal shape (with a side of 2.5 cm). Therefore PEI/PSS/TiO_2 (classical approach) and PEI/PSS (one-pot synthesis) films were first built on 36 cm² silicon wafers, which were then cut into 3 parts (12 cm², 4.5 x 2.6 cm) in order to be fully irradiated by UV light during AgNP synthesis. After synthesis, the 3 parts were then reassembled and placed in the designed cavity of the reactor for the photocatalytic tests.

II.1 Stability of PEI/PSS/TiO_2 films submitted to AgNP photoinduced synthesis protocol

One can note that the AgNP photoinduced synthesis required irradiation by UV light, therefore TiO_2 nanoparticles deposited in PEI/PSS/TiO_2 films will be activated upon this irradiation for both synthesis approaches. Therefore a study of the stability of the films upon UV irradiation from the

lamp used for the AgNP photoinduced synthesis has been performed. The stability of the films was evaluated by testing the photocatalytic activity of the films after being irradiated by the UV lamp used for AgNP synthesis according to the parameters described in chapter 2.III.2. The photocatalytic tests were made by monitoring the degradation of gas phase HCOOH and the formation of CO_2 upon UV-A irradiation of PEI/PSS/TiO_2 films after being submitted to different UV treatments. The UV treatments applied to the films and the photocatalytic test results are shown in Table 17 and Figure 70. The results showed that the UV irradiation of the PEI/PSS/TiO_2 film does not affect the photocatalytic performances of the single layer pair film, whatever the conditions of the UV treatment. Likewise the addition of water and a glass slide on the top of the film prior to the irradiation (related to the classical approach), or the irradiation of the film after depositing the titania layer (related to one-pot photoinduced synthesis) showed a similar activity to a non-irradiated PEI/PSS/TiO_2 film.

	AgNP synthesis approach relationship	**Conversion rate (%)**	**CO_2 formed (ppm_v)**	**Theoretical CO_2 amount (ppm_v)**
1 LP film without UV irradiation treatment	None	13 ± 1	28 ± 1	17 ± 1
1 LP film after UV irradiation treatment	None	12 ± 1	27 ± 1	17 ± 1
10 µl of water is deposited on 1 LP film. The sample is covered by a glass slide and is irradiated under UV light	Classical approach	13 ± 1	25 ± 1	20 ± 1
Deposition of the titania layer on PEI/PSS film. The sample is then covered by a glass slide and irradiated by UV	One-pot photoinduced synthesis	16 ± 1	31 ± 2	25 ± 1

Table 17: Stability of PEI/PSS/TiO_2 films after UV irradiation from the lamp used in the AgNP photoinduced synthesis. Experimental parameters: [HCOOH] = 145 ppm_v, air flow = 20 mL/min, speed = 0.7 cm/s, UV-A irradiance = 2.5 mW/cm², films built on 36 cm² silicon wafers.

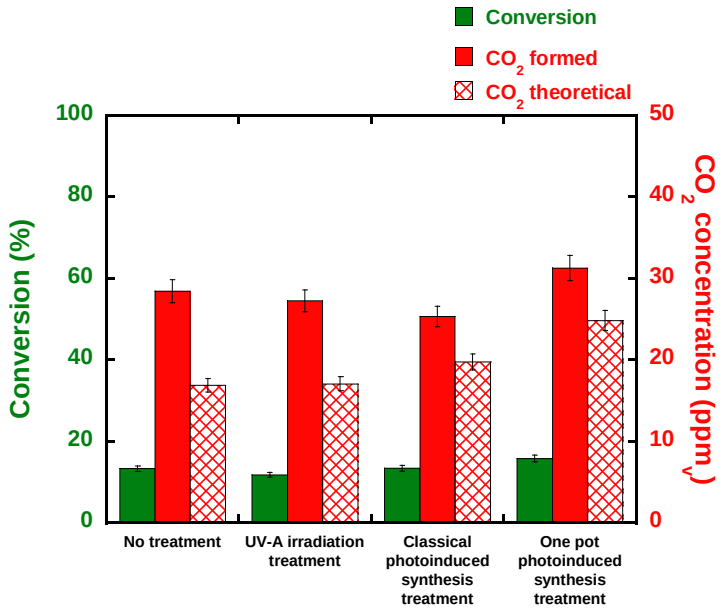

Figure 70 : Comparison of photocatalytic performances of PEI/PSS/TiO_2 films in terms of HCOOH conversion and CO_2 formation, after irradiation by the UV lamp used for AgNP photoinduced synthesis. Experimental parameters: [HCOOH] = 145 ppm_v, air flow = 20 mL/min, speed = 0.7 cm/s, UV-A irradiance = 2.5 mW/cm², films built on 36 cm² silicon wafers.

II.2 Classical Ag nanoparticles photoinduced synthesis on single layer pair films

While LbL deposition of AgNP has allowed the deposition of AgNP on PEI/PSS/TiO_2 films, the classical photoinduced synthesis allowed AgNP to be directly synthesised onto the film. Moreover the deposition of a certain volume of the photosensitive solution onto the film will allow the silver precursor (silver nitride, $AgNO_3$) to diffuse in the film due to its porous structure. Therefore after UV irradiation, AgNP may not only be present at the surface of the film, but also within the titania layer. Two types of films will be investigated with the classical approach: (1) films which will be UV irradiated after depositing the photosensitive solution onto the PEI/PSS/TiO_2 film, and (2) films where 3 rinsing steps in distilled water will be applied between the deposition step of the photosensitive solution on the PEI/PSS/TiO_2 film and the irradiation step. **These films will be addressed as PEI/PSS/TiO_2/x%Ag and PEI/PSS/TiO_2/x%Ag^R,** with x being the weight percentage of $AgNO_3$ in regards to the weight of solvent (i.e. water) used in the photosensitive solution, and "R" referring to the rinsing step.

In the classical AgNP photoinduced synthesis on PEI/PSS/TiO_2 film, 10 µl of photosensitive solution was found to be sufficient in order to cover the entire surface of the film with the help of a glass slide being carefully deposited onto the solution and the film. It has to be mentioned that mechanical

pressure was not applied on the glass slide in order to spread the entire solution on the sample surface. This highlighted an issue that may occur during the photoinduced AgNP synthesis: a displacement of the deposited glass slide may occur during the irradiation of photosensitive formulation, therefore leading to some differences in AgNP synthesis kinetics along the substrate's surface. The first experiment was dedicated to the synthesis and characterisations of AgNP using the original synthesis before changing the amount of $AgNO_3$ in the photosensitive solutions (classical approach).

We studied the influence of a rinsing step based on the LbL self-assembly technique parameters, and applied on the film between the deposition of photosensitive formulation and UV irradiation of the film. Once the formulation was deposited on the PEI/PSS/TiO_2 film, the placed glass slide was kept on top of the substrate for a minute, allowing maximum diffusion of photosensitive formulation in the film. The glass slide was then removed and the substrate was rinsed by dipping it 3 times for 3 min in acidic Milli-Q water (pH 2.5, adjusted by HNO_3). Once rinsed, a new glass slide was deposited on top of the sample and was irradiated by the UV lamp for 10 min.

II.2.1. Characterisation of photoinduced silver nanoparticles

The photosensitive solution is deposited on a glass slide and the samples are irradiated for 10 min with an irradiance of 20 mW/cm² measured at the sample surface. UV irradiation of the deposited photosensitive formulation (classical photoinduced synthesis), usually shows a change in colour on the substrate surface, indicating a successful AgNP synthesis. In addition, this change in colour gives an indication on the shape or size of AgNP.

In this work, the influence of AgNP concentration in PEI/PSS/TiO_2 films was investigated. To do so, the amount of chromophore was kept constant (0.5 wt.%), while the amount of $AgNO_3$ in the formulations varied to obtain x%$AgNO_3$ photosensitive formulations, with x equal to 0, 0.1, 0.5 and 1 wt.%. One can note that the silver-free photosensitive formulation investigated (0%Ag), is only made of chromophore (0.5 wt%) dissolved in water. Therefore PEI/PSS/TiO_2/0%Ag represented a film on which a silver-free photosensitive formulation was irradiated on a PEI/PSS/TiO_2 single layer pair film.

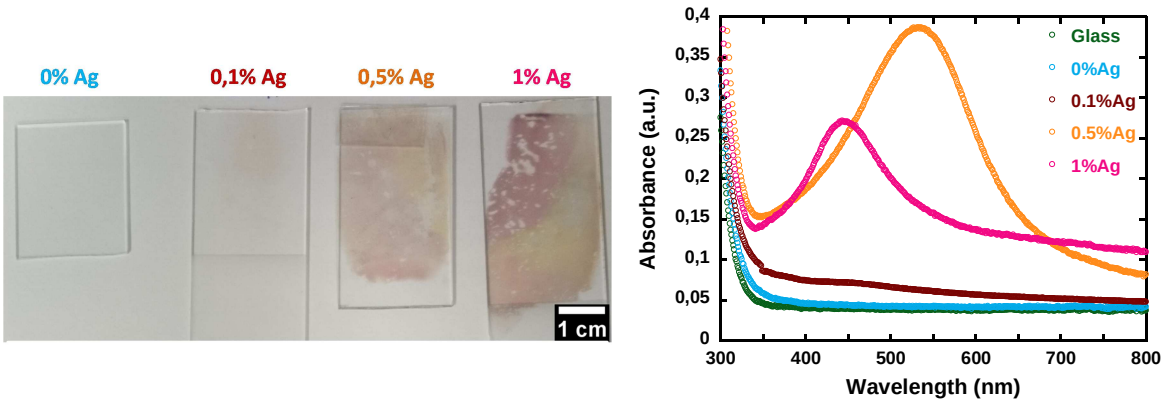

Figure 71 : Characterisations of photoinduced AgNP synthesised with photosensitive formulation containing different amounts of $AgNO_3$. (Left) Pictures of irradiated photosentive formulations deposited on glass slides. (Right) UV-Visible spectroscopy characterisation of photoinduced AgNP, in transmission mode. Photosentive formulations: x wt.% $AgNO_3$, 0,5 wt.% Irgacure and water (100 wt.%).

On glass slides, the use of the silver-free photosensitive solution did not lead, as expected, to any visual evidence of either AgNP synthesis, a change in the UV-Visible absorbance spectrum in transmission compared to the one of a bare glass slide (Figure 71). The formulation containing 0.1% $AgNO_3$ did show a slight yellow colour in the middle of the glass slide, which is most probably due to the low amount of $AgNO_3$ in the formulation. AgNP formation could be observed by UV-Visible spectroscopy, with a low increase in absorbance, but without any clearly visible peak. On the other hand, formulations containing 0,5% and 1% $AgNO_3$ both showed visual evidences of AgNP being formed. The 0.5%$AgNO_3$ and the 1%$AgNO_3$ formulations showed a mixture of yellow and pink colour along the surface of the sample, that may indicate polydispersity in size and/or shape of the photoinduced AgNP. UV-Visible spectrophotometry showed a broad absorbance band centred on 530 nm. This result could be correlated to the one of Zaier *et al.*, where photoinduced AgNP were synthesised with different solvents in the photosensitive formulation [19]. In Zaier's work, photoinduced AgNP synthesised (0.5wt.% $AgNO_3$ and 0.5wt.% irgacure) with water as the solvent in the photosensitive formulation, with 10 min of irradiation time and 20 mW/cm² fluence, had a pink colour and were found to have a hexagonal shape, with an average side distance of 24 nm (determined by AFM) and an absorbance peak centred at 530 nm (determined UV-Visible in transmission). In fact yellow samples with an absorbance peak at 482 nm were obtained at the beginning of irradiation (few seconds) before turning pink while increasing the irradiation time and the absorbance peak was shifted to 530 nm. They suggested that yellow coloured AgNPs had a smaller size than pink coloured AgNP.

Poor homogeneity in colours was obtained for the 1%$AgNO_3$ formulation along the surface of the slide. A pink colour was located at the top left side of the sample and a mixture of yellow and pink colour at the bottom and right side of the slide. By looking at the UV-Visible characterisations, both the intensity of the absorbance peak of AgNP was highly dependent on the location where the spectrophotometer beam passes through the sample. In fact when characterising photoinduced AgNP synthesised on glass/quartz slides by transmission UV-Visible spectroscopy, the peak of the plasmon band of AgNP may vary depending on the sample area where the spectrometer beam passes through. Figure 71 shows an example of a recorded spectrum with a maximum absorbance around 530 nm, but other spectra recorded on other parts of the slide showed plasmon peaks centred on lower wavelengths, similar to those observed with the 0.5%$AgNO_3$ formulation. One could assume that the broad absorbance band here indicates that the spectrometer beam passed through both yellow and pink areas. Should the band pass mainly through a pink area, a red shift of the plasmon band could be obtained. It must be mentioned that a slight displacement of the deposited glass slide on the photosensitive solution was observed during the UV irradiation, and that may influence AgNP synthesis kinetics resulting in a difference in AgNP size and shape and therefore a change in colour along the glass slide surface. This heterogeneity in colours was probably resulting from a slight movement of the deposited glass slide during the synthesis. Also, it could be that a concentration of 1% in $AgNO_3$ is not optimised in our operating conditions for a smooth substrate, by contrast to the conditions used by Zaier *et al*. For further experiments with TiO_2, shifting of the deposited glass slide was prevented as much as possible during the next experiment by placing a bigger sized glass slide onto the sample.

II.2.2. Construction and characterisations of PEI/PSS/TiO_2/x%Ag films

II.2.2.1. Visual evidence of AgNP synthesis and film construction

First the PEI/PSS/TiO_2 films were built on different substrates (glass slides, silicon wafers and TEM copper grid) before synthesising AgNP by a classical photoinduced approach with the different photosensitive solutions described in the previous section. Zaier *et al.* found that the type of surface on which AgNP were synthesised, does have an influence on the size and shape of the nanoparticles. In our work AgNP were synthesised by depositing the photosensitive formulation on pre-built PEI/PSS/TiO_2 films on different substrates. It was assumed that the structure of the titania film could influence the photoinduced AgNP synthesis and that the results could probably differ from that obtained on a bare glass slide. Moreover electron-hole pairs will be generated in TiO_2 upon UV-irradiation of the film, which may also affect AgNP synthesis due to the presence of holes at the TiO_2 surface, or to the formation of oxidising radicals provided by water from photosensitive

formulations. Likewise TiO_2 may also contribute to AgNP synthesis since direct photoreduction of adsorbed silver ions to metallic silver by photogenerated electrons may occur.

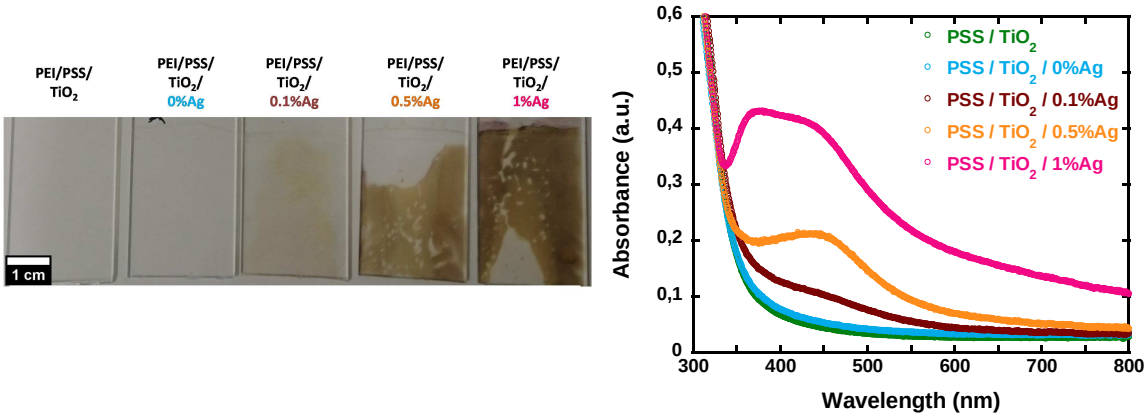

Figure 72: Classical photoinduced AgNP synthesis on PEI/PSS/TiO_2 films on glass slides (left) and the UV-Visible characterisation of PEI/PSS/TiO_2/x%Ag films in transmission mode (right).

After depositing the photosensitive formulation and being UV irradiated, visual evidence of AgNP synthesis on PEI/PSS/TIO_2 films were obtained when $AgNO_3$ was added in the formulation, whereas PEI/PSS/TiO_2/0%Ag did not show any change in colour (Figure 72). A yellow colour along the surface of the substrate could be observed for the PEI/PSS/TiO_2/0.1%Ag sample. When increasing the silver precursor content, a darker yellow colour was observed after UV irradiation on the PEI/PSS/TiO_2/0.5%Ag sample, and ever darker for PEI/PSS/TiO_2/1%Ag. This result was associated to the silver precursor concentration in the photosensitive formulation, leading to a higher amount of AgNP in the films. The AgNP synthesised provided a yellow colour to the films, therefore the denser in AgNP the films are, the darker in colour the film will appear. However it was also observed that the colour was not homogeneous all along the surface of both 0.5%Ag and 1%Ag samples, the variation from areas with lighter yellow colour to some areas with an absence of appearing colour. Although colouring of samples provides visual evidences of AgNP synthesis, the appearing transparent area could also indicate a lower density of AgNP located in these areas.

UV-Visible spectrophotometry in transmission mode was performed on PEI/PSS/TiO_2/x%Ag films where no rinsing step was applied. All 3 samples were constructed on glass slides and showed a higher absorbance than the silver-free film in the visible range, with an increase in absorbance according to the amount of silver present in the films. This evidences the synthesis of AgNP in the film. Characterisations of the PEI/PSS/TiO_2/0.1%Ag film showed similar results than when the irradiated photosensitive formulation was irradiated on a glass slide, in regards to the absorbance

related to silver. Films containing AgNP synthesised with 0.5%Ag in photosensitive formulation also showed a broad absorbance band with a peak at 440 nm. This result differed from the AgNP synthesised on a bare glass slide where the absorbance peak was located at 550 nm, suggesting that photoinduced AgNP synthesised on PEI/PSS/TiO_2 might have a smaller diameter. An even broader absorbance band was obtained for the PEI/PSS/TiO_2/1%Ag film, with a high absorbance band between 340 and 500 nm and absorbance peaks located at 365 and 450 nm. This result suggested that polydispersity in sizes and/or shapes of AgNP for the PEI/PSS/TiO_2/1%Ag sample should be higher than for the PEI/PSS/TiO_2/0.5%Ag film. Interestingly the maximum absorbance of the different films was found to be shifted to the blue wavelengths with increasing silver precursor concentration. So, the results suggest that titania has an influence on the synthesis of AgNP.

Two effects can be observed when a titania LbL film is deposited on a surface. The first effect will be an increase in surface area, as well as an increase in hydrophilic properties of the surface due to the coating of TiO_2 nanoparticles [11], [165]. Therefore when depositing the photosensitive solution on the TiO_2 layer, the interaction of the silver salt with the TiO_2 layer will allow a higher dispersion of $AgNO_3$ than on a glass slide. Therefore the formation of Ag clusters will be more dispersed on the PEI/PSS/TiO_2 film compared to on a glass slide, leading to a lower probability for the AgNP to aggregate and therefore allowing the formation of lower size nanoparticles upon UV irradiation in the photoinduced synthesis. The second effect is related to the direct reduction of the silver ions by the photogenerated electrons from the TiO_2 conduction band, which could accelerate the synthesis process, allowing also the synthesised AgNP to remain more dispersed. Also It is known that the dielectric constant of the surrounding environment will influence the plasmon band resonance of metallic nanoparticles. When the environment dielectric constant is high, a red shift in the metallic nanoparticles' plasmon band is observed, whereas a blue shift of the plasmon band occurs for a low dielectric constant. Therefore the blue shift in the Ag plasmon band observed in PEI/PSS/TiO_2/x%Ag films may also indicate a lower dielectric constant of the environment compared to AgNP synthesised on a glass slide, indicating also a contact between titania and AgNPs [223], [224].

Also, Hirakawa et al. proposed that the change of electron density in silver in a Ag-TiO_2 system, after being irradiated under UV, may also explain the blue shift in the plasmon band [225], [226]. In their studies, they found that UV-A irradiation applied on a Ag@TiO_2 core-shell system showed a blue shift in wavelength on the plasmon band when characterised by UV-Visible spectrophotometry just after UV-A irradiation. They associated this effect to the injection of the photogenerated electrons in the Ag core, thus increasing the electron density and therefore shifting the plasmon band to the blue wavelengths. They also observed that the plasmon band reverted to its original position once the irradiated colloids were in contact with air. Although we performed the UV-Visible characterisations

just after UV-irradiation of the PEI/PSS/TiO_2/Ag films, this hypothesis remains highly improbable in our case.

Ellipsometry characterisation was performed on the films in order to determine the thickness of the films. However this characterisation appeared to be difficult since the laser alignment could not be properly calibrated (i.e. maximum reflexion and intensity) on PEI/PSS/TiO_2/x%Ag and PEI/PSS/TiO_2/x%Ag^R films. The laser alignment was then performed on a PEI/PSS/TiO_2 film, before characterising the silver-containing films. Therefore the values determined by the ellipsometer did not give an estimation of the films' thickness, but an indication that the AgNP synthesis did not de-construct the film. The characterisation was made on 4 samples for each film constructed on a silicon wafer, providing the calculations of the error bars (Table 18). The result did not highlight a particular increase in film thickness compared to a single layer pair film and was found to be similar whether or not the rinsing step was applied prior to UV irradiation for AgNP photoinduced synthesis.

Sample	**Ellipsometry results (nm)**	**Concentration of AgNP in film (ICP-AES) (µg/cm²)**	**Percentage of AgNP in regards to TiO_2 (wt.%) (at.%)**
PEI/PSS/TiO_2	78 ± 14	-	-
PEI/PSS/TiO_2/0%Ag	54 ± 4	-	-
PEI/PSS/TiO_2/0.1%Ag	55 ± 2	-	-
PEI/PSS/TiO_2/0.5%Ag	50 ± 2	-	-
PEI/PSS/TiO_2/1%Ag	53 ± 5	-	-
PEI/PSS/TiO_2/0%Ag^R	46 ± 4	0	0
PEI/PSS/TiO_2/0.1%Ag^R	48 ± 7	0.030	0.42 (0.32)
PEI/PSS/TiO_2/0.5%Ag^R	55 ± 12	0.067	0.95 (0.71)
PEI/PSS/TiO_2/1%Ag^R	47 ± 5	0.084	1.20 (0.89)

Table 18 : Ellipsometry characterisation and silver content of PEI/PSS/TiO_2/AgNP films. "R" represents the additional rinsing step prior UV irradiation of the film; "-": not measured.

II.2.2.2. Determination of Ag content by ICP-AES

The Ag content in the PEI/PSS/TiO_2/x%Ag films was obtained only on films where the rinsing step was applied prior UV irradiation for AgNP photoinduced synthesis (Table 18). Since the AgNP photoinduced synthesis was applied on pre-built PEI/PSS/TiO_2 films, the amount of TiO_2 was found to have an average content of 7 µg/cm². Therefore the AgNP contents will be expressed in regards to the TiO_2 content in the film. The results showed an increase in AgNP content in regards to the amount of silver precursor used in the photosensitive solution, with 0.42 wt.% AgNP for the film constructed with 0.1 wt.% $AgNO_3$, 0.95 wt.% AgNP for the film constructed with 0.5 wt.% $AgNO_3$ and 1.2 wt.% AgNP for the film constructed with 1 wt.% $AgNO_3$. While the rinsing step was applied prior to UV irradiation, we suggest that the films where the rinsing step was not applied should have a higher Ag content and that should increase with the amount of silver salt used in the photosensitive solution.

II.2.2.3. Transmission electron microscopy characterisation

Characterisation by transmission electron microscopy (TEM) was made on silver-titania films (Figure 73). PEI/PSS/TiO_2 films were first built on TEM copper grid before depositing the photosensitive formulation onto them. The addition of a deposited glass slide on the grid was omitted in this procedure in order to prevent the grid from being damaged by the slide. Hence the grid was directly irradiated by UV light for 10 min and kept in a dark place prior to TEM characterisation. First it is worth noting that independently of the concentration of silver precursor in the photosensitive solution, all PEI/PSS/TiO_2/Ag films showed spherical AgNP being in contact with TiO_2 nanoparticles, no free AgNP being observed.

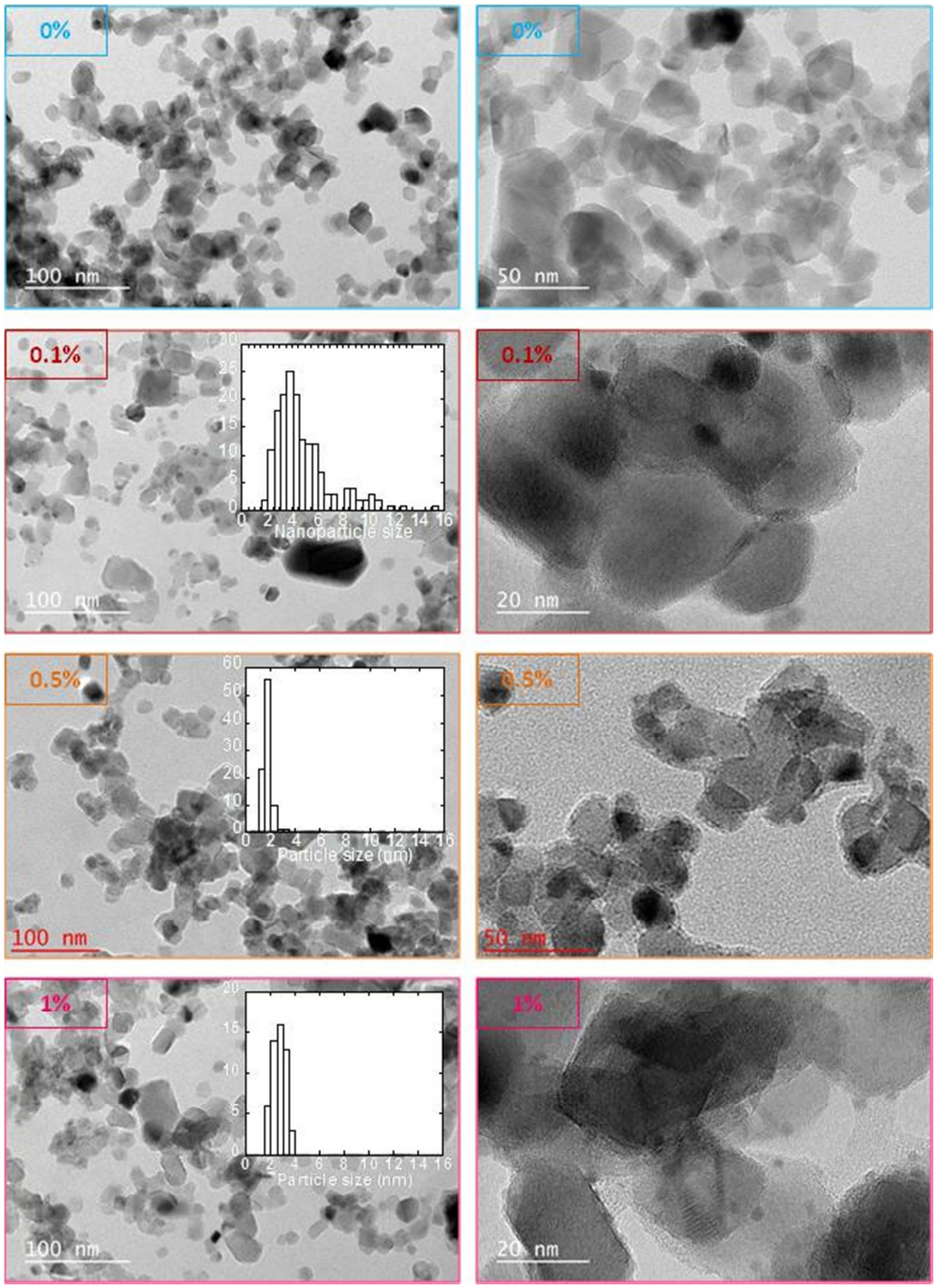

Figure 73 : TEM images of PEI/PSS/TiO_2/x%Ag films. x = 0%, 0.1%, 0.5% and 1%. The size distribution was assessed only on 56 nanoparticles for the sample with x=1%.

The images showed different distributions in sizes of AgNP according to the photosensitive formulation used for the AgNP photoinduced synthesis. The PEI/PSS/TiO_2/0.1%Ag film contained AgNP with a size distribution centred on 3.5 nm, but with a broad size distribution. AgNP size distribution was narrower in both PEI/PSS/TiO_2/0.5%Ag and PEI/PSS/TiO_2/1%Ag films, and centred on

smaller diameter sizes in both cases (1-1.5 nm vs. 2-2.5 nm, respectively). Additional information regarding the size distribution of AgNP was obtained by scanning transmission electron microscopy (STEM) characterisation on PEI/PSS/TiO_2/0.1%Ag and PEI/PSS/TiO_2/1%Ag films (Figure 74). The results showed a similar trend to that of TEM characterisation, with a higher polydispersity of AgNP sizes on the PEI/PSS/TiO_2/0.1%Ag film, while AgNP displayed a narrow size distribution, centred on 1.5 nm for the PEI/PSS/TiO_2/0.1%Ag film.

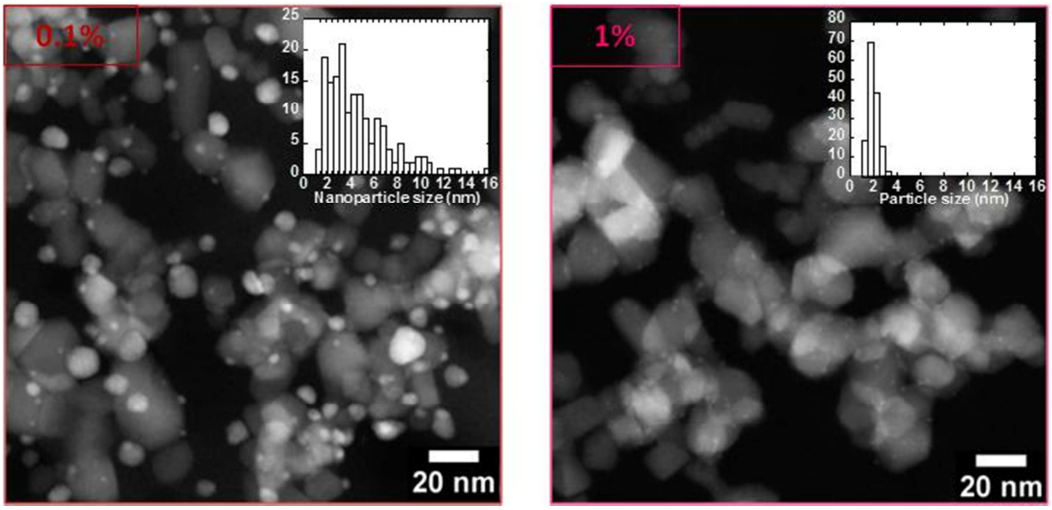

Figure 74 : STEM images of PEI/PSS/TiO_2/0.1%Ag and PEI/PSS/TiO_2/1%Ag.

In the investigations of Zaier et al., they noticed that the surface on which AgNP are synthesised using the classical photoinduced approach, may influence the synthesis [19]. While using the same photosensitive formulation, they observed different surface colourations when AgNP were synthesised on glass slides and mica surfaces. Their TEM characterisations provided information on AgNP sizes when synthesised on a copper grid, and the size of AgNP was found to be smaller than that determined by UV-Visible spectroscopy characterisation, where AgNP were synthesised on a glass slide. In a previous work on photochemical synthesis of AgNP from Mustatae *et al.*, this difference in AgNP sizes synthesised on several surfaces, was also attributed to the chemical nature of the surface [101]. In our work not only the type of substrate may influence the AgNP photoinduced synthesis, but the deposited titania on the substrate may provide different growth and kinetics rates for AgNP.

II.2.2.4. Discussion on characterisations of PEI/PSS/TiO_2/x%Ag

Mustatea *et al*. studied the effect of the concentration of $AgNO_3$ used in the photosensitive formulation, while keeping a constant amount of chromophore, the same incident fluence and irradiation time during AgNP synthesis [101]. Though the solvent used was ethanol in their work, UV-Visible characterisations showed that the AgNP absorbance peak shifted to the red while increasing the silver precursor content. This was attributed to a progressive increase in particle size as the concentration of AgNP increased. Additional investigation on the concentration of the chromophore in the photosensitive formulation, while keeping the silver precursor concentration constant, showed a maximum absorbance band for a 1:1 chromophore-silver precursor ratio, showing that the chromophore concentration has an influence on the amount of AgNP generated. In our work, the chromophore concentration was kept constant in order to have different particle sizes by changing the silver precursor content. Interestingly when synthesised on the PEI/PSS/TiO_2 film, both UV-Visible and TEM characterisations showed that AgNP size was globally decreasing while increasing silver precursor content. This suggested that the nucleation and growth rate of AgNP may be influenced by a combined effect resulting from the free radicals generated by the chromophore, the oxidising radical generated by the titania nanoparticles, as well as the possible direct reduction by the photogenerated electrons. It is very difficult to un-couple those different effects, but they probably together are modifying the value of the optimum chromophore-silver precursor ratio, the nucleation and growth rate of AgNPs, with consequently an influence on the dispersion of TiO_2. Since a high polydispersity in AgNP size was observed in the PEI/PSS/TiO_2/0.1%Ag film, the nucleation speed could have been too fast, leading to both small and bigger AgNP particle sizes [227].

By changing the chromophore concentration in the photosensitive formulation and characterising the film by UV-Visible spectroscopy in transmission mode, Mustatea *et al*. observed a maximum AgNP absorbance for a 1:1 chromophore-silver precursor ratio [101]. In our case PEI/PSS/TiO_2/0.5%Ag was the film with AgNP synthesised with a 1:1 chromophore-silver precursor ratio, which gave AgNP with the lowest size distribution. In this case, the AgNP nucleation and growth rate seemed to be optimum using a 1:1 chromophore-silver precursor ratio (0,5 wt.% $AgNO_3$). On the other hand STEM images showed AgNP nanoparticle sizes for PEI/PSS/TiO_2/1%Ag films as small as that of PEI/PSS/TiO_2/0,5%Ag (determined on TEM images). This may suggest that since the silver precursor concentration was higher than that of the chromophore in the photosensitive formulation, nucleation and growth rate may also be governed by TiO_2 upon UV irradiation, via the oxidising (h^+_{VB}, OH•) or the reduction properties of TiO_2 under irradiation, respectively towards the chromophore or the silver salt.

II.2.3. Photocatalytic activity of PEI/PSS/TiO_2/x%Ag films

II.2.3.1 Photocatalytic activity results

The activity of PEI/PSS/TiO_2/x%Ag and PEI/PSS/TiO_2/x%Ag^R films was tested on films built on silicon wafers. Similarly to films containing commercial AgNP, the three 12 cm² samples, cut from the 36 cm² silicon wafers, were reassembled and placed in the designed cavity of the photoreactor before gas stabilisation onto them. The photocatalytic tests were carried out three times on each film, providing the calculation of the error bars. Results of photocatalytic performance of PEI/PSS/TiO_2/x%Ag and PEI/PSS/TiO_2/x%Ag^R films are summarised in Table 19 and shown in Figure 75 and Figure 76. While the effect of the UV lamp used for AgNP photoinduced synthesis was evaluated on the PEI/PSS/TiO_2 film and described in Chap 3.II.1, the effect of the chromophore on the film was investigated by testing the activity of PEI/PSS/TiO_2/0%Ag and PEI/PSS/TiO_2/0%Ag^R films. In the case of the film constructed without the rinsing step prior to UV irradiation, the results show neither conversion of gas phase HCOOH, nor formation of CO_2, while the addition of the rinsing step showed a regain in the photocatalytic performance of the film. This suggested that the excess chromophore adsorbed in the film may block the active sites of TiO_2, resulting in the inhibition of photocatalytic properties of the thin films, while the rinsing step has allowed the removal of the excess chromophore in the film. In the case of the PEI/PSS/TiO_2/0%Ag film, another (non-exclusive) hypothesis could be that the chromophore is in fact partially degraded by the film, with degradation by-products being not CO_2 but partially oxidised organics whch were non-detectable, or in too low amounts to be monitored by the gas chromatography.

Photocatalytic activity of both types of films could be observed for the degradation of gas-phase HCOOH, upon UV-A irradiation. In the case of the PEI/PSS/TiO_2/x%Ag film, a lower HCOOH conversion rate could be observed for the PEI/PSS/TiO_2/0.1%Ag film compared to the silver-free film, whilst the amount of CO_2 formed showed a similar result. This may suggest that not all the chromophore has been used during AgNP photoinduced synthesis, blocking some active sites in the film, while being oxidised to form a higher amount of CO_2 upon UV-A irradiation. The two other films, containing higher amounts of AgNP, both showed similar photocatalytic performances to the silver-free film. While these results suggested that all the chromophore was used during AgNP photoinduced synthesis and that the AgNP were in contact with the TiO_2 nanoparticles (TEM characterisation), the photocatalytic properties of the film were not enhanced. But in all cases, non-rinsed films only led to minor change in behaviour compared to AgNP-free films.

Sample	Weight percentage of AgNP in regards to TiO_2 (wt.%)	Conversion (%)	CO_2 formed (ppm_v)	Theoretical CO_2 formed (ppm_v)
PEI/PSS/TiO_2	0	13 ± 1	28 ± 1	17 ± 1
PEI/PSS/TiO_2/0%Ag	0	0	0	0
PEI/PSS/TiO_2/0.1%Ag	-	10 ± 1	27 ± 1	16 ± 1
PEI/PSS/TiO_2/0.5%Ag	-	15 ± 1	30 ± 2	23 ± 1
PEI/PSS/TiO_2/1%Ag	-	15 ± 1	28 ± 1	26 ± 1
PEI/PSS/TiO_2/0%Ag^R	0	15 ± 1	24 ± 1	22 ± 1
PEI/PSS/TiO_2/0.1%Ag^R	0.42	29 ± 2	45 ± 2	42 ± 2
PEI/PSS/TiO_2/0.5%Ag^R	0.95	31 ± 2	46 ± 2	44 ± 2
PEI/PSS/TiO_2/1%Ag^R	1.20	18 ± 1	40 ± 2	27 ± 1

Table 19 : Photocatalytic results of PEI/PSS/TiO_2/x%Ag films towards the degradation of gas phase HCOOH. "-": not measured.

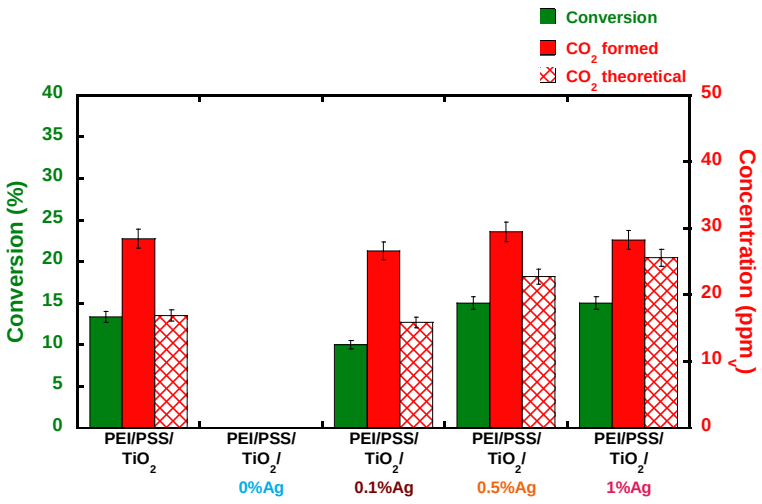

Figure 75 : Photocatalytic performance of PEI/PSS/TiO_2/x%Ag films towards the degradation of gas phase HCOOH. Experimental parameters: [HCOOH] = 145 ppm_v, air flow = 20 mL/min, speed = 0.7 cm/s, UV-A irradiance = 2.5 mW/cm², films built on 36 cm² silicon wafers.

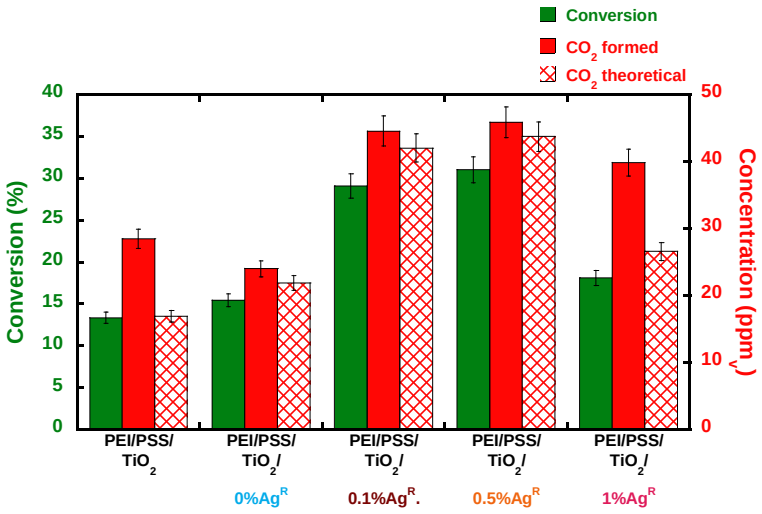

Figure 76: Photocatalytic performance of PEI/PSS/TiO_2/x%Ag^R films (with additional rinsing steps prior UV irradiation for AgNP photoinduced synthesis). Experimental parameters: [HCOOH] = 145 ppm_v, air flow = 20 mL/min, speed = 0.7 cm/s, UV-A irradiance = 2.5 mW/cm², films built on 36 cm² silicon wafers.

By contrast, after the rinsing step, the photocatalytic performances of the PEI/PSS/TiO_2/x%Ag^R films with silver content were found to be significantly higher than those of the silver-free film implying a positive effect by the rinsing step. The results showed a 29% conversion rate and 44 ppm_v of CO_2 formed for PEI/PSS/TiO_2/0.1%Ag^R, and 31% conversion rate and 46 ppm_v of CO_2 formed for PEI/PSS/TiO_2/0.5%Ag^R. Since the theoretical concentration of CO_2 formed is almost equal to the actual concentration of CO_2 formed, the amount of CO_2 formed is related to the degradation of HCOOH upon UV-A irradiation. By contrast, only a slight gain in activity was observed for the PEI/PSS/TiO_2/1%Ag compared to the silver-free film (from 13% to 18% conversion).

II.2.3.2 Discussion of photocatalytic performances of films with photoinduced AgNP

The photocatalytic tests for the degradation of gas-phase formic acid have shown an inhibition of the photocatalytic performance of PEI/PSS/TiO_2 film if no rinsing step was applied. The addition of the rinsing step helped to regain the photocatalytic activity of the film and the blocking of the photocatalytic sites by the chromophore or chromophore residue was suggested when being present in the films. This rinsing step prior the UV irradiation of the film for AgNP photoinduced synthesis also implied a removal of excess material deposited on the film.

The photocatalytic performance of the PEI/PSS/TiO_2/x%Ag film (no addition of rinsing step) showed globally photocatalytic performance results similar to the silver-free PEI/PSS/TiO_2 film, and that in the

best cases, the addition of AgNP had no significant effect. PEI/PSS/TiO_2/0.1%Ag films showed however a slightly lower result in HCOOH conversion, which may suggest that some chromophore or chromophore residues are still present in the film. The addition of the rinsing step prior the UV irradiation of the photosensitive solution deposited on the PEI/PSS/TiO_2 film showed an increase in the photocatalytic performances up to two times for samples with Ag/TiO_2 wt.% of 0.42 and 0.95. On the other hand, PEI/PSS/TiO_2/1%Ag^R showed lower photocatalytic results. Chemical analysis ICP-AES allowed the determination of Ag content in the film where the rinsing step was applied, and showed an increase in Ag content in regards to the concentration of the silver precursor used in the photosensitive solution. It was reported that associating TiO_2 may allow on improvement in the photocatalytic properties of TiO_2 under UV-A, usually assigned to electron trapping by AgNP upon the UV-A irradiation of TiO_2 nanoparticles, lowering the recombination rate of the photogenerated charge carriers [129], [223], [228]. However this electron trapping effect may also act as a charge carrier recombination centre at the Ag-TiO_2 interface, should the Ag concentration be too high [129], [226], [229]–[231]. This Ag content may lead to a higher rate of h^+/e^- charge recombination rather than photogenerated holes to react with the target molecule to degrade, eventually resulting in a drop of photocatalytic performances of TiO_2. Our results after rinsing may suggest that a 1.20 wt.% ratio is too high and that 0.42-0.95 ratio are more suitable here. This hypothesis can also be applied for the PEI/PSS/TiO_2/x%Ag films (no rinsing steps) where the conversion rate was similar to the silver-free PEI/PSS/TiO_2 film, suggesting that the silver content in these films may be higher than 1.20 wt.%.

It is worth noting that the PEI/PSS/TiO_2/0.1%Ag^R film and PEI/PSS/TiO_2/^5Ag_C, with AgNP deposited using the LbL blade-assisted technique, have a similar Ag content (0.45 wt.%), but a conversion rate slightly higher for the PEI/PSS/TiO_2/0.1%Ag^R (29% compared to 23% for the PEI/PSS/TiO_2/^5Ag_C film).

Overall the AgNP photoinduced synthesis may either provide the same photocatalytic performance of a silver-free PEI/PSS/TiO_2 film, or improve the photocatalytic properties with AgNP acting as an electron trap, or, in the worst case, even hindering the activity by having too much chromophore or chromophore residue present in the film. In the most favoured case, the activity of the film was increased twofold.

II.3 One-pot photoinduced synthesis of AgNP in PEI/PSS/(x%Ag-TiO_2) films

Two approaches were presented in the previous sections in order to construct PEI/PSS/TiO_2/AgNP films. One was by depositing commercially available AgNP by blade-assisted LbL deposition on PEI/PSS/TiO_2 films, the other by synthesising AgNP in the PEI/PSS/TiO_2 films by irradiating a

photosensitive formulation by UV light. These two approaches required the deposition of the TiO_2 layer on a PEI/PSS film prior to deposition/synthesis of AgNP.

In this project, a new approach, combining the LbL self-assembly technique and the photoinduced synthesis of AgNP was developed in order to synthesise AgNP while depositing the TiO_2 layer on the PEI/PSS film. This one-pot synthesis approach consisted of dipping the PEI/PSS film in the photosensitive formulation, in which the solvent, distilled water, was replaced by the TiO_2 suspension used for building the PEI/$(PSS/TiO_2)_n$ LbL films. Once the photosensitive formulation containing TiO_2 was deposited, films were irradiated by UV light using the same parameters than those used for the photoinduced synthesis of AgNP. This part is dedicated to the investigation of this novel approach with the characterisation of the PEI/PSS/(x%Ag-TiO_2) films with different concentrations of AgNP, followed by the evaluation of their photocatalytic properties. Like the classical approach, the characterisation of the photosensitive formulation with TiO_2 suspension used as the solvent, was investigated prior to the construction of the films.

II.3.1. Characterisations of AgNP synthesised with the x%Ag-TiO_2 photosensitive suspension

As explained above, the water used as a solvent in the classical photosensitive formulation, was replaced by the TiO_2 suspension (12 g/L) used for LbL film construction. The experimental procedure for making the photosensitive suspension is detailed in Chap. 2.II.3.2. The AgNP synthesis was made on bare glass slides (no LbL deposition) by following the same procedure for the classical AgNP photoinduced synthesis for evidencing that x%Ag-TiO_2 can be used as photosensitive suspensions with different $AgNO_3$ concentrations. Like in the previous approach, four $AgNO_3$ concentrations were used in x%$AgNO_3$-TiO_2 photosensitive TiO_2 suspensions, where x was equal to 0, 0.1, 0.5 and 1 wt.% in regards to suspension weight.

A yellow colour, becoming darker with the increase in $AgNO_3$ content, could be seen for the three samples containing silver, indicating the heterogeneity of the samples (Figure 77). Dark spots could be observed in the middle of the samples, which may be due to the higher concentration of TiO_2 deposited in the middle of the glass surface. Indeed while water could be spread along the whole surface of the glass slide, when a second glass slide is deposited onto it, TiO_2 nanoparticles may stay in the middle of the glass slide. These dark spots appeared after UV-irradiation, suggesting a high concentration of AgNP synthesised on the slide. The heterogeneity in colours was more pronounced for the 1%Ag-TiO_2 sample, where a pink area could be observed at the edges of the sample, which

may be additionally associated to a slight displacement of the deposited glass slide during UV irradiation.

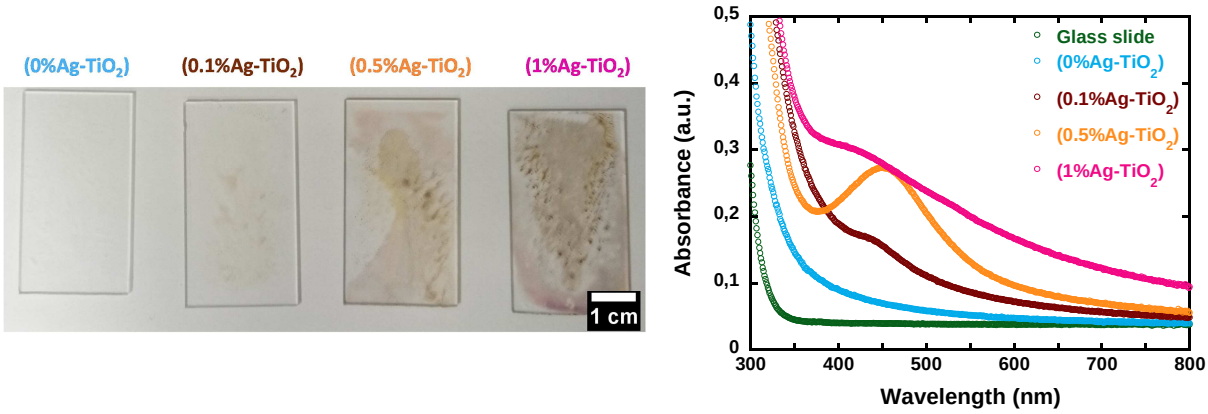

Figure 77: Characterisations of photoinduced AgNP synthesised on glass slide with TiO_2-based x%$AgNO_3$-TiO_2 photosensitive suspensions, containing different amounts of $AgNO_3$. (Left) Pictures of the photosentive suspensions on glass slides after UV irradiation. (Right) Corresponding transmission mode UV-Visible spectra.

Once having been UV irradiated, the samples were characterised by UV-Visible spectroscopy in transmission mode. The spectrum of a bare glass slide was acquired in order to highlight the presence of titania at the surface of the glass slide when the photosensitive suspensions were deposited. While the minimum of absorbance is found at about 350 nm for glass, all samples showed an absorbance minimum at about 380 nm due to the deposition of TiO_2 nanoparticles on the glass slides. The three samples prepared using $AgNO_3$-TiO_2 showed a more or less intense absorbance in the visible range that increased according to the amount of $AgNO_3$ contained in the photosensitive suspension.

The 0.1%$AgNO_3$-TiO_2 suspension showed a weak plasmon band with a peak centred at 435 nm, while 0.5%$AgNO_3$-TiO_2 also had a stronger wide plasmon band, but the peak was centred at 450 nm. As discussed in the previous section (Chap. 4.II.2.2.1.), the AgNP may have a larger mean diameter size when synthesised using 0.5%$AgNO_3$-TiO_2 photosensitive suspension compared to the one synthesised with 0.1%$AgNO_3$-TiO_2 suspension. The irradiation of 1%$AgNO_3$-TiO_2 photosensitive gave a broad AgNP plasmon band, which could be associated with a higher polydispersity in AgNP size (cf. visual heterogeneity).

Transmission electron microscopy characterisation was only performed using the 0.5%$AgNO_3$-TiO_2 photosensitive suspension. 10 µl of the photosensitive suspension was deposited on the TEM copper grid and was irradiated by UV light without adding a glass slide onto the TEM copper grid. AgNP were

found to be evenly distributed at the surface of TiO_2 nanoparticles, with a narrow size distribution between 1 and 4 nm, centred at 2 nm (Figure 78). This shows that the x%$AgNO_3$-TiO_2 suspension can be used as photosensitive suspension for synthesising AgNP with a narrow particle size distribution at the surface of TiO_2.

Since visual evidence of AgNP formation and the two characterisation methods highlighted AgNP synthesis while using TiO_2 suspension as a solvent in the photosensitive solution, the four photosensitive suspensions were used for building the AgNP-TiO_2 layer on the PEI/PSS films in the next section.

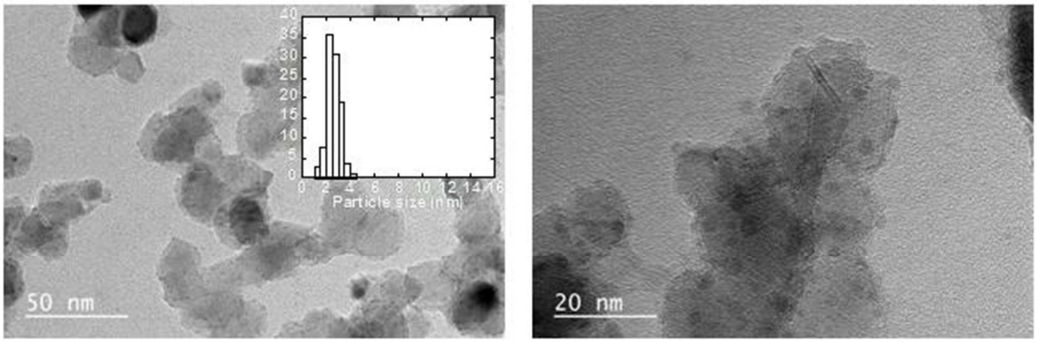

Figure 78 : TEM images of the Ag-TiO_2 system obtained after irradiation of the 0.5%$AgNO_3$-TiO_2 photosentive suspension.

II.3.2. Construction and characterisations of PEI/PSS/(x%Ag-TiO_2) films

II.3.2.1. Visual evidence of AgNP synthesis and UV-Visible characterisation

Once the photosensitive suspension has been prepared, the substrates with PEI/PSS films built onto them (11.25 cm^2), were dipped in the photosensitive suspension and rinsed in acidic milli-Q water according to the LbL dipping parameters used for constructing the films. Films constructed on glass slides where used for providing visual evidence of AgNP, as well as for UV-Visible characterisation in transmission mode (Figure 79). The presence of AgNP was not evidenced whatever the concentration of the photosensitive suspension, and no plasmon band was observed. This abscence of any visual evidence of the hybrid Ag-TiO_2 film is therefore very interesting from an applicative point of view. This probably resulted from the combined approach, which led to homogeneously synthesising AgNP directly, while building the film. Absorbance difference between 0-0.1% $AgNO_3$-TiO_2 samples may result from different amounts of TiO_2 being deposited. All absorbance spectra have an absorbance minimum around 380 nm, resulting from the deposition of TiO_2.

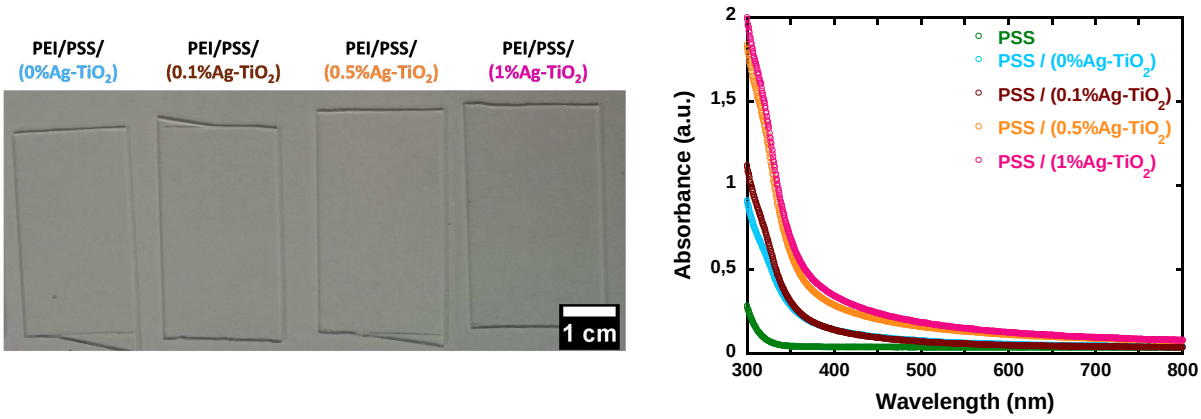

Figure 79 : Characterisations of PEI/PSS/(x%Ag-TiO_2) film, with x = 0, 0.1, 0.5 and 1wt% $AgNO_3$. (Left) Pictures of irradiated films constructed on glass slides. (Right) Transmission mode UV-Visible spectra of the films after being UV irradiated for AgNP one-pot synthesis.

II.3.2.2. Film thickness and determination of AgNP concentration

After preliminary visual and UV-Visisble spectrophotometry characterisation, other $AgNO_3$ concentrations have been in the photosensitive suspension used for the LbL film construction (i.e. 0.2, 0.7, 1.5 and 2 wt.%).

As for the films containing AgNP synthesised using the photoinduced classical approach, ellipsometry characterisation was performed on the films in order to determine evidence of the deposition of the Ag-TiO_2 layer. Once again maximum reflection and intensity of the ellipsometer laser could not be obtained for the PEI/PSS/(x%Ag-TiO_2) films. The laser alignment was then performed on a PEI/PSS/TiO_2 film. Therefore the values determined by the ellipsometer did not give an estimation of the films' thickness, but an indication of the actual deposition of the Ag-TiO_2 hybrid layer on the PEI/PSS film. The characterisation was made on 4 samples for each film constructed on silicon wafer, providing the calculations of the error bars (Table 20). The results showed that every x%$AgNO_3$-TiO_2 layers were successfully deposited.

Sample	**Ellipsometry results (nm)** **(increment after Ag-TiO_2 layer deposition (nm))**	**TiO_2 concentration (µg/cm²)**	**Ag concentration (ng/cm²)**	**Ag/TiO_2 (wt. %) (at.%)**
PEI/PSS/ TiO_2	78 ± 14 (+71)	7 ± 1	0	0
PEI/PSS/ (0%Ag-TiO_2)	37 ± 8 (+30)	7 ± 1	0	0
PEI/PSS/ (0.1%Ag-TiO_2)	40 ± 12 (+33)	7 ± 1	151 ± 1	2.2 (1.9)
PEI/PSS/ (0.2%Ag-TiO_2)	47 ± 3 (+40)	10 ± 2	168 ± 1	1.7 (1.5)
PEI/PSS/ (0.5%Ag-TiO_2)	61 ± 13 (+54)	9. ± 2	140 ± 2	1.6 (1.5)
PEI/PSS/ (0.7%Ag-TiO_2)	39 ± 16 (+32)	17 ± 3	105 ± 2	0.6 (0.5)
PEI/PSS/ (1%Ag-TiO_2)	73 ± 19 (+42)	18 ± 4	44 ± 2	0.2 (0.2)
PEI/PSS/ (1.5%Ag-TiO_2)	-	12 ± 2	56 ± 1	0.5 (0.4)
PEI/PSS/ (2%Ag-TiO_2)	-	6 ± 1	111 ± 2	1.7 (1.5)

Table 20 : Evidences of Ag-TiO_2 layer deposited on a PEI/PSS film. Increment after Ag-TiO_2 layer deposition represent the difference between the ellipsometry result of the PEI/PSS/(Ag-TiO_2) film, and the thickness of the PEI/PSS film (7 ± 1 nm).

The sample were characterised by chemical analysis ICP-AES, and the amounts of Ag synthesised in the film was assessed. Since the addition of silver precursor and the chromophore may influence the deposition of TiO_2 by modifying the LbL suspension, the amount of TiO_2 was also assessed and the values were reported in Table 20.

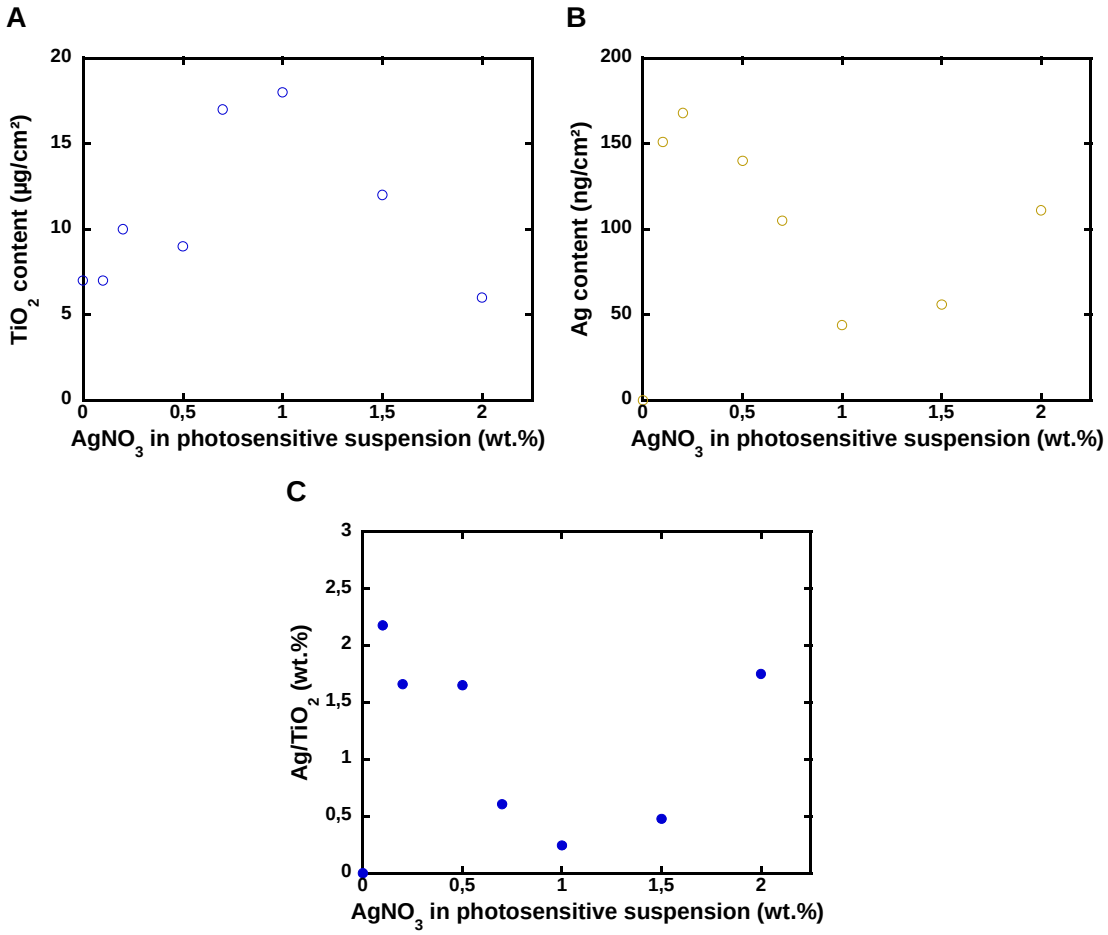

Figure 80 : (A) TiO_2 and (B) Ag content in regards to the $AgNO_3$ concentration in the TiO_2 photosensitive suspension. (C) Ag/TiO_2 wt.% in $Ag\text{-}TiO_2$ hybrid films in regards to the $AgNO_3$ concentration in TiO_2 photosensitive suspension.

The amount of TiO_2 deposited on the PEI/PSS film showed a bell-like curve with increasing amounts of silver precursor in the photosensitive TiO_2 suspension, with an increase up to 1 wt.% of $AgNO_3$ (from 7 µg/cm² to 18 µg/cm²), and subsequently a decrease until getting a deposited TiO_2 content close to that of a silver-free film (7 µg/cm²) (Figure 80A). As for Ag content, the concentration was found to be the highest for the samples made using the lowest $AgNO_3$ concentration, and was found to decrease while increasing $AgNO_3$ concentration, with a silver concentration of 44 ng/cm² for the PEI/PSS/(1%$Ag\text{-}TiO_2$) film (Figure 80B). The Ag concentration went up again while increasing the silver precursor concentration in the photosensitive TiO_2 suspension. When looking at the $Ag{:}TiO_2$ content

in regards to the silver precursor content in the photosensitive TiO_2 suspension, it is found that the Ag content decreases from 2.2 wt.% for PEI/PSS/(0.1%Ag-TiO_2) film, to 0.2 wt.% for PEI/PSS/(1%Ag-TiO_2 film) (Figure 80C). The Silver content went up to 0.5 wt.% and 1.8 wt.% when increasing the silver precursor to 1.5% and 2% respectively in the photosensitive TiO_2 suspension.

II.3.2.3. X-ray photoelectron spectroscopy characterisations of the films

Orbital and contribution	**PEI/$(PSS/TiO_2)_{10}$ (eV)**	**PEI/PSS/ (0.2%Ag-TiO_2) (eV)**	**PEI/PSS/ (1%Ag-TiO_2) (eV)**
C 1s, C=C	284.9	284.9	284.9
C 1s, C-O	286.5	286.5	286.8
C 1s, C=O	388.9	288.7	288.8
Ti $2p_{3/2}$, Ti^{4+}-O	458.7	458.7	458.5
Ti $2p_{1/2}$, Ti^{4+}-O	464.4	464.3	464.2
O 1s, O-Ti	529.9	529.9	529.7
O 1s, O-H	531.6	533.2	531.8
O 1s, O-Si	532.9	532.3	532.8
N 1s	400.2	400.2	400.1
Ag $3d_{5/2}$	-	367.3	-
Ag $3d_{3/2}$	-	373.5	-
Ag $M_5N_{45}N_{45}$	-	351.4 (K.E)	351.5 (K.E)
Ag $M_4N_{45}N_{45}$	-	359.1 (K.E)	359.4 (K.E)

Table 21: XPS results in terms of binding energy (in eV) for the C 1s, Ti 2p, O 1s, N 1s and Ag 3d orbitals. Kinetic energies (K.E.) are shown for Ag MNN.

X-ray photoelectron spectroscopy (XPS) characterisations were performed on 3 samples: a silver-free LbL film and the samples containing the highest and the lowest Ag content. This characterisation technique provides information on the chemical and oxidation state of the different elements at the surface of the samples. The element analysed were carbon 1s (present in PSS, PEI and Irgacure 2959 chromophore, but is used also as a reference for charge-effect corrections by setting the C=C peak to a binding energy of 284.9 eV), titanium 2p (present in TiO_2), oxygen 1s (present in TiO_2, HNO_3, SiO_2, PSS, PEI and Irgacure 2959 chromophore, but also in Ag since this compound may be oxidised i.e. Ag_2O or AgO), silicon 2p (present in SiO_2 on which films were constructed), nitrogen 1s (present in PEI, HNO_3 and Irgacure 2959 chromophore), sulphur 2p (present in PSS), and silver 3d and MNN (present in samples constructed with the one pot photoinduced approach). The binding energy of each element, with their corresponding peak is shown in Table 21 and the surface atomic composition is showed in the appendix.

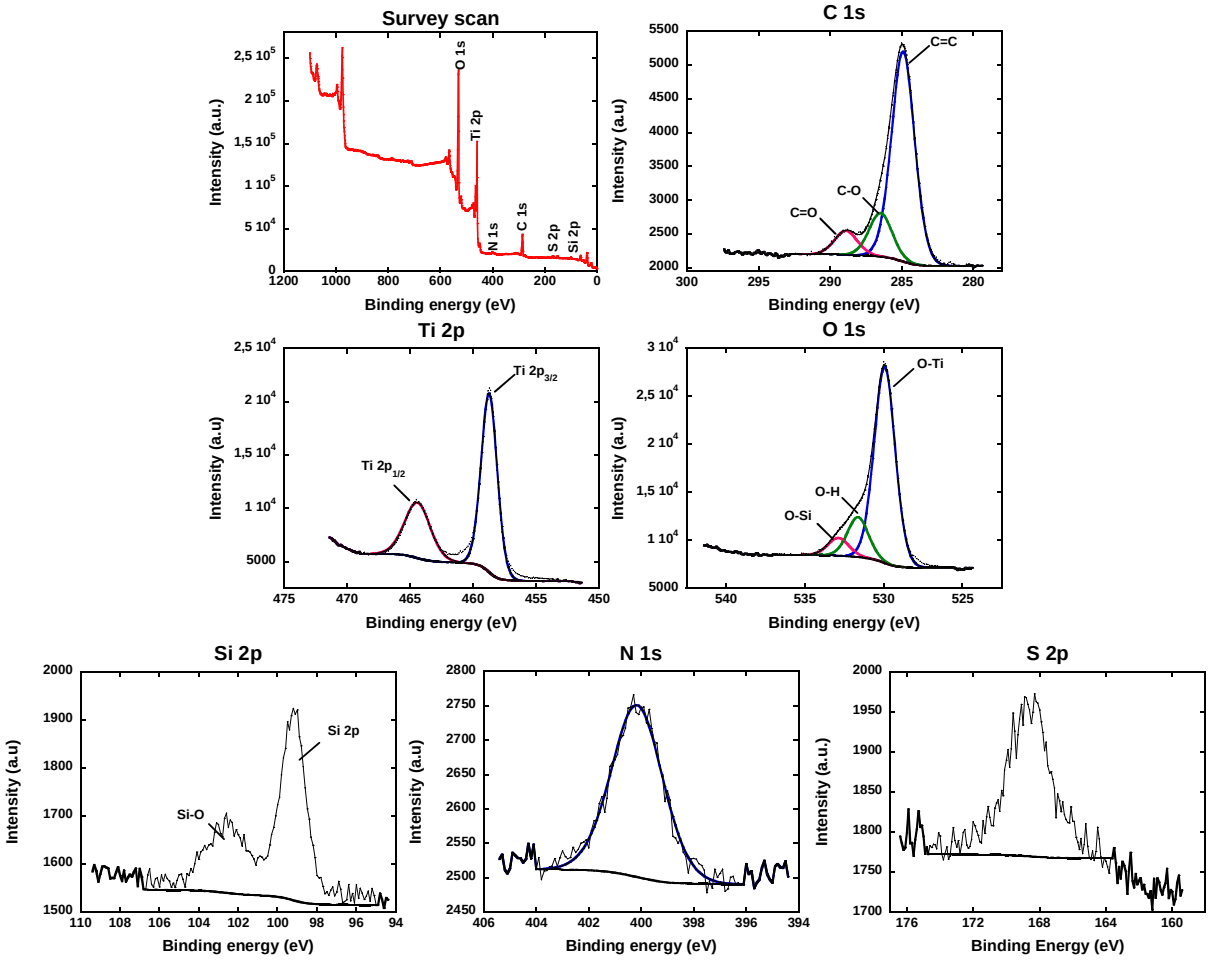

Figure 81 : XPS characterisation of the PEI/$(PSS/TiO_2)_{10}$ LbL film.

Characterisations of PEI/$(PSS/TiO_2)_{10}$ (Figure 81) showed a Ti 2p core level with Ti $2p_{3/2}$ peak at 458.7 eV and Ti $2p_{1/2}$ peak at 464.4 eV, giving a spin-orbit coupling of 5.7 eV. The O 1s XPS spectrum showed 3 regions attributed to the O-Ti bond (529.9 eV), O-H bond (531.6 eV). Using the O-Ti bond and Ti $2p_{3/2}$, the O:Ti ratio was found to be 2.2. The third region was attributed to the O-Si bond (532.9 eV) from the silicon wafer, which was confirmed by the presence of a the Si 2p core level XPS spectra [232]. A single peak contribution was found for the N 1s core orbital, at a binding energy of 400.2 eV. Most probably, this contribution can be assigned to adsorbed nitrogen (γ-N_2) or nitrogen atoms from the PEI polyelectrolyte used for constructing the first layer of the film [233], [234]. Contamination of the film by residues of nitrates used for adjusting pH in TiO_2 suspensions was discarded due to the absence of higher binding energy peak. S 2p core level signal could not be properly treated due to the background noise, but the S 2p peak at 168.5 eV could be attributed to the S-O bond from PSS. The low intensity of the Si 2p and N 1s orbital signals (if N 1s orbital signal results from the PEI) may be attributed to the very good coverage of the substrate for the 10 layer pairs film.

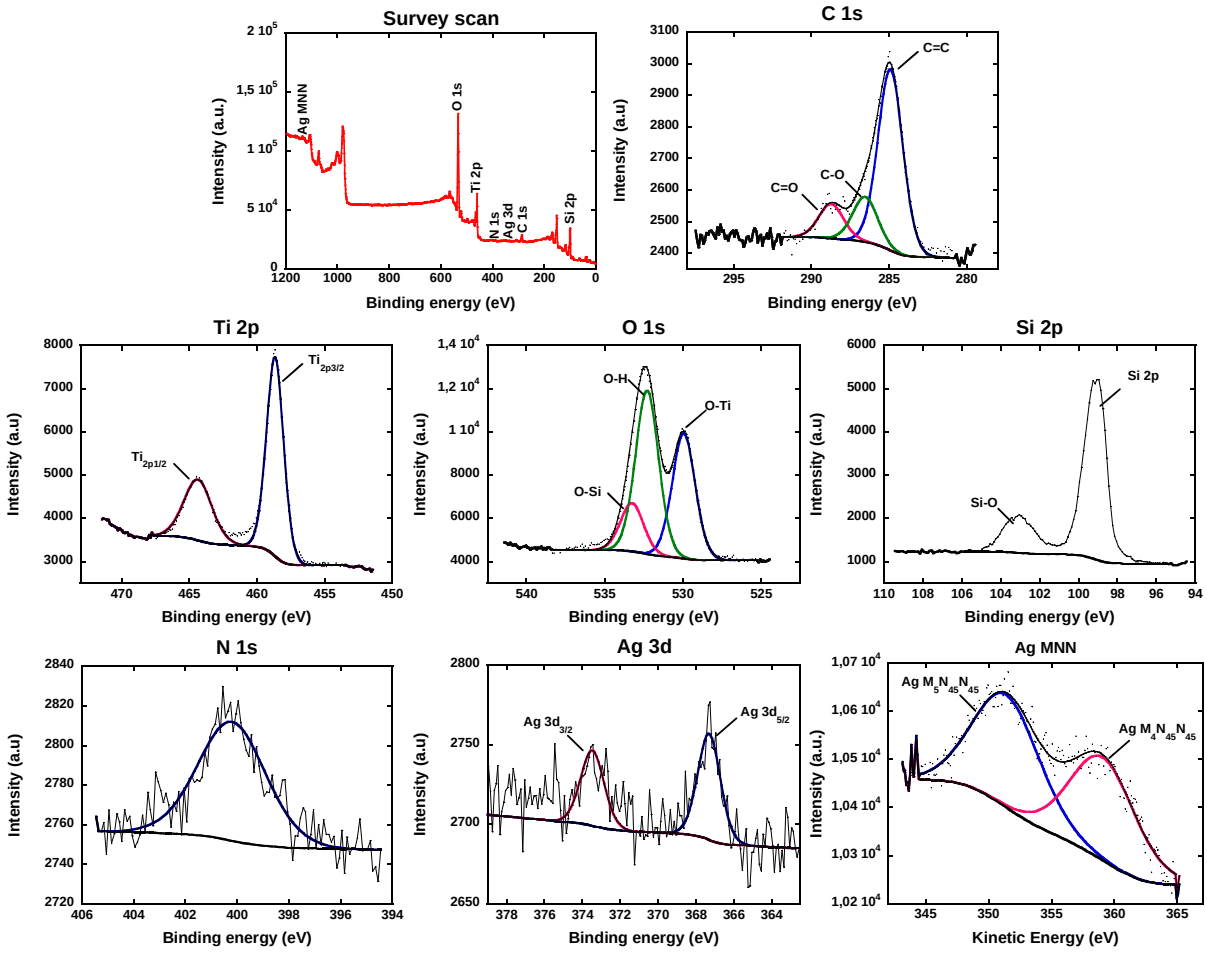

Figure 82: XPS characterisations of PEI/PSS/(0.2%Ag-TiO_2) LbL film

XPS analysis recorded on the PEI/PSS/(0.2%Ag-TiO_2) and the PEI/PSS/(1%Ag-TiO_2) are reported in Figure 82 and Figure 83. XPS orbital spectra were similar to those recorded on the silver-free 10 layer pairs film. However there is some differences:

- In terms of Si/Ti surface atomic ratio, that is higher for both single layer films than the 10 layer pairs film, as a result of a lower coverage of the substrate. This was also visible on the O 1s spectra, which showed higher contributions from O-Si and O-H, attributed to the SiO_2 layer of the substrate.
- The presence of silver in the single layer PEI/PSS/(0.2%Ag-TiO_2) film was evidenced with the Ag $3d_{5/2}$ peak which is relatively narrow, suggesting only one predominant contribution, assigned to metallic Ag^0 (at 367.3 eV). However, the peak has a very low intensity, so that the Ag/Ti surface atomic ratio was found to be 0.0066 (i.e. 0.66 at.%), strongly lower than the Ag/Ti ratio determined by ICP-AES at 1.77 at.%. This may indicate that Ag may be located in the film porosity or at the PSS and TiO_2 interface, rather than at the surface of the sample. Indeed, one can note that Ag^+ ions may also interact with the PSS surface due to the high density of negative charges on the surface of the polyelectrolyte. Therefore there is a possibility that AgNP in these films may be not located on the top of the film surface, but rather located deeper in the film compared to the previous films constructed with commercially available AgNP or via the photoinduced synthesis of AgNP on pre-built PEI/PSS/TiO_2 films.

Considering the small difference in binding energy between Ag^0 and Ag^+ [200], [235], we cannot exclude partial oxidation of Ag particles in air, or maybe during the photo-induced synthesis, due to the photocatalytic activity of TiO_2 under UV-A irradiation. The Ag MNN core levels analysis was not fully conclusive, probably due also to the very low signal intensity. Kinetic energies of 1135.18 eV for Ag $M_5N_{45}N_{45}$ and 1127.54 eV for Ag $M_4N_{45}N_{45}$ were obtained, allowing Auger parameters to be calculated. On the other hand, regarding Auger parameter of Ag $M_4N_{45}N_{45}$, the value was found to be 726.4 eV, corresponding to silver in its metal form (726.5 eV for Ag^0). However the Auger parameter for Ag $M_5N_{45}N_{45}$ was found to be 719.3 eV, neither corresponding to Ag^+ (718.3 eV) or Ag^0 (720.5 eV) according to the work of Ferraria *et al* [200]. With such low intensity signals, it would be necessary to compare our parameters to Auger parameters determined by recording Ag^0 and Ag^+ references on the same XPS, rather than to refer to the literature data.

In the case of PEI/PSS/(1%Ag-TiO_2), the observation due to the possible specific location of AgNP in the film was amplified, no Ag $3d_{5/2}$ orbital peaks were observed due to the 0.2 wt.% of Ag/TiO_2

content, vs. 1.7 wt.% for the previous sample. On the other hand, Ag MNN core levels could be acquired, with kinetic energies of 351.5 eV for Ag $M_5N_{45}N_{45}$ and 359.4 eV for Ag $M_4N_{45}N_{45}$. Although Ag $3d_{5/2}$ binding energy could not be obtained for this sample, by taking the Ag $3d_{5/2}$ binding energy of the PEI/PSS/(0.2%Ag-TiO_2) sample, Auger parameters for Ag $M_5N_{45}N_{45}$ would have been 719.4 eV, while on the other hand the Auger parameter for Ag $M_4N_{45}N_{45}$ would have been 726.7 eV, corresponding to Ag^0 (726.5 eV) [200].

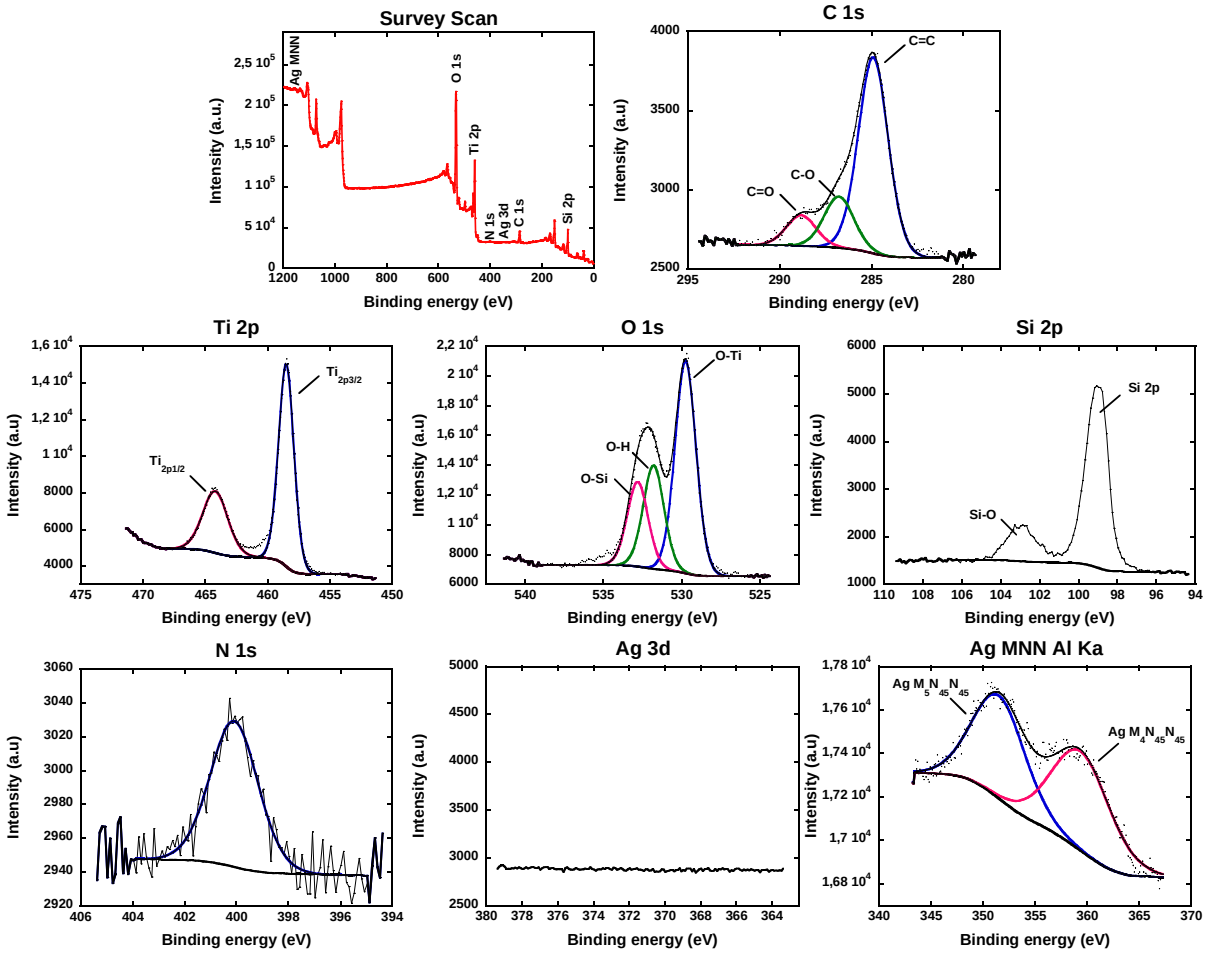

Figure 83 : XPS characterisations of PEI/PSS/(1%Ag-TiO_2) LbL film

II.3.2.4. TEM characterisations

TEM characterisations were performed on films constructed on TEM copper grids. In this project only two films were chosen for these characterisations. Our choices were made on the film containing the lowest and the highest amount of AgNP i.e. PEI/PSS/(0.2%Ag-TiO_2) (168 ng/cm² and 1.7 wt.%) and PEI/PSS/(1%Ag-TiO_2) films (44 µg/cm² and 0.2 wt.%) respectively (Figure 84). The analysis parameter had to be modified compared to the previous Ag-Ti system characterised by TEM. In fact when

observing the first images on the screen, it was possible to observe for a short time dark spots on TiO_2 nanoparticles, which represented AgNP. Once focussing on certain parts of the sample, fast disappearance of AgNP could be observed. Therefore the first TEM characterisation attempts were not conclusive and the analysis parameter had to be modified for characterising PEI/PSS/(x%Ag-TiO_2) films. Since an electron beam is received by the sample, we believe that AgNP may react with the electron from the beam and be oxidised back to their ion state Ag^+. As a consequence the power of the electron beam had to be lowered in order to acquire decent TEM images, although no high resolution images could unfortunately be recorded.

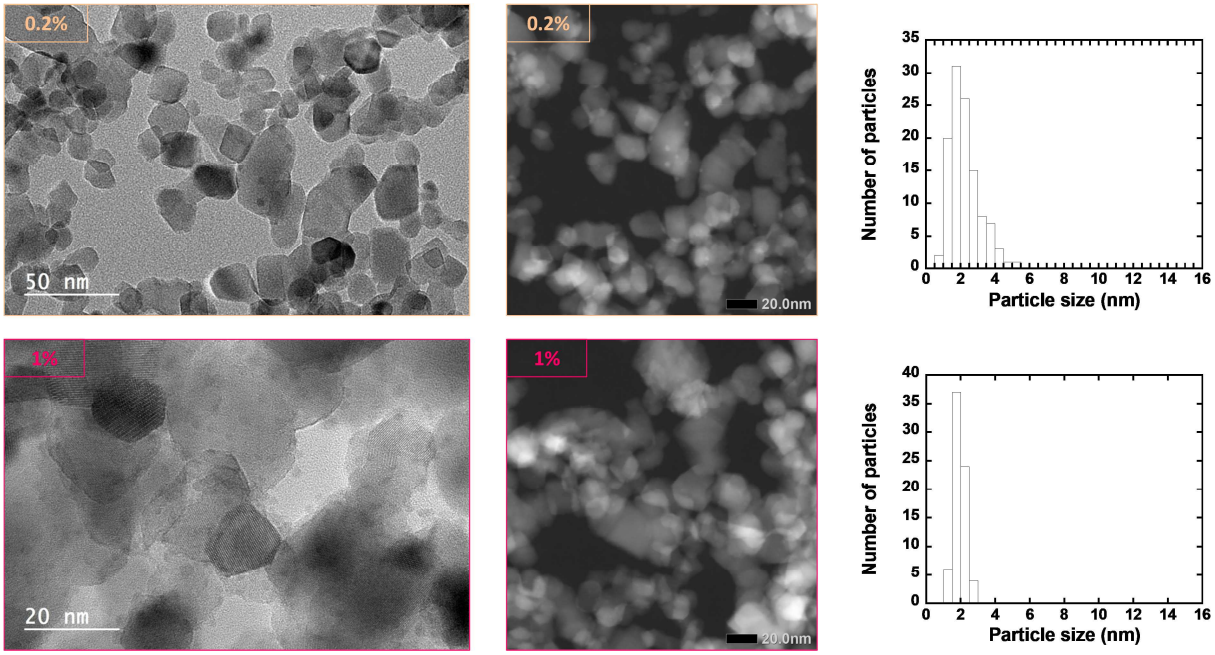

Figure 84 : TEM and STEM images of PEI/PSS/(0.2%Ag-TiO_2) and PEI/PSS/(1%Ag-TiO_2) films, with their particles counting assessed on STEM image (0.2%Ag-TiO_2) and TEM image (1%Ag-TiO_2).

On both films, it is worth noting that no free AgNP were observed: all AgNP were found in contact with TiO_2 nanoparticles, with a distribution in size from 0.5 to 4 nm, centred on 1.5 nm. TEM images of PEI/PSS/(0.2%Ag-TiO_2) films showed only a low amount of AgNP, however STEM images allowed a better image contrast between AgNP and TiO_2 nanoparticles. A slightly narrower AgNP size distribution (1-2.5 nm) was observed on PEI/PSS/(1%Ag-TiO_2), but also found to be centred on 1.5 nm.

II.3.3. Photocatalytic performances of PEI/PSS/(x%Ag-TiO_2) films

II.3.3.1. Results

The first photocatalytic tests on PEI/PSS/(x%Ag-TiO_2) films were performed by following the same protocol than that used for the Ag-TiO_2 films with silver deposited by the LbL blade-assisted method and classical photoinduced synthesis. While dark adsorption of gas phase HCOOH was performed during the night and the photocatalytic test was started the next day with UV-A irradiation of the films, 140 min were usually required to reach the HCOOH concentration set up for the test (145 ppm_v).

In contrast to the tests made with Ag-TiO_2 LbL films constructed by the blade-assisted technique and the classical photoinduced approach, the PEI/PSS/(AgNP-TiO_2) one-pot photoinduced films required a longer stabilisation time in the dark, and longer UV-A irradiation time for more than 3 h in order to reach stability in the conversion rate (stabilisation in the dark curves shown in Appendix 9). Photocatalytic results after 24 h of UV-A irradiation are presented in Table 22 and Figure 85.

While PEI/PSS/(0%Ag-TiO_2) gave a 4% HCOOH conversion after 3 h of UV-A irradiation, the conversion continued to increase until reaching a conversion rate of 14%, similar to that achieved on the silver-free single layer pair film. This increase with time may be assigned to the photocatalytic degradation of some chromophore residue under UV-A irradiation, leading to the unblocking of some TiO_2 active sites. The PEI/PSS/(0.5%Ag-TiO_2) film achieved a conversion of 50%, whereas the PEI/PSS/(1%Ag-TiO_2) film reached a 98%-100% conversion. Furthermore, the CO_2 formed was in good agreement with the theoretical value resulting from the HCOOH conversion.

Sample	**TiO_2 amount ($\mu g/cm^2$)**	**Ag amount (wt.%)**	**HCOOH Conversion (%)**	**CO_2 formed (ppm_v)**	**Theoretical CO_2 formed (ppm_v)**
PEI/PSS/TiO_2	7 ± 1	0	13 ± 1	29 ± 1	17 ± 1
PEI/PSS/(0%Ag-TiO_2)	7 ± 1	0	14 ± 1	26 ± 1	21 ± 1
PEI/PSS/(0.5%Ag-TiO_2)	9 ± 2	1.65	50 ± 3	72 ± 4	78 ± 4
PEI/PSS/(1%Ag-TiO_2)	18 ± 4	0.24	98 ± 5	136 ± 7	147 ± 7

Table 22 : Photocatalytic results of PEI/PSS/(x%Ag-TiO_2) films under UV-A irradiation.

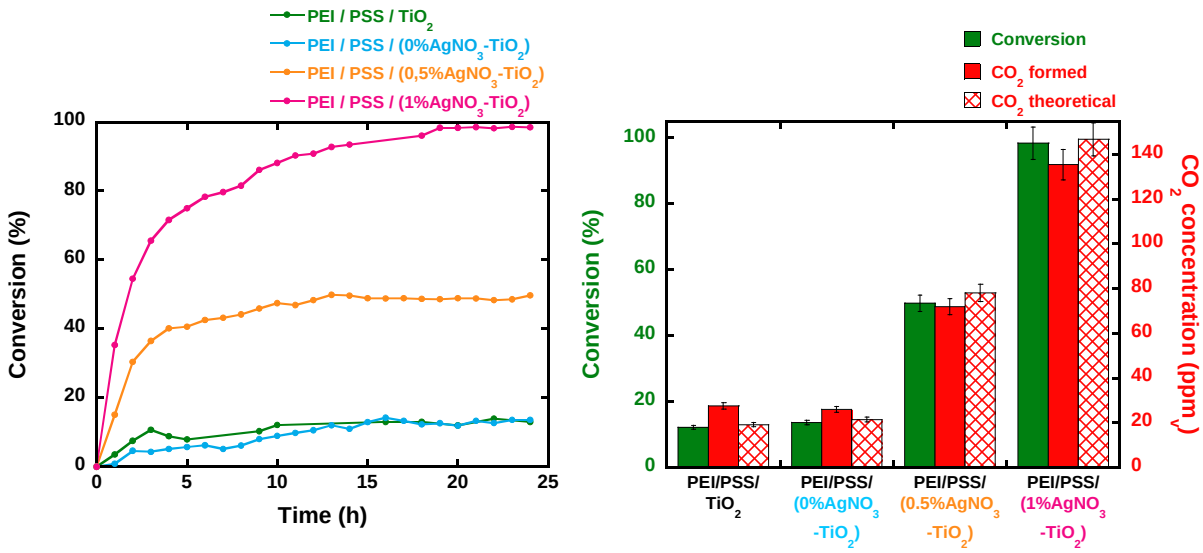

Figure 85 : (Left) Evolution of gas-phase HCOOH conversion during UV-A irradiation of PEI/PSS/(x%Ag-TiO_2) films. (Right) Photocatalytic performance of PEI/PSS/(x%Ag-TiO_2) films. Experimental parameters: [HCOOH] = 145 ppm_v, air flow = 20 mL/min, speed = 0.7 cm/s, UV-A irradiance = 2.5 mW/cm², films built on 36 cm² silicon wafers.

Since the PEI/PSS/(1%Ag-TiO_2) film showed almost 100% conversion of formic acid, the photocatalytic tests were performed once again on the PEI/PSS/(x%Ag-TiO_2) films, with a higher concentration of HCOOH (255 ppm_v), i.e. in stronger reaction conditions. Moreover, films constructed with $AgNO_3$ concentrations of the TiO_2 photosensitive suspension ranging from 0 to 2%, were tested in order to see if there is a critical AgNP concentration for which the photocatalytic tests showed a significant change in results. This corresponded to a AgNP content ranging from 0 to 2.2 wt.% in regards to the amount of TiO_2 deposited. Results of photocatalytic tests with an increase in HCOOH concentration are shown in Table 23-24 and Figure 86-87. The PEI/PSS/TiO_2 reference film showed a decrease in conversion from 13% to 6%. The results clearly evidenced that the elaboration of a hybrid PEI/PSS/(Ag-TiO_2) film could strongly enhance the photocatalytic activity of films. Indeed, whatever the AgNP content within the films, the HCOOH conversion was strongly enhanced, from 6% for the silver-free film, to 64% and 77% for the films containing 0.2 wt.% and 0.5 wt.% of AgNP in regards to the TiO_2 amount. The HCOOH conversion was as high as the AgNP/TiO_2 ratio was low (Figure 87A).

The results of the photocatalytic tests results for all LbL films, with an input gas-phase HCOOH concentration of 255 ppm_v, were combined to the UV-Visible characterisation for calculating the quantum yields (Table 24 and Figure 88).

Sample	TiO_2 amount (µg/cm²)	Ag/TiO_2 (wt.%)	HCOOH conversion (%)	CO_2 formed (ppm_v)	Theoretical CO_2 formed (ppm_v)
PEI/PSS/TiO_2	7 ± 1	0	6 ± 1	23 ± 1	15 ± 1
PEI/PSS/(0%Ag-TiO_2)	7 ± 1	0	13 ± 1	34 ± 2	32 ± 2
PEI/PSS/(0.1%Ag-TiO_2)	7 ± 1	2.2	13 ± 1	26 ± 1	32 ± 2
PEI/PSS/(0.2%Ag-TiO_2)	10 ± 2	1.7	32 ± 2	56 ± 3	77 ± 4
PEI/PSS/(0.5%Ag-TiO_2)	9. ± 2	1.6	26 ± 1	65 ± 3	69 ± 3
PEI/PSS/(0.7%Ag-TiO_2)	17 ± 3	0.6	32 ± 3	70 ± 7	82 ± 8
PEI/PSS/(1%Ag-TiO_2)	18 ± 4	0.2	77 ± 4	140 ± 7	195 ± 10
PEI/PSS/(1.5%Ag-TiO_2)	12 ± 2	0.4	64 ± 3	121 ± 6	164 ± 8
PEI/PSS/(2%Ag-TiO_2)	6 ± 1	1.7	28 ± 1	67 ± 3	72 ± 4

Table 23 : Photocatalytic results of PEI/PSS/(x%Ag-TiO_2) films under 24h of UV-A irradiation with an input HCOOH concentration of 255 ppm_v. Experimental parameters: [HCOOH] = 255 ppm_v, air flow = 20 mL/min, speed = 0.7 cm/s, UV-A irradiance = 2.5 mW/cm², films built on 36 cm² silicon wafers.

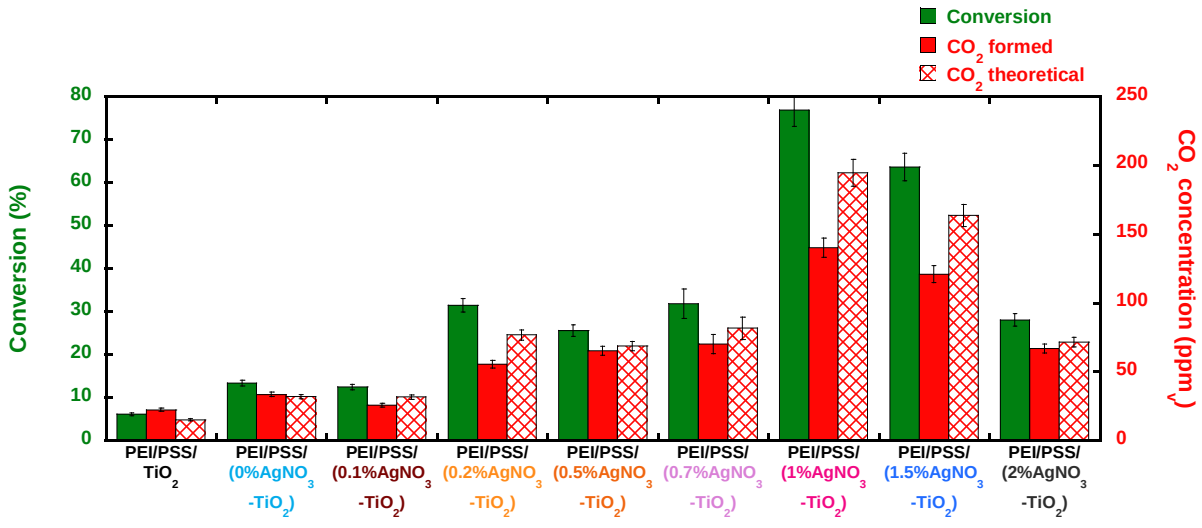

Figure 86 : Photocatalytic performance of PEI/PSS/(x%Ag-TiO_2) films under 24h of UV-A irradiation. Experimental parameters: [HCOOH] = 255 ppm_v, air flow = 20 mL/min, speed = 0.7 cm/s, UV-A irradiance = 2.5 mW/cm², films built on 36 cm² silicon wafers.

Sample	TiO_2 amount (µg/cm²)	Ag-TiO_2 (wt.%)	HCOOH Conversion (%)	HCOOH degraded ($x10^{-11}$ mol/µg TiO_2•min)	Apparent quantum yield η_{app} (%)	Quantum yield η (%)
PEI/PSS/TiO_2	7 ± 1	0	6 ± 1	5.2 ± 0.3	0.12	0.30
PEI/PSS/(0.1%Ag-TiO_2)	7 ± 1	2.18	13 ± 1	10.7 ± 0.5	0.22	0.54
PEI/PSS/(0.2%Ag-TiO_2)	10 ± 2	1.66	32 ±1	17.7 ± 0.9	-	-
PEI/PSS/(0.5%Ag-TiO_2)	9. ± 2	1.65	26 ± 1	18.8 ± 0.9	0.48	0.73
PEI/PSS/(0.7%Ag-TiO_2)	17 ± 3	0.61	32 ± 3	11.6 ± 0.6	-	-
PEI/PSS/(1%Ag-TiO_2)	18 ± 4	0.24	77 ± 4	25.2 ± 1.3	1.34	1.87
PEI/PSS/(1.5%Ag-TiO_2)	12 ± 2	0.48	64 ± 3	33.3 ± 1.7	-	-
PEI/PSS/(2%Ag-TiO_2)	6 ± 1	1.75	28 ± 1	26.3 ± 1.3	-	-

Table 24 : Number of mol of HCOOH degraded by PEI/PSS/(x%Ag-TiO_2) films and quantum yields.

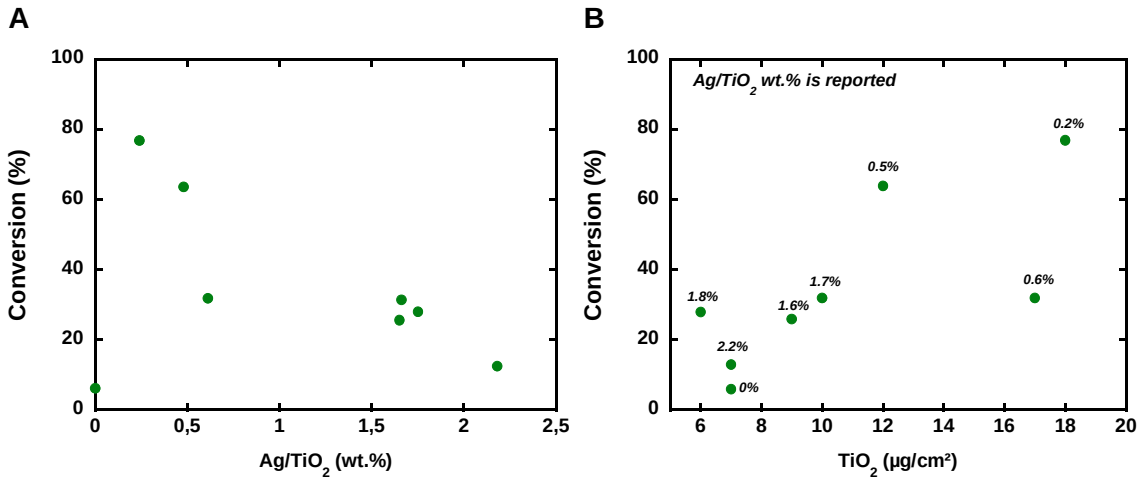

Figure 87 : (A) HCOOH conversion in regards to the Ag/TiO_2 content. (B) HCOOH conversion in regards to the amount of TiO_2 in PEI/PSS/(AgNP-TiO_2) film. Experimental parameters: [HCOOH] = 255 ppm_v, air flow = 20 mL/min, speed = 0.7 cm/s, UV-A irradiance = 2.5 mW/cm², films built on 36 cm² silicon wafers.

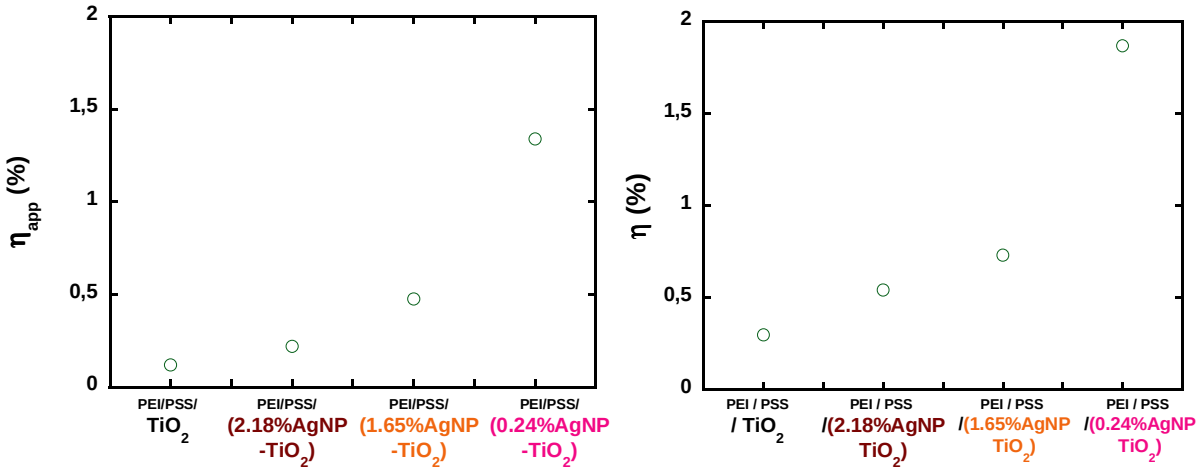

Figure 88 : Apparent quantum yield (left) and quantum yield (right) of PEI/PSS/(x%Ag-TiO_2) films upon UV-A irradiation, with x = 0.1, 0.5 and 1%.

The elaboration of films with different contents of TiO_2 made the comparison more complex. By looking at the amount of HCOOH degraded (per µg TiO_2•min) in regards to the silver content in the film, no trend could be highlighted (graph showed in appendix). However the HCOOH conversion curve in regards to the TiO_2 content has allowed to evidence that both TiO_2 content in the film and Ag/TiO_2 wt.% were influencing the HCOOH conversion (Figure 87B). On one hand, at a given TiO_2 content, the smaller the Ag/TiO_2 wt.% content, the higher the HCOOH conversion. On the other hand, the deposition of higher TiO_2 contents led to higher HCOOH conversion. Both effects could be combined and the films with 12 and 18 µg/cm² of TiO_2 associating silver with the low Ag/TiO_2 weight ratio of 0.2-0.5 displayed HCOOH conversion 10-11 times higher than that achieved on the bare Ag-free reference films.

The apparent quantum yield results increased when decreasing the silver/TiO_2 content. The results assessed on 4 values followed the same trend as the HCOOH conversion in regards to silver content in the films. Here the apparent quantum yield was found to be 11 times higher for a film containing 0.24 wt.% AgNP (1.34% efficiency), compared to the silver-free film PEI/PSS/TiO_2 (0.12% efficiency). This behaviour was also found in the efficient quantum yield (taking into account the film absorption). The results showed an increase in film efficiency while decreasing the silver content, from 0.54% (2.18%Ag-TiO_2 film) to 1.87% (0.24%Ag-TiO_2 film). Note that the silver free film PEI/PSS/TiO_2 showed 0.3% quantum efficiency, showing therefore an increase in efficiency by 6.2 when having 0.24% AgNP.

It must be mentioned that the quantum yields of the Ag-TiO_2 hybrid film cannot be compared to those calculated for silver-free PEI/$(PSS/TiO_2)_n$ LbL films in Chap 3.II.2.1, due to a difference in the type of substrate (quartz for silver-free film, and glass for Ag-TiO_2 films) on which the film were constructed. Moreover, the data were acquired with two different UV-Visible spectrophotometers, that are different in the parameters' settings, related to the optics.

II.3.3.2. Time resolved microwaved conductivity characterisations

TRMC characterisations were applied on PEI/$(PSS/TiO_2)_n$ films in Chap 3.II.2.2.1. and results showed an increase in I_{max} while I_{40}/I_{max} remained constant with the increase in the number of layer pairs increased. The PEI/PSS/TiO_2 single layer pair film did not provide any TRMC signal, which was associated to a low amount of titania deposited on the film.

Here TRMC characterisations were performed on films constructed with 0%$AgNO_3$-TiO_2, 0.5%$AgNO_3$-TiO_2 and 1%$AgNO_3$-TiO_2 photosensitive TiO_2 suspension. However, taking into account the apparent linearity of the relationship between the number of layers and I_{max}, a I_{max} value could be extrapolated at about 0.006 for a single layer pair film (Figure 89). Like the single layer pair PEI/PSS/TiO_2 film, the PEI/PSS/(0%Ag-TiO_2) film did not present a suitable TRMC signal to be analysed. On the other hand, a TRMC signal could be acquired for the single layer pair films constructed with the photosensitive TiO_2 suspension containing the silver precursor (Figure 89). Values of I_{max} and I_{40}/I_{max} are reported in Table 25 and are compared to those of silver-free samples TRMC results (n = 2-4).

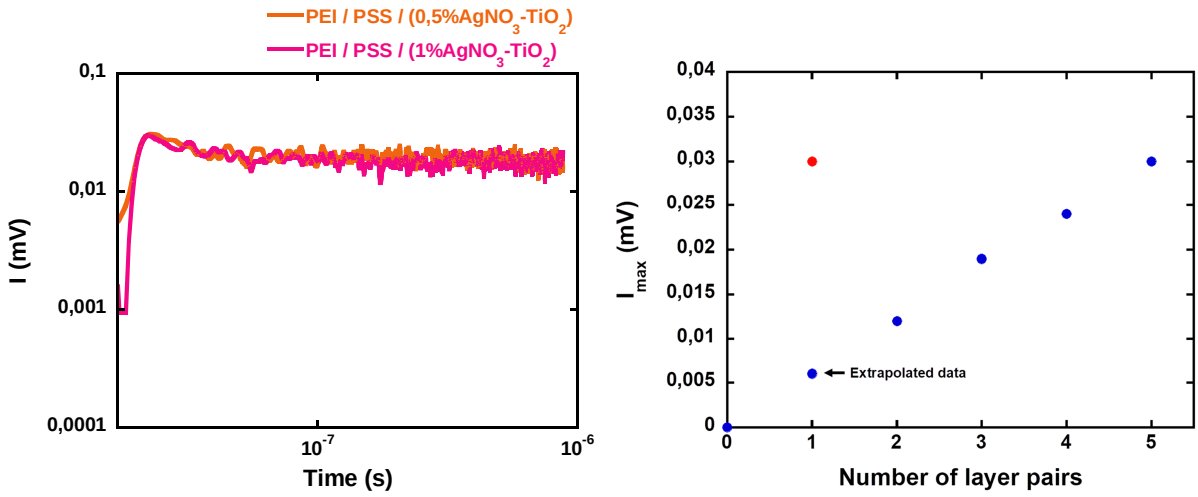

Figure 89: (Left) TRMC characterisations of PEI/PSS/(0.5%Ag-TiO_2) and PEI/PSS/(1%Ag-TiO_2) films. (Right) I_{max} values for the PEI/$(PSS/TiO_2)_n$ films (●) and Ag-TiO_2 hybrid film I_{max} value (●).

Sample	I_{max} (mV)	I_{40}/I_{max} (a.u)
PEI/(PSS/TiO_2)$_2$	0.012	0.471
PEI/(PSS/TiO_2)$_3$	0.019	0.573
PEI/(PSS/TiO_2)$_4$	0.024	0.537
PEI/PSS/(0.5%Ag-TiO_2)	0.031	0.630
PEI/PSS/(1%Ag-TiO_2)	0.030	0.588

Table 25 : Comparison of I_{max} and I_{40}/I_{max} values of PEI/(PSS/TiO_2)$_n$ and PEI/PSS/(x%Ag-TiO_2) films.

Interestingly, by contrast to the PEI/PSS/TiO_2 single layer pair film, both films with a single layer of AgNP-TiO_2 showed a measurable TRMC signal, with I_{max} equal to 0.03 mV. This measurable value was significantly higher than that extrapolated for the PEI/PSS/TiO_2 silver-free film. While this higher value could be attributed to the higher amount of TiO_2 for the PEI/PSS/(1%Ag-TiO_2), this hypothesis can be ruled out for the 0.5%$AgNO_3$-TiO_2 system, that had the same amount of TiO_2 as the silver-free PEI/PSS/TiO_2 film. So, this may indicate that the PEI/PSS/(Ag-TiO_2) film is generating a higher number of photogenerated charges under UV-A irradiation. The ratio I_{40}/I_{max} gives indication on the life-time of charge carriers of titania LbL film. It appeared that both films had I_{40}/I_{max} ratio away the highest compared to the Ag-free films. But we have to say that the difference remains moderate, so that we cannot conclude positively or negatively on a possible extension of the charge carriers.

II.3.3.3. Discussion

The association of LbL self-assembly technique and the silver photoinduced synthesis has allowed the *in situ* synthesis of AgNP in the titania layer, by changing the solvent from the photosensitive formulation to the titania suspension. While samples with Ag synthesised by the classical approach showed an increase in the silver content in the films by increasing the concentration of the silver precursor in the photosensitive solution, films containing silver nanoparticles synthesised with the one-pot photoinduced synthesis showed a different result. A decrease in Ag/TiO_2 wt.% content could be observed in films built with 0.1 to 1 wt.% $AgNO_3$ in the photosensitive TiO_2 suspension (from 2.18 wt.% to 0.24 wt.%, respectively), with a further increase in Ag/TiO_2 wt.% content by further increasing the silver precursor content (up to 1.75 wt.%). Interestingly, the Ag-TiO_2 LbL hybrid films constructed with the one-pot photoinduced approach did not provide any visual evidences of AgNP

synthesis, and transmission UV-Visible spectroscopy did not show any clear plasmon band associated with AgNPs, although the presence of silver as small size AgNP was shown by combining characterization techniques such as chemical analysis ICP-AES, TEM/STEM microscopy and XPS surface analysis. The absence of any visible evidence, although rendering the systems more difficult to characterize, is very interesting for the targeted applications of such photoactive films.

It was worth nothing that a very low Ag/Ti surface atomic ratio was obtained from XPS surface analysis when compared to the bulk ratio determined by chemical analysis ICP-AES, with (when observed) a very low intensity signal corresponding to the silver atoms. This led us to suggest that, rather than being synthesized at the external surface of the TiO_2 layer, AgNPs could be located in the porosity of the TiO_2 layer or at the interface of the PSS and TiO_2 layer where Ag ions from the photosensitive TiO_2 suspension may interact with the PSS layer prior UV irradiation of the film.

The one-pot photoinduced method appeared to be interesting for synthesizing fully selectively calibrated AgNP in contact with TiO_2 particles, no free AgNP being synthesized, thanks to the adsorption/interaction of the silver precursor on the TiO_2 within the film. Very narrow particle size distributions centred at about 2 nm for different AgNP contents were obtained.

Surprisingly, TRMC characterisations did not allow us to evidence a lowering of the photogenerated charge carrier recombination for two very active PEI/PSS/(Ag-TiO_2) films, as an electron trap effect is usually proposed in the literature for explaining enhanced performances obtained when associating AgNP and TiO_2 in a proper way. So, the positive role played by the AgNP at the surface of TiO_2 acting as an electron acceptor and thus improving the charge separation, is still a valid hypothesis, despite the fact that we could not evidence it via TRMC. As a result, a higher concentration of photogenerated charge carriers could be supported in the TiO_2 particles.

Moreover, very surprisingly, TRMC characterization may suggest that PEI/PSS/(Ag-TiO_2) films obtained by the one-pot approach could provide a higher number of photogenerated charge carriers than a Ag-free PEI/PSS/TiO_2 film, considering data extrapolated from a linear relationship with increasing the number of layer pairs. While this higher value could be explained by the higher amount of TiO_2 in one of the samples, a different explanation has to be provided for the other sample, that contained a similar amount of titania than the Ag-free reference film.

So, we suggest to put forward and to discuss also a second hypothesis, which may be related to the plasmon resonance of AgNP. It is admitted that silver is one of the most interesting metals due to the plasmonic resonance of Ag nanoparticles in the optical range of UV and near-UV visible light, that depends mostly on the particle size and shape [14]. Using large size AgNP at 40 ± 12 nm with a broad

absorption centered around 450 nm, P.A. Gross observed an increase in photocurrent under visible light (especially at low bias), and he suggested that AgNP improved the electron/hole pair generation under visible light photons. This was attributed to the absorption of visible light photons by AgNP by interaction with collective plasmon resonance followed by the energy transfer into TiO_2 [15]. Higher photocatalytic activities in the oxidation of organic dyes on Ag-modified TiO_2 particles have been attributed to the excitation of Ag plasmon resonance [236]. In our work, the films were active under UV-A irradiation, so that a plasmon band in the UV region of the spectra is required for such an hypothesis. The very broad absorption band observed in the beginning of the visible part of the spectra with Ag-TiO_2 systems on glass slides, and the increase in absorbance in the UV-A region on the Ag-TiO_2 LbL film, may suggest that the AgNP plasmon band could however slightly overlap with the UV-A region. In this case, the AgNP could also absorb a fraction of the UV-A irradiation.

The mechanisms involved in the possible plasmon band-assisted enhancement of photocatalytic activity is largely still under debate.

It may concern the injection of hot (excited, energetic) electrons from the AgNP to the conduction band of TiO_2 particles, thanks to intimate (electro)chemical contact between the plasmonic particle and the semiconductor, this direct charge injection mechanism being quite similar to the mechanism of photosensitization. This aspect is somehow at the moment controversial for silver.

On another hand, the second mechanism relates to the enhanced near-field hypothesis, which assumes radiative energy transfer between the metal and the semiconductor. In this case, field enchancement can only be effective with an overlap of the plasmon wavelength and the photocatalyst absorption (here the case with UV-A active TiO_2). The electrical field associated with charge accumulation on the metal surface can be quite intense. Since the number of electron/hole pair is directly proportional to the intensity of the surrounding electromagnetic field, it is to be expected that more charge carriers are formed in the close vicinity of plasmonic nanoparticles (the field intensity drops exponentially with increasing distance from the nanoparticle, but it can still be significant at a distance of several nanometers). Because the field intensity strongly decreases with distance, more charge carriers are generated close to the TiO_2 surface, rather than in the bulk , and consequently short charge carrier diffusion distances apply that minimize charge recombination, and potentially lead to higher photocatalytic efficiency [13].

Finally, the extension of the effective optical path length by means of multiple scattering is unprobable here, since it is reported to be mainly important for large plasmonic nanoparticles, i.e. with diameters of the same order of magnitude as the incident light wavelength.

All the three methods used led to higher photocatalytic performances of the films, to a more or less extent. However, by comparing the 3 methods investigated in this work, the one-pot photoinduced AgNP synthesis approach definitively provided the highest photocatalytic activity for the degradation of gas phase HCOOH, even for films with higher AgNP content than that of both PEI/PSS/TiO_2/AgNP films (with AgNP deposited via blade-assisted LbL approach, or synthesised by the classical photoinduced approach). Figure 90 summarizes a comparison of the photocatalytic results obtained on the more interesting Ag-TiO_2 films constructed with the three approaches investigated in this work. Different Ag/TiO_2 wt.% contents are showed in the graph, highlighting the influence of the type of film construction.

.

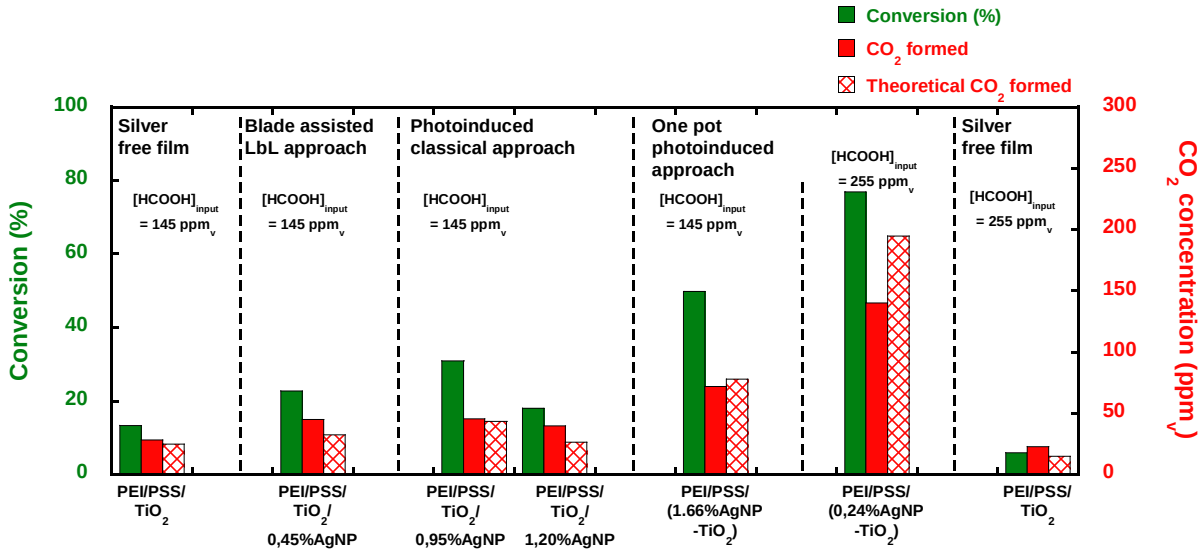

Figure 90: Comparison of the photocatalytic performances shown by Ag-TiO_2 films prepared $_{via}$ the three approaches.

III – Biocidal activity of Ag and titania hybrid thin films

III.1. Choice of Ag-TiO_2 hybrid thin films

In the previous section, the photocatalytic activity toward the degradation of gas HCOOH was evaluated for the three Ag-TiO_2 films investigated in this work, obtained with different ways of depositing or synthesising AgNP. The best photocatalytic performances were observed for the

PEI/PSS/(AgNP-TiO_2) films, where the AgNP photoinduced synthesis was combined with the LbL deposition of the titania layer, resulting in a one-pot photoinduced approach. The bacteria assays were therefore performed on Ag-TiO_2 films constructed with the one-pot photoinduced approach. In this study, two Ag-TiO_2 LbL films that showed different photocatalytic performances while having a similar Ag content in the films, were chosen for evaluating their biocidal properties under UV-A light and in the dark (Table 26).

Sample	**Amount of TiO_2 (µg/cm²)**	**Ag/TiO_2 content (wt.%)**	**HCOOH conversion (%)**
PEI/PSS/TiO_2	7 ± 1	0	6 ± 1
PEI/PSS/(0.1%Ag-TiO_2)	7 ± 1	2.18	13 ± 1
PEI/PSS/(0.5%Ag-TiO_2)	9 ± 2	1.65	26 ± 1

Table 26 : Silver content and HCOOH conversion results of the Ag-TiO_2 LbL films to be tested for antibacterial assay. Experimental parameters: [HCOOH] = 255 ppm_v, air flow = 20 mL/min, speed = 0.7 cm/s, UV-A irradiance = 2.5 mW/cm², films built on 36 cm² silicon wafers

The two Ag-TiO_2 LbL films were compared to a silver-free single layer PSS/TiO_2 film, which showed biocidal properties for 60 min of UV-A irradiation (Chap 3.III.3).The samples were also compared to a bare silicon wafer and a PEI/PSS film as reference samples. The LbL films were all constructed on silicon wafer and the 5 samples were labelled as follow:

- WF: Silicon wafer
- PEI/PSS: film with a PEI and PSS layer, labelled as REF 2 in Chap 3.III.
- PEI/PSS/TiO_2: Single layer pair film, labelled as 1 LP in Chap 3.III.
- (0.1%$AgNO_3$-TiO_2): PEI/PSS/(0.1%Ag-TiO_2) film
- (0.5%$AgNO_3$-TiO_2): PEI/PSS/(0.5%Ag-TiO_2) film

The biocidal properties of the LbL films containing AgNP were evaluated under UV-A irradiation using the same experimental procedure to that used for the PEI/$(PSS/TiO_2)_n$ films. All bacteria assays were performed by assessing the number of active bacteria (*E. Coli*),"ALIVE", and the damaged bacteria, "DEAD", before and after UV-A irradiation of the LbL films.

III.2. Biocidal properties of Ag-TiO_2 LbL thin film results and discussion

Results of the bacteria assay performed on the reference samples and the Ag-TiO_2 films are shown in Figure 91 to Figure 93.

Before irradiation, the bacteria were incubated on the films for 3 h. The bacteria colony was found to be higher on the PEI/PSS, PEI/PSS/TiO_2, PEI/PSS/(0.1%Ag-TiO_2) and PEI/PSS/(0.5%Ag-TiO_2) than the bare silicon wafer. Due to the neutral nature of the silicon wafer for bacteria adhesion (no positive, nor negative control), the LbL films could be considered as suitable surfaces for bacteria adhesion and proliferation. All LbL films were concerned, as well as the films containing Ag, in which the Ag content appeared to be too low to provide a significant biocidal effect. However, the number of aggregated colonies is lower on the TiO_2 films, and decreases further on the Ag-containing films. On the Ag-TiO_2 hybrid films, this decrease in bacteria aggregation suggested a low toxic effect from Ag, but insufficient to induce bacteria death. XPS characterisation of the PEI/PSS/(AgNP-TiO_2) films (Chap 4.II.3.2.3) showed that AgNP are most likely located in the film porosity and/or at the interface of the PSS and TiO_2 layer, rather than at the external surface of the film. Therefore most of AgNP are not accessible to the bacteria and the biocidal activity of the film in the dark, induced by leaching of Ag^+ from AgNP, is not observed in our work.

After UV-A irradiation, the number of metabolically active bacteria decreased by 2 on the PEI/PSS/(0.5Ag-TiO_2) films, whilst the isolated bacteria were slightly more affected than the bacteria in colonies (“aggregates”). Moreover, a high number of active bacteria were found to have a damaged membrane, indicating that a photocatalytic biocidal effect occurred, but not pronounced enough for leading to the death of bacteria, that can stay metabolically active (confocal images not shown).

On the other hand, the number of metabolically active bacteria was found to remain the same after UV-A irradiation of the PEI/PSS/TiO_2 and PEI/PSS/(0.1Ag-TiO_2) films. Coherently with the expected proliferation of the adhered bacteria, it appeared that the bacteria proliferation has even slightly increased on the PEI/PSS, PEI/PSS/TiO_2 and PEI/PSS/TiO_2/(0.1%Ag-TiO_2). Once again, these films have appeared to be more suitable for bacteria adhesion and proliferation than the bare silicon wafer.

However, it was found that a low number of isolated bacteria with damaged membranes was observed for PEI/PSS/TiO_2 and PEI/PSS/(0.1%Ag-TiO_2) film, suggesting that an antibacterial photocatalytic effect of the films under UV-A irradiation occurred, although at a low level. The aggregated bacteria were not affected, and appeared to be somehow protected compared to isolated bacteria.

Overall the antibacterial photocatalytic effect of the PEI/PSS/TiO_2 film was not high enough to cause a significant reduction of *E. Coli* bacteria population probably due to the low concentration of TiO_2 in the film, but was efficient enough for damaging the membrane of some bacteria. The addition of AgNP in the films leads to an enhancement in biocidal properties under UV-A irradiation. This enhancement was low for the PEI/PSS/(0.1%Ag-TiO_2) film (2.2 Ag/TiO_2 wt.%), with no decrease in number of active bacteria , as well as only a low amount of bacteria with a damaged membrane. The enhancement is higher and significant for the PEI/PSS/(0.5%Ag-TiO_2) film (1.6 Ag/TiO_2 wt.%), with a decrease in number of adhered bacteria, demonstrating a biocidal effect. The effect can be related to the photocatalytic activity of the association of Ag and TiO_2, since no direct biocidal effect of silver was observed (the initial number of bacteria being similar to the one of the Ag-free PEI/PSS/TiO_2 film).

So between those Ag-TiO_2 films, the most active in the degradation of gas-phase HCOOH was also the most active in terms of biocidal properties against *E. Coli* bacteria.

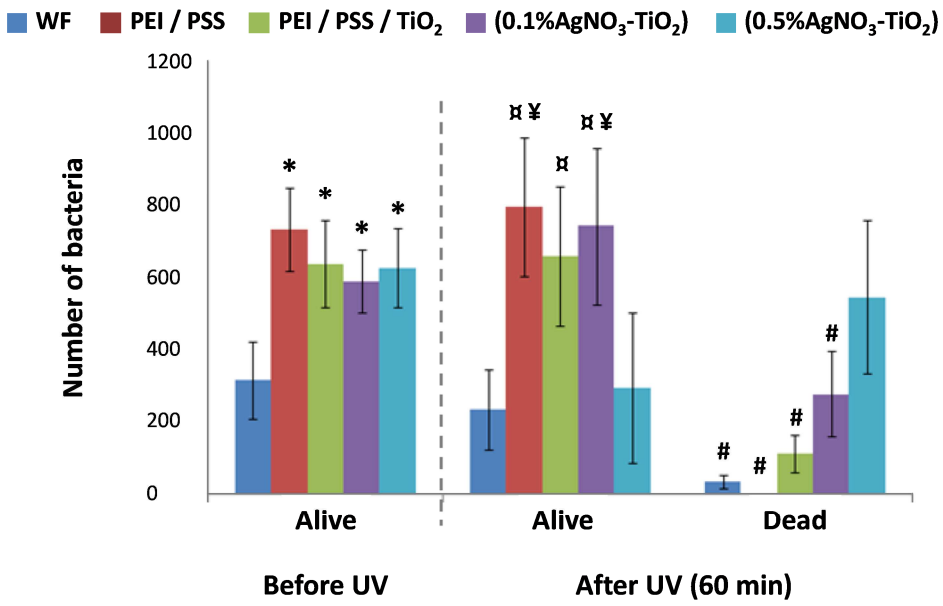

Figure 91: Number of active and damaged bacteria before and after UV-A irradiation of the films. Tested bacteria: *Echerichia Coli*, UV-A irradiance = 2.5 mW/cm², irradiation time = 60 min, films built on 2 cm² silicon wafers. (*) significantly different than WF before UV (*p*-value < 0.05); (¤) significantly different than WF after UV (ALIVE) (*p*-value < 0.05); (¥) significantly different than 0.5%$AgNO_3$-TiO_2 after UV (ALIVE) (*p*-value < 0.05); (#) significantly different than 0.5%$AgNO_3$-TiO_2 after UV (DEAD) (*p*-value < 0.05).

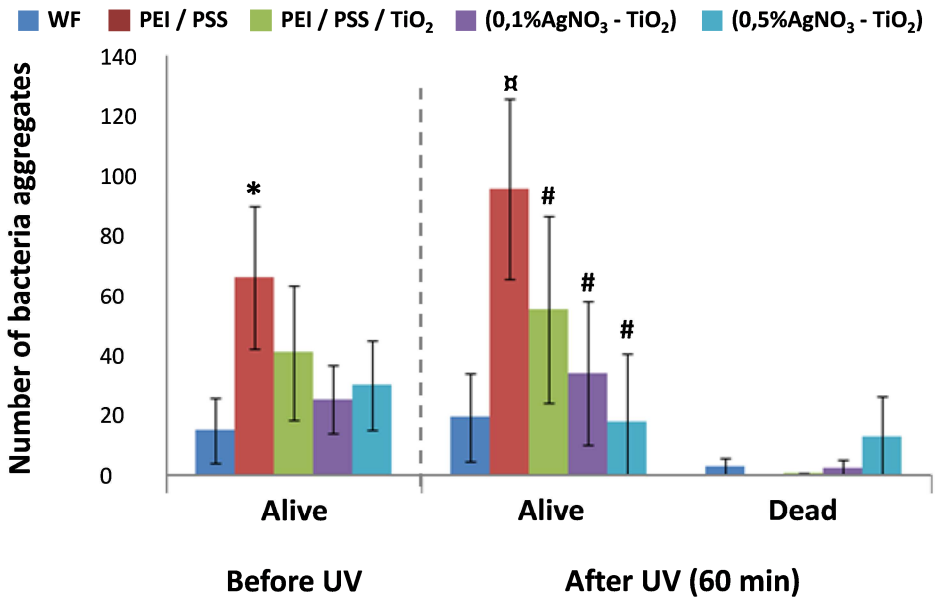

Figure 92 : Number of bacteria aggregates before and after UV-A irradiation of the films. Tested bacteria: *Echerichia Coli*, UV-A irradiance = 2.5 mW/cm², irradiation time = 60 min, films built on 2 cm² silicon wafers. (*) significantly different than WF before UV (*p*-value < 0.05); (¤) significantly different than WF after UV (ALIVE) (*p*-value < 0.05); (¥) significantly different than PEI/PSS after UV (ALIVE) (*p*-value < 0.05).

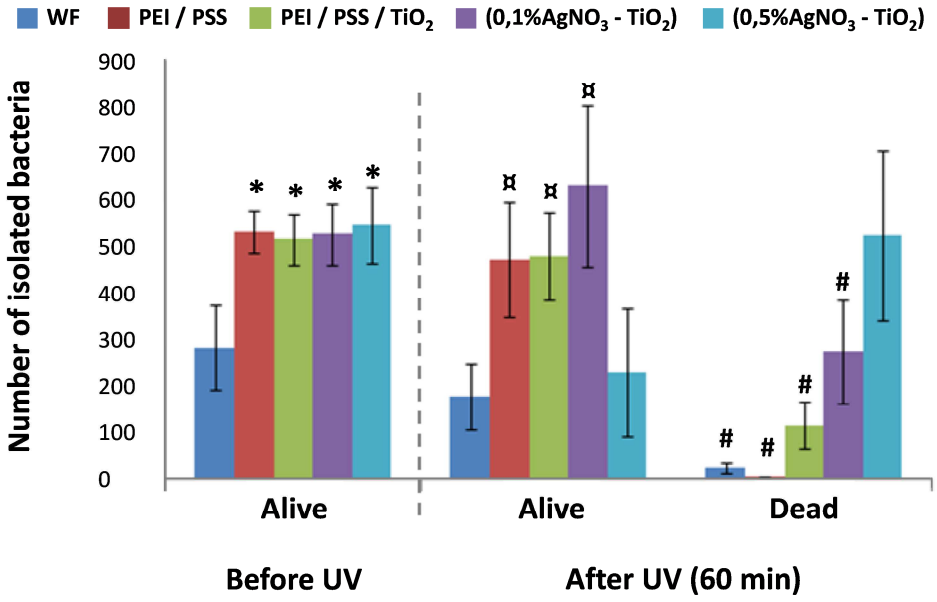

Figure 93 Number of isolated bacteria before and after UV-A irradiation of the films. Tested bacteria: *Echerichia Coli*, UV-A irradiance = 2.5 mW/cm², irradiation time = 60 min, films built on 2 cm² silicon wafers. (*) significantly different than WF before UV (*p*-value < 0.05); (¤) significantly different than 0.5%$AgNO_3$-TiO_2 after UV (ALIVE) (*p*-value < 0.05); (¥) significantly different than 0.5%$AgNO_3$-TiO_2 after UV (DEAD) (*p*-value < 0.05).

Chapter 4: Titania and silver nanoparticles hybrid thin films – construction on model surfaces

This chapter was dedicated to the elaboration of Layer-by-Layer Ag and titania nanoparticle films constructed on model surfaces and was focussed on single layer pairs films. Since a suitable contact between TiO_2 and AgNP must be obtained in order to enhance the photocatalytic activity of the film. Different approaches were developed and studied in this work. The first approach was by depositing commercial AgNP on PEI/PSS/TiO_2 by developing a blade-assisted LbL deposition method. The second approach was by directly synthesising AgNP on a pre-built PEI/PSS/TiO_2 film, using a AgNP photoinduced synthesis approach developed in the team of Lavinia Balan (IS2M, Mulhouse, France). The third approach was by combining the AgNP photoinduced synthesis approach with the LbL self-assembly technique, by developing a one-pot photoinduced synthesis where the solvent of photosensitive solution was replaced by the titania suspension, and was used for depositing the Ag-TiO_2 layer, before being irradiated by UV-A for AgNP synthesis within the film.

All approaches used in this work showed a successful deposition/synthesis of AgNP in the film, and all showed a more or less marked enhancement of the photocatalytic properties of the TiO_2 film towards the degradation of gas phase HCOOH. Hypotheses related to a role of electron acceptor (trapping) of AgNP in optimum amount and to a plasmon band-assisted enhancement, have been suggested and discussed. The best photocatalytic results were obtained for films with AgNP synthesised with the one-pot combined photoinduced approach, that allows construction in one step of the LbL film incorporating calibrated AgNP (2 nm) with a narrow size distribution in contact with TiO_2.

Film containing 0.24 wt.% of AgNP showed a 76% HCOOH conversion ($[HCOOH]_{input}$=255 ppmv) and a quantum yield of 1.87 %, so **one order of magnitude higher** compared to a single layer pair PEI/PSS/TiO_2 film (conversion of 6.2% and quantum yield of 0.3%). A combined effect of a higher content of TiO_2 in PEI/PSS/(AgNP-TiO_2) film, and of an optimum amount of AgNP was suggested to be responsible for the high activity of the film. Interestingly, it appeared that the Ag/TiO_2 wt.% content can be tuned by putting the appropriate amount of $AgNO_3$ in the photosensitive TiO_2 suspension.

While films constructed with the 3 approaches gave some Ag-TiO_2 films with similar AgNP content, the photocatalytic performances of the films were found to be different, highlighting the importance of the association of AgNP to TiO_2 nanoparticles in order to enhance the photocatalytic properties of the TiO_2 film under UV-A irradiation.

The biocidal performances of the Ag-TiO_2 films were evaluated on two films with AgNP synthesised with the one pot photoinduced synthesis approach, and the results showed a significant increase (even if moderate) in biocidal performance for both films under UV-A irradiation, thanks to the TiO_2-Ag association, rather than due to a biocidal effect of AgNP.

Chapter 5: Titania and silver-titania thin films – construction on textile surfaces

Introduction

The previous two chapters were dedicated to the LbL construction of titania and polyelectrolytes films, and of titania and AgNP films, on model surfaces. These studies have allowed monitoring the films construction, their characterisations, as well as evaluating their photocatalytic performances towards the degradation of gas phase formic acid, and their biocidal properties. The aim of this more applicative chapter is to evaluate the possibility to transfer the LbL construction of TiO_2 and AgNP-TiO_2 thin films from model surfaces to textiles to obtain textiles with photocatalytic activity under UV-A irradiation.

The transfer of the film construction on textile surfaces for both systems, as well as their characterisations, will be presented in the first part. The photocatalytic properties of the films under UV-A towards the degradation of gas-phase HCOOH will be evaluated in the second part. Then their biocidal properties towards different types of bacteria, upon UV-A irradiation or not, will be presented in the third part. Next their stability to different treatments i.e. abrasion and washing/cleaning treatment, will be evaluated.

I – Film construction on textile surfaces

I.1 Titania and polyelectrolytes LbL film on textile

As in the case of the PEI/$(PSS/TiO_2)_n$ films constructed on model surfaces, the influence of the number of PSS/TiO_2 layer pairs on the photocatalytic activity of the film was investigated. As a result, films containing up to 10 layer pairs were constructed on textile surfaces using the LbL dipping

technique. The experimental procedure was similar to that of the films constructed on model surfaces, with a slight modification regarding the drying step. When constructed on model surfaces, a drying step with compressed air was performed between the rinsing step and the deposition of the following layer on the sample. Since the textile fabrics were not as rigid as the model surfaces, the drying step was performed by placing the fabrics in a centrifuge, which allowed removal of the excess water absorbed in the textile fibres. The detailed experimental procedure is described in Chap 2.III.3.

I.1.1 Monitoring of film construction

The polyester textile used in this study has a white colour and remained the same while constructing the polyelectrolyte and titania layers onto it: no visual evidences of film construction could be observed (Figure 94).

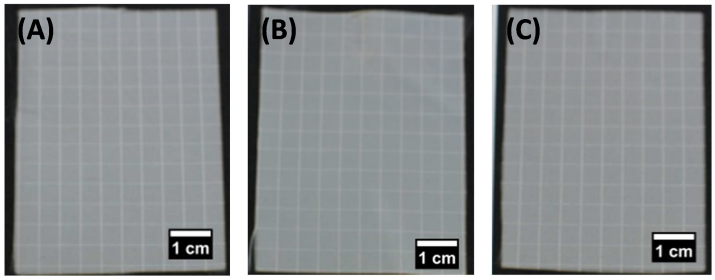

Figure 94 : Images of polyester textile used for LbL film construction. (A) Bare textile, (B) textile coated with a 1 layer pair film, (C) textile coated with a 10 layer pair film.

Since it is impossible to monitor the film construction on textile surfaces by ellipsometry or QCM-D, the qualitative quantification of the amount of deposited material on textiles was performed by measuring first the successive mass increment of the textile during the deposition process, by a conventional balance (mass measured on 29.25 cm^2 samples). The results were then compared to the mass of deposited material determined by thermogravimetric analysis (TGA, on 1 cm^2 samples) and to the amount of TiO_2 deposited, obtained by chemical analysis ICP-AES (1 cm^2 samples). Each system was measured on 3 samples, allowing an average estimation of the mass of deposited material, to be obtained with the calculation of the error bars. In the case of TGA, a bare textile was characterised in order to obtain the content of ashes (un-burnt residues) contained in the textile. This mass was then subtracted from the residual mass after the textiles functionalised by LbL films have been degraded/oxidised. It must be mentioned that the textiles were first dried in the TGA oven at 120°C for 1 h, in order to remove the excess water from the film. After this drying step, the measured mass was considered as the initial mass of the functionalised textiles. The results are displayed in Table 27 and compared in Figure 95.

Sample	Amount of TiO_2 deposited on model surfaces (µg/cm²)	Amount of deposited material (µg/cm²)		Amount of TiO_2 deposited on textile (µg/cm²)
	ICP-AES	Conventional balance	TGA	ICP-AES
PEI/PSS/TiO_2	7	34 ± 3	13 ± 4	38 ± 3
PEI/(PSS/TiO_2)$_2$	14	-	35 ± 1	60 ± 4
PEI/(PSS/TiO_2)$_3$	21	-	80 ± 8	90 ± 13
PEI/(PSS/TiO_2)$_4$	28	143 ± 11	101 ± 10	120 ± 13
PEI/(PSS/TiO_2)$_6$	42	194 ± 9	174 ± 4	182 ± 7
PEI/(PSS/TiO_2)$_{10}$	70	347 ± 36	236 ± 4	271 ± 18

Table 27 : Amount of deposited material on textile fibres, determined by weighting the mass increment with a conventional balance, and by TGA. Amount of TiO_2 deposited on textile determined by ICP-AES. "-": not measured.

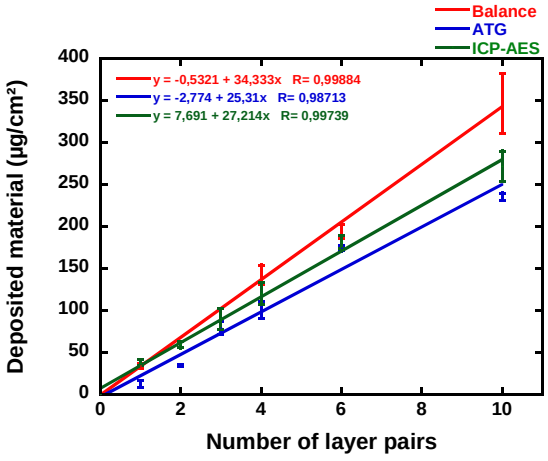

Figure 95 : Comparison of the amount of deposited material on textile surface using different characterisation methods.

The amount of deposited materials derived from the conventional balance measurements showed a material mass increment of 34 µg/cm², while TGA results showed a 25 µg/cm² increment. This difference could be explained by the error provided by the balance: the textile mass was obtained

with ± 0.01 mg precision. Also the water absorbed at ambient temperature in the textile is not considered in the TGA value (due to a prior in-situ drying), by contrast to the conventional balance analysis. Chemical analysis provided an estimation of TiO_2 deposited on the textile surface, which was found to be 26 µg/cm² per layer pair. This result was found to be lower than the one obtained by weighting the textiles on the balance, and similar to the amount of material determined by TGA. ICP-AES result highlights the fact that the increment of deposited material is mainly due to the amount of TiO_2 deposited. However the ICP-AES results also showed that the amount of TiO_2 was slightly higher than the amount of material deposited determined by TGA. This may show some limitations to provide a precise result with TGA, when subtracting the final mass of a burnt bare textile from a textile functionalised by LbL film, considering that the amount of ashes may vary from sample to sample. Therefore ICP-AES results will be used for determining the estimated amount of TiO_2 deposited per layer pair in this chapter. Although measuring the mass of textile by conventional balance may not be suitable for obtaining an estimation of the deposited material, but is a quick method which allows monitoring of the film construction on textile surface.

When compared to the titania LbL films constructed on model surfaces, the amount of deposited TIO_2 was found to be lower (5 µg/cm² per layer pairs) than that deposited on textile surfaces (27 µg/cm² per layer pairs). This can be due to the geometry of the textile samples, where the surface of the micrometer-size fibres will allow will allow more materials to be deposited, as opposed to the flat and smooth surface provided by the model surfaces exposing a pure geometric surface (silicon wafers, glass/quartz slides)..

I.1.2 SEM characterisation

SEM characterisations were performed on films with several PSS/TiO_2 layer pairs and compared to an untreated polyester textile (Figure 96). The first observation made on the sample without any film constructed onto the fibres, was that the textile charges quickly when characterised by SEM. Therefore images were difficult to obtain with a high magnification. This charging effect was not observed when characterising the films built on the textile surfaces, even for a single layer pair. While low magnification could not highlight a difference between a single and a 10 layer pairs film higher magnification showed an homogeneous distribution of TiO_2 nanoparticles over the fibres, providing them with a porous surface, although the fibre coverage was not total for the single layer pair film. This TiO_2 coating appeared denser for a 4-10 layer pairs film compared to a single layer pair film. On the 10 layer pair film, in addition to an homogeneous TiO_2 coverage over the fibres, TiO_2 aggregates were found to be located between the fibres in contrary to the 1-4 layer pairs film.

Overall SEM characterisations showed that the PEI/$(PSS/TiO_2)_n$ films were successfully constructed on polyester textile, with a homogeneous titania distribution from a single layer of TiO_2 deposited.

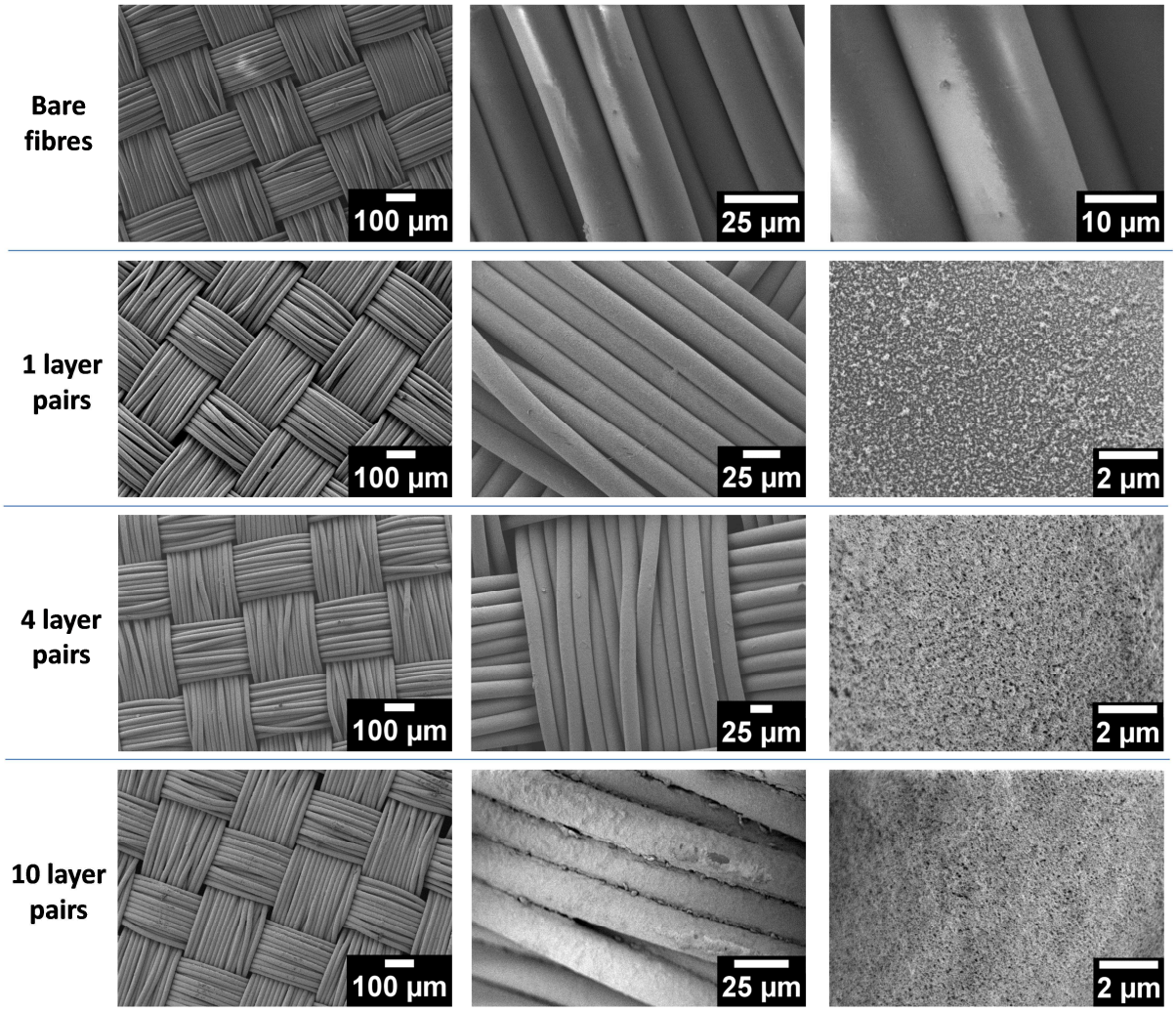

Figure 96 : SEM characterisation of PEI/$(PSS/TiO_2)_n$ LbL films constructed on polyester textile surface.

I.2 Silver-titania hybrid film constructed on textile

The study of single layer pair AgNP-containing PEI/PSS/TiO_2 films, constructed on model surfaces was discussed in Chapter 4. Three AgNP depositions/syntheses were investigated and the films showed photocatalytic activity towards the conversion of gas-phase formic acid under UV-A. The films constructed using the one-pot AgNP photoinduced approach showed the highest photocatalytic performances, and in addition displayed biocidal properties against *E. Coli* bacteria under UV-A. Therefore only the one-pot photoinduced synthesis was used in order to construct Ag-TiO_2 hybrid

films on textile surfaces. Two silver salt concentrations were used in the photosensitive TiO_2 suspension, 0.2 wt.% $AgNO_3$ that provides the highest concentration of AgNP synthesised in the film constructed on model surfaces, and 1 wt.% $AgNO_3$ that provides the best photocatalytic performances towards the degradation of gas-phase HCOOH. The deposition and the photoinduced synthesis of AgNP are described in Chap 2.III.2. SEM characterisation did not provide any evidences of synthesis of AgNP on the fibres, but it was found that TiO_2 was coated on the textile fibres, with a homogeneous surface coverage (images shown in Appendix 11). The amount of deposited material was determined by TGA analysis, and chemical analysis provided the amount of TiO_2 and Ag deposited on the textile surfaces. All characterisations were performed on three samples of each system (1 cm²) and results are shown in Table 28. These characterisations have evidenced deposition of TiO_2 on the textile fibres, as well as a successful *in-situ* AgNP synthesis.

Sample	**Amount of deposited material, TGA analysis (µg/cm²)**	**Amount of deposited materials on <u>textile</u> surfaces, ICP-AES analysis**			**Amount of deposited materials on <u>model</u> surfaces, ICP-AES analysis**		
		TiO_2 (µg/cm²)	**Ag (ng/cm²)**	**Ag/TiO_2 (wt.%)**	**TiO_2 (µg/cm²)**	**Ag (ng/cm²)**	**Ag/TiO_2 (wt.%)**
PEI/PSS/ TiO_2	25 ± 3	27 ± 3	0	0	7 ± 1	0	0
PEI/PSS/ (0.2%Ag-TiO_2)	44 ± 2	63 ± 4	160 ± 29	0.25	10 ± 2	168 ± 1	1.7
PEI/PSS/ (1%Ag-TiO_2)	57 ± 2	89 ± 3	123 ± 9	0.14	18 ± 4	44 ± 1	0.2

Table 28 : PEI/PSS/(x%$AgNO_3$-TiO_2) films constructed on textile. Amount of deposited materials and their concentrations.

TGA analysis showed that the amount of deposited material was higher than that of a single layer pair constructed on textile, with 44 µg/cm² and 57 µg/cm² for films constructed with 0.2%$AgNO_3$ and 1%$AgNO_3$ in the photosensitive TiO_2 suspension, respectively. Likewise chemical analysis results showed that the amount of TiO_2 deposited in the PEI/PSS/(x%$AgNO_3$-TiO_2) films was higher than in a silver-free PEI/PSS/TiO_2 film, with 63 µg/cm² and 89 µg/cm² of TiO_2 deposited. The ICP-AES results were once again higher than the one of TGA, which highlighted once again the limitation of TGA for

determination of the amount of TiO_2 deposited on textile compared to chemical analysis. Like for the Ag-TiO_2 hybrid films constructed on model surfaces, the amount of Ag was found to decrease while adding a higher silver precursor concentration in the photosensitive TiO_2 suspension. The Ag content (Ag/TiO_2 wt.%) was found to be 0.25 wt.% in the PEI/PSS/(0.2%$AgNO_3$-TiO_2) film, and 0.14 wt.% in the PEI/PSS/(1%$AgNO_3$-TiO_2) film. Therefore the two Ag-TiO_2 hybrid films will be addressed as PEI/PSS/(0.25%AgNP-TiO_2) and PEI/PSS/(0.14%AgNP-TiO_2) in this chapter.

Interestingly, the trend of the deposited material on the PEI/PSS film has appeared to be similar to that when the films are constructed on model surfaces with the one-pot photoinduced approach. While increasing the silver precursor, an increase in TiO_2 amount deposited could be observed, while the silver content was found to decrease. While films constructed with the 1%$AgNO_3$-TiO_2 photosensitive suspension showed a similar Ag/TiO_2 when built on textile and model surfaces (0.14 wt.% and 0.2 wt.%, respectively), the films constructed on textile with the 0.2%$AgNO_3$-TiO_2 photosensitive suspension gave a lower Ag/TiO_2 content (0.25 wt.%) compared to the films constructed on model surfaces (1.7 wt.%).

II – Photocatalytic properties of functionalised textiles towards the degradation of HCOOH

II.1 Formic acid degradation by titania and polyelectrolytes LbL film coated on textile

LbL films constructed on textile surfaces were tested for the degradation of gas-phase HCOOH under UV-A. The 29.25 cm^2-size textiles were cut and assembled on a 36 cm^2 silicon wafer in order to be immobilised during the tests. The tests were performed 3 times on each sample in order to obtain the average HCOOH conversion, CO_2 formation and theoretical CO_2 conversion, with their respective error bars (Table 29 and Figure 97). A bare textile was used as a control sample under UV-A irradiation, and neither HCOOH photocatalytic degradation could be observed, nor CO_2 formation.

The result showed a traditional behaviour of the photocatalytic activity in regards to the amount of photocatalyst. Photocatalytic activity could be observed for a single layer pair film, with a conversion rate of 41%. The conversion rate increased and reached already a plateau region for a two layer pairs film, with a conversion rate of 86%. In terms of CO_2 formation, the concentration appeared to increase according to the number of layer pairs (from to 58 to 159 ppm_v). These results were found to be different to that of PEI/$(PSS/TiO_2)_n$ constructed on model surfaces. However since the geometry influences the amount of deposited material, the film structure may be different on textile surfaces

compared to the one built on model surfaces. Therefore the density of the film could be higher in the films built on textile, resulting in a traditional trend of the photocatalytic performances of the film upon UV-A irradiation.

Sample	Conversion (%)	CO_2 formation (ppm_v)	Theoretical CO_2 formation (ppm_v)
PEI/PSS/TiO_2	41 ± 4	58 ± 6	19 ± 2
PEI/(PSS/TiO_2)$_2$	87 ± 7	105 ± 16	39 ± 4
PEI/(PSS/TiO_2)$_4$	87 ± 9	111 ± 17	39 ± 4
PEI/(PSS/TiO_2)$_6$	85 ± 9	101 ± 15	38 ± 4
PEI/(PSS/TiO_2)$_{10}$	86 ± 8	159 ± 24	38 ± 4

Table 29 : Photocatalytic results of PEI/(PSS/TiO_2)$_n$ LbL films constructed on polyester textile, towards the degradation of gas-phase HCOOH

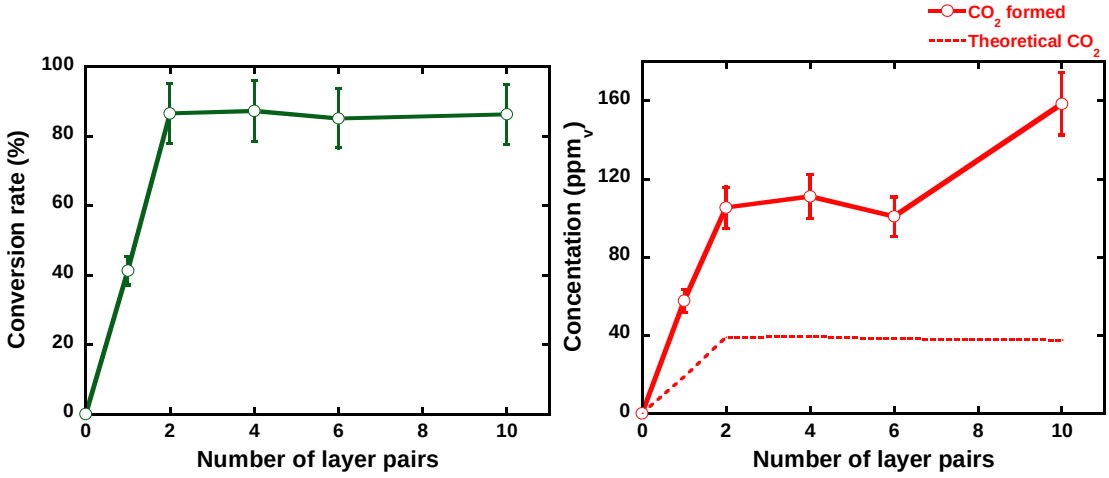

Figure 97 : (Left) Evolution of HCOOH conversion in regards to the number of layer pairs deposited in LbL films. (Right) Evolution of CO_2 formed upon irradiation of LbL films, in regards to the number of layer pairs. Experimental parameters: [HCOOH] = 45 ppm_v, air flow = 20 mL/min, speed = 0.7 cm/s, UV-A irradiance = 2.5 mW/cm^2, films built on polyester textile.

The photocatalytic tests perfomed on LbL films constructed on textile surfaces also showed a CO_2 concentration exceeding the theoretical amount resulting from the HCOOH conversion, whatever the number of layer pairs deposited. As a result, tests with air flow that does not contain formic acid

were performed on the LbL PEI/$(PSS/TiO_2)_n$ films. Again, the tests were performed 3 times on each film, and the average with their calculated error bars are showed in Table 30 and Figure 98. The tests showed an increase in CO_2 concentration upon UV-A irradiation, from 17 (single layer pair film) to 74 ppm_v (4 layer pairs film). This concentration remained the same while increasing the number of layer pairs and highlighted a degradation of the polyelectrolytes deposited on the textile fibres. As opposed to the films constructed on model surfaces, where an average concentration of 15 ppm_v was found in the photocatalytic test without HCOOH in the air flow, the PEI/$(PSS/TiO_2)_n$ films built on textiles showed a higher CO_2 concentration formed. Since ICP-AES analyses showed a higher TiO_2 amount in the TiO_2 LbL films built on textile fibres, it should also be expected that a higher amount of polyelectrolytes was also deposited around the fibres in the film. Therefore a higher degradation of the polyelectrolyte should be expected upon UV-A irradiation of the film.

Sample	**CO_2 formation (ppm_v)**
PEI/PSS/TiO_2	17 ± 2
PEI/$(PSS/TiO_2)_2$	26 ± 3
PEI/$(PSS/TiO_2)_3$	40 ± 4
PEI/$(PSS/TiO_2)_4$	75 ± 7
PEI/$(PSS/TiO_2)_6$	73 ± 7
PEI/$(PSS/TiO_2)_{10}$	71 ± 7

Table 30 : Results of CO_2 concentration formed during UV-A irradiation in the absence of HCOOH, in regards to the number of layer pairs deposited on textile surfaces.

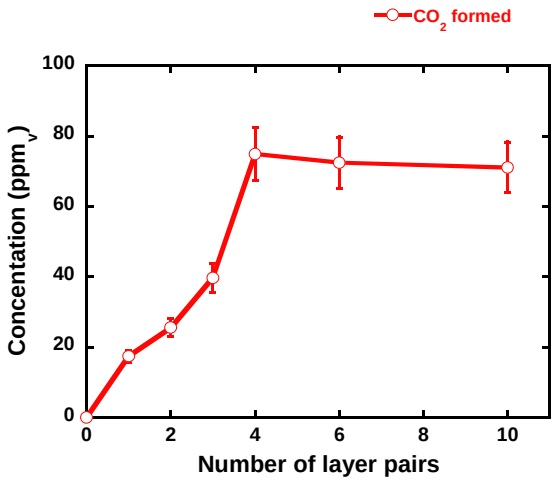

Figure 98 : Evolution of CO_2 formation UV-A irradiation, in the absence of HCOOH, in regards to the number of layer pairs deposited on textile surfaces. Experimental parameters: [HCOOH] = 0 ppm_v, air flow = 20 mL/min, speed = 0.7 cm/s, UV-A irradiance = 2.5 mW/cm^2, films built on polyester textile.

II.2 Formic acid degradation by silver-titania hybrid film coated on textile

12 cm^2 textiles were assembled and immobilised on a 36 cm^2 silicon-wafer in order to be used for the photocatalytic degradation of gas-phase HCOOH under UV-A irradiation. The first photocatalytic tests were performed with an input HCOOH concentration of 45 ppm_v, and the results are displayed in Table 31 and compared in Figure 99.

Sample	Amount of deposited material		Conversion (%)		CO_2 formation (ppm_v)		Theoretical CO_2 formation (ppm_v)	
	TiO_2 ($\mu g/cm^2$)	Ag/TiO_2 (wt.%)	45 ppm_v	145 ppm_v	45 ppm_v	145 ppm_v	45 ppm_v	145 ppm_v
PEI/PSS/ TiO_2	**27 ± 3**	**0**	41 ± 4	23 ± 2	58 ± 6	65 ± 6	19 ± 2	33 ± 3
PEI/PSS/ (0.2%$AgNO_3$-TiO_2)	**63 ± 4**	**0.25**	56 ± 6	65 ± 6	70 ± 7	85 ± 8	25 ± 3	52 ± 5
PEI/PSS/ (1%$AgNO_3$-TiO_2)	**89 ± 3**	**0.14**	97 ± 9	80 ± 8	104 ± 10	141 ± 14	39 ± 4	123 ± 12

Table 31 : Photocatalytic results of PEI/PSS/(AgNP-TiO_2) films constructed on textiles.

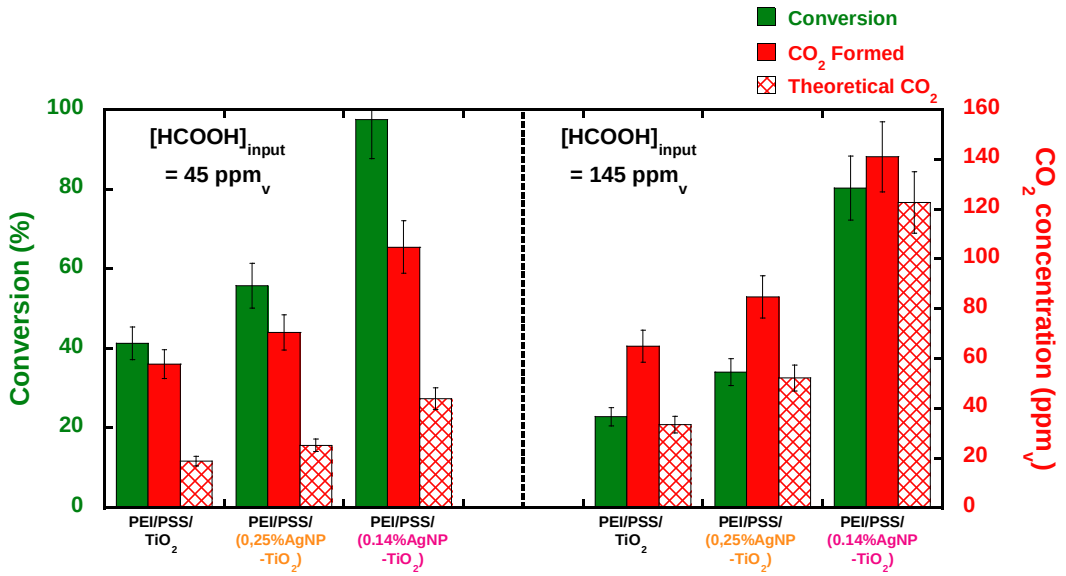

Figure 99 : Comparison of photocatalytic results of PEI/PSS/(AgNP-TiO_2) films obtained at different input HCOOH concentrations. Experimental parameters: [HCOOH] = (left) 45 and (right) 145 ppm_v, air flow = 20 mL/min, speed = 0.7 cm/s, UV-A irradiance = 2.5 mW/cm^2, films built on polyester textile.

While PEI/PSS/(0.25%AgNP-TiO_2) film showed a conversion rate of 56%, almost a maximum HCOOH conversion could be observed for the PEI/PSS/(0.14%AgNP-TiO_2) film (97%). The input HCOOH concentration was then set to 145 ppm_v, allowing a 65 and 80% conversion rate for films containing

0.25 and 0.14 wt.% AgNP respectively to be obtained; whereas the conversion rate achieved on the silver-free film dropped from a 41% to a 23%. Similarly to the AgNP-TiO_2 films built on model surfaces, the photocatalytic performances of the films constructed on the textile fibres were strongly enhanced when incorporating synthesised AgNP within the single layer pair TiO_2 film with the one-pot photoinduced synthesis method. However, the amount of TiO_2 in the film was also strongly enhanced, from 27 µg/cm² to 63 and 89 µg/cm², so that the conversion per unit mass of TiO_2 in the film was globally similar for Ag-free and Ag-containing TiO_2 films. So a beneficial effect of the presence of AgNP could not be evidenced here.

III – Biocidal properties of functionalised textiles

The second part of the evaluation of the photocatalytic properties of the LbL titania films, with and without AgNP, is related to their ability to show biocidal properties upon UV-A irradiation. The tests were performed by using the standard experimental procedure BS ISO 27447 and the films were tested against 4 types of bacteria, which were:

- *Escherichia coli* K12 CIP 54117 n° 1311
- *Staphylococcus aureus* CIP 7525 ATCC 25925 n° 300
- *Pseudomonas fluorescens* CIP 6910 n° 1183
- *Listeria monocytogene* CIP 7838 ATCC 13932 n° 367

The biocidal properties of the films were evaluated at the *Aérial-CRT* (Illkirch, France). The bacteria assays were performed and analysed by Bernard Hezard and Marie-Hélène Desmonts.

III.1 Biocidal properties of PEI/$(PSS/TiO_2)_n$ films constructed on textile surfaces

The tests were conducted on 4 types of films constructed on textile surfaces. The biocidal properties of three titania and polyelectrolytes LbL films (1, 4 and 10 layer pairs) were evaluated under UV-A irradiation and were compared to those of bare textile samples and textiles with a PEI/PSS film constructed onto them. The results are showed in Table 32 and Figure 100, and the detailed results are displayed in Appendix 13.

All films containing TiO_2 presented biocidal activity upon UV-A irradiation. The test on the reference bare textile sample showed a low abatement for *E. Coli, Pseudomonas fluorescens* and *Staphylococcus aureus*, while a higher abatement (-3.3 log) could be observed for Listeria monocytogenes (not shown in table). PEI/PSS films showed bacteria abatement only for *Pseudomonas fluorescens* and *Listeria monocytogenes* (-2 log). Single layer pair film showed biocidal properties toward every type of bacteria studied, especially for *Staphylococcus aureus* and *Listeria monocytogenes* (bacteria counting reached the detection threshold). This observation could also be seen for the 4 layer pairs films, with a higher abatement in *Escherichia coli* (-5 log) and for *Pseudomonas flurescens* (-4 log). As for the 10 layer pairs films, results were similar to the one of 4 layer pairs films, with a lower abatement for *Escherichia Coli* (-2 log).

Sample		**log (UV) – log (bare textile)**			
		Pseudomonas fluorescens	***Staphylococcus aureus***	***Escherichia coli***	***Listeria monocytogenes***
PEI/PSS	D	-2.3	-0.3	-0.2	-2.4
	p	0.01	0.23	0.01	0.05
PEI/PSS/TiO_2	D	-2.2	**-5.6**	-2.0	**-3.3**
	p	0.003	**< 0.0001**	0.03	**< 0.0001**
PEI/(PSS/TiO_2)$_4$	D	**-4.3**	**-5.6**	-5.6	**-3.3**
	p	**< 0.0001**	**< 0.0001**	< 0.0001	**< 0.0001**
PEI/(PSS/TiO_2)$_{10}$	D	**-4.0**	**-5.6**	-2.4	**-3.3**
	p	**0.0002**	**< 0.0001**	< 0.0001	**< 0.0001**

Table 32 : Microbial abatement on PEI/(PSS/TiO_2)$_n$ films constructed on textile. Results are expressed in log CFU. Number of seeded bacteria: log 5 (*Pseudomonas fluorescens*) and log 6 (*Staphylococcus aureus, Escherichia Coli* and *Listeria monocytogene*). Note: p = p-value; p < 0.05 : 5% significantly different between a bare textile sample and the treated functionalised textile sample.

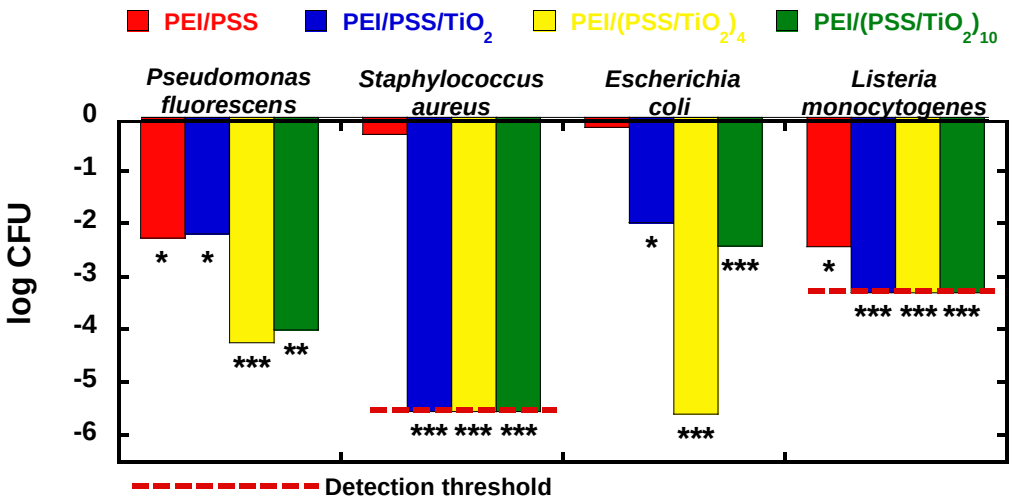

Figure 100 : Bacteria assays performed on PEI/$(PSS/TiO_2)_n$ LbL film on different types of bacteria. Tested bacteria: *Pseudomonas fluorescens, Staphylococcus aureus, Escherichia Coli* and *Listeria monocytogene*, UV-A irradiance = 2.5 mW/cm², irradiation time = 3 h, films built on 2 cm² polyester textiles. Number of seeded bacteria: log 5 (*Pseudomonas fluorescens*) and log 6 (*Staphylococcus aureus, Escherichia Coli* and *Listeria monocytogene*). (*) $p < 0.05$, (**) $p < 0.001$, (***) $p < 0.0001$.

III.2 Biocidal properties of Ag-TiO_2 hybrid films constructed on textile surfaces

The evaluation of the biocidal properties of TiO_2 and polyelectrolytes LbL films showed that single layer pair films could already display biocidal properties towards different type of bacteria under UV-A irradiation. Since the detection threshold was obtained for *Staphylococcus aureus* and *Listeria monocytogenes*, only *Pseudomonas fluorescens* and *Escherichia Coli* were used for evaluating the performances of Ag-TiO_2 hybrid films constructed on textiles. In this study, the Ag-TiO_2 hybrid films were compared to 2 types of functionalised textiles, on which PEI/PSS and PEI/PSS/TiO_2 films were constructed, and also compared to bare textiles. The possible biocidal properties of the film in the dark, due to the presence of AgNP in the film, were also assessed in this study. The results are displayed in Table 33 and compared in Figure 101.

Sample		***Pseudomonas fluorescens***			***Escherichia Coli***		
		log UV – log dark	**log dark – log (dark $_{bare\ textile}$)**	**log UV – log (dark $_{bare\ textile}$)**	**log UV – log dark**	**log dark – log (dark $_{bare\ textile}$)**	**log UV – log (dark $_{bare\ textile}$)**
Bare textile	D	-0.36	-	-	-0.02	-	-
PEI/PSS	D	-0.10	0.27	0.53	**-0.76**	0.22	**-0.51**
	p	-	0.07	0.16	-	0.50	**0.25**
PEI/PSS/TiO_2	D	-0.28	0.14	0.22	**-3.23**	-0.23	**-3.44**
	p	-	0.56	0.21	-	0.21	**0.001**
PEI/PSS/(0.25%AgNP-TiO_2)	D	**-1.21**	0.10	**-0.75**	**-4.52**	0.50	**-3.99**
	p	**-**	0.63	**0.20**	**-**	0.13	**0.0004**
PEI/PSS/(0.14%AgNP-TiO_2)	D	-0.05	-0.40	-0.08	**-2.89**	0.22	**-2.65**
	P	-	0.23	0.84	-	0.54	**0.01**

Table 33 : Microbial abatement on Ag-TiO_2 hybrid films built on textile surfaces. Average values of 3 samples assessed on 2 assays. The results are expressed in log CFU. "log UV - log dark" gives the bacteria abatement after UV-A irradiation of the samples, "log dark - log $dark_{bare\ textile}$" provides indication on the biocidal properties of the film in the dark. Number of seeded bacteria: log 5-6 (*Pseudomonas fluorescens* and *Escherichia Coli*). Note: p = p-value; $p < 0.01$: 1% significantly different between a bare textile sample and the treated functionalised textile sample.

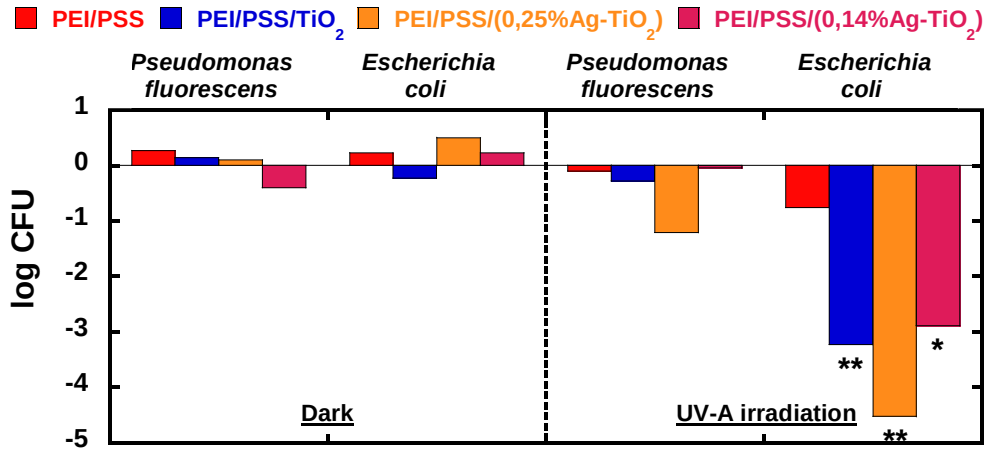

Figure 101 : Bacteria assays performed on PEI/PSS/(x%AgNP-TiO_2) hybrid films. Tested bacteria: *Pseudomonas fluorescens* and *Escherichia Coli*, UV-A irradiance = 2.5 mW/cm², irradiation time = 3 h, films built on 2 cm² polyester textiles. Number of seeded bacteria: log 5-6 (*Pseudomonas fluorescens* and *Escherichia Coli*). (*) $p < 0.01$, (**) $p < 0.001$.

In terms of biocidal properties in the dark, the results did not highlight any significant abatement for both types of bacteria, with all films. We have proposed that the films, elaborated with the one-pot photoinduced approach (Chap 4.II.3) may be constructed with AgNP being located within the porosity of the titania layer or at the PSS and TiO_2 interface, rather than at the surface of the film. Therefore, most of AgNP could not be accessible to the micrometer-size bacteria, resulting in a low, or even no antibacterial effect induced by AgNP in the dark.

Once irradiated under UV-A, a significant *Pseudomonas fluorescens* abatement could be observed for the PEI/PSS/(0.25%AgNP-TiO_2) film (-1 log). On the other hand, the *Escherichia coli* abatement was found to be significant (-4 log). In the case of PEI/PSS/(0.14%AgNP-TiO_2) film , no antibacterial effect under UV-A was found against *Pseudomonas fluorescens*, while the test using *Escherichia Coli* showed a bacteria abatement similar to the one of the silver-free PEI/PSS/TiO_2 film.

In Chap 5.I.2, it was found that the amount of TiO_2 was higher in the PEI/PSS/(0.14%AgNP-TiO_2) film (89 µg/cm²), than that of the silver-free film (34 µg/cm²), as well as the one of the film containing 0.25 wt.% AgNP (63 µg/cm²). This results highlight positive effect of the silver nanoparticles in the PEI/PSS/(0.25%AgNP-TiO_2) films on the biocidal photocatalytic properties of the film when being irradiated by UV-A, rather than an increase in biocidal properties due to a higher amount of TiO_2 contained in the film. The amount of silver content may be too low in the PEI/PSS/(0.14%AgNP-TiO_2) in order to see a beneficial effect from the AgNP upon UV-A irradiation.

IV – Stability of films constructed on textile

The final tests regarding the films constructed on textiles, consisted in the evaluation of their stability after being mechanically treated and washed using different types of processes. These treatments are standardised and were performed at the *Institut Français du Textile et de l'Habillement* (IFTH, Mulhouse, France). Two types of treatments were performed on TiO_2 and polyelectrolytes LbL films, which were abrasion and washing tests. The washing tests consisted actually in 3 types of tests, where the solidity of the textile was tested for 1 and 10 washing cycles, and also to dry cleaning. In this study, two types of films were chosen to evaluate their durability:

- the single layer pair film, which provided a 41 % HCOOH conversion under UV-A irradiation.
- the 2 layer pairs film, that is the lowest layer pair film where the HCOOH conversion rate was observed to reach the plateau region (86% conversion).

Once treatment was applied onto the textile samples, SEM and ICP-AES characterisations were applied and photocatalytic degradation of gas-phase HCOOH was used to test the durability/stability of the functionalised samples. It must be mentioned that the photocatalytic tests were only performed one time for each system.

IV.1 Abrasion tests

The resistance of the textile was tested according to the NF EN ISO 12945 standard. In this test, the functionalised textiles (225 cm^2, 15 x 15 cm) were set in a support and with 415 g mass applied on every sample (Figure 102). The samples were then abraded on a wool rep for 500 cycles, using a modified Martindale method. Three types of textile were treated for this test: a bare textile, 1 and 2 layer pairs functionalised textiles. Whatever the textile, after the treatment, visual evidences of fibres wearing could not be observed on either the textile surfaces or on the wool reps' surfaces (Figure 103).

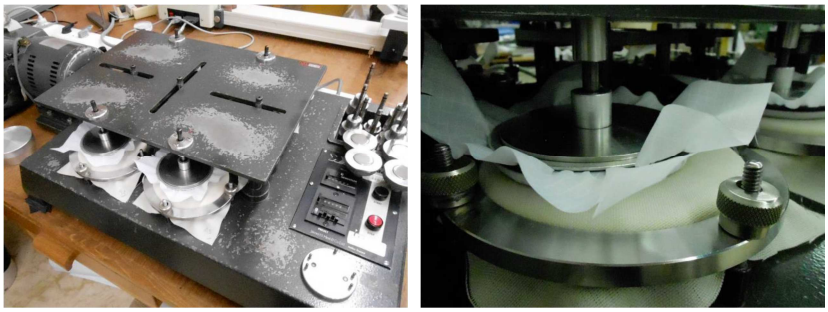

Figure 102 : (Left) Functionalised textiles placed against wool reps for abrasion test. (Right) zoom of the interface between the textile and the wool rep.

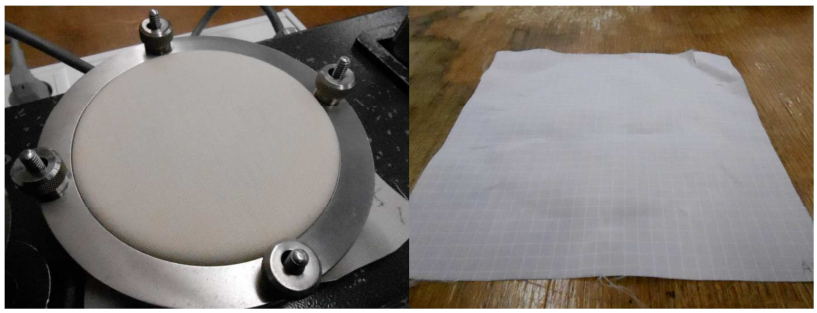

Figure 103 : Wool rep (left) and 2 layer pairs functionalised polyester textile (right) after an abrasion test of 500 cycles.

SEM Images of the abraded bare textile did not highlight any evidences of microscopic wears (Figure 104). As mentioned in Chap 4.I.1.2, SEM characterisations of bare textile fibres are difficult to acquire since charging of the fibres occurs during the characterisations. This charging effect could be observed when characterising the abraded textiles, functionalised with a PEI/PSS/TiO_2 and a PEI/(PSS/TiO_2)$_2$ film. By using the Energy Selecting Backscattered electron detector (ESB), it was observed that a non negligible amount of TiO_2 was mainly after treatment located between the fibres, while TiO_2 was quasi exclusively on top of them for both untreated textiles functionalised by titania LbL films (SEM-ESB images of an untreated PEI/PSS/TiO_2 are showed in appendix).

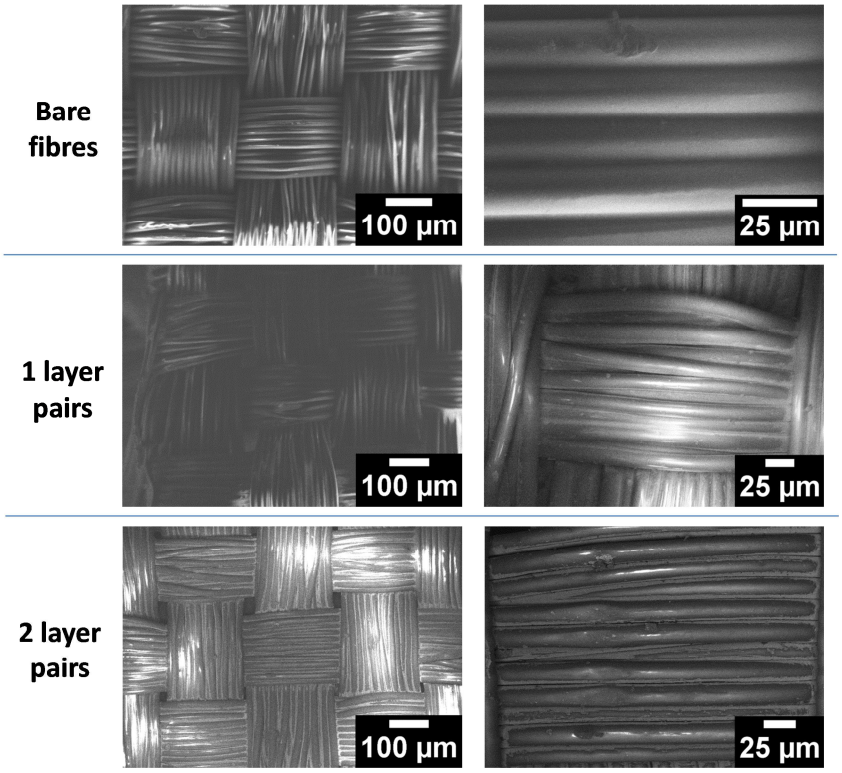

Figure 104: SEM images of textiles after abrasion test.

The amount of titania deposited at the surface of the textile, was obtained using chemical analysis ICP-AES. The analyses were performed on three 1 cm² samples, to get an average of TiO_2 deposited of the textile surface, and calculate the standard deviations. The amount for the titania found on a treated 1 layer pair film, was found to be 26 µg/cm², which is a lower amount than the one obtained for an untreated single layer pair film built on a textile surface in Chap 5.I.1.1. However, considering the mass increment of TiO_2 per layer pairs of 27 µg/cm², we can consider that the amount of TiO_2 on the abraded textile functionalised by a PEI/PSS/TiO_2 film, stays within the range of the TiO_2 amount in a single layer pair film expected to be deposited on the fibres. The textile functionalised with a 2 layer pairs film showed a similar amount than that of an untreated 2 layer pairs functionalised textile (66 vs. 60 ± 4 µg/cm²).

The photocatalytic tests for the degradation of gas phase HCOOH were performed on the treated textiles (cut into 36 cm² samples), and the results are shown in Table 34 and compared in Figure 105. Very interestingly, similar performances were obtained for treated textiles compared to those achieved on the untreated ones, whether the textiles were functionalised with a single layer pair or a 2 layer pairs film. However a lower CO_2 concentration formed was observed for the abraded 2 layer pairs functionalised textile (64 ppm_v instead of 105 ppm_v). This result could be explained by a lower

degradation of polyelectrolytes upon UV-A irradiation when the 2 layer pairs functionalised textiles were abraded.

The abrasion treatment results suggest that the film structure is affected, whilst very interestingly the materials remained coated and stabilised on the textile fibres. No loss of TiO_2 was observed despite the re-arrangement of the TiO_2 particles at the surface of the fibres. SEM images showed that more TiO_2 particles were located between the fibres, whilst keeping the same amount of TiO_2 coated on the fibres. This may suggest a film structure rearrangement, which may positively lead to lower contact between TiO_2 and the polyelectrolytes, resulting in a lower concentration of formed CO_2 upon UV-A irradiation.

Sample	Amount of TiO_2 ($\mu g/cm^2$)	Conversion (%)	CO_2 formation (ppm_v)	Theoretical CO_2 formation (ppm_v)
PEI/PSS/TiO_2	38 ± 3	41 ± 4	58 ± 6	19 ± 2
PEI/PSS/TiO_2 treated	26 ± 1	40	59	17
PEI/(PSS/TiO_2)$_2$	60 ± 4	87 ± 7	105 ± 16	39 ± 4
PEI/(PSS/TiO_2)$_2$ treated	66 ± 1	85	64	38

Table 34 : ICP-AES and photocatalytic results obtained for textiles before and after abrasion process.

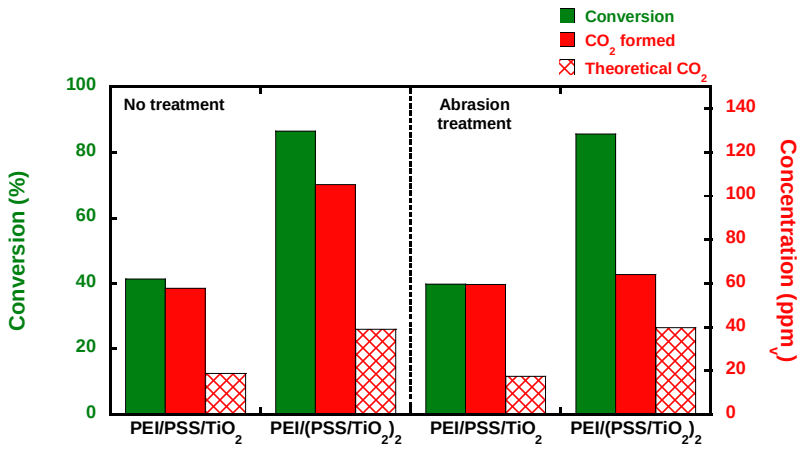

Figure 105 : Photocatalytic performances of functionalised textiles before and after dry abrasion treatment. Experimental parameters: [HCOOH] = 45 ppm_v, air flow = 20 mL/min, speed = 0.7 cm/s, UV-A irradiance = 2.5 mW/cm^2, films built on polyester textile.

IV.2 Washing treatments

The washing treatments were performed by placing the functionalised textiles in a stainless steel container, placed on a rotated holder allowing the container to be immersed in a controlled temperature bath (Figure 106). The rotation frequency was set at 40 turns per min.

Figure 106 : (Left) sealed stainless steel container. (Right) stainless steel container placed on the rotated holder.

IV.2.1 Washing treatment with 1 and 10 cycles

The textile resistance to washing processes (1 and 10 successive cycles) was tested according to the NF EN ISO 105-C06 standard. In these tests, the textile sample is placed in a glass-lined containing 150 mL (per sample) of ECE detergent standard solution (4 g/L). 10 small stainless steel balls (6 mm in diameter) were added in the glass-lined in order to provide a mechanical motion during the washing process (Figure 107). The sealed container with the glass-lined inside, was then placed on the rotative holder and the water temperate was set at 40°C. The washing duration was set at 30 min per cycle. Once washed, the textiles were rinsed twice for 1 min in 100 mL water at 40°C and were placed in the dark until being dried (open air).

Figure 107 : (left) opened stainless steel container where the textiles and the stainless steel balls will be placed. (Right) Zoom on the stainless steel balls.

SEM characterisation (with ESB detector) of samples washed for 1 cycle showed that the textile fibres were still coated with TiO_2 nanoparticles (Figure 108). However it appeared that the distribution of TiO_2 on the fibres was less homogeneous on the 1 cycle washed PEI/$(PSS/TiO_2)_2$ sample. This effect was more pronounced on textiles washed for 10 cycles, where charging of the "apparent top" fibres occurred in both samples.

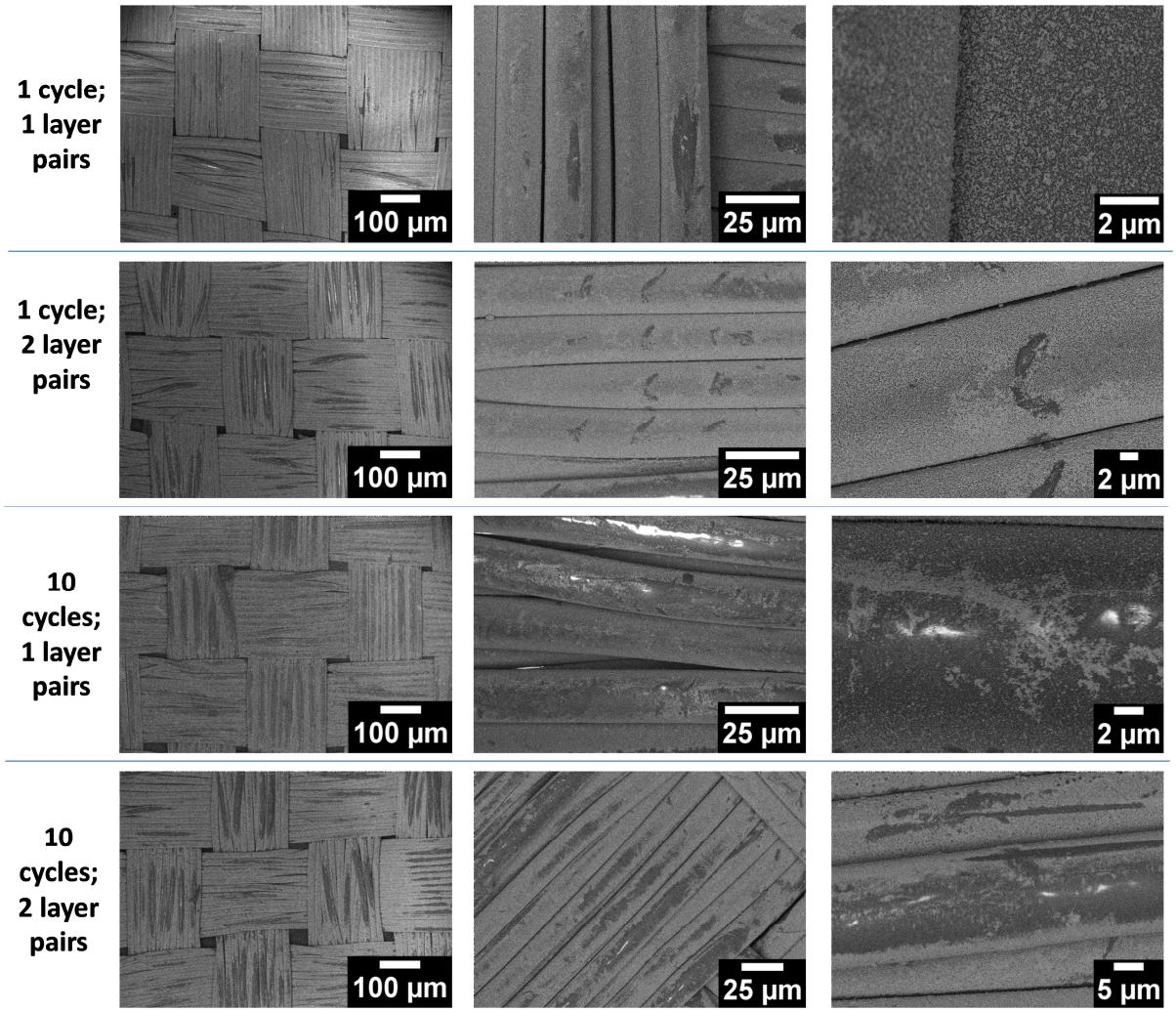

Figure 108: SEM images of functionalised textiles after 1 and 10 cycles washing process.

Chemical analysis did not highlight any changes in amount of TiO_2 deposited on the polyester textile surface, suggesting that the washing process does not remove titania from 1 and 2 layer pairs films constructed on textile, however the washing treatment was found to affect the photocatalytic properties of the film. The single layer pair film showed an enhancement of the photocatalytic performances of the film after a 1 cycle wash, where the HCOOH conversion went from 41 to 81%. On the other hand, a 10 cycles wash led to a negative effect on the PEI/PSS/TiO_2 film, where a 6% conversion could be observed upon UV-A irradiation of the film. The treated 2 layer pairs film did not

show a difference in HCOOH conversion after a 1 cycle wash, although an increase in CO_2 concentration upon UV-A irradiation could be observed (from 105 to 129 ppm_v). The 10 cycles washing showed a slight increase in HCOOH conversion (from 87 to 96%), along with the same increase in CO_2 formation observed in the PEI/$(PSS/TiO_2)_2$ with a single cycle treatment (134 ppm_v).

Like for the abrasion test, we suggest that a film structure rearrangement after the washing process may provide a positive or negative effect on the photocatalytic properties of the film. Nevertheless the washing process, whether with 1 or 10 cycles, has appeared to not remove TiO_2 from the textile fibres.

Sample	**Amount of TiO_2 ($\mu g/cm^2$)**	**Conversion (%)**	**CO_2 formation (ppm_v)**	**Theoretical CO_2 formation (ppm_v)**
PEI/PSS/TiO_2	38 ± 3	41 ± 4	58 ± 6	19 ± 2
PEI/PSS/TiO_2 – 1 cycle	44 ± 1	81	64	36
PEI/PSS/TiO_2 – 10 cycles	37 ± 1	6	17	3
PEI/$(PSS/TiO_2)_2$	60 ± 4	87 ± 7	105 ± 16	39 ± 4
PEI/$(PSS/TiO_2)_2$ - 1 cycle	61 ± 3	83	129	39
PEI/$(PSS/TiO_2)_2$ - 10 cycles	60 ± 2	96	134	43

Table 35: ICP-AES and photocatalytic results obtained for textiles before and after 1 and 10 cycles washing process

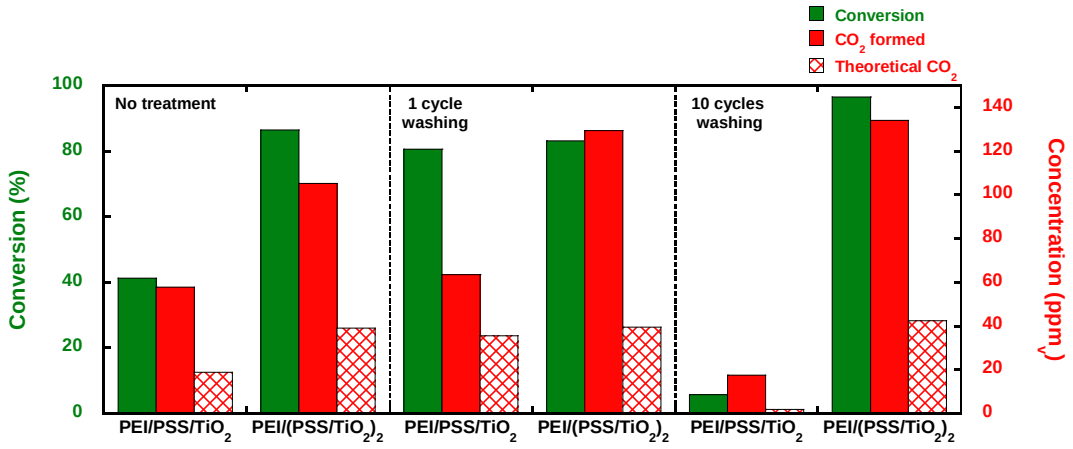

Figure 109 : Photocatalytic performances of functionalised textiles before and after 1 and 10 cycles washing. Experimental parameters: [HCOOH] = 45 ppm_v, air flow = 20 mL/min, speed = 0.7 cm/s, UV-A irradiance = 2.5 mW/cm^2, films built on polyester textile.

IV.2.2 Dry cleaning

This test was used to evaluate the resistance of functionalised textiles to perchloroethylene washing, according to the NF EN ISO 105-D01 standard. The textile samples were placed in a glass-lined containing 200 mL perchloroethylene solution (per sample). 12 stainless discs were added in order to provide mechanical motions during the tests (Figure 110). The glass-line was placed in the sealed container, which was then set in the holder. The water bath temperature was set at 60°C and the washing process lasted for 30 min. The textiles were then wringed and dried in warm air (60°C) in the dark.

Figure 110: Stainless steel discs used in dry cleaning treatment.

SEM images showed once again that TiO_2 is still present at the surface of the fibres after being dry cleaned (Figure 111). Charging of the textile could be observed on the single layer pair textile, and the effect decreased with the 2 layer pair film.

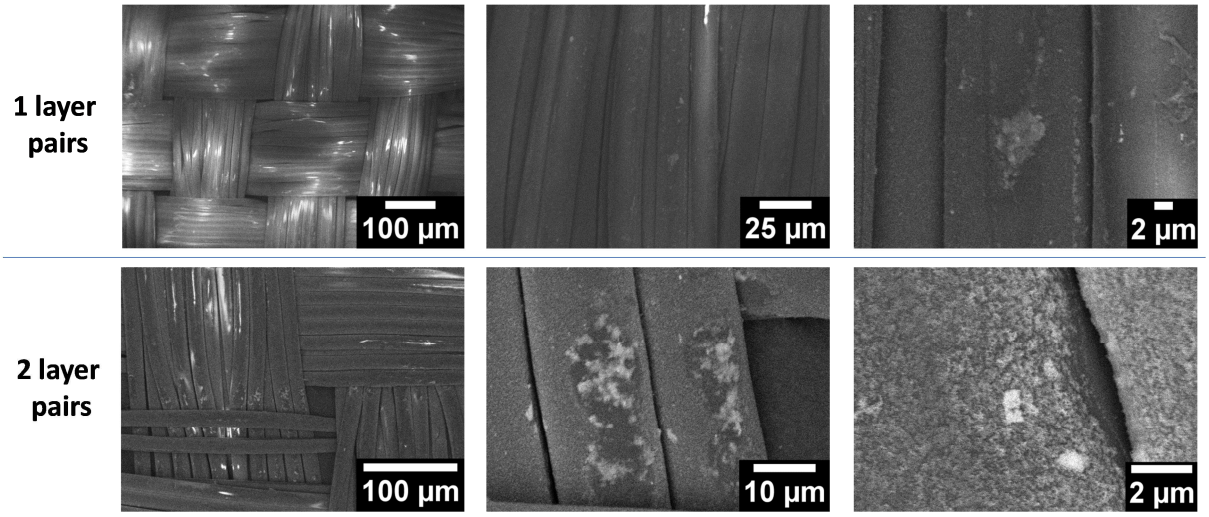

Figure 111: SEM images of functionalised textile after dry cleaning process

Like the previous films where abrasion and cleaning process were applied, it is worth noting that the amount of TiO_2 remained unchanged on the fibres. The photocatalytic tests showed a decrease in photocatalytic performances for both treated samples (Table 36 and Figure 112). The treated PEI/PSS/TiO_2 film showed a slight decrease in conversion (from 41% to 34 %) but the CO_2 formation was found to be at 33 ppm_v instead of 58 ppm_v. This decrease in activity was more visible for the treated PEI/(PSS/TiO_2)$_2$ film, that showed to have similar photocatalytic efficiency than the treated single layer pair film, with a 34 % HCOOH conversion and 35 ppm_v of CO_2 formed upon UV-A irradiation. While film rearrangement can also be suggested after dry cleaning treatment, perchloroethylene adsorbed on the titania surface may also block the active sites, leading to a decrease in photocatalytic activity of the films. These photocatalytic tests were only performed one time and should be repeated in order to get a better understanding of the photocatalytic behaviour of the treated functionalised textile.

Sample	Amount of TiO_2 ($\mu g/cm^2$)	Conversion (%)	CO_2 formation (ppm_v)	Theoretical CO_2 formation (ppm_v)
PEI/PSS/TiO_2	38 ± 3	41 ± 4	58 ± 6	19 ± 2
PEI/PSS/TiO_2 treated	38 ± 1	34	33	17
PEI/(PSS/TiO_2)$_2$	60 ± 4	87 ± 7	105 ± 16	39 ± 4
PEI/(PSS/TiO_2)$_2$ treated	61 ± 4	34	35	15

Table 36: ICP-AES and photocatalytic results obtained for textile before and after dry cleaning process.

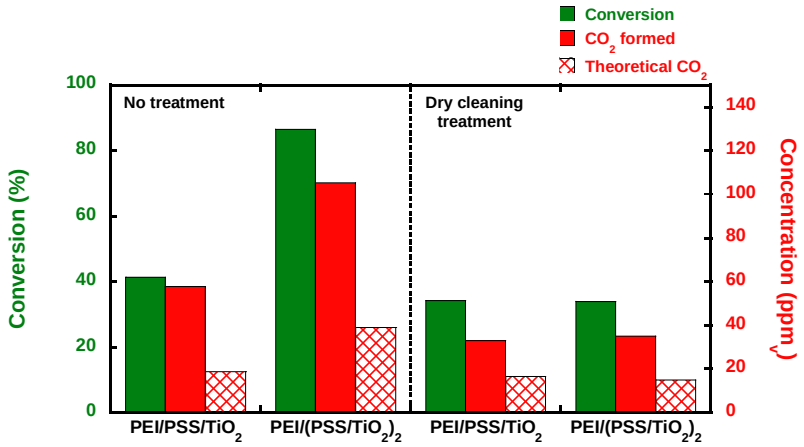

Figure 112 : Photocatalytic performances of functionalised textiles before and after dry cleaning treatment. Experimental parameters: [HCOOH] = 45 ppm_v, air flow = 20 mL/min, speed = 0.7 cm/s, UV-A irradiance = 2.5 mW/cm^2, films built on polyester textile.

Chapter 5: Titania and Silver-Titania thin films – construction on textile surfaces

This chapter, more oriented toward the application, was dedicated to the transfer of the Layer-by-Layer construction technique by dipping, as well as the one-pot AgNP photoinduced synthesis, from model surfaces to polyester textile surfaces. Both PEI/$(PSS/TiO_2)_n$ and single layer pair PEI/PSS/(AgNP-TiO_2) film construction were successfully transferred and both types of films showed photocatalytic performances under UV-A irradiation for the degradation of gas-phase HCOOH and different types of bacteria. The addition of AgNP in the titania layer (Ag-TiO_2 hybrid layer) led to elaborate a film with higher TiO_2 contents so that the strongly enhanced HCOOH conversion achieved on both PEI/PSS/(AgNP-TiO_2) films was not attributed to the presence of AgNP in the films. However the Ag-TiO_2 films did not show any biocidal properties in the dark, suggesting that the amount of AgNP is too low.

Abrasion and different washing treatments were applied on single and two layer pairs films in order to evaluate their stability and resistance. The films were characterised by SEM and the amount of TiO_2 was determined by ICP-AES, while their stability was evaluated by studying their ability to degrade gas-phase HCOOH under UV-A irradiation. SEM characterisation showed that TiO_2 particles were not evenly coated on the textile fibres after being treated, while chemical analysis results showed that the amount of TiO_2 remained the same whatever the treatment applied on the functionalised textile. While the abrasion tests showed that the photocatalytic performances of the films remained the same, the different washing processes have showed to have either positive or negative impact on the photocatalytic performances of the functionalised films.

Conclusion and perspectives

This thesis is part of the PLASMOTEX project funded by the *Institut Carnot MICA* (Mulhouse, France) and was realised at the *Institut de Chime des Procédés pour l'Energie, l'Environnement et la Santé* (ICPEES, UMR 7515, Strasbourg, France) under the supervision of Dr. Nicolas Keller, and at the *Institut Charles Sadron* (ICS, UPR 22, Strasbourg, France) under the supervision of Pr. Gero Decher. The project also involved collaborations with the *Institut des Sciences des Matériaux de Mulhouse* (IS2M, UMR 7361, Mulhouse, France) with Dr. Lavinia Balan and Dr. Lydie Ploux, and with *CRITT Aerial* (Illkirch, France) with Dr. Marie-Hélène Desmonts.

The main aim of this work was to functionalise a model surface and a textile with silver and titania nanoparticles *via* the Layer-by-Layer (LbL) self-assembly construction technique, in order to provide the textile simultaneously photocatalytic properties against chemical pollutant (under UV-A irradiation) and biocidal properties (with or without UV-A irradiation). This work was divided in four main tasks that were:

- the elaboration and characterisations of the multilayer titania films with and without silver nanoparticles on model surfaces,
- the evaluation of the films photocatalytic performances under UV-A irradiation in the degradation of a gaseous pollutant
- the evaluation of the films' biocide properties under UV-A irradiation
- the transfer of films construction technique from model surfaces to textile surfaces, with evaluation of the photocatalytic activity towards gas-phase pollutant, and the biocidal properties.

This PhD manuscript was divided in three main parts in regards to the type of material used for constructing the multilayered films. Every films constructed were characterised and their photocatalytic performances towards the degradation of gas-phase formic acid under UV-A, as well as their biocidal properties, were evaluated.

1 – The **construction of titania and polyelectrolytes thin films on model surfaces** via the LbL self-assembly was studied prior to the addition of silver nanoparticles in the film. Films containing several polyeletrolytes/TiO_2 layer pairs were successfully constructed and characterised on model surfaces, according to the characterisation techniques used. The PEI/$(PSS/TiO_2)_n$ LbL films showed a porous structure and a homogeneous TiO_2 surface coverage, with an average thickness of 40 nm and a TiO_2 density of 7 µg/cm² per layer pairs. The photocatalytic degradation of gas-phase HCOOH was evaluated in regards to the number of layer pairs deposited on the film. The results showed an unusual trend of the HCOOH conversion rate in regards to the amount of photocatalyst, where the single layer pair film PEI/PSS/TiO_2 showed surprisingly the best photocatalytic activity under UV-A. Two hypotheses were suggested for explaining this unusual behaviour. The first hypothesis was about the difference in film density when constructing additional PSS/TiO_2 layers onto the PEI/PSS/TiO_2 film, whilst remaining porous. This change in film structure may lead to a decrease in HCOOH diffusion in the film, therefore decreasing the photocatalytic activity of the film by adding a second PSS/TiO_2 layer pair on the PEI/PSS/TiO_2 film. The second hypothesis was related to the hindrance of TiO_2 active sites by the PSS deposited. It was suggested that the film construction parameters used will induce a change in PSS conformation i.e. from a fuzzy to an extended conformation. While polyelectrolytes in an extended conformation are added, blocking of TiO_2 active sites may occur, eventually leading to a drop in the photocatalytic activity of the films under UV-A irradiation.

The biocidal performances of the PEI/$(PSS/TiO_2)_n$ film under UV-A irradiation showed Escherichia Coli bacteria reduction in regards to the number of layer pairs deposited on model surfaces (i.e. silicon wafers). The maximum biocidal effect could already be observed for a 3 layer pairs film, and PEI/PSS/TiO_2 single layer pair film already showed antibacterial effect under UV-A irradiation. We suggested that the usual behaviour of the biocidal performances of the films was related to the difference in size between bacteria (micrometric size) and to PSS/TiO_2 film structure (nanometric), rather than to a light screening effect.

2 – The **construction of silver and titania hybrid thin films on model surfaces** using different types of silver nanoparticles deposition and photoinduced syntheses was investigated. These investigations were focussed on the addition of AgNP in LbL film containing a single layer pair, since both photocatalytic activity in the degradation of gas-phase HCOOH and photocatalytic biocidal effect could be observed under UV-A irradiation. Three types of Ag-TiO_2 hybrid films, with different Ag/TiO_2 contents (wt.%) were successfully constructed and were investigated in this thesis. While a novel

blade-assisted LbL deposition method has allowed the deposition of commercially available AgNP, the implementation of a photoinduced AgNP synthesis has allowed the particles to be synthesised on a prebuilt PEI/PSS/TiO_2 film. The third type of Ag-TiO_2 film was constructed using a one-pot AgNP photoinduced synthesis, by combining the LbL deposition dipping method to the photoinduced AgNP synthesis. This combined synthesis/elaboration method allowed the construction of a single layer pair AgNP-TiO_2 hybrid film with calibrated (2 nm) small size AgNP with a narrow particle size distribution, in contact with TiO_2 nanoparticles. In this third type of Ag-TiO_2 hybrid films, the films had different Ag/TiO_2 content from 0.2 to 2.2 wt.%, and remained transparent. XPS analysis showed that only a low amount of AgNP can be found at the surface of the film and it was suggested that AgNPs are most likely localised in the film porosity or at the PSS/TiO_2 interface.

The photocatalytic tests towards the degradation of gas-phase HCOOH showed that the photocatalytic properties of the film could be enhanced by the presence of AgNP in all types of Ag-TiO_2 hybrid films studied in the work. However the films constructed with the one-pot photoinduced approach showed the best photocatalytic activity, especially for the film containing 0.2 wt.% Ag/TiO_2, with a one order magnitude improvement of the performances compared to a AgNP-free TiO_2 film. We suggested a positive role of AgNP acting as electron acceptor for lowering the charge recombination, and hypothesised a positive plasmon-band-assisted enhancement of the photocatalytic performances under UV-A irradiations.

The biocidal performances of Ag-TiO_2 films were only evaluated on films with AgNP synthesised with the one-pot photoinduced approach. While no Ag-TiO_2 hybrid films showed a real biocidal effect in the dark, an enhancement of the photocatalytic antibacterial properties of the Ag-TiO_2 films upon UV-A irradiation could be observed. This enhancement was significant and resulted from the association of Ag and TiO_2 since no biocidal properties could be observed in the dark.

3 – The **transfer of titania/polyelectrolytes and Ag/titania films construction from model to textile surfaces** was successfully achieved, using the same LbL dipping parameter for the silver-free LbL films, and the one-pot photoinduced approach for the deposition of a Ag-TiO_2 layer. While no visual evidences of PEI/$(PSS/TiO_2)_n$ films construction on textile surface could be observed, SEM images highlighted a homogeneous distribution of the TiO_2 nanoparticles on the fibres, with an increase in apparent density while depositing more layer pairs. The higher surface coverage of the polyester fibres has led to an increase in amount of deposited TiO_2 (27 µg/cm² per layer pairs) than that deposited on model surface (7 µg/cm² per layer pairs). The photocatalytic activity for both gas-phase HCOOH degradation, and bacteria removal upon UV-A irradiation was shown to increase with the

number of layer pairs deposited, with a photocatalytic activity observed for a single layer pair film. The one-pot photoinduced approach was found to be suitable for simultaneously synthesising AgNP and constructing the LbL film on textile fibres. However, the enhanced photocatalytic performances achieved on the Ag-TiO_2 hybrid films compared to a silver-free single layer pair film were attributed to the higher amount of TiO_2 deposited.

In addition, standardised stability and resistance tests were performed on PEI/PSS/TiO_2 and PEI/(PSS/TiO_2)$_2$ films constructed on textile. The results showed that the amount of TiO_2 remained the same whatever the applied treatment, no loss of TiO_2 being observed. However SEM images highlighted a change in the film structure and the photocatalytic tests toward the degradation of gas-phase HCOOH under UV-A irradiation could either increase of decrease the photocatalytic activity of the films.

As perspectives, opened by this work:

- on model surfaces, the hypothesis of diffusional behaviour in the film with increasing the number of layer pairs has to be tested, by implementing adequate gas-phase activity tests for evidencing the kinetic/diffusion regime turn of films. A change in the dipping parameters or by using a different type of polyelectrolyte in the film construction could also provide valuable information. This aspect could enter in further more detailed characterisation for going further in understanding the unusual behaviour of the film.
- the photoinduced approach using a chromophore appeared to be promising for being combined with the LbL construction. However, while a chromophore was always used in the work in the AgNP photoinduced synthesis, it could be interesting to investigate in the one pot photoinduced approach by using a chromophore-free photosensitive suspension. This study was begun in parallel with the investigations on the construction of Ag-TiO_2 hybrid films on model surfaces, but the results were not presented in this thesis manuscript. In addition, the potential of the approach has to be studied for preparing bimetallic M_1M_2-TiO_2 hybrid films, since bimetallic nanoparticles are developing very interesting adsoption and electronic properties useful in gas-phase photocatalysis.
- Since a plasmon effect was hypothesised due to the presence of Ag in Ag-TiO_2 hybrid films, test under visible light could be performed to evaluate a potential activity in the visible range. However this will require the synthesis of TiO_2 nanoparticles, rather than usin TiO_2

P25, as well as associate them to the adequate AgNp that provide a plasmon band in the visible range by playing on size and shapes wavelengths.

References

[1] E. Heseltine, J. Rosen, and World Health Organization, Eds., *WHO guidelines for indoor air quality: dampness and mould*. Copenhagen: WHO, 2009.

[2] World Health Organization, 'Evolution of World Health Organization air quality guidelines: past, present and future', 2017.

[3] B. Guieysse, C. Hort, V. Platel, R. Munoz, M. Ondarts, and S. Revah, 'Biological treatment of indoor air for VOC removal: Potential and challenges', *Biotechnol. Adv.*, vol. 26, no. 5, pp. 398–410, Sep. 2008.

[4] World Health Organization, Ed., *Indoor air quality guidelines: household fuel combustion*. 2014.

[5] A. Luengas, A. Barona, C. Hort, G. Gallastegui, V. Platel, and A. Elias, 'A review of indoor air treatment technologies', *Rev. Environ. Sci. Biotechnol.*, vol. 14, no. 3, pp. 499–522, Sep. 2015.

[6] J.-M. Herrmann, 'Heterogeneous photocatalysis: fundamentals and applications to the removal of various types of aqueous pollutants', *Catal. Today*, vol. 1, pp. 115–129, 1999.

[7] J. Zhao and X. Yang, 'Photocatalytic oxidation for indoor air purification: a literature review', *Build. Environ.*, vol. 38, no. 5, pp. 645–654, May 2003.

[8] B. Ohtani, O. O. Prieto-Mahaney, D. Li, and R. Abe, 'What is Degussa (Evonik) P25? Crystalline composition analysis, reconstruction from isolated pure particles and photocatalytic activity test', *J. Photochem. Photobiol. Chem.*, vol. 216, no. 2–3, pp. 179–182, Dec. 2010.

[9] M. R. Hoffmann, S. T. Martin, W. Choi, and D. W. Bahnemann, 'Environmental applications of semiconductor photocatalysis', *Chem. Rev.*, vol. 95, no. 1, pp. 69–96, 1995.

[10] S. W. Verbruggen, 'TiO_2 photocatalysis for the degradation of pollutants in gas phase: From morphological design to plasmonic enhancement', *J. Photochem. Photobiol. C Photochem. Rev.*, vol. 24, pp. 64–82, Sep. 2015.

[11] K. Nakata and A. Fujishima, 'TiO_2 photocatalysis: Design and applications', *J. Photochem. Photobiol. C Photochem. Rev.*, vol. 13, no. 3, pp. 169–189, Sep. 2012.

[12] A. L. Linsebigler, G. Lu, and J. T. Yates Jr, 'Photocatalysis on TiO_2 surfaces: principles, mechanisms, and selected results', *Chem. Rev.*, vol. 95, no. 3, pp. 735–758, 1995.

[13] S. Linic, P. Christopher, and D. B. Ingram, 'Plasmonic-metal nanostructures for efficient conversion of solar to chemical energy', *Nat. Mater.*, vol. 10, no. 12, pp. 911–921, Dec. 2011.

[14] M. Rycenga *et al.*, 'Controlling the Synthesis and Assembly of Silver Nanostructures for Plasmonic Applications', *Chem. Rev.*, vol. 111, no. 6, pp. 3669–3712, Jun. 2011.

[15] P. Christopher, D. B. Ingram, and S. Linic, 'Enhancing Photochemical Activity of Semiconductor Nanoparticles with Optically Active Ag Nanostructures: Photochemistry Mediated by Ag Surface Plasmons', *J. Phys. Chem. C*, vol. 114, no. 19, pp. 9173–9177, May 2010.

[16] M. Rai, A. Yadav, and A. Gade, 'Silver nanoparticles as a new generation of antimicrobials', *Biotechnol. Adv.*, vol. 27, no. 1, pp. 76–83, Jan. 2009.

[17] G. Decher, 'Fuzzy Nanoassemblies: Toward Layered Polymeric Multicomposites', *Science*, vol. 277, no. 5330, pp. 1232–1237, Aug. 1997.

[18] G. Decher and J. B. Schlenoff, *Multilayer Thin Films: Sequential Assembly of Nanocomposite Materials*, 2nd edition. Wiley-VCH Verlag GmbH & Co. KGaA, 2012.

[19] M. Zaier, L. Vidal, S. Hajjar-Garreau, J.-L. Bubendorff, and L. Balan, 'Tuning the morphology of silver nanostructures photochemically coated on glass substrates: an effective approach to large-scale functional surfaces', *Nanotechnology*, vol. 28, no. 10, p. 105603, Mar. 2017.

[20] World Health Organization, Ed., *Air quality guidelines for Europe*, 2nd ed. Copenhagen: World Health Organization, Regional Office for Europe, 2000.

[21] A. P. Jones, 'Indoor air quality and health', *Atmos. Environ.*, vol. 33, no. 28, pp. 4535–4564, 1999.

[22] O. Carp, C. L. Huisman, and A. Reller, 'Photoinduced reactivity of titanium dioxide', *Prog. Solid State Chem.*, vol. 32, no. 1–2, pp. 33–177, 2004.

[23] J. C. Kennedy and A. K. Datye, 'Photothermal Heterogeneous Oxidation of Ethanol over Pt/TiO_2', *J. Catal.*, vol. 179, no. 2, pp. 375–389, Oct. 1998.

[24] V. Subramanian, E. Wolf, and P. V. Kamat, 'Semiconductor-Metal Composite Nanostructures. To What Extent Do Metal Nanoparticles Improve the Photocatalytic Activity of TiO_2 Films?', *J. Phys. Chem. B*, vol. 105, no. 46, pp. 11439–11446, Nov. 2001.
[25] B. N. Nunes, L. F. Paula, Í. A. Costa, A. E. H. Machado, L. G. Paterno, and A. O. T. Patrocinio, 'Layer-by-layer assembled photocatalysts for environmental remediation and solar energy conversion', *J. Photochem. Photobiol. C Photochem. Rev.*, vol. 32, pp. 1–20, Sep. 2017.
[26] Y. Huang *et al.*, 'Removal of Indoor Volatile Organic Compounds via Photocatalytic Oxidation: A Short Review and Prospect', *Molecules*, vol. 21, no. 1, p. 56, Jan. 2016.
[27] J. T. Brinke *et al.*, 'Development of new volatile organic compound (VOC) exposure metrics and their relationship to "sick building syndrome" symptoms', *Indoor Air*, vol. 8, no. 3, pp. 140–152, 1998.
[28] C. Guerreiro, F. de Leeuw, V. Foltescu, J. Horálek, and European Environment Agency, *Air quality in Europe: 2014 report*. Luxembourg: Publications Office, 2014.
[29] B. O. Brooks, G. M. Utter, J. A. DeBroy, and R. D. Schimke, 'Indoor Air Pollution: An Edifice Complex', *J. Toxicol. Clin. Toxicol.*, vol. 29, no. 3, pp. 315–374, Jan. 1991.
[30] C.-Y. Peng, C.-H. Lan, and T.-J. Wu, 'Investigation of indoor chemical pollutants and perceived odor in an area with complaints of unpleasant odors', *Build. Environ.*, vol. 44, no. 10, pp. 2106–2113, Oct. 2009.
[31] G. D. Nielsen, L. F. Hansen, B. Andersen, N. Poulsen, and O. Melchior, 'Indoor air guideline levels for formic, acetic, propionic and butyric acid', *Indoor Air*, vol. 8, no. S5, pp. 8–24, 1998.
[32] M. Simões, L. C. Simões, and M. J. Vieira, 'A review of current and emergent biofilm control strategies', *LWT - Food Sci. Technol.*, vol. 43, no. 4, pp. 573–583, May 2010.
[33] J. D. Bryers and B. D. Ratner, 'Bioinspired Implant Materials Befuddle Bacteria', *ASM News*, vol. 70, pp. 232–237, 2004.
[34] 'Biofilm - Traitement de Surfaces', *rd_technologiques*. [Online]. Available: https://wwz.ifremer.fr/rd_technologiques_eng/Moyens/Laboratoires/Microbiologie-Interfaces-materiaux-et-milieu-marin/Biofilm-Traitement-de-Surfaces. [Accessed: 26-Apr-2018].
[35] S. Josset *et al.*, 'UV-A photocatalytic treatment of Legionella pneumophila bacteria contaminated airflows through three-dimensional solid foam structured photocatalytic reactors', *J. Hazard. Mater.*, vol. 175, no. 1–3, pp. 372–381, Mar. 2010.
[36] R. G. Sinclair and C. P. Gerba, 'Microbial contamination in kitchens and bathrooms of rural Cambodian village households: Microbes in Cambodian households', *Lett. Appl. Microbiol.*, vol. 52, no. 2, pp. 144–149, Feb. 2011.
[37] A. Kramer, I. Schwebke, and G. Kampf, 'How long do nosocomial pathogens persist on inanimate surfaces? A systematic review', *BMC Infect. Dis.*, vol. 6, no. 1, Dec. 2006.
[38] A. P. Williams, L. M. Avery, K. Killham, and D. L. Jones, 'Persistence of Escherichia coli O157 on farm surfaces under different environmental conditions', *J. Appl. Microbiol.*, vol. 98, no. 5, pp. 1075–1083, May 2005.
[39] S. A. Wilks, H. Michels, and C. W. Keevil, 'The survival of Escherichia coli O157 on a range of metal surfaces', *Int. J. Food Microbiol.*, vol. 105, no. 3, pp. 445–454, Dec. 2005.
[40] G. Carré *et al.*, 'Antibacterial textiles functionalized by layer-by-layer assembly of polyelectrolytes and TiO_2 photocatalyst', *RSC Adv*, vol. 5, no. 49, pp. 38859–38867, 2015.
[41] W. W. Nazaroff, 'Four principles for achieving good indoor air quality', *Indoor Air*, vol. 23, no. 5, pp. 353–356, Oct. 2013.
[42] F. Thevenet, L. Sivachandiran, O. Guaitella, C. Barakat, and A. Rousseau, 'Plasma–catalyst coupling for volatile organic compound removal and indoor air treatment: a review', *J. Phys. Appl. Phys.*, vol. 47, no. 22, p. 224011, Jun. 2014.
[43] S.-W. Baek, J.-R. Kim, and S.-K. Ihm, 'Design of dual functional adsorbent/catalyst system for the control of VOC's by using metal-loaded hydrophobic Y-zeolites', *Catal. Today*, vol. 93–95, pp. 575–581, Sep. 2004.
[44] F. Qu, L. Zhu, and K. Yang, 'Adsorption behaviors of volatile organic compounds (VOCs) on porous clay heterostructures (PCH)', *J. Hazard. Mater.*, vol. 170, no. 1, pp. 7–12, Oct. 2009.

[45] Y.-C. Chiang, P.-C. Chiang, and C.-P. Huang, 'Effects of pore structure and temperature on VOC adsorption on activated carbon', *Carbon*, vol. 39, no. 4, pp. 523–534, 2001.
[46] C. Long, P. Liu, Y. Li, A. Li, and Q. Zhang, 'Characterization of Hydrophobic Hypercrosslinked Polymer as an Adsorbent for Removal of Chlorinated Volatile Organic Compounds', *Environ. Sci. Technol.*, vol. 45, no. 10, pp. 4506–4512, May 2011.
[47] L. Pei, J. Zhou, and L. Zhang, 'Preparation and properties of Ag-coated activated carbon nanocomposites for indoor air quality control', *Build. Environ.*, vol. 63, pp. 108–113, May 2013.
[48] Z. Hagiwara, S. Hoshino, H. Ishino, S. Nohara, K. Tagawa, and K. Yamanaka, 'Zeolite particles retaining silver ions having antibacterial properties', US4911898 A, 27-Mar-1990.
[49] J.-S. Chang, 'Recent development of plasma pollution control technology: a critical review', *Sci. Technol. Adv. Mater.*, vol. 2, no. 3–4, pp. 571–576, Jan. 2001.
[50] A. M. Vandenbroucke, R. Morent, N. De Geyter, and C. Leys, 'Non-thermal plasmas for non-catalytic and catalytic VOC abatement', *J. Hazard. Mater.*, vol. 195, pp. 30–54, Nov. 2011.
[51] H. F. Hubbard, B. K. Coleman, G. Sarwar, and R. L. Corsi, 'Effects of an ozone-generating air purifier on indoor secondary particles in three residential dwellings', *Indoor Air*, vol. 15, no. 6, pp. 432–444, Dec. 2005.
[52] W. Zhao, Y. Yang, J. Dai, F. Liu, and Y. Wang, 'VUV photolysis of naphthalene in indoor air: Intermediates, pathways, and health risk', *Chemosphere*, vol. 91, no. 7, pp. 1002–1008, May 2013.
[53] S.-S. Kim, D.-H. Kang, D.-H. Choi, M.-S. Yeo, and K.-W. Kim, 'Comparison of strategies to improve indoor air quality at the pre-occupancy stage in new apartment buildings', *Build. Environ.*, vol. 43, no. 3, pp. 320–328, Mar. 2008.
[54] O. Carp, 'Photoinduced reactivity of titanium dioxide', *Prog. Solid State Chem.*, vol. 32, no. 1–2, pp. 33–177, 2004.
[55] J.-W. Lee, T. Mayer-Gall, K. Opwis, C. E. Song, J. S. Gutmann, and B. List, 'Organotextile Catalysis', *Science*, vol. 341, pp. 1225–1229, Sep. 2013.
[56] J. R. Windmiller and J. Wang, 'Wearable Electrochemical Sensors and Biosensors: A Review', *Electroanalysis*, vol. 25, no. 1, pp. 29–46, Jan. 2013.
[57] M. Radetić, 'Functionalization of textile materials with TiO_2 nanoparticles', *J. Photochem. Photobiol. C Photochem. Rev.*, vol. 16, pp. 62–76, Sep. 2013.
[58] M. Radetić, 'Functionalization of textile materials with silver nanoparticles', *J. Mater. Sci.*, vol. 48, no. 1, pp. 95–107, Jan. 2013.
[59] W. Chen, J. S. Zhang, and Z. Zhang, 'Performance of air cleaners for removing multiple volatile organic compounds in indoor air', *ASHRAE Trans.*, vol. 111, no. 1, pp. 1101–1114, 2005.
[60] S. E. Braslavsky, 'Glossary of terms used in photochemistry, 3rd edition (IUPAC Recommendations 2006)', *Pure Appl. Chem.*, vol. 79, no. 3, Jan. 2007.
[61] A. Kubacka, M. Fernández-García, and G. Colón, 'Advanced Nanoarchitectures for Solar Photocatalytic Applications', *Chem. Rev.*, vol. 112, no. 3, pp. 1555–1614, Mar. 2012.
[62] R. Daghrir, P. Drogui, and D. Robert, 'Modified TiO_2 For Environmental Photocatalytic Applications: A Review', *Ind. Eng. Chem. Res.*, vol. 52, no. 10, pp. 3581–3599, Mar. 2013.
[63] A. Fujishima, X. Zhang, and D. Tryk, 'TiO_2 photocatalysis and related surface phenomena', *Surf. Sci. Rep.*, vol. 63, no. 12, pp. 515–582, Dec. 2008.
[64] T. Yoshihara *et al.*, 'Identification of Reactive Species in Photoexcited Nanocrystalline TiO_2 Films by Wide-Wavelength-Range (400−2500 nm) Transient Absorption Spectroscopy', *J. Phys. Chem. B*, vol. 108, no. 12, pp. 3817–3823, Mar. 2004.
[65] A. Yamakata, T. Ishibashi, and H. Onishi, 'Water- and Oxygen-Induced Decay Kinetics of Photogenerated Electrons in TiO_2 and Pt/TiO_2 : A Time-Resolved Infrared Absorption Study', *J. Phys. Chem. B*, vol. 105, no. 30, pp. 7258–7262, Aug. 2001.
[66] C. Colbeau-Justin, M. Kunst, and D. Huguenin, 'Structural influence on charge-carrier lifetimes in TiO_2 powders studied by microwave absorption', *J. Mater. Sci.*, vol. 38, no. 11, pp. 2429–2437, 2003.

[67] T. Noguchi, A. Fujishima, P. Sawunyama, and K. Hashimoto, 'Photocatalytic degradation of gaseous formaldehyde using TiO_2 film', *Environ. Sci. Technol.*, vol. 32, no. 23, pp. 3831–3833, 1998.

[68] D. S. Bhatkhande, V. G. Pangarkar, and A. A. Beenackers, 'Photocatalytic degradation for environmental applications - a review', *J. Chem. Technol. Biotechnol.*, vol. 77, no. 1, pp. 102–116, Jan. 2002.

[69] C. Turchi, 'Photocatalytic degradation of organic water contaminants: Mechanisms involving hydroxyl radical attack', *J. Catal.*, vol. 122, no. 1, pp. 178–192, Mar. 1990.

[70] H. Kisch, *Semiconductor photocatalysis - Principles and Applications*, Wiley-VCH. 2015.

[71] A. G. Agrios and P. Pichat, 'State of the art and perspectives on materials and applications of photocatalysis over TiO_2', *J. Appl. Electrochem.*, vol. 35, no. 7–8, pp. 655–663, Jul. 2005.

[72] A. N. Kouamé, R. Masson, D. Robert, N. Keller, and V. Keller, 'β-SiC foams as a promising structured photocatalytic support for water and air detoxification', *Catal. Today*, vol. 209, pp. 13–20, Jun. 2013.

[73] D. Lee, M. F. Rubner, and R. E. Cohen, 'All-Nanoparticle Thin-Film Coatings', *Nano Lett.*, vol. 6, no. 10, pp. 2305–2312, Oct. 2006.

[74] M. B. Gawande *et al.*, 'Cu and Cu-Based Nanoparticles: Synthesis and Applications in Catalysis', *Chem. Rev.*, vol. 116, no. 6, pp. 3722–3811, Mar. 2016.

[75] H. Ding, M. K. Ram, and C. Nicolini, 'Nanofabrication of Organic/Inorganic Hybrids of TiO_2 with Substituted Phthalocyanine or Polythiophene', *J. Nanosci. Nanotechnol.*, vol. 1, no. 2, pp. 207–213, Jun. 2001.

[76] D. Dontsova, V. Keller, N. Keller, P. Steffanut, O. Félix, and G. Decher, 'Photocatalytically Active Polyelectrolyte/Nanoparticle Films for the Elimination of a Model Odorous Gas', *Macromol. Rapid Commun.*, vol. 32, no. 15, pp. 1145–1149, Aug. 2011.

[77] K. Sunada, T. Watanabe, and K. Hashimoto, 'Studies on photokilling of bacteria on TiO_2 thin film', *J. Photochem. Photobiol. Chem.*, vol. 156, no. 1–3, pp. 227–233, Mar. 2003.

[78] M. Landmann, E. Rauls, and W. G. Schmidt, 'The electronic structure and optical response of rutile, anatase and brookite TiO_2', *J. Phys. Condens. Matter*, vol. 24, no. 19, p. 195503, May 2012.

[79] M. F. J. Dijkstra, H. J. Panneman, J. G. M. Winkelman, J. J. Kelly, and A. A. C. M. Beenackers, 'Modeling the photocatalytic degradation of formic acid in a reactor with immobilized catalyst', *Chem. Eng. Sci.*, vol. 57, pp. 4895–4907, 2002.

[80] N. Serpone, 'Relative photonic efficiencies and quantum yields in heterogeneous photocatalysis', *J. Photochem. Photobiol. Chem.*, vol. 104, no. 1–3, pp. 1–12, 1997.

[81] K. M. Schindler and M. Kunst, 'Charge-carrier dynamics in titania powders', *J. Phys. Chem.*, vol. 94, no. 21, pp. 8222–8226, 1990.

[82] M. Maeda and T. Watanabe, 'Effects of crystallinity and grain size on photocatalytic activity of titania films', *Surf. Coat. Technol.*, vol. 201, no. 22–23, pp. 9309–9312, Sep. 2007.

[83] T. Matsunaga, R. Tomoda, T. Nakajima, N. Nakamura, and T. Komine, 'Continuous-sterilization system that uses photosemiconductor powders.', *Appl. Environ. Microbiol.*, vol. 54, no. 6, pp. 1330–1333, 1988.

[84] J. Kiwi and V. Nadtochenko, 'Evidence for the Mechanism of Photocatalytic Degradation of the Bacterial Wall Membrane at the TiO_2 Interface by ATR-FTIR and Laser Kinetic Spectroscopy', *Langmuir*, vol. 21, no. 10, pp. 4631–4641, May 2005.

[85] V. A. Nadtochenko, O. M. Sarkisov, V. V. Nikandrov, P. A. Chubukov, and N. N. Denisov, 'Inactivation of pathogenic microorganisms in the photocatalytic process on nanosized TiO_2 crystals', *Russ. J. Phys. Chem. B Focus Phys.*, vol. 2, no. 1, pp. 105–114, 2008.

[86] H. A. Foster, I. B. Ditta, S. Varghese, and A. Steele, 'Photocatalytic disinfection using titanium dioxide: spectrum and mechanism of antimicrobial activity', *Appl. Microbiol. Biotechnol.*, vol. 90, no. 6, pp. 1847–1868, Jun. 2011.

[87] Y. Li, W. Zhang, J. Niu, and Y. Chen, 'Mechanism of Photogenerated Reactive Oxygen Species and Correlation with the Antibacterial Properties of Engineered Metal-Oxide Nanoparticles', *ACS Nano*, vol. 6, no. 6, pp. 5164–5173, Jun. 2012.
[88] I. Fridovich, 'Superoxide Radical and Superoxide Dismutases', *Annu Rev Biochem*, p. 16.
[89] A. Azam, Ahmed, Oves, Khan, Habib, and A. Memic, 'Antimicrobial activity of metal oxide nanoparticles against Gram-positive and Gram-negative bacteria: a comparative study', *Int. J. Nanomedicine*, p. 6003, Dec. 2012.
[90] V. Aruoja, H.-C. Dubourguier, K. Kasemets, and A. Kahru, 'Toxicity of nanoparticles of CuO, ZnO and TiO_2 to microalgae Pseudokirchneriella subcapitata', *Sci. Total Environ.*, vol. 407, no. 4, pp. 1461–1468, Feb. 2009.
[91] I. Sondi and B. Salopek-Sondi, 'Silver nanoparticles as antimicrobial agent: a case study on E. coli as a model for Gram-negative bacteria', *J. Colloid Interface Sci.*, vol. 275, no. 1, pp. 177–182, Jul. 2004.
[92] A. Simon-Deckers *et al.*, 'Size-, Composition- and Shape-Dependent Toxicological Impact of Metal Oxide Nanoparticles and Carbon Nanotubes toward Bacteria', *Environ. Sci. Technol.*, vol. 43, no. 21, pp. 8423–8429, Nov. 2009.
[93] E. Friehs *et al.*, 'Toxicity, phototoxicity and biocidal activity of nanoparticles employed in photocatalysis', *J. Photochem. Photobiol. C Photochem. Rev.*, vol. 29, pp. 1–28, Dec. 2016.
[94] M.-C. Daniel and D. Astruc, 'Gold nanoparticles: assembly, supramolecular chemistry, quantum-size-related properties, and applications toward biology, catalysis, and nanotechnology', *Chem. Rev.*, vol. 104, no. 1, pp. 293–346, 2004.
[95] V. K. Sharma, R. A. Yngard, and Y. Lin, 'Silver nanoparticles: Green synthesis and their antimicrobial activities', *Adv. Colloid Interface Sci.*, vol. 145, no. 1–2, pp. 83–96, Jan. 2009.
[96] N. R. Jana, L. Gearheart, and C. J. Murphy, 'Wet chemical synthesis of silver nanorods and nanowires of controllable aspect ratio', *Chem. Commun.*, no. 7, pp. 617–618, 2001.
[97] J. J. Mock, M. Barbic, D. R. Smith, D. A. Schultz, and S. Schultz, 'Shape effects in plasmon resonance of individual colloidal silver nanoparticles', *J. Chem. Phys.*, vol. 116, no. 15, pp. 6755–6759, Apr. 2002.
[98] R. Jin, Y. Cao, C. A. Mirkin, K. L. Kelly, G. C. Schatz, and J. G. Zheng, 'Photoinduced Conversion of Silver Nanospheres to Nanoprisms', *Science*, vol. 294, no. 5548, pp. 1901–1903, Nov. 2001.
[99] M. Sakamoto, M. Fujistuka, and T. Majima, 'Light as a construction tool of metal nanoparticles: Synthesis and mechanism', *J. Photochem. Photobiol. C Photochem. Rev.*, vol. 10, no. 1, pp. 33–56, Mar. 2009.
[100] G. Mustatea, I. Calinescu, A. Diacon, and L. Balan, 'Photoinduced synthesis of silver/polymer nanocomposites', *Rev. Mater. Plast.*, vol. 51, no. 1, 2014.
[101] G. Mustatea, L. Vidal, I. Calinescu, A. Dobre, M. Ionescu, and L. Balan, 'A photochemical approach designed to improve the coating of nanoscale silver films onto food plastic wrappings intended to control bacterial hazards', *J. Nanoparticle Res.*, vol. 17, no. 1, Jan. 2015.
[102] S. W. Verbruggen *et al.*, 'Plasmonic gold–silver alloy on TiO_2 photocatalysts with tunable visible light activity', *Appl. Catal. B Environ.*, vol. 156–157, pp. 116–121, Sep. 2014.
[103] J. S. Hoskins, T. Karanfil, and S. M. Serkiz, 'Removal and Sequestration of Iodide Using Silver-Impregnated Activated Carbon', *Environ. Sci. Technol.*, vol. 36, no. 4, pp. 784–789, Feb. 2002.
[104] A. Kędziora, M. Speruda, E. Krzyżewska, J. Rybka, A. Łukowiak, and G. Bugla-Płoskońska, 'Similarities and Differences between Silver Ions and Silver in Nanoforms as Antibacterial Agents', *Int. J. Mol. Sci.*, vol. 19, no. 2, p. 444, Feb. 2018.
[105] W. K. Jung, H. C. Koo, K. W. Kim, S. Shin, S. H. Kim, and Y. H. Park, 'Antibacterial Activity and Mechanism of Action of the Silver Ion in Staphylococcus aureus and Escherichia coli', *Appl. Environ. Microbiol.*, vol. 74, no. 7, pp. 2171–2178, Apr. 2008.
[106] M. Yamanaka, K. Hara, and J. Kudo, 'Bactericidal Actions of a Silver Ion Solution on Escherichia coli, Studied by Energy-Filtering Transmission Electron Microscopy and Proteomic Analysis', *Appl. Environ. Microbiol.*, vol. 71, no. 11, pp. 7589–7593, Nov. 2005.

[107] D. W. Hatchett and H. S. White, 'Electrochemistry of sulfur adlayers on the low-index faces of silver', *J. Phys. Chem.*, vol. 100, no. 23, pp. 9854–9859, 1996.
[108] Q. L. Feng *et al.*, 'A mechanistic study of the antibacterial effect of silver ions on Escherichia coli and Staphylococcus aureus', *J. Biomed. Mater. Res.*, vol. 52, no. 4, pp. 662–668, 2000.
[109] T. C. Dakal, A. Kumar, R. S. Majumdar, and V. Yadav, 'Mechanistic Basis of Antimicrobial Actions of Silver Nanoparticles', *Front. Microbiol.*, vol. 7, Nov. 2016.
[110] S. Shrivastava, T. Bera, A. Roy, G. Singh, P. Ramachandrarao, and D. Dash, 'Characterization of enhanced antibacterial effects of novel silver nanoparticles', *Nanotechnology*, vol. 18, no. 22, p. 225103, Jun. 2007.
[111] R. Cai, K. Hashimoto, K. Itoh, Y. Kubota, and A. Fujishima, 'Photokilling of Malignant Cells with Ultrafine TiO_2 Powder', *Bull. Chem. Soc. Jpn.*, vol. 64, no. 4, pp. 1268–1273, 1991.
[112] T. Vitanov and A. Popov, 'Adsorption of SO_4^{2-} on growth steps of (111) and (100) faces of silver single crystals', *J. Electroanal. Chem. Interfacial Electrochem.*, vol. 159, no. 2, pp. 437–441, Dec. 1983.
[113] J. R. Morones *et al.*, 'The bactericidal effect of silver nanoparticles', *Nanotechnology*, vol. 16, no. 10, pp. 2346–2353, Oct. 2005.
[114] S. Pal, Y. K. Tak, and J. M. Song, 'Does the Antibacterial Activity of Silver Nanoparticles Depend on the Shape of the Nanoparticle? A Study of the Gram-Negative Bacterium Escherichia coli', *Appl. Environ. Microbiol.*, vol. 73, no. 6, pp. 1712–1720, Mar. 2007.
[115] N. Niño-Martínez, G. A. Martínez-Castañón, A. Aragón-Piña, F. Martínez-Gutierrez, J. R. Martínez-Mendoza, and F. Ruiz, 'Characterization of silver nanoparticles synthesized on titanium dioxide fine particles', *Nanotechnology*, vol. 19, no. 6, p. 065711, Feb. 2008.
[116] H. Zhang and G. Chen, 'Potent Antibacterial Activities of Ag/TiO_2 Nanocomposite Powders Synthesized by a One-Pot Sol−Gel Method', *Environ. Sci. Technol.*, vol. 43, no. 8, pp. 2905–2910, Apr. 2009.
[117] L. Miao *et al.*, 'Fabrication and photochromic study of titanate nanotubes loaded with silver nanoparticles', *Surf. Sci.*, vol. 601, no. 13, pp. 2792–2799, Jul. 2007.
[118] E. Baur and A. Perret, 'Über die Einwirkung von Licht auf gelöste Silbersalze in Gegenwart von Zinkoxyd', *Helv. Chim. Acta*, vol. 7, no. 1, pp. 910–915, 1924.
[119] A. Fujishima, X. Zhang, and D. Tryk, 'TiO_2 photocatalysis and related surface phenomena', *Surf. Sci. Rep.*, vol. 63, no. 12, pp. 515–582, Dec. 2008.
[120] P. D. Cozzoli, E. Fanizza, R. Comparelli, M. L. Curri, A. Agostiano, and D. Laub, 'Role of Metal Nanoparticles in TiO_2 /Ag Nanocomposite-Based Microheterogeneous Photocatalysis', *J. Phys. Chem. B*, vol. 108, no. 28, pp. 9623–9630, Jul. 2004.
[121] H. Li, X. Duan, G. Liu, and X. Liu, 'Photochemical synthesis and characterization of Ag/TiO_2 nanotube composites', *J. Mater. Sci.*, vol. 43, no. 5, pp. 1669–1676, Mar. 2008.
[122] E. Kowalska *et al.*, 'Silver-modified titania with enhanced photocatalytic and antimicrobial properties under UV and visible light irradiation', *Catal. Today*, vol. 252, pp. 136–142, Sep. 2015.
[123] E. Albiter, Z. Hai, S. Alfaro, H. Remita, M. A. Valenzuela, and C. Colbeau-Justin, 'A Comparative Study of Photo-Assisted Deposition of Silver Nanoparticles on TiO_2', *J. Nanosci. Nanotechnol.*, vol. 13, no. 7, pp. 4943–4948, Jul. 2013.
[124] D. Guin, S. V. Manorama, J. N. L. Latha, and S. Singh, 'Photoreduction of Silver on Bare and Colloidal TiO_2 Nanoparticles/Nanotubes: Synthesis, Characterization, and Tested for Antibacterial Outcome', *J. Phys. Chem. C*, vol. 111, no. 36, pp. 13393–13397, Sep. 2007.
[125] A. Takai and P. V. Kamat, 'Capture, Store, and Discharge. Shuttling Photogenerated Electrons across TiO_2–Silver Interface', *ACS Nano*, vol. 5, no. 9, pp. 7369–7376, Sep. 2011.
[126] A. Henglein, A. Holzwarth, and P. Mulvaney, 'Fermi level equilibration between colloidal lead and silver particles in aqueous solution', *J. Phys. Chem.*, vol. 96, no. 22, pp. 8700–8702, 1992.
[127] D. Tsukamoto, Y. Shiraishi, Y. Sugano, S. Ichikawa, S. Tanaka, and T. Hirai, 'Gold Nanoparticles Located at the Interface of Anatase/Rutile TiO_2 Particles as Active Plasmonic Photocatalysts for Aerobic Oxidation', *J. Am. Chem. Soc.*, vol. 134, no. 14, pp. 6309–6315, Apr. 2012.

[128] H. E. Chao, Y. U. Yun, H. U. Xingfang, and A. Larbot, 'Effect of silver doping on the phase transformation and grain growth of sol-gel titania powder', *J. Eur. Ceram. Soc.*, vol. 23, no. 9, pp. 1457–1464, Sep. 2003.

[129] N. Sobana, M. Muruganadham, and M. Swaminathan, 'Nano-Ag particles doped TiO_2 for efficient photodegradation of Direct azo dyes', *J. Mol. Catal. Chem.*, vol. 258, no. 1–2, pp. 124–132, Oct. 2006.

[130] H. M. Sung-Suh, J. R. Choi, H. J. Hah, S. M. Koo, and Y. C. Bae, 'Comparison of Ag deposition effects on the photocatalytic activity of nanoparticulate TiO_2 under visible and UV light irradiation', *J. Photochem. Photobiol. Chem.*, vol. 163, no. 1–2, pp. 37–44, Apr. 2004.

[131] B. Xin *et al.*, 'Photocatalytic activity and interfacial carrier transfer of Ag–TiO_2 nanoparticle films', *Appl. Surf. Sci.*, vol. 252, no. 5, pp. 2050–2055, Dec. 2005.

[132] A. Vohra, D. Y. Goswami, D. A. Deshpande, and S. S. Block, 'Enhanced photocatalytic inactivation of bacterial spores on surfaces in air', *J. Ind. Microbiol. Biotechnol.*, vol. 32, no. 8, pp. 364–370, Aug. 2005.

[133] A. Biswas, I. S. Bayer, A. S. Biris, T. Wang, E. Dervishi, and F. Faupel, 'Advances in top–down and bottom–up surface nanofabrication: Techniques, applications & future prospects', *Adv. Colloid Interface Sci.*, vol. 170, no. 1–2, pp. 2–27, Jan. 2012.

[134] C. J. Tavares *et al.*, 'PVD-Grown photocatalytic TiO_2 thin films on PVDF substrates for sensors and actuators applications', *Thin Solid Films*, vol. 517, no. 3, pp. 1161–1166, Dec. 2008.

[135] L. A. Brook *et al.*, 'Highly bioactive silver and silver/titania composite films grown by chemical vapour deposition', *J. Photochem. Photobiol. Chem.*, vol. 187, no. 1, pp. 53–63, Mar. 2007.

[136] S. Shahidi, B. Moazzenchi, and M. Ghoranneviss, 'A review-application of physical vapor deposition (PVD) and related methods in the textile industry', *Eur. Phys. J. Appl. Phys.*, vol. 71, no. 3, p. 31302, Sep. 2015.

[137] G. Rosace, R. Canton, and C. Colleoni, 'Plasma enhanced CVD of SiOxCyHz thin film on different textile fabrics: Influence of exposure time on the abrasion resistance and mechanical properties', *Appl. Surf. Sci.*, vol. 256, no. 8, pp. 2509–2516, Feb. 2010.

[138] D. P. Macwan, P. N. Dave, and S. Chaturvedi, 'A review on nano-TiO_2 sol–gel type syntheses and its applications', *J. Mater. Sci.*, vol. 46, no. 11, pp. 3669–3686, Jun. 2011.

[139] B. Mahltig, H. Haufe, and H. Böttcher, 'Functionalisation of textiles by inorganic sol–gel coatings', *J. Mater. Chem.*, vol. 15, no. 41, p. 4385, 2005.

[140] M. Wang, J. Zhao, X. Wang, A. Liu, and K. K. Gleason, 'Recent progress on submicron gas-selective polymeric membranes', *J. Mater. Chem. A*, vol. 5, no. 19, pp. 8860–8886, 2017.

[141] G. Ladam, P. Schaad, J. C. Voegel, P. Schaaf, G. Decher, and F. Cuisinier, 'In Situ Determination of the Structural Properties of Initially Deposited Polyelectrolyte Multilayers', *Langmuir*, vol. 16, no. 3, pp. 1249–1255, Feb. 2000.

[142] J. B. Schlenoff, S. T. Dubas, and T. Farhat, 'Sprayed Polyelectrolyte Multilayers', *Langmuir*, vol. 16, no. 26, pp. 9968–9969, Dec. 2000.

[143] A. Izquierdo, S. S. Ono, J.-C. Voegel, P. Schaaf, and G. Decher, 'Dipping versus Spraying: Exploring the Deposition Conditions for Speeding Up Layer-by-Layer Assembly', *Langmuir*, vol. 21, no. 16, pp. 7558–7567, Aug. 2005.

[144] Y. H. Ko, Y. H. Kim, J. Park, K. T. Nam, J. H. Park, and P. J. Yoo, 'Electric-Field-Assisted Layer-by-Layer Assembly of Weakly Charged Polyelectrolyte Multilayers', *Macromolecules*, vol. 44, no. 8, pp. 2866–2872, Apr. 2011.

[145] J. J. Richardson, M. Bjornmalm, and F. Caruso, 'Technology-driven layer-by-layer assembly of nanofilms', *Science*, vol. 348, no. 6233, pp. aaa2491–aaa2491, Apr. 2015.

[146] S. T. Dubas and J. B. Schlenoff, 'Factors Controlling the Growth of Polyelectrolyte Multilayers', *Macromolecules*, vol. 32, no. 24, pp. 8153–8160, Nov. 1999.

[147] S. S. Shiratori and M. F. Rubner, 'pH-Dependent Thickness Behavior of Sequentially Adsorbed Layers of Weak Polyelectrolytes', *Macromolecules*, vol. 33, no. 11, pp. 4213–4219, May 2000.

[148] P. Bieker and M. Schönhoff, 'Linear and Exponential Growth Regimes of Multilayers of Weak Polyelectrolytes in Dependence on pH', *Macromolecules*, vol. 43, no. 11, pp. 5052–5059, Jun. 2010.

[149] J. Rongé *et al.*, 'Tailoring preparation, structure and photocatalytic activity of layer-by-layer films for degradation of different target molecules', *Catal. Today*, vol. 246, pp. 28–34, May 2015.

[150] R. Merindol, S. Diabang, O. Felix, T. Roland, C. Gauthier, and G. Decher, 'Bio-Inspired Multiproperty Materials: Strong, Self-Healing, and Transparent Artificial Wood Nanostructures', *ACS Nano*, vol. 9, no. 2, pp. 1127–1136, Feb. 2015.

[151] R. Blell *et al.*, 'Generating in-Plane Orientational Order in Multilayer Films Prepared by Spray-Assisted Layer-by-Layer Assembly', *ACS Nano*, vol. 11, no. 1, pp. 84–94, Jan. 2017.

[152] G. Ladam, P. Schaaf, F. J. G. Cuisinier, G. Decher, and J.-C. Voegel, 'Protein Adsorption onto Auto-Assembled Polyelectrolyte Films', *Langmuir*, vol. 17, no. 3, pp. 878–882, Feb. 2001.

[153] L. Szyk, P. Schaaf, C. Gergely, J. C. Voegel, and B. Tinland, 'Lateral Mobility of Proteins Adsorbed on or Embedded in Polyelectrolyte Multilayers', *Langmuir*, vol. 17, no. 20, pp. 6248–6253, Oct. 2001.

[154] Y. Lvov *et al.*, 'Successive Deposition of Alternate Layers of Polyelectrolytes and a Charged Virus', *Langmuir*, vol. 10, no. 11, pp. 4232–4236, Nov. 1994.

[155] A. P. R. Johnston, E. S. Read, and F. Caruso, 'DNA Multilayer Films on Planar and Colloidal Supports: Sequential Assembly of Like-Charged Polyelectrolytes', *Nano Lett.*, vol. 5, no. 5, pp. 953–956, May 2005.

[156] J. Cho and F. Caruso, 'Investigation of the Interactions between Ligand-Stabilized Gold Nanoparticles and Polyelectrolyte Multilayer Films', *Chem. Mater.*, vol. 17, no. 17, pp. 4547–4553, Aug. 2005.

[157] F. N. Crespilho, F. Huguenin, V. Zucolotto, P. Olivi, F. C. Nart, and O. N. Oliveira, 'Dendrimers as nanoreactors to produce platinum nanoparticles embedded in layer-by-layer films for methanol-tolerant cathodes', *Electrochem. Commun.*, vol. 8, no. 2, pp. 348–352, Feb. 2006.

[158] S. Kidambi, J. Dai, J. Li, and M. L. Bruening, 'Selective Hydrogenation by Pd Nanoparticles Embedded in Polyelectrolyte Multilayers', *J. Am. Chem. Soc.*, vol. 126, no. 9, pp. 2658–2659, Mar. 2004.

[159] P. Podsiadlo *et al.*, 'Layer-by-layer assembly of nacre-like nanostructured composites with antimicrobial properties', *Langmuir*, vol. 21, no. 25, pp. 11915–11921, 2005.

[160] S. Srivastava and N. A. Kotov, 'Composite Layer-by-Layer (LBL) Assembly with Inorganic Nanoparticles and Nanowires', *Acc. Chem. Res.*, vol. 41, no. 12, pp. 1831–1841, Dec. 2008.

[161] M. Grandcolas, A. Louvet, N. Keller, and V. Keller, 'Layer-by-Layer Deposited Titanate-Based Nanotubes for Solar Photocatalytic Removal of Chemical Warfare Agents from Textiles', *Angew. Chem. Int. Ed.*, vol. 48, no. 1, pp. 161–164, Jan. 2009.

[162] G. S. Lee, Y.-J. Lee, and K. B. Yoon, 'Layer-by-Layer Assembly of Zeolite Crystals on Glass with Polyelectrolytes as Ionic Linkers', *J. Am. Chem. Soc.*, vol. 123, no. 40, pp. 9769–9779, Oct. 2001.

[163] P. Podsiadlo *et al.*, 'Ultrastrong and Stiff Layered Polymer Nanocomposites', *Science*, vol. 318, no. 5847, pp. 80–83, Oct. 2007.

[164] T. Sasaki, Y. Ebina, K. Fukuda, T. Tanaka, M. Harada, and M. Watanabe, 'Titania Nanostructured Films Derived from a Titania Nanosheet/Polycation Multilayer Assembly via Heat Treatment and UV Irradiation', *Chem. Mater.*, vol. 14, no. 8, pp. 3524–3530, Aug. 2002.

[165] D. S. Kommireddy, A. A. Patel, T. G. Shutava, D. K. Mills, and Y. M. Lvov, 'Layer-by-Layer Assembly of TiO_2 Nanoparticles for Stable Hydrophilic Biocompatible Coatings', *J. Nanosci. Nanotechnol.*, vol. 5, no. 7, pp. 1081–1087, Jul. 2005.

[166] D. N. Priya, J. M. Modak, and A. M. Raichur, 'LbL Fabricated Poly(Styrene Sulfonate)/TiO_2 Multilayer Thin Films for Environmental Applications', *ACS Appl. Mater. Interfaces*, vol. 1, no. 11, pp. 2684–2693, Nov. 2009.

[167] H. Wang, S. Ishihara, K. Ariga, and Y. Yamauchi, 'All-Metal Layer-by-Layer Films: Bimetallic Alternate Layers with Accessible Mesopores for Enhanced Electrocatalysis', *J. Am. Chem. Soc.*, vol. 134, no. 26, pp. 10819–10821, Jul. 2012.

[168] J. Dai and M. L. Bruening, 'Catalytic Nanoparticles Formed by Reduction of Metal Ions in Multilayered Polyelectrolyte Films', *Nano Lett.*, vol. 2, no. 5, pp. 497–501, May 2002.

[169] T. Kruk, K. Szczepanowicz, D. Kregiel, L. Szyk-Warszynska, and P. Warszynski, 'Nanostructured multilayer polyelectrolyte films with silver nanoparticles as antibacterial coatings', *Colloids Surf. B Biointerfaces*, vol. 137, pp. 158–166, Jan. 2016.

[170] S. T. Dubas, P. Kumlangdudsana, and P. Potiyaraj, 'Layer-by-layer deposition of antimicrobial silver nanoparticles on textile fibers', *Colloids Surf. Physicochem. Eng. Asp.*, vol. 289, no. 1–3, pp. 105–109, Oct. 2006.

[171] I. Pastoriza-Santos, D. S. Koktysh, A. A. Mamedov, M. Giersig, N. A. Kotov, and L. M. Liz-Marzán, 'One-Pot Synthesis of Ag@TiO_2 Core−Shell Nanoparticles and Their Layer-by-Layer Assembly', *Langmuir*, vol. 16, no. 6, pp. 2731–2735, Mar. 2000.

[172] D. s. Koktysh *et al.*, 'Biomaterials by Design: Layer-By-Layer Assembled Ion-Selective and Biocompatible Films of TiO_2 Nanoshells for Neurochemical Monitoring', *Adv. Funct. Mater.*, vol. 12, no. 4, pp. 255–265, Apr. 2002.

[173] F. Xiao, 'Layer-by-Layer Self-Assembly Construction of Highly Ordered Metal-TiO_2 Nanotube Arrays Heterostructures (M/TNTs, M = Au, Ag, Pt) with Tunable Catalytic Activities', *J. Phys. Chem. C*, vol. 116, no. 31, pp. 16487–16498, Aug. 2012.

[174] M. M. Mahlambi, A. K. Mishra, S. B. Mishra, A. M. Raichur, B. B. Mamba, and R. W. Krause, 'Layer-by-Layer Self-Assembled Metal-Ion- (Ag-, Co-, Ni-, and Pd-) Doped TiO_2 Nanoparticles: Synthesis, Characterisation, and Visible Light Degradation of Rhodamine B', *J. Nanomater.*, vol. 2012, pp. 1–12, 2012.

[175] Z. Tang, Y. Wang, P. Podsiadlo, and N. A. Kotov, 'Biomedical Applications of Layer-by-Layer Assembly: From Biomimetics to Tissue Engineering', *Adv. Mater.*, vol. 18, no. 24, pp. 3203–3224, Dec. 2006.

[176] J. P. DeRocher, P. Mao, J. Y. Kim, J. Han, M. F. Rubner, and R. E. Cohen, 'Layer-by-Layer Deposition of All-Nanoparticle Multilayers in Confined Geometries', *ACS Appl. Mater. Interfaces*, vol. 4, no. 1, pp. 391–396, Jan. 2012.

[177] J. A. Lee, Y. S. Nam, G. C. Rutledge, and P. T. Hammond, 'Enhanced Photocatalytic Activity using Layer-by-Layer Electrospun Constructs for Water Remediation', *Adv. Funct. Mater.*, vol. 20, no. 15, pp. 2424–2429, Aug. 2010.

[178] J.-H. Kim and S. Shiratori, 'Characterization of TiO_2/Polyelectrolyte thin film fabricated by a layer-by-layer self-assembly method', *Jpn. J. Appl. Phys.*, vol. 44, no. 10R, p. 7588, 2005.

[179] N. Dal'Acqua *et al.*, 'Characterization and Application of Nanostructured Films Containing Au and TiO_2 Nanoparticles Supported in Bacterial Cellulose', *J. Phys. Chem. C*, vol. 119, no. 1, pp. 340–349, Jan. 2015.

[180] M. Grandcolas, L. Sinault, F. Mosset, A. Louvet, N. Keller, and V. Keller, 'Self-decontaminating layer-by-layer functionalized textiles based on WO_3-modified titanate nanotubes. Application to the solar photocatalytic removal of chemical warfare agents', *Appl. Catal. Gen.*, vol. 391, no. 1–2, pp. 455–467, Jan. 2011.

[181] R. Dastjerdi and M. Montazer, 'A review on the application of inorganic nano-structured materials in the modification of textiles: Focus on anti-microbial properties', *Colloids Surf. B Biointerfaces*, vol. 79, no. 1, pp. 5–18, Aug. 2010.

[182] J. H. Xin, W. A. Daoud, and Y. Y. Kong, 'A New Approach to UV-Blocking Treatment for Cotton Fabrics', *Text. Res. J.*, vol. 74, no. 2, pp. 97–100, Feb. 2004.

[183] A. Bozzi, T. Yuranova, and J. Kiwi, 'Self-cleaning of wool-polyamide and polyester textiles by TiO_2-rutile modification under daylight irradiation at ambient temperature', *J. Photochem. Photobiol. Chem.*, vol. 172, no. 1, pp. 27–34, May 2005.

[184] K. T. Meilert, D. Laub, and J. Kiwi, 'Photocatalytic self-cleaning of modified cotton textiles by TiO2 clusters attached by chemical spacers', *J. Mol. Catal. Chem.*, vol. 237, no. 1–2, pp. 101–108, Aug. 2005.

[185] E. Galoppini, 'Linkers for anchoring sensitizers to semiconductor nanoparticles', *Coord. Chem. Rev.*, vol. 248, no. 13–14, pp. 1283–1297, Jul. 2004.

[186] M. Montazer and E. Pakdel, 'Functionality of nano titanium dioxide on textiles with future aspects: Focus on wool', *J. Photochem. Photobiol. C Photochem. Rev.*, vol. 12, no. 4, pp. 293–303, Dec. 2011.

[187] W. A. Daoud and J. H. Xin, 'Nucleation and Growth of Anatase Crystallites on Cotton Fabrics at Low Temperatures', *J. Am. Ceram. Soc.*, vol. 87, no. 5, pp. 953–955, May 2004.

[188] E. Kulaga, L. Ploux, L. Balan, G. Schrodj, and V. Roucoules, 'Mechanically Responsive Antibacterial Plasma Polymer Coatings for Textile Biomaterials: Mechanically Responsive Antibacterial Plasma Polymer Coatings', *Plasma Process. Polym.*, vol. 11, no. 1, pp. 63–79, Jan. 2014.

[189] B. Xu, M. Niu, L. Wei, W. Hou, and X. Liu, 'The structural analysis of biomacromolecule wool fiber with Ag-loading SiO_2 nano-antibacterial agent by UV radiation', *J. Photochem. Photobiol. Chem.*, vol. 188, no. 1, pp. 98–105, Apr. 2007.

[190] K. Hyde, M. Rusa, and J. Hinestroza, 'Layer-by-layer deposition of polyelectrolyte nanolayers on natural fibres: cotton', *Nanotechnology*, vol. 16, no. 7, pp. S422–S428, Jul. 2005.

[191] L. Truong-Phuoc *et al.*, 'Layer-by-Layer Photocatalytic Assembly for Solar Light-Activated Self-Decontaminating Textiles', *ACS Appl. Mater. Interfaces*, vol. 8, no. 50, pp. 34438–34445, Dec. 2016.

[192] Z. Lu, M. Meng, Y. Jiang, and J. Xie, 'UV-assisted in situ synthesis of silver nanoparticles on silk fibers for antibacterial applications', *Colloids Surf. Physicochem. Eng. Asp.*, vol. 447, pp. 1–7, Apr. 2014.

[193] M. Meng, H. He, J. Xiao, P. Zhao, J. Xie, and Z. Lu, 'Controllable in situ synthesis of silver nanoparticles on multilayered film-coated silk fibers for antibacterial application', *J. Colloid Interface Sci.*, vol. 461, pp. 369–375, Jan. 2016.

[194] H. Yang and P. Jiang, 'Self-Cleaning Diffractive Macroporous Films by Doctor Blade Coating', *Langmuir*, vol. 26, no. 15, pp. 12598–12604, Aug. 2010.

[195] H. Tompkins and E. A. Irene, *Handbook of Ellipsometry*. William Andrew, 2005.

[196] M. Rodahl, F. Höök, A. Krozer, P. Brzezinski, and B. Kasemo, 'Quartz crystal microbalance setup for frequency and *Q* -factor measurements in gaseous and liquid environments', *Rev. Sci. Instrum.*, vol. 66, no. 7, pp. 3924–3930, Jul. 1995.

[197] J. F. Moulder, *Handbook of X-ray Photoelectron Spectroscopy: A Reference Book of Standard Spectra for Identification and Interpretation of XPS Data*. Physical Electronics, 1995.

[198] J. M. Hollander and W. L. Jolly, 'X-ray photoelectron spectroscopy', *Acc. Chem. Res.*, vol. 3, no. 6, pp. 193–200, 1970.

[199] J. H. Scofield, 'Hartree-Slater subshell photoionization cross-sections at 1254 and 1487 eV', *J. Electron Spectrosc. Relat. Phenom.*, vol. 8, no. 2, pp. 129–137, 1976.

[200] A. M. Ferraria, A. P. Carapeto, and A. M. Botelho do Rego, 'X-ray photoelectron spectroscopy: Silver salts revisited', *Vacuum*, vol. 86, no. 12, pp. 1988–1991, Jul. 2012.

[201] C. D. Wagner and A. Joshi, 'The auger parameter, its utility and advantages: a review', *J. Electron Spectrosc. Relat. Phenom.*, vol. 47, pp. 283–313, 1988.

[202] V. K. Kaushik, 'XPS core level spectra and Auger parameters for some silver compounds', *J. Electron Spectrosc. Relat. Phenom.*, vol. 56, no. 3, pp. 273–277, 1991.

[203] J. M. Meichtry, C. Colbeau-Justin, G. Custo, and M. I. Litter, 'TiO_2-photocatalytic transformation of Cr(VI) in the presence of EDTA: Comparison of different commercial photocatalysts and studies by Time Resolved Microwave Conductivity', *Appl. Catal. B Environ.*, vol. 144, pp. 189–195, Jan. 2014.

[204] C. C. Rowlands and D. M. Murphy, 'EPR Spectroscopy, Theory', in *Encyclopedia of Spectroscopy and Spectrometry*, Elsevier, 2017, pp. 517–526.

[205] M. Twardoch, 'Layer-by-Layer modification of textiles: development of self decontaminating functionalized textiles', PhD Thesis, Université de Strasbourg, Strasbourg, 2016.

[206] D. Martel, A. Guerra, P. Turek, J. Weiss, and B. Vileno, 'Pertinent parameters in photo-generation of electrons: Comparative study of anatase-based nano-TiO_2 suspensions', *J. Colloid Interface Sci.*, vol. 467, pp. 300–306, Apr. 2016.

[207] M. Twardoch *et al.*, 'Development of an electron paramagnetic resonance methodology for studying the photo-generation of reactive species in semiconductor nano-particle assembled films', *Mol. Phys.*, 2018.
[208] B. Chu, 'Dynamic Light Scattering', in *Soft Matter Characterization*, Springer., R. Borsali and R. Pecora, Eds. 2008, pp. 335–372.
[209] D. N. Priya, J. M. Modak, P. Treb?e, R. ?abar, and A. M. Raichur, 'Photocatalytic degradation of dimethoate using LbL fabricated TiO_2/polymer hybrid films', *J. Hazard. Mater.*, vol. 195, pp. 214–222, Nov. 2011.
[210] K. C. Krogman, N. S. Zacharia, D. M. Grillo, and P. T. Hammond, 'Photocatalytic Layer-by-Layer Coatings for Degradation of Acutely Toxic Agents', *Chem. Mater.*, vol. 20, no. 5, pp. 1924–1930, Mar. 2008.
[211] T.-H. Kim and B.-H. Sohn, 'Photocatalytic thin films containing TiO_2 nanoparticles by the layer-by-layer self-assembling method', *Appl. Surf. Sci.*, vol. 201, no. 1, pp. 109–114, 2002.
[212] D. Dontsova, 'Titania based photocatalytically active layer-by-layer coatings on model surfaces and textile materials', PhD Thesis, Université de Strasbourg, Strasbourg, 2011.
[213] H. de Lasa, B. Serrano, and M. Salaices, 'The energy efficiency factors in photocatalytic processes', in *Photocatalytic reaction engineering*, Springer., pp. 119–123.
[214] P. Barrois, 'Textiles de protection fonctionnalisés auto-décontaminants vis-à-vis d'agents chimiques associant des propriétés photocatalytiques et d'adsorption/filtration', PhD Thesis, Université de Strasbourg, Strasbourg, 2018.
[215] M. A. Fox and M. T. Dulay, 'Heterogeneous photocatalysis', *Chem. Rev.*, vol. 93, no. 1, pp. 341–357, 1993.
[216] K. Matsumoto, K. Nagata, H. Yamamoto, K. Endo, K. Anzai, and I. Aoki, 'Visualization of free radical reactions in an aqueous sample irradiated by 290 MeV carbon beam', *Magn. Reson. Med.*, vol. 61, no. 5, pp. 1033–1039, May 2009.
[217] M. Schönhoff, 'Self-assembled polyelectrolyte multilayers', *Curr. Opin. Colloid Interface Sci.*, vol. 8, no. 1, pp. 86–95, 2003.
[218] R. Kniprath *et al.*, 'Internal Structure of Nanoporous TiO_2 /Polyion Thin Films Prepared by Layer-by-Layer Deposition', *Langmuir*, vol. 23, no. 19, pp. 9860–9865, Sep. 2007.
[219] J. Ma, Y. Jia, Y. Jing, Y. Yao, and J. Sun, 'Synthesis and photocatalytic activity of TiO_2-hectorite layer-by-layer thin films', *Appl. Clay Sci.*, vol. 47, no. 3–4, pp. 433–437, Feb. 2010.
[220] Y. Yan, 'TiO_2 photocatalysts prepared via a sol-gel route assisted by P- and F- containing additives. Applications to the degradation fo MEK and to the elimination of bacteria on surfaces.', PhD Thesis, Université de Strasbourg, Strasbourg, 2016.
[221] T. Salammal Shabi *et al.*, 'Enhancement in crystallinity of poly(3-hexylthiophene) thin films prepared by low-temperature drop casting', *J. Appl. Polym. Sci.*, vol. 125, no. 3, pp. 2335–2341, Aug. 2012.
[222] A. Sarbu, L. Biniek, J.-M. Guenet, P. J. Mésini, and M. Brinkmann, 'Reversible J- to H-aggregate transformation in thin films of a perylenebisimide organogelator', *J. Mater. Chem. C*, vol. 3, no. 6, pp. 1235–1242, 2015.
[223] K. Awazu *et al.*, 'A Plasmonic Photocatalyst Consisting of Silver Nanoparticles Embedded in Titanium Dioxide', *J. Am. Chem. Soc.*, vol. 130, no. 5, pp. 1676–1680, Feb. 2008.
[224] P.-A. Gross, 'Modification de nanotubes de TiO_2 pour la production d'hydrogène par photodissociation de l'eau sous lumière solaire', PhD Thesis, Université de Strasbourg, Strasbourg, 2014.
[225] T. Hirakawa and P. V. Kamat, 'Photoinduced Electron Storage and Surface Plasmon Modulation in Ag@TiO_2 Clusters', *Langmuir*, vol. 20, no. 14, pp. 5645–5647, Jul. 2004.
[226] T. Hirakawa and P. V. Kamat, 'Charge Separation and Catalytic Activity of Ag@TiO_2 Core−Shell Composite Clusters under UV−Irradiation', *J. Am. Chem. Soc.*, vol. 127, no. 11, pp. 3928–3934, Mar. 2005.
[227] M. Blosi, S. Albonetti, M. Dondi, C. Martelli, and G. Baldi, 'Microwave-assisted polyol synthesis of Cu nanoparticles', *J. Nanoparticle Res.*, vol. 13, no. 1, pp. 127–138, Jan. 2011.

[228] A. Takai and P. V. Kamat, 'Capture, Store, and Discharge. Shuttling Photogenerated Electrons across TiO_2–Silver Interface', *ACS Nano*, vol. 5, no. 9, pp. 7369–7376, Sep. 2011.

[229] A. Sclafani and J.-M. Herrmann, 'Influence of metallic silver and of platinum-silver bimetallic deposits on the photocatalytic activity of titania (anatase and rutile) in organic and aqueous media', *J. Photochem. Photobiol. Chem.*, vol. 113, no. 2, pp. 181–188, Feb. 1998.

[230] L. Elsellami, F. Dappozze, A. Houas, and C. Guillard, 'Effect of Ag + reduction on the photocatalytic activity of Ag-doped TiO 2', *Superlattices Microstruct.*, vol. 109, pp. 511–518, Sep. 2017.

[231] J. Yu, J. Xiong, B. Cheng, and S. Liu, 'Fabrication and characterization of Ag–TiO2 multiphase nanocomposite thin films with enhanced photocatalytic activity', *Appl. Catal. B Environ.*, vol. 60, no. 3–4, pp. 211–221, Oct. 2005.

[232] Y. Leprince-Wang, 'Study of the initial stages of TiO_2 growth on Si wafers by XPS', *Surf. Coat. Technol.*, vol. 150, no. 2–3, pp. 257–262, Feb. 2002.

[233] J. R. Pels, F. Kapteijn, J. A. Moulijn, Q. Zhu, and K. M. Thomas, 'Evolution of nitrogen functionalities in carbonaceous materials during pyrolysis', *Carbon*, vol. 33, no. 11, pp. 1641–1653, 1995.

[234] J. L. Hueso, J. P. Espinós, A. Caballero, J. Cotrino, and A. R. González-Elipe, 'XPS investigation of the reaction of carbon with NO, O2, N2 and H2O plasmas', *Carbon*, vol. 45, no. 1, pp. 89–96, Jan. 2007.

[235] P. A. Gross, S. N. Pronkin, T. Cottineau, N. Keller, V. Keller, and E. R. Savinova, 'Effect of deposition of Ag nanoparticles on photoelectrocatalytic activity of vertically aligned TiO_2 nanotubes', *Catal. Today*, vol. 189, no. 1, pp. 93–100, Jul. 2012.

[236] S. Ko, C. K. Banerjee, and J. Sankar, 'Photochemical synthesis and photocatalytic activity in simulated solar light of nanosized Ag doped TiO2 nanoparticle composite', *Compos. Part B Eng.*, vol. 42, no. 3, pp. 579–583, Apr. 2011.

APPENDIX

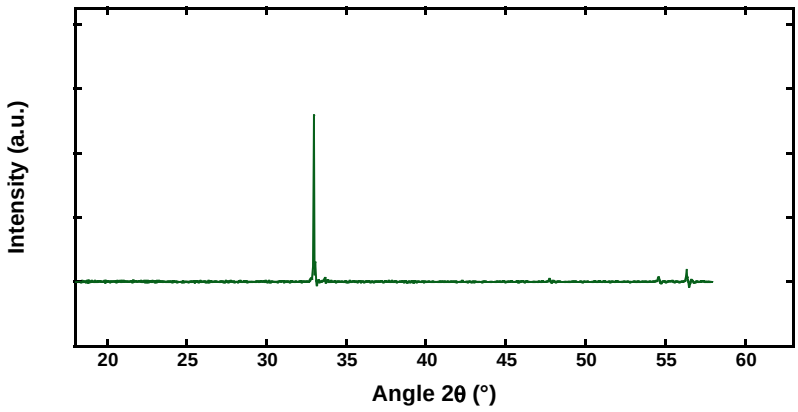

Appendix 1 : XRD characterisation of a bare silicon wafer.

Layer deposited	Mass of material deposited (ng/cm²)		
	3rd overtone	5th overtone	7th overtone
PEI	119.6	125.1	129.7
PSS 1	201.1	201.5	194.2
TiO_2 1	6343.9	5515.6	4998.9
PSS 2	527.1	551.5	563.8
TiO_2 2	9514.4	8336.3	7530.3
PSS 3	1024.2	1077.6	1086.4
TiO_2 3	10857.8	9049.6	7618.7
PSS 4	1865.2	1739.6	1641.1
TiO_2 4	9989.3	5397.2	2671.5

Appendix 2 : Amount of deposited materials on LbL film calculated with QCM-D data.

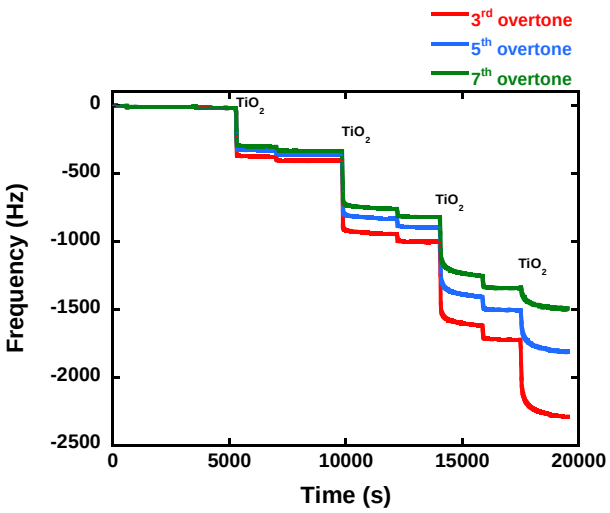

Appendix 3 : Change of frequency overlaying of 3rd, 5th and 7th overtones when film is constructed on QCM quartz slide.

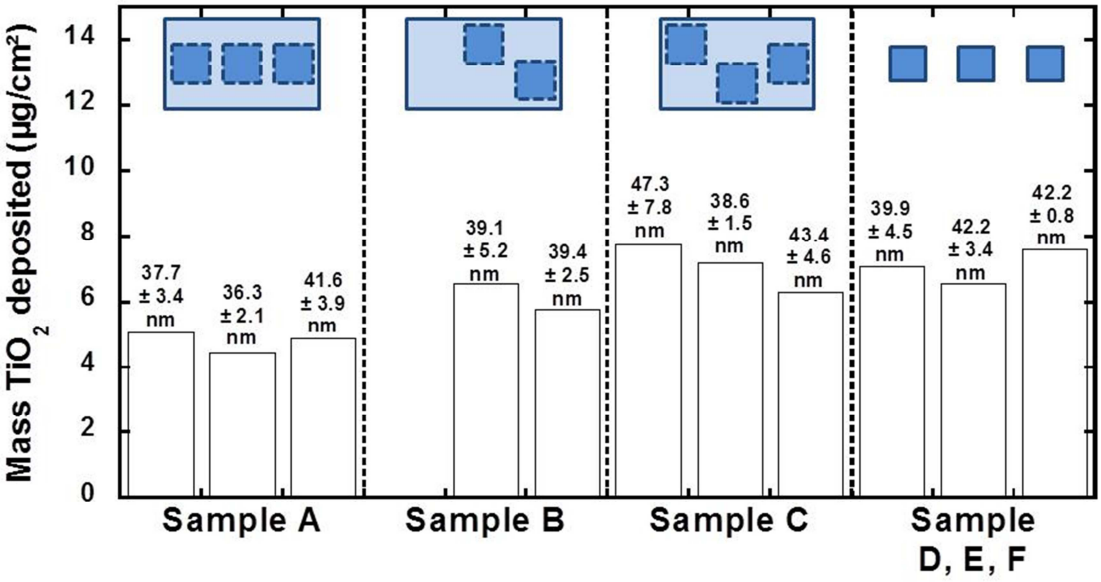

Appendix 4 : Amount of TiO_2 deposited in single layer pair films investigated by ICP-AES. Blue rectangles above every set of samples represent a 36 cm² silicon wafer and dash lines are the area where 4 cm² samples were cut for chemical analysis. Sample D, E and F were directly constructed on 4 cm² silicon wafer. Film thickness is reported above each histogram (measured by ellipsometry).

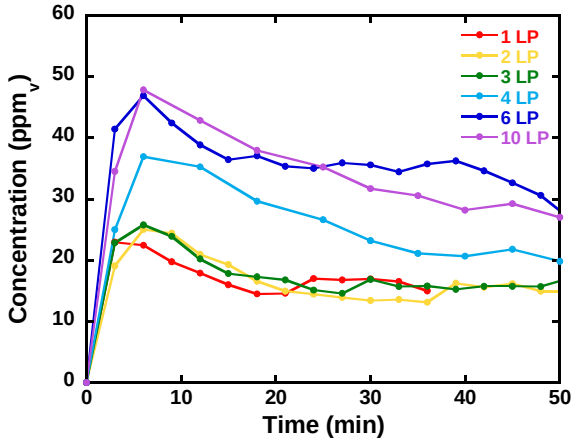

Appendix 5 : Evolution of CO_2 formation during photocatalysis tests without HCOOH

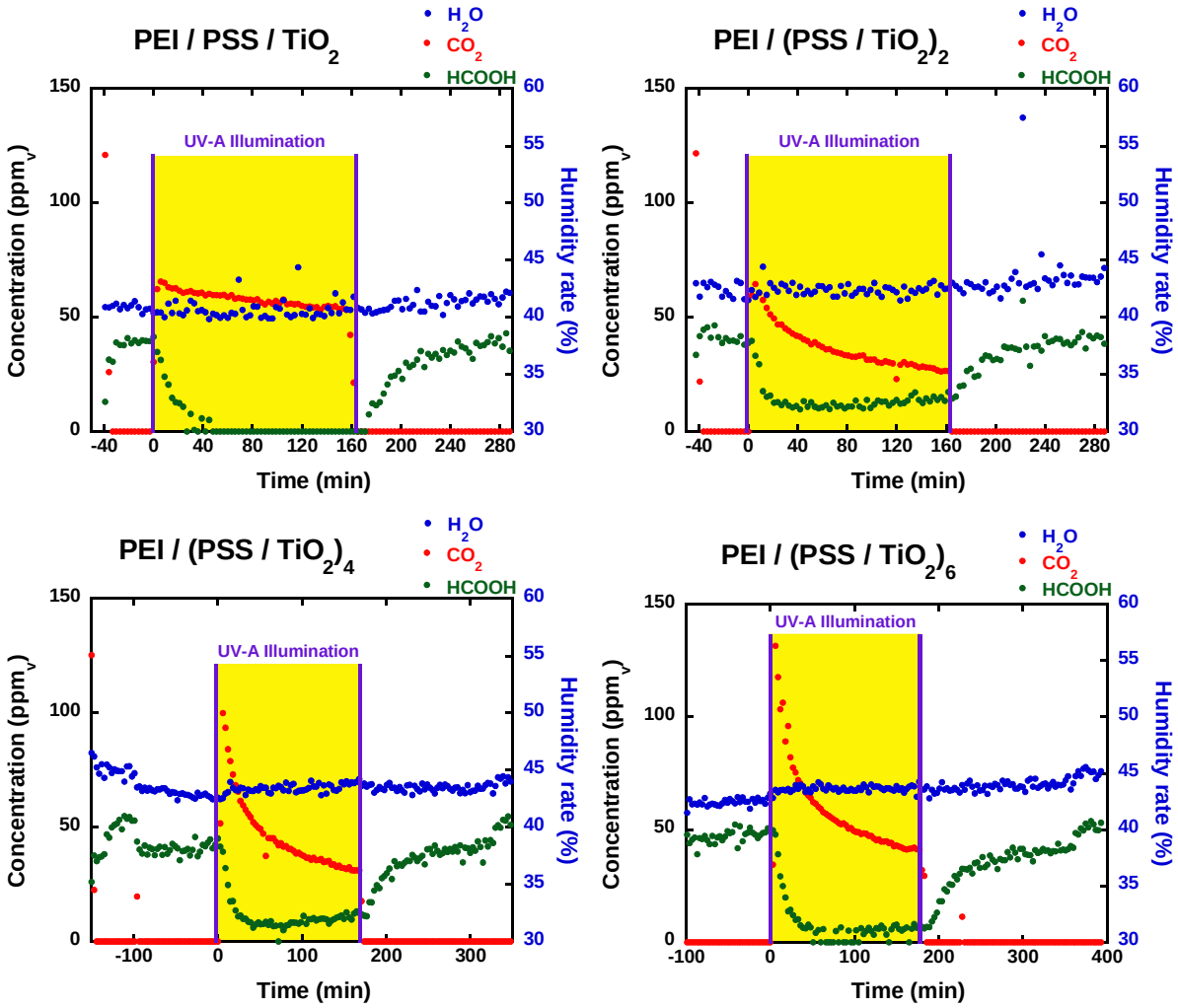

Appendix 6: Evolution of CO_2 and HCOOH concentration curve of LbL film under UV-A illumination.

Method of AgNP deposition	**Film**	**Ag/TiO_2 wt%**	**Ag/TiO_2 at%**
Doctor Blade	PEI/PSS/ TiO_2/$^{5}Ag_C$	0.45	0.34
	PEI/PSS/ TiO_2/$^{20}Ag_C$	0.15	0.12
Photoinduce synthesis with rinsing steps	PEI/PSS/ TiO_2/0,1%Ag^R	0.42	0.32
	PEI/PSS/ TiO_2/0,5%Ag^R	0.95	0.71
	PEI/PSS/ TiO_2/1%Ag^R	1.20	0.89
One-pot synthesis	PEI/PSS/ (0.1%Ag-TiO_2)	2.18	1.93
	PEI/PSS/ (0.2%Ag-TiO_2)	1.66	1.47
	PEI/PSS/ (0.5%Ag-TiO_2)	1.65	1.46
	PEI/PSS/ (0.7%Ag-TiO_2)	0.61	0.54
	PEI/PSS/ (1%Ag-TiO_2)	0.24	0.22
	PEI/PSS/ (1.5%Ag-TiO_2)	0.48	0.42
	PEI/PSS/ (2%Ag-TiO_2)	1.75	1.55

Appendix 7 : Ag content in every film constructed and studied in this work (calculated vs. TiO_2 content)

Core level	**PEI/$(PSS/TiO_2)_{10}$**	**PEI/PSS/(0.2%Ag-TiO_2)**	**PEI/PSS/(1%Ag-TiO_2)**
C 1s	25.02	10.23	12.04
Ti 2p	20.6	12.53	15.63
O 1s	46.49	32.58	39.06
Si 2p	2.022	43.59	32.74
N 1s	1.368	0.9769	0.5308

S 2p	4.502	-	-
Ag 3d	-	0.08335	-
Si/Ti (at.%)	9	77.67	67.68
Ag/Ti (at.%)	-	0.66	-

Appendix 8 : Surface atomic composition of films characterised by XPS

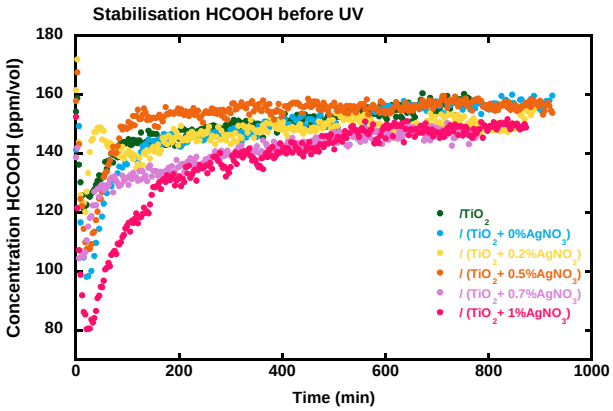

Appendix 9 : Stabilisation of PEI/PSS/(x%Ag-TiO_2) samples prior UV-A irradiation of the films. Experimental parameters: [HCOOH] = 145 ppm_v, air flow = 20 mL/min, speed = 0.7 cm/s, UV-A irradiance = 2.5 mW/cm², films built on 36 cm² silicon wafers

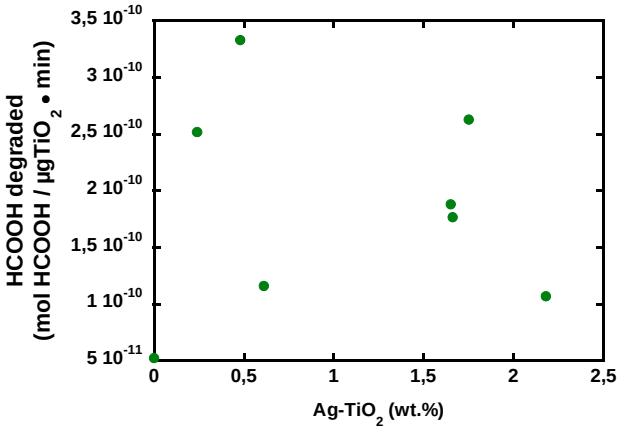

Appendix 10 : Degradation of HCOOH per µg TiO_2•min, in regards to the silver content in PEI/PSS/(x%Ag-TiO_2) films.

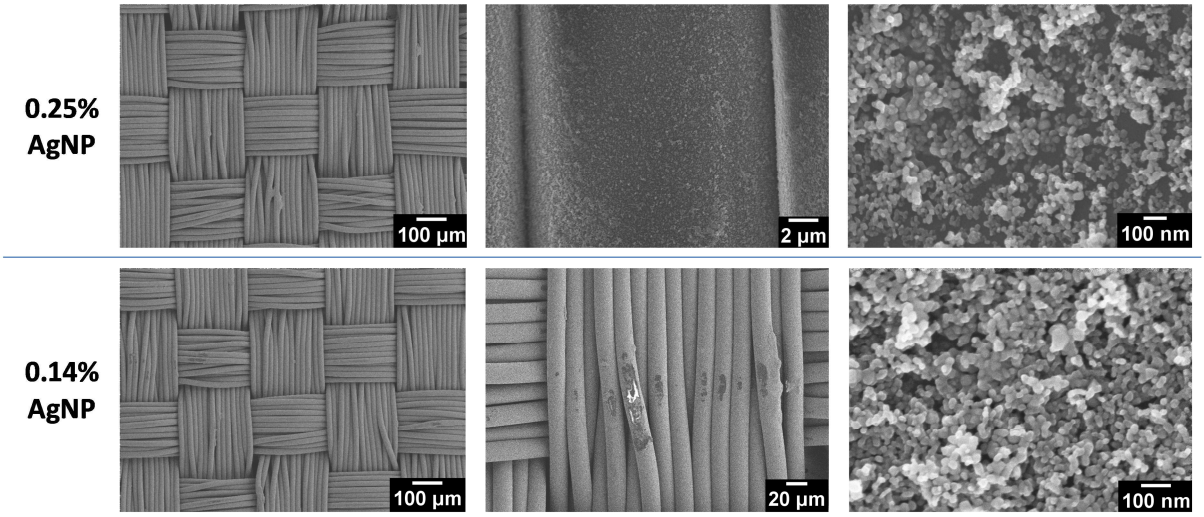

Appendix 11 : SEM images of PEI/PSS/(AgNP-TiO_2) film. No evidences of AgNP can be observed.

	in log UFC				
	Sample	Pseudomonas fluorescens	Stephylococcus aureus	Escherichia coli K12	Listeria monocytogenes
Bare textile	1	3,9	5,16	5,92	3,26
	2	4,41	5,9	5,9	3,36
	3	4,45	5,6	5,95	3,3
PEI / PSS	1	1,17	5,2	5,68	0
	2	2,15	5,17	5,81	0
	3	2,6	5,34	5,72	2,6
PEI / PSS / TiO2	1	2,56	0	3,3	0
	2	1,6	0	3,3	0
	3	2	0	5,19	0
PEI / (PSS / TiO2)4	1	0	0	0	0
	2	0	0	0	0
	3	0	0	0,98	0
PEI / (PSS / TiO2)10	1	0	0	3,62	0
	2	0,72	0	3,51	0
	3	0,02	0	3,34	0
Bacteria seeded		4,98	6,02	6,08	6

Appendix 12 : Assessment of bacteria counting on PEI/$(PSS/TiO_2)_n$ films; in log CFU

Pseudomonas Fluorescens				Eschericha coli			
		Dark	After UV			Dark	After UV
Bare textile	1	5,25	5,03	Bare textile	1	5,08	4,87
	2	5,37	4,70		2	4,81	4,97
	3	5,05	4,85		3	4,75	4,73
	Average	5,22	4,86		Average	4,88	4,86
	stdev	0,16	0,17		stdev	0,18	0,12
PEI / PSS	1	5,38	5,23	PEI / PSS	1	5,62	4,7
	2	5,53	5,55		2	5,04	4,75
	3	5,56	5,38		3	4,64	3,58
	Average	5,49	5,39		Average	5,10	4,34
	stdev	0,10	0,16		stdev	0,49	0,66
PEI / PSS / TiO2	1	5,75	5,32	PEI / PSS / TiO2	1	4,72	2,82
	2	5,26	5,03		2	4,81	0,72
	3	5,08	4,90		3	4,41	0,72
	Average	5,36	5,08		Average	4,65	1,42
	stdev	0,35	0,22		stdev	0,21	1,21
PEI / PSS / (0,25%AgNP-TiO2)	1	5,51	3,16	PEI / PSS / (0,25%AgNP-TiO2)	1	5,53	1,14
	2	5,51	4,58		2	5,71	1,45
	3	4,96	4,60		3	4,9	0
	Average	5,33	4,11		Average	5,38	0,86
	stdev	0,32	0,83		stdev	0,43	0,76
PEI / PSS / (0,14%AgNP-TiO2)	1	4,30	5,09	PEI / PSS / (0,14%AgNP-TiO2)	1	4,76	2,64
	2	5,18	5,16		2	5,74	2,12
	3	4,99	4,08		3	4,81	1,87
	Average	4,82	4,78		Average	5,10	2,21
	stdev	0,46	0,60		stdev	0,55	0,39

Appendix 13 : Assessment of bacteria counting on PEI/PSS/(AgNP-TiO_2) films; in log CFU.

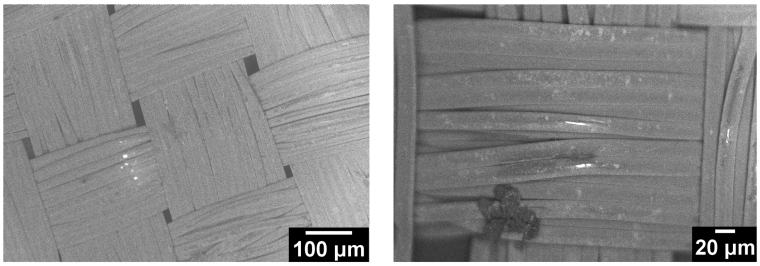

Appendix 14 : SEM images of PEI/PSS/TiO_2 film acquired with ESB detector equipped to the apparatus.

Marvin MOTAY

Multifunctional photocatalytic substrates and textiles constructed *via* Layer-by-Layer self-assembly of Ag and TiO_2 nanoparticles

Résumé

Des films multicouches à base de nanoparticules de TiO_2 et d'Ag ont été construits sur des substrats modèles et des textiles *via* la technique du *Layer-by-Layer* (LbL). Les films à base de nanoparticules de TiO_2 construits sur substrats modèles ont montré un comportement photocatalytique non conventionnel pour la minéralisation de l'acide formique en phase gaz sous irradiation UV-A, et une minéralisation très importante a été obtenue avec un film possédant une unique couche de nanoparticule de TiO_2. Ces films ont également montré des propriétés biocides sous irradiation UV-A. La mise en œuvre d'une méthode *one-pot*, combinant la synthèse photo-induite des nanoparticules d'Ag et dépôt de la couche de TiO_2 par LbL, a permis la synthèse de nanoparticules d'Ag directement au sein des films et une exaltation très importante des propriétés photocatalytiques des films. Les méthodes de constructions ont été transférées avec succès sur textiles. Les films restent photocatalytiquement actifs et biocides sous irradiation UV-A après plusieurs cycles de lavages.

Mots-clés : Photocatalyse, auto-décontamination, Layer-by-Layer, TiO_2, nanoparticules d'Ag, bactérie, acide formique, textile

Résumé en anglais

TiO_2 and Ag nanoparticle multilayered films were constructed on model substrates and textiles via Layer-by-Layer (LbL) assembly. The TiO_2 nanoparticle based films constructed on model substrates showed a non-conventional photocatalytic behaviour for gas phase formic acid mineralisation upon UV-A irradiation, and a high mineralisation was obtained for a single layer TiO_2 nanoparticle film. These films also showed biocidal properties upon UV-A irradiation. The elaboration of a one-pot method, combining the photo-induced synthesis of Ag nanoparticles and the LbL deposition of TiO_2 nanoparticle layer, allowed the direct synthesis of Ag nanoparticles within the films and a high enhancement of the film photocatalytic properties. The construction methods were successfully transfered on textile surfaces. The films were photocatalytically active and biocidal under UV-A irradiation after several washing treatment cycles.

Keywords: Photocatalysis, auto-decontamination, Layer-by-Layer, TiO_2, Ag nanoparticles, bacteria, formic acid, textile